

Aerosol-Assisted Chemical Vapour Deposition (AACVD) of Silver Nanoparticle Decorated Tungsten Oxide Nanoneedle for Use in Oxygen Gas Sensing

Yiyun Zhu

A thesis presented for the degree of
Doctor of Philosophy

Supervised by

Prof. Christopher S. Blackman

Department of Chemistry
The Faculty of Mathematical and Physical
University College London

2021

Declaration

I, Yiyun Zhu, declare that this thesis titled "*Aerosol-Assisted Chemical Vapour Deposition (AACVD) of Silver Nanoparticle Decorated Tungsten Oxide Nanoneedle for Using in Oxygen Gas Sensing*" and the work presented in it are my own and has been generated by me as the result of my own original research. Where the information and technical support has been derived from other sources, I certify that this has been cited and indicated in the thesis.

Acknowledgement

I began to engage in the research of gas sensor since my graduate study. My supervisor Prof. Christopher S. Blackman chose such a topic for me, which is at the forefront of gas sensor research and is of great significance in academic study.

During my PhD research project, I devoted myself to the research of Aerosol-Assisted Chemical Vapour Deposition (AACVD) of Silver Oxide Nanoparticle Decorated Tungsten Oxide Nanoneedles for Using in Oxygen Gas Sensing. This is a relatively new research direction in this academic field, which is filled many difficulties and barriers: such as inability to form films on the substrates and the bottleneck of experimental optimization. My supervisor Prof. Christopher S. Blackman, teachers from other groups and colleagues in the lab all helped me a lot.

First, I would like to express my special gratitude to my supervisor, Prof. Christopher S. Blackman, for giving me this opportunity to further my study. Thank you for giving me valuable advice and continuous support during my four-year doctoral career, encouraging me to overcome academic difficulties and guiding me to grow into a professional researcher.

Besides my supervisor, I would like to thank Dr. Caroline E. Knapp, Dr. Sanjay Sathasivam, for their precious academic advice, guidance and help in my research life. I want to thank Mr. Martin Vickers, Dr. Steve Firth, Dr. Tom Gregory, Dr. Chi Pang and Dr. Robert G. Palgrave for the training and assistance of XRD, SEM, TEM and XPS. Meanwhile, I would like to thank Mr. Tom Bridges for the regular maintenance of the lab equipment for me especially in some urgent time. Special thanks to my colleagues from our research group Dr. Francesco Di Maggio, Dr. Min Ling, Dr. Yaomin Li, Miss Xueming Xia and Mr. Jone-him Tsang, who provided me with a pleasant office environment to and brought me a lot of cherished memories in daily life. I also would

like to thank Mr. Tony Field, Mrs. Ninik Smith, Mrs Judith James and Dr. Jadranka Butorac for their great kindness.

Furthermore, I would like to thank the academic management staff in the department of chemistry for organizing various talks and seminars during the semesters, which broadened my knowledge in different aspects of science and inspired my enthusiasm for learning.

Finally, I would especially like to thank my family members for their trust and love, always inspires me to overcome problems in research and life. I would like to thank my parents not only for their financial support over these years but also their enormous encouragement for me to pursue my PhD study. Most importantly, I would like to thank my deep loving and supportive wife, Xinyi, who decided to give up the high-salary job in China and come to take care of me. I would not finish my PhD dissertation without her selfless dedication and thoughtful kindness along the way.

Abstract

Semiconducting metal oxides (SMOX) gas sensors, such as tungsten oxide (WO_3), have been developed in depth for use in toxic gas detection, such as nitrogen oxides (NO_x). With the addition of catalytic nanoparticles, like Ag, Pt, Pd and etc., the sensing properties, the three 'S' (sensitivity, selectivity and stability), can be significantly improved.

This thesis details a two-step synthesis method for the fabrication of Ag nanoparticle decorated WO_3 nanoneedle by using different silver metal precursors, including silver nitrate (AgNO_3), silver 2-aminoethanol (Ag-EA), silver 1-aminopropan-2-ol (Ag-AP) and silver 2-methyl-2-aminopropan-1-ol (Ag-AMP), in a vapour deposition process. A series of experiments were conducted to investigate the parameters that affect the growth of the materials microstructure including deposition temperature, deposition time, flow rate of N_2 carrier gas and concentration of precursor solution. Physical property characterization techniques including UV/Vis, XRD, XPS, SEM and TEM, have been systematically applied for all WO_3 and Ag-decorated WO_3 samples and sensor materials.

Oxygen sensors' have been considered as the critical component of Engine Management System for several decades. Gas sensing performance was carried out toward different O_2 concentration between 1 and 20% at various operating temperatures. The sensing response revealed that the decoration of Ag nanoparticle on WO_3 sensors significantly improved sensing properties as compared to undecorated WO_3 sensors. An optimal gas response with silver-decorated WO_3 is enhanced 400% compared to an undecorated WO_3 sensor at an optimum operating temperature at 350 °C towards 20% oxygen at a relative humidity level ~ 85% by using AgNO_3 as a precursor. An enhancement was also observed for the Ag decorated WO_3 sensors fabricated using organometallic silver precursors, with a dramatically

increasing in baseline resistance for these Ag@WO₃ sensors. Sensing mechanisms, are proposed to explain the enhancement in sensing response.

Impact Statement

Inside academia

- i. This research widens the selection range of silver metal precursors (AgNO_3 , silver 2-aminoethanol (Ag-EA), silver 1-aminopropan-2-ol (Ag-AP) and silver 2-methyl-2-aminopropan-1-ol (Ag-AMP)) available for aerosol-assisted chemical vapour deposition (AACVD) and makes the growth of Ag@WO_3 thin film morphology controllable simply by altering the deposition parameters.
- ii. The systematic study and characterization of the Ag@WO_3 thin films benefits to the body of knowledge on film growth mechanisms.
- iii. The facile synthesis of Ag@WO_3 nanoneedle opens up a new direction in gas sensing fields as compared to more commonly encountered noble metals, such as Au/Pt/Pd functionalized WO_3 materials, which have been extensively explored and studied.
- iv. The systematic studied on the gas sensing response ascribes the gas sensing enhancement mechanism to two aspects, chemical and electronic sensitization.

Outside academia

- i. The successful synthesis of Ag@WO_3 thin films via AACVD potentially allows manufacture at an industrial relevant scale due to its simple production method, low cost/energy consumption.
- ii. The technology for oxygen sensor has remained in place for twenty years. Though Pb-free alternative electrochemical gas sensors to oxygen have been developed by introducing Zn, Fe or Al on various semiconducting metal oxides (SMOX), like SnO_2 , ZnO , In_2O_3 , and CeO_2 . Ag functionalized WO_3 materials provide an alternative for use as an oxygen gas sensor.

Contents

Declaration.....	2
Acknowledgement.....	3
Abstract.....	5
Impact Statement.....	7
List of Figures.....	11
List of Tables.....	21
List of Abbreviations.....	23
Chapter 1 Introduction.....	24
1.1 Overview.....	24
1.2 Nano-scaled semiconducting metal oxide gas sensor.....	24
1.2.1 Background of nanomaterials.....	24
1.2.2 Background of semiconducting metal oxide gas sensor.....	26
1.2.3 Main parameters of semiconducting metal oxide gas sensors.....	28
1.2.4 Fundamental operating principles of SMOX gas sensors.....	31
1.2.5 Limitations and improvements of semiconducting metal oxide gas sensors.....	36
1.2.6 Background of oxygen gas sensors.....	45
1.3 Background of tungsten oxide and silver metal materials.....	46
1.3.1 Crystal Structure of tungsten oxide.....	46
1.3.2 Different morphologies of WO ₃ nanomaterials for gas sensing.....	48
1.3.3 Silver metal decorated metal oxide nanostructures.....	55
1.4 Aerosol-assisted chemical vapour deposition.....	57
1.4.1 Process and principle of AACVD.....	57
1.4.2 AACVD fabricated tungsten oxide nanostructures.....	59
1.4.3 AACVD fabricated noble metal decorated tungsten oxide.....	61
1.5 Motivation and aims.....	63
Chapter 2 Experimental.....	65
2.1 Aerosol-assisted chemical vapour deposition.....	66
2.2 Measurement of gas sensing tests.....	67
2.3 Physical characterization.....	69

Chapter 3 Nanostructured Tungsten Oxide Thin Film and Sensor: Synthesis and Characterization	71
3.1 Introduction.....	71
3.2 Experimental.....	72
3.2.1 Preparation of WO ₃ thin film.....	72
3.2.2 Preparation of WO ₃ sensor.....	73
3.3 Results and discussion.....	74
3.3.1 Characterization of the WO ₃ thin film	74
3.3.2 Characterization of WO ₃ sensor	83
3.4 Conclusion.....	90
Chapter 4 Nanostructured Silver Decorated Tungsten Oxide Thin Films and Sensors Using Silver Nitrate Precursor: Synthesis and Characterization	92
4.1 Introduction.....	92
4.2 Experimental.....	93
4.2.1 Preparation of Ag thin films	93
4.2.2 Preparation of Ag@WO ₃ thin films on glass substrates	93
4.2.3 Preparation of Ag@WO ₃ thin films on sensors.....	94
4.3 Results and discussions (AgNO ₃)	95
4.3.1 Characterization of Ag thin films.....	95
4.3.2 Characterization of Ag@WO ₃ thin films on glass substrates.....	102
4.3.3 Characterization of Ag@WO ₃ thin films on sensors.....	108
4.4 Conclusion.....	113
Chapter 5 Silver Decorated Tungsten Oxide Thin Films and Sensors Using Organometallic Silver Metal Precursors: Synthesis and Characterization.....	115
5.1 Introduction.....	115
5.2 Experimental.....	117
5.2.1 Preparation of Ag thin films	117
5.2.3 Preparation of organometallic Ag@WO ₃ thin films on sensors.....	118
5.3 Results and discussion	119
5.3.1 Characterization of Ag thin films.....	119
5.3.2 Characterization of Ag@WO ₃ gas sensor	131
5.4 Conclusion	143

Chapter 6 Gas sensing response	145
6.1 Gas sensing response of Ag@WO ₃ prepared using AgNO ₃ as precursor.....	145
6.2 Gas sensing response of Ag@WO ₃ by using organometallic Ag precursors..	148
6.4 Inferred sensing 'mechanism'	157
6.4.1 AgNO ₃ (Ag@WO ₃ sensor).....	157
6.4.2 Organometallic Ag precursors (Ag@WO ₃ sensor)	158
6.5 Conclusion	159
Chapter 7 Conclusion and future work	161
7.1 Conclusions.....	161
7.2 Future work.....	162
REFERENCE	164
APPENDIX.....	187

List of Figures

Chapter 1

Figure 1.1 Different dimensions of the nano-building blocks and of the corresponding hierarchical nanostructures ⁸	25
Figure 1.2 Receptor and transduction functions semiconducting metal oxide gas sensors ³³	32
Figure 1.3 n-type metal oxide semiconductor with an electron depletion layer ⁴¹	33
Figure 1.4 Illustration of conduction processes under depletion layer model ⁴³	34
Figure 1.5 The illustration diagram of change of depletion layer of ZnO when exposure to (a) reductive and (b)oxidative gas ⁴⁵	35
Figure 1.6 Explanation of Band bending at n-p heterojunction interface with no adsorbed species at the surface. (a) Tendency of forming a p-n junction between p-type Co_3O_4 and n-type ZnO. Holes at the lower-energy valance band stimulate electrons at the high-energy conduction band transfer across the interface to get an equilibrium in the Fermi energies (E_F) (b) The formation of depletion layers at the interface on both side of p-n junction due to recombination, generating a potential barrier for electron flow ⁵⁷	37
Figure 1.7 (a), (b) and (c) TEM images of Co_3O_4 -ZnO composite metal oxide; (d) high-angle annular dark field (HAADF) scanning TEM (STEM) image ⁷⁰	38
Figure 1.8 Gas response of pristine ZnO nanofibers (grey squares), Cr_2O_3 decorated ZnO nanofibers (red circles) and ZnO- Cr_2O_3 core-shell nanofibers (blue triangles) towards TMA ⁷⁰	39
Figure 1.9 Structures of additional metal compounds (red) to SMOX (blue) (a) Doped SMOX and (b) loaded SMOX ⁴²	39
Figure 1.10 Sensitization mechanisms of additives loaded on SMOX gas sensors (a) electronic sensitization by Fermi-level control and (b) chemical sensitization by spill-over ³³	40
Figure 1.11 TEM images of Pd nanoparticles loaded on SnO_2 ^{77,85}	41

Figure 1.12 Schematic diagram of the processes taking place at a Pd nanoparticle loaded SnO ₂ surface (R _S is the effective radius of the spill-over zone in process 2 and R _C is the effective capture radius of the collection zone in process 3) ⁷⁷	41
Figure 1.13 Schematic mechanisms of Au-loaded SnO ₂ gas sensors in case of (a) reducing gases (CO and H ₂) and (b) oxidising gases (O ₃) ⁸⁶	42
Figure 1.14 The illustration diagram of electronically coupled additive and SMOX interface for a loaded SMOX (A) unaffected surface and (B) heterojunction/space charge layer formed and controlled by the Fermi-level of the loading ⁴²	43
Figure 1.15 Effect of particle size of SnO ₂ on gas sensitivity to 500 ppm CO ⁸⁸	43
Figure 1.16 Schematic mechanisms of water molecules adsorbed on the surface of SnO ₂ (a) one water molecule for two metal oxides and (b) one water molecular per metal oxide ⁹⁵	45
Figure 1.17 Crystal structure of WO ₃ (A) ideal cubic structure of WO ₃	47
Figure 1.18 (a) low- and (b) high-magnification FESEM images, (c) TEM image and (d) EDS spectrum of prepared WO ₃ nanoparticles ¹²⁶	50
Figure 1.19 Sensitivity of WO ₃ microspheres gas sensor to various 150 ppm gases at 200 °C; (insert) sensitivity of WO ₃ microspheres gas sensor at 200 °C with an increase in concentration of acetone vapour ¹²⁵	50
Figure 1.20 SEM images of 1-D WO ₃ nanostructures (a) nanowires, (b) nanorods, (c) nanofibers and (d) nanobelts ^{127,129,130,132}	52
Figure 1.21 (left) FESEM images of WO ₃ nanosheets (inset is the cross sectional FESEM of WO ₃ nanosheets); (right) Response vs. temperature diagram for WO ₃ nanosheet based sensor to 0.06 and 1% H ₂ ¹³⁶	52
Figure 1.22 FESEM images of WO ₃ nanosheets synthesized under different hydrothermal processing time (a) 5 min, (b) 1 h, (c) 2 h, (d) 4 h, (e) 8 h and (f) Response of M ₁ (WO ₃ nanosheets) and M ₂ (WO ₃ nanoparticles) to various gases (C ₂ H ₅ OH, CO, H ₂ and NH ₃ at 100ppm and NO ₂ at 50 ppb) at 140 °C ¹³⁷	53
Figure 1.23 (a) SEM image of the 3-D WO ₃ nanowall based nanostructures and (b) Response of 3-D WO ₃ sensor as a function of operating temperature as compared	

to commercial WO ₃ sensor ¹³⁹	54
Figure 1.24 (a) SEM image as-synthesized hierarchical flower-like WO ₃ nanostructures, (b) HRTEM image of an individual flower-like WO ₃ structure, (c) HRTEM image of a nanosheet of the flower and (d) Response of WO ₃ based sensor to 40 ppb NO ₂ as a function of operating temperature ¹⁴¹	55
Figure 1.25 (a) TEM and (b-c) HRTEM images of the ZG-Ag 3 wt% hybrid sample. Inset: the corresponding SAED pattern of the ZG-Ag 3 wt% sample ¹⁴⁶	56
Figure 1.26 TEM image of WO ₃ nanowires and Ag ₂ O nanoparticles ¹⁴⁵	57
Figure 1.27 Schematic diagram of AACVD process for deposition of thin films ¹⁶²	58
Figure 1.28 SEM images of as-deposited WO _x thin films on quartz substrate with a varying morphologies from planar to nanorods as function of distance from the reactor inlet (left) to outlet (right) and corresponding substrate surface temperature ¹⁶⁴	59
Figure 1.29 SEM image of plain and doped WO _x thin films produced via AACVD on silica glass substrate at 400 °C by varying the concentration of MTCNTs (a) 0% (b) 0.1% (c) 0.15% (d) 0.2% (e) 0.25% (f) 0.3% and (g) 0.35%-CNTWO ¹⁶⁵	60
Figure 1.30 FESEM images of WO ₃ thin films deposited on alumina substrate by AACVD at (a) 425 °C and (b) 450 °C ¹⁶⁶	61
Figure 1.31 TEM images of WO ₃ nanoneedles with dispersed Au nanoparticles on surface under (a) low magnification and (b) high magnification ⁸¹	62
Figure 1.32 TEM and HRTEM images of the as-deposited Cu ₂ O functionalized WO ₃ (a and b) low magnification; (c and d) high magnification ¹⁷³	63

Chapter 2

Figure 2.1 Schematic diagram of reaction process of AACVD technique.....	66
Figure 2.2 The internal design of homebuilt (a) rectangular-based and (b) square-based AACVD reactors.....	66
Figure 2.3 Equipment used in the oxygen gas sensing tests (a) OWLSTONE OVG-4 which controls the concentration of the oxygen, humidity environment and the	

operating temperature of the tested sensors (b) humidity adjust settings and (c) tested sensor chamber which allows eight sensors to be tested at a same time.

..... 68

Chapter 3

Figure 3.1 XRD patterns of as-deposited WO_{3-x} thin films on glass, quartz and alumina substrates before annealing with reference pattern of alumina Al₂O₃ (PDF 82-1467)..... 76

Figure 3.2 XRD patterns of WO₃ thin film on glass substrate after annealing at 500 °C in air for 2 h with reference pattern of Na₂W₄O₁₃ (PDF#70-2022) and WO₃ (PDF#85-2459)..... 77

Figure 3.3 XRD patterns of tungsten oxide thin film on quartz and alumina substrates after annealing at 500 °C in air for 2 h with reference pattern of Al₂O₃ (PDF#82-1467) and WO₃ (PDF#72-0677)..... 78

Figure 3.4 SEM images of cross section of as-deposited WO_{3-x} thin films..... 80

Figure 3.5 SEM images of as-deposited WO_{3-x} and WO₃ AA thin films on various substrates (a) WO_{3-x} on glass, (b) WO₃ AA on glass, (c) WO_{3-x} on alumina, (d) WO₃ AA on alumina, (e) WO_{3-x} on quartz and (f) WO₃ AA on quartz..... 81

Figure 3.6 XPS W 4f core-level spectra (a) as-deposited WO_{3-x} on glass, (b) WO₃ AA on glass, (c) as-deposited WO_{3-x} on quartz, (d) WO₃ AA on quartz, (e) as-deposited WO_{3-x} on alumina and (f) WO₃ AA on alumina..... 82

Figure 3.7 XPS O 1s core-level spectra (a) as-deposited WO_{3-x} on glass, (b) WO₃ AA on glass, (c) as-deposited WO_{3-x} on quartz, (d) WO₃ AA on quartz, (e) as-deposited WO_{3-x} on alumina and (f) WO₃ AA on alumina..... 83

Figure 3.8 Samples of 2 mm x 2mm blank alumina sensor (left), as-deposited WO₃ on alumina sensor(mid) and WO₃ AA on alumina sensor(right)..... 84

Figure 3.9 XRD patterns of plain alumina sensor with reference pattern of Al₂O₃ (PDF#82-1467) and Au (PDF#01-1174)..... 85

Figure 3.10 XRD patterns of as-deposited WO₃ before annealing and WO₃ after annealing at 500 °C in air for 2 h on alumina sensor with reference pattern of WO₃

(PDF#72-0677).....	86
Figure 3.11 SEM images of (a) bare alumina sensor at low magnification, (b) at high magnification, (c) as-deposited WO_{3-x} on alumina sensor at low magnification, (d) at high magnification, (e) WO_3 AA on alumina sensor at low magnification and (f) at high magnification	87
Figure 3.12 XPS W 4f core-level spectra of (a) as-deposited WO_{3-x} and (b) WO_3 AA on alumina sensor platform.....	88
Figure 3.13 HRTEM images of (a) as-deposited WO_{3-x} with a length of 2.14 μm , (b) high magnification of selected section of as-deposited WO_{3-x} , (c) a cluster of as-deposited WO_{3-x} NNs, (d) annealed WO_3 NNs, (e) high magnification of selected section of annealed WO_3 NNs and (f) a cluster of annealed WO_3 NNs.....	89

Chapter 4

Figure 4.1 XRD patterns of as-deposited Ag thin film on glass substrate by using 0.06g $AgNO_3$ in a 2 :1 mixture of acetone and methanol, at 150 °C and a constant flow of N_2 at 300 sccm, as compared to standard pattern of $AgNO_3$ (PDF#70-0198).	96
Figure 4.2 XRD patterns of as-deposited Ag thin film on glass substrate by using 0.06g $AgNO_3$ in a 2 :1 mixture of acetone and methanol, at 200, 250, 300 and 350 °C and a constant flow of N_2 at 300 sccm, as compared to standard pattern of metal Ag (PDF#87-0718).....	97
Figure 4.3 UV-Vis absorption spectra of as-deposited Ag thin film on glass substrate by using 0.06g $AgNO_3$ in a 2 :1 mixture of acetone and methanol, at 200, 250 and 300 °C and a constant flow of N_2 at 300 sccm.....	98
Figure 4.4 SEM images of as-deposited Ag thin film on glass substrate by using 0.06g $AgNO_3$ in a 2 :1 mixture of acetone and methanol, at 250 °C and a constant flow of N_2 at 300 sccm under different magnifications (a) 1000, (b) 5000, (c) 10000 and (d) 45000.....	99
Figure 4.5 XPS Ag 3d core-level spectra of as-deposited Ag thin film on glass	

substrate by using 0.06g AgNO ₃ in a 2 :1 mixture of acetone and methanol, at 250 °C and a constant flow of N ₂ at 300 sccm.....	100
Figure 4.6 XPS survey spectra of as-deposited Ag thin film on glass by using AgNO ₃ 0.06g at 250 °C and a flow of N ₂ at 300 sccm and plain glass.....	101
Figure 4.7 SEM-EDS spectrum of spherical structures of Ag nanoparticles deposited on glass substrate with 0.06g AgNO ₃ at 250 °C and flow rate of N ₂ at 300 sccm	101
Figure 4.8 XRD patterns of Ag@WO ₃ thin film on glass substrate by using 0.06g AgNO ₃ in a 2 :1 mixture of acetone and methanol, at 200, 225 and 250 °C and a constant flow of N ₂ at 300 sccm, as compared to standard pattern of Na ₂ W ₄ O ₁₃ (PDF#70-2022) and metal Ag (PDF#87-0718).....	103
Figure 4.9 XRD patterns of as-deposited Ag@WO ₃ thin film on glass substrate with various initial amount of AgNO ₃ (0.03 and 0.09 g with 300 sccm of N ₂) and different flow rate of N ₂ (200 and 400 sccm with 0.06 g of AgNO ₃) at 250 °C.....	104
Figure 4.10 XPS Ag 3d core level spectra of as-deposited (a) Ag thin film on glass substrate, (b) Ag@WO ₃ on glass substrate by using 0.06 g AgNO ₃ in a 2 :1 mixture of acetone and methanol, at 250 °C and a constant flow of N ₂ at 300 sccm, (c) O 1s core level spectra of as-deposited Ag@WO ₃ on glass substrate, (d) W 4f spectra of WO ₃ AA on glass substrate and (e) W 4f spectra of as-deposited Ag@WO ₃ AA on glass substrate	105
Figure 4.11 SEM images of as-deposited Ag@WO ₃ thin film on glass substrate by using 0.06g AgNO ₃ in a 2 :1 mixture of acetone and methanol, at 250 °C and a constant flow of N ₂ at 300 sccm under different magnifications (a and b) 30000, (c) 50000 and (d) 70000.....	106
Figure 4.12 SEM-EDS mapping of as-deposited Ag@WO ₃ on glass substrate by using 0.03g AgNO ₃ at 250 °C and a flow of N ₂ at 300 sccm	107
Figure 4.13 EDS spectra of as-deposited Ag@WO ₃ on glass substrate by using 0.03g AgNO ₃ at 250 °C and a flow of N ₂ at 300 sccm.....	108
Figure 4.14 XRD patterns of as-deposited WO ₃ and Ag@WO ₃ deposited on alumina	

gas sensor with 0.09g AgNO ₃ at 250 °C and a flow of N ₂ at 300 sccm	109
Figure 4.15 XPS core level spectra of as-deposited Ag@WO ₃ on alumina sensor (a) W 4f and (b) Ag 3d	110
Figure 4.16 SEM images of (a) as-deposited WO ₃ thin film on alumina sensor substrate, as-deposited Ag@WO ₃ thin film on glass substrate by using 0.06g AgNO ₃ in a 2 :1 mixture of acetone and methanol, at 250 °C and a constant flow of N ₂ at 300 sccm under different magnifications (b) 5000, (c)20000 and (d) 200000	111
Figure 4.17 TEM image of (a) as-deposited Ag@WO ₃ thin film on sensor by using 0.09 g AgNO ₃ in a 2 :1 mixture of acetone and methanol, at 250 °C and a constant flow of N ₂ at 300 sccm and (b) HR-TEM of Ag@WO ₃ sample.....	112
Figure 4.18 HR-TEM EDS spectrum of Ag@WO ₃ on sensor regarding to Figure 4.17a	112

Chapter 5

Figure 5.1 Chemical formula of three organometallic Ag precursors: Ag-EA, Ag-AP	116
Figure 5.2 Ag-AMP deposited on glass with constant deposition temperature at 275°C and flow rate adjustment 400, 200, 190, 170, 160 and 150 sccm.....	120
Figure 5.3 Ag-AMP deposited on glass with constant flow rate of N ₂ at 170 sccm and different deposition temperature 200, 225, 250, 275, 300, 350 and 400 °C	121
Figure 5.4 XRD patterns of as-deposited Ag-AMP thin film on glass with different temperatures, ranging from 225 to 350 °C and a constant flow rate of N ₂ at 170 sccm.....	122
Figure 5.5 UV-VIS adsorption spectra of as-deposited Ag-AMP thin film on glass with increase in temperature from 225 to 350 °C	123
Figure 5.6 Ag-AP deposited on glass with constant flow rate of N ₂ at 170 sccm and different deposition temperature at 225, 250, 275, 300 and 350°C.....	124
Figure 5.7 XRD patterns of as-deposited Ag-AP thin film on glass with different	

temperatures, ranging from 225 to 350 °C and a constant flow rate of N ₂ at 170 sccm	125
Figure 5.8 UV/VIS adsorption spectra of as-deposited Ag-AP thin film on glass with increase temperature from 225 to 350 °C	126
Figure 5.9 Ag-EA deposited on glass with constant flow rate of N ₂ at 170 sccm and different deposition temperature at 225, 250, 275, 300 and 350 °C.....	127
Figure 5.10 XRD patterns of as-deposited Ag-EA thin film on glass with different temperatures, ranging from 225 to 350 °C and a constant flow rate of N ₂ at 170 sccm	128
Figure 5.11 UV/VIS adsorption spectra of as-deposited Ag-EA thin film on glass with increase temperature from 225 to 350 °C	129
Figure 5.12 SEM image of (a) as-deposited Ag-AMP thin film on glass with 10 μL Ag-AMP silver precursor, deposition temperature at 275 °C and flow rate of N ₂ at 170 sccm and (b) literature SEM image of silver film ²¹¹	130
Figure 5.13 HR-TEM image of Ag nanoparticles on as-deposited Ag-AMP thin film on glass with 10 μL silver Ag-AMP precursor, deposition temperature at 275 °C and flow rate of N ₂ at 170 sccm under (a) high magnification and (b) low magnification.	130
Figure 5.14 Pictures of the as-deposited Ag thin film on WO ₃ on alumina sensors with an increasing volume of initial Ag precursor (1, 3, 5 and 10μL, left to right).....	131
Figure 5.15 XRD patterns of as-deposited Ag decorated WO ₃ sensors by using three organometallic Ag metal precursors with 10 μL of the initial precursor solution deposited at 275 °C with a flow rate of N ₂ at 170 sccm and the XRD pattern of annealed WO ₃ sensor, along with reference pattern of Ag (PDF#87-0718)	132
Figure 5.16 XPS Ag3d core-level spectra of (a)Ag-AMP, (b) Ag-AP and (c) Ag-EA with various volume of initial precursor solution used and their corresponding area ratio Ag 3d: W 4f (d) Ag-AMP, (e)Ag-AP and (f)Ag-EA.....	134
Figure 5.17 SEM images of as-deposited Ag@WO ₃ sensors by using Ag-AMP as precursor with various amount of initial precursor solution (a) and (b) 1μL, (c) and	

(d) 3 μL , (e) and (f) 5 μL and (g) and (h) 10 μL , taken under low and high magnification, respectively.....	136
Figure 5.18 SEM images of as-deposited Ag@WO_3 sensors by using Ag-AP as precursor with various amount of initial precursor solution (a) and (b) 1 μL , (c) and (d) 3 μL , (e) and (f) 5 μL and (g) and (h) 10 μL , taken under low and high magnification, respectively.....	137
Figure 5.19 SEM images of as-deposited Ag@WO_3 sensors by using Ag-EA as precursor with various amount of initial precursor solution (a) and (b) 1 μL , (c) and (d) 3 μL , (e) and (f) 5 μL and (g) and (h) 10 μL , with low and high magnification, respectively	139
Figure 5.20 TEM images of as-deposited Ag@WO_3 sensor by using Ag-AMP as precursor with various amount of initial precursor solution (a) and (b) 1 μL , (c) and (d) 3 μL , (e) and (f) 5 μL and (g) and (h) 10 μL ; (i) and (j) the inset shows the crystalline structure of WO_3 NNs and Ag NPs, respectively	141
Figure 5.21 Size distribution of Ag nanoparticles on WO_3 sensors via Ag-AMP precursor (a) 1 μL (b) 3 μL (c) 5 μL and (d) μL 10 corresponding to Figure 5.18 (b), (c), (e) and (g), respectively	142
Figure 5.22 EDS mapping images of Ag@WO_3 on sensor platform (a) electronic image of Ag@WO_3 sample, (b) Ag distribution, (c) O distribution, (d) W distribution and (e) EDS spectrum of the Ag@WO_3 sensor sample	143

Chapter 6

Figure 6.1 Response of undecorated and Ag@WO_3 sensor to 20% O_2 as a function of operating temperature	146
Figure 6.2 Sensor resistance changes of (a) WO_3 sensor and (b) $\text{Ag/Ag}_2\text{O@WO}_3$ sensor to various O_2 concentration at 85% RH.	147
Figure 6.3 Response and recovery time of (a) WO_3 and (b) Ag@WO_3 sensors at various operating temperature	148
Figure 6.4 Sensor resistance changes of (a) Ag-AMP@ WO_3 sensors, (b) Ag-	

AP@WO ₃ sensors and (c) Ag-EA@WO ₃ sensors to various O ₂ concentration (1-5-10-15-20 %) at different operating temperatures ranging from 150 to 300 °C with an undecorated WO ₃ for comparison.....	151
Figure 6.5 Sensor resistance changes of WO ₃ sensor and Ag-AMP 3μL@WO ₃ sensor to various O ₂ concentration (1-5-10-15-20 %) and temperature (150-175-200-225-250-275-300 °C) in ambient environment (~50 % RH)	152
Figure 6.6 Response of WO ₃ and Ag-AMP 3μL@WO ₃ sensor to 20% O ₂ as a function of operating temperature.....	153
Figure 6.7 Sensor resistance changes of WO ₃ sensor and Ag-AP 10μL@WO ₃ sensor to various O ₂ concentration (1-5-10-15-20 %) and temperature (150-175-200-225-250-275-300 °C) in ambient environment (~50 % RH).....	154
Figure 6.8 Response of WO ₃ and Ag-AP 10μL@WO ₃ sensor to 20% O ₂ as a function of operating temperature	155
Figure 6.9 Sensor resistance changes of WO ₃ sensor and Ag-EA 3μL@WO ₃ sensor to various O ₂ concentration (1-5-10-15-20 %) and temperature (150-175-200-225-250-275-300 °C) in ambient environment (~50 % RH).....	156
Figure 6.10 Response of WO ₃ and Ag-EA 3μL@WO ₃ sensor to 20% O ₂ as a function of operating temperature	157
Figure 6.11 Energy band structure schematic diagrams of Ag and n-type WO ₃ semiconductors (a) before contact (b) in contact and (c) Ag-WO ₃ M-S junction ²²⁰	159
Figure 6.12 Schematic model of depletion layer for (a) undecorated WO ₃ nanosheets and (b) Ag decorated WO ₃ nanosheets when exposure in air(O ₂) ²²⁰	159
Apx 1 TGA (red) and DSC (black) curves of three organometallic Ag precursors ...	187

List of Tables

Chapter 1

Table 1.1 Metal oxide response type behaviour	28
Table 1.2 Formula to calculate the sensitivity of SMO gas sensors regarding to different conductive type and target gas	29
Table 1.3 Lattice constant of different polymorphs of WO_3^{110}	47

Chapter 3

Table 3.1 Deposition conditions of as-deposited WO_3 -x on different substrate, in which A and M stand for acetone and methanol	73
Table 3.2 Deposition conditions of as-deposited WO_3 -x on alumina sensor	74
Table 3.3 As-deposited WO_3 -x and annealed WO_3 thin film on glass, quartz and alumina substrate as compared to the plain substrates, respectively	75

Chapter 4

Table 4.1 Reaction conditions of $AgNO_3$ deposited on glass substrate	93
Table 4.2 Reaction conditions of $Ag@WO_3$ AA on glass substrate	94
Table 4.3 Reaction conditions of formation of $Ag@WO_3$ on alumina sensor	95
Table 4.4 Elemental analysis of SEM-EDS spectrum of Ag decorated WO_3 substrate	108

Chapter 5

Table 5.1 Reaction conditions of organometallic Ag metal precursor on glass	118
Table 5.2 Reaction conditions of organometallic Ag metal precursors on WO_3 sensors	

.....	119
Table 5.3 XPS peaks for Ag nanoparticles	133

List of Abbreviations

1-D	One-dimensional
2-D	Two-dimensional
3-D	Three-dimensional
AACVD	Aerosol-assisted chemical vapour deposition
Acac	Acetylacetone
Ag-AMP	Silver 2-methyl-2-aminopropan-1-ol
Ag-AP	Silver 1-aminopropan-2-ol
Ag-EA	Silver 2-aminoethanol
CVD	Chemical Vapour Deposition
CNT	Carbon nanotubes
E_f	Fermi level or Fermi energy
E_g	Bandgap Energy
eV	Electronvolt
EDS	Energy-dispersive X-ray spectroscopy
FESEM	Field emission scanning electron microscopy
HRTEM	High resolution transmission electron microscopy
JCPDS	Joint Committee on Powder Diffraction Standards
NNs	Nanoneedles
NPs	Nanoparticles
O_v	Oxygen vacancy
SHE	Standard hydrogen electrode
sccm	Standard cubic centimeters per minute
SEM	Scanning electron microscopy
SMOX	Semiconducting metal oxides
SPR	Surface plasmon resonance
Uv-Vis	Ultraviolet-visible
XPS	X-ray photoelectron spectroscopy
XRD	X-ray diffraction

Chapter 1 Introduction

1.1 Overview

The issue of air pollution is still a major concern all over the world. Even though the human nose serves as a highly sensitive sensing system, it still fails if absolute gas concentration or odourless gases need to be detected, which poses a serious threat to human health^{1,2}. Semiconducting metal oxides (SMOX) gas sensors have been widely studied and used in gas detection fields due to advantages including low cost, compact size, simple measurement and easy production^{3,4}. Noble metal nanoparticles, typically Pt, Pd and Au, significantly enhance the gas sensing properties when doped or loaded on the SMOX surface. Tungsten oxide (WO_3) have been widely studied and developed in many applications due to its unique physical and chemical properties. What's more, numerous fabrication techniques have been reported for the synthesis of nano-scaled WO_3 in various microstructures to further enhance its outstanding properties in many fields⁵. In this chapter, the basic operating principle and sensing mechanism of nano-scaled semiconducting metal oxide gas sensor, the limitation and improvements of SMOX gas sensors, the properties and applications of tungsten oxide, noble metal decorated tungsten oxide and silver decorated metal oxide materials, the operating principle of the aerosol-assisted chemical vapour deposition (AACVD) technique and the motivation and aims of this research project will be introduced.

1.2 Nano-scaled semiconducting metal oxide gas sensor

1.2.1 Background of nanomaterials

Nanomaterials refer to powders, fibres, blocks and other structures composed of particles of nanometre size (1-100 nm), in which the specific surface area, surface energy and surface tension of nanoparticles increase sharply with the reduction of particle size⁶. Due to characteristics of small size effect, surface interface effect,

quantum confinement effect and macroscopic quantum tunnelling effect, nanomaterials show different physical and chemical properties from bulk materials, such as unique optical, electrical, magnetic and mechanical properties, which has attracted much attention⁷⁻¹².

Nano Building Blocks	Hierarchical nanostructures
0-D nanoparticles	0-3 hollow
1-D nanowires, nanorods	1-1 comb 1-1 comb 1-1 Brush
	1-2 dendrite
	1-3 urchin 1-3 thread 1-3 hollow urchin
2-D nanosheets	2-3 flower 2-3 hollow flower
3-D nanocubes	3-3 hollow

Figure 1.1 Different dimensions of the nano-building blocks and of the corresponding hierarchical nanostructures⁸.

Gas sensing using nanomaterials such as pure metal, metal oxide and organic based materials has received growing attention due to potential for enhancement of sensing properties, such as sensitivity, selectivity and response time. It is well known that the properties of materials are determined by their structure, and the crystal surface activity and specific surface ratio exposed by different morphologies of nanostructured metal oxide materials have a significant influence on the functional properties of the material. Nanomaterial's crystals are often anisotropic and the periodicity and density of the original arrangement along the different directions of the crystal lattice are distinct.

Therefore, it can be inferred that the crystal surface exposed by different morphologies is also different leading to different physical and chemical characteristics in different directions. In general, dimension control, heterogeneous control and doping are regarded as the main methods to realize new functional characteristics in nanomaterials. So far, a variety of nanostructured materials with different morphologies have been synthesized, including from zero-dimensional materials to three-dimensional materials, such as nanoparticles, nanorods, nanotubes, nanowires, nano fibre, nanobelts, nano slice, nano needle, nano flowers, nano-sea urchins, nano comb and nano cube, as shown in Figure 1.1, and the controllable synthesis of the morphology and size of semiconducting metal oxide nanomaterials in order to achieve the regulation of their properties is an important aspect of the field. This thesis mainly describes work on n-type WO_3 and Ag-decorated WO_3 semiconducting metal oxide nanomaterials and this chapter focuses on this material in detail.

1.2.2 Background of semiconducting metal oxide gas sensor

Gas sensing is an important branch of the sensor field. Human daily life and industrial activities are closely related to the surrounding environmental atmosphere, and the change of atmosphere caused by industrial waste gas, combustion of fossil fuel and great discharge of automobile exhaust can greatly affect human beings. However, due to the limited sensitivity of the human olfactory system, the sensitivity to some poisonous and harmful gases and inflammable and explosive gases, especially colourless and odourless gases, is weak. For instance, lack of oxygen can ultimately lead to death, whilst even small, undetectable (by humans), concentrations of harmful or poisonous gases and volatile organic compounds (VOCs), such as NO_2 , NH_3 , SO_2 , HCHO and C_7H_8 in the atmosphere can pose a serious chronic danger to people's health. Therefore, a great deal of effort is targeted on development of advanced gas sensors for gas detection, control and alarm in complex conditions with superior performance, simple fabrication and low cost.

The complexity and adjustability of the electrical properties of metal oxides make them interesting in various applications such as optoelectronics¹³⁻¹⁵, gas sensors¹⁶⁻¹⁸, solar cells¹⁹ and catalysts^{20,21}. Braver et al. discovered that the conductivity of CuO changed with the adsorption of water vapour, fabricating the first kind of semiconductor-based humidity sensor in 1931²². In the 1950s, Walter Brattain, Nobel laureate in physics, first reported the phenomenon of changes in the electrical conductivity of semiconductors caused by changes in the surrounding gas composition at Bell Labs, thus shifting the focus of gas sensitivity research to the study of gas adsorption by semiconductor materials²³⁻²⁵. Since the 1960s, the study of gas sensing began to shift to the practical stage of device development. In 1962, Seiyama et al. first developed a gas sensor based on semiconducting zinc oxide film and monitored O₂, CO and flammable gases on the characteristics of resistance change caused by gas adsorption and desorption at a certain temperature²⁶⁻²⁸. In 1968, Taguchi et al. produced the first commercial gas sensor based on a semiconducting metal oxide (SnO₂), ('Taguchi' sensors are still marketed to this day)²⁹. Subsequently, the research focus of gas sensing has shifted to how to improve the gas sensing properties of such gas sensing devices.

Over the past few decades, a great number of methods to detect the composition of gases have been explored and corresponding gas sensor technologies developed, such as (i) optical, (ii) catalytic, (iii) thermal, (iv) electrochemical, (v) infrared, (vi) surface acoustic wave and (vii) semiconductor gas sensors^{30,31}. This thesis mainly focuses on semiconductor gas sensors and therefore their working principle will be explained in detail. Semiconducting metal oxide gas sensors can be divided into two general operating principles; resistive (or conductive) and non-resistive (non-conductive). In the former, when the sensitive material is in contact with the analyte gas, its resistance changes with the concentration and composition of the detected gas; the latter is based on the adsorption and reaction of the gas, so that some of its relationship characteristics are changed to directly or indirectly detect the gas, such as

the volt-ampere characteristics of the diode and the threshold voltage change of the field effect transistor. For a resistive gas sensor, the change in the interaction between the semiconducting material and the analyte gas can be further divided into a surface control type and a body control type.

Semiconducting metal oxide nanomaterials can be divided into n-type and p-type metal oxide semiconductors based on their resistance response to gases classed as 'oxidising' or 'reducing'. For materials in which the conductivity increases (resistance decreases) with increasing concentration of a reducing gas is an n-type semiconductor, and the main carriers are considered to be free electrons whereby the electron concentration is larger than the hole concentration. Its representative materials are, ZnO, WO₃ and SnO₂. A p-type sensing material is one in which conductivity increases (resistance decreases) with increasing concentration of oxidizing gas, the main carrier being holes whereby the hole concentration is greater than the concentration of free electrons. Representative materials are Cu₂O, NiO, and Cr₂O₃. The response type of several metal oxides is summarized and listed in Table 1.1

Table 1.1 Metal oxide response type behaviour

Material	Type of conductivity	
	n	p
Metal oxides	SnO ₂ , ZnO, TiO ₂ , In ₂ O ₃ , MoO ₃ , MgO, Al ₂ O ₃ , Ga ₂ O ₃ , Nb ₂ O ₅ , ZrO ₂ , CaO, V ₂ O ₅ , Ta ₂ O ₅ , WO ₃	NiO, CeO ₂ , Mn ₂ O ₃ , Co ₃ O ₄ , La ₂ O ₃ , Y ₂ O ₃ , PdO, Ag ₂ O, Bi ₂ O ₃ , Sb ₂ O ₃ , TeO ₂ , CuO, Cr ₂ O ₃

1.2.3 Main parameters of semiconducting metal oxide gas sensors

Gas sensors have been in use for monitoring and detecting toxic, combustible and explosive gases in industrial and domestic environment. In order to evaluate the quality of gas sensor, the most significant performance parameters are summarized, named the three 'S' (sensitivity, selectivity and stability). Other than these, recovery time, response time, operating temperature and power consumption are also other important parameters.

1.2.3.1 Sensitivity

Sensitivity, or gas response, is an index to measure the change in the sensor resistance caused by the change of the target gas concentration. The higher the sensitivity of material, the better the accuracy of the gas sensor and the more conducive to the practical application of the device made by such material. For semiconducting metal oxide gas sensors, the sensitivity is generally expressed by the ratio of the resistance of the sensor before and after the reaction with the target gas, which shown in the table below. R_a is the resistance of the gas sensor in the air or inert gas and R_g is the resistance of the gas sensor in the target gas.

Table 1.2 Formula to calculate the sensitivity of SMO gas sensors regarding to different conductive type and target gas

SMO gas sensor	Reducing gas	Oxidising gas
'n type'	$S = R_a/R_g$	$S = R_g/R_a$
'p type'	$S = R_g/R_a$	$S = R_a/R_g$

1.2.3.2 Selectivity

Selectivity refers to the ability of gas sensor to independently distinguish a particular target gas among different gases under the same test condition. If the sensitivity of the sensor to a certain gas is much higher than the sensitivity to other gases, it indicates that the sensor has a good selectivity to the target gas. Most semiconducting metal oxide (SMOX) gas sensors, they tend to respond to several gases at the same time. To improve their selectivity, it is necessary to improve the response value of one or a particular kind of gases, so as to carry out selection distinction.

1.2.3.3 Stability

Stability is an important factor to evaluate the reliability of the gas sensor and whether

it can be applied to practical use. The operating environment of the gas sensors is affected by dust, humidity, and temperature in the environment, as well as the temperature and humidity carried by the target gas itself. And with the extension of gas sensor working time, its base resistance, sensitivity and other characteristics inevitably drift. In short, the stability is reflected in the anti-interference ability of gas sensors to the environment.

1.2.3.4 Response and Recovery time

Response and recovery time is an important index to evaluate whether a gas sensitive material has the ability to monitor target gas in real time. The shorter the response and recovery time, the faster the sensor's response and the faster it resets to baseline condition.

Response time is defined as the time taken for the resistance value of the sensor to reach 90% of the difference between the initial resistance value of the sensor (baseline) and the stable resistance value after interaction with target gas (sensing resistance).

$$t_{res} = | R_a - R_g | \cdot 90\%$$

After removing the target gas, the time taken for the resistance value of the sensor to change to 90% of the difference between the initial sensing resistance value and the final stable baseline value is defined as the recovery time.

$$t_{rec} = | R_g - R_a | \cdot 90\%$$

The above listed are the basic characteristic parameters for evaluating the performance of gas sensors. However, in practical applications, it is necessary to comprehensively consider the specific environment of gas sensors, the lower limit of

gas concentration detection, gas concentration detection range, energy consumption, volume, life span, fabrication cost and later maintenance and other factors.

1.2.3.5 Operating temperature

Operating temperature is the temperature at which the sensor is tested. Lower operating temperature means longer service life and lower energy consumption. In general, MOS gas sensors need to be tested at high temperature (e.g., range between 200 and 400 °C). The MOS gas sensors' gas-sensitive reaction kinetics is closely related to temperature; at a lower operating temperature the chemical activity of MOS gas-sensitive material is lower and hence the sensitivity and/or response times are negatively affected. With increasing test temperature, the chemical activity of the material increases, and sensitivity increases, and response time reduces. As the temperature rises further, the gas adsorption reaction will be inhibited which will result in the decrease in the gas sensitivity. Therefore, the MOS gas-sensitive material will have an optimal operating temperature, at which the material will have the highest sensitivity and the best response rate to a specific target gas. (Metal Oxide Gas Sensor: Sensitivity and Influencing Factors)

1.2.4 Fundamental operating principles of SMOX gas sensors

The exact mechanisms that cause a gas response are complex, but for chemiresistive SMOX gas sensors, the working principle involves two main functions, namely the receptor and the transduction functions. The receptor function is the target gas molecules interacting with surface of metal oxide, acting either as an electron donor (hole acceptor; reducing gases) or an electron acceptor (hole donor; oxidizing gas). The transduction function means the conversion of these surface phenomena into an electrical resistance change within the sensors^{4,32,33}. Both receptor and transduction functions are illustrated in Figure 1.2.

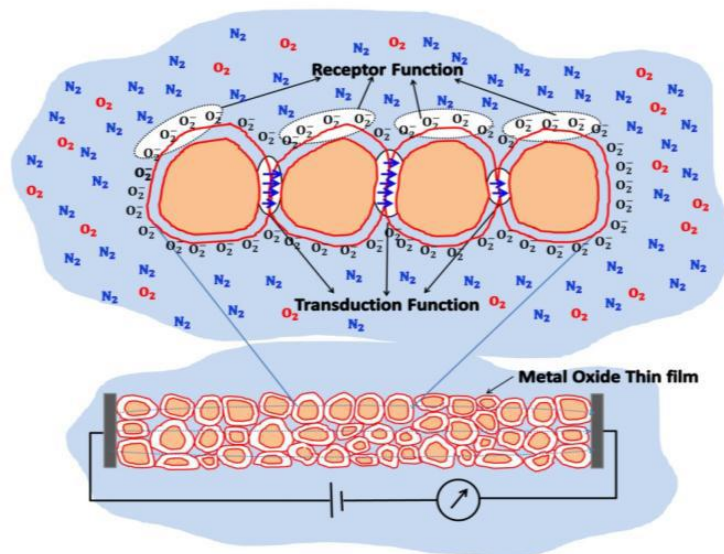


Figure 1.2 Receptor and transduction functions semiconducting metal oxide gas sensors³³.

Korotcenkov and Cho concluded that the receptor function involves the ability of the oxide surface to interact with the target gas. In pure oxide devices, the chemical properties of the surface oxygen on oxides are considered to be responsible for this function, in other word, oxygen vacancy (O_v) defects. As reported, O_v defects on the material surfaces benefit the exchanging of the surface charge by introducing more coordinately unsaturated metal atoms, resulting in accumulating more free electrons^{34–36}. But when an additive, like a noble metal, is applied to the oxide surface, this function can be greatly altered to cause a large change in sensitivity. The transduction function is responsible for converting signals generated by the chemical interactions of the oxide surface (change of work function) into electrical signal, and this function is considered to be mainly controlled by the size of grain boundary contacts between particles.

Given its concentration in the atmosphere, oxygen (20%, 200000 ppm) plays a predominant role in the adsorption process, and its lone pair of electrons and high electronegativity (~ 3.65 on the Pauling scale), makes it readily adsorb on the metal oxide surface. When interacting with the metal oxide surface, oxygen is thought to act as an electron acceptor, in the process becoming ionized³⁷, with the diatomic oxygen

molecule turning into an ionic form (O_2^-) by gaining an electron from the conduction band of metal oxide surface (for an n-type material)³⁸. According to Barsan and Weimer³⁹ and Yamazoe et al.⁴⁰, at higher temperatures (over 200°C), oxygen molecular species are further ionized into atomic species by accepting two electrons; either a dissociative form (O^-) or as lattice oxygen (O^{2-}) as shown in Eq. 1 and Eq. 2. As shown in Figure 1.3, this adsorption and ionization of ambient molecular oxygen results in a reduction in the number of surface electrons (for an n-type metal oxide), called the space charge region⁴¹.

Increasing numbers of electrons trapped on the surface of grains increase the depth of the space charge region and hence the height of the potential barrier between grains, which reduces the conduction of electrons between grains hence influencing the transduction function of the metal oxide surface³².

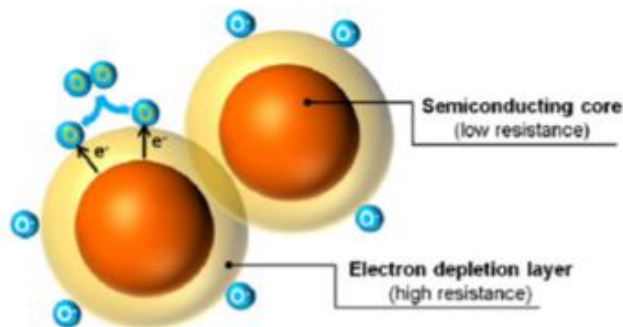
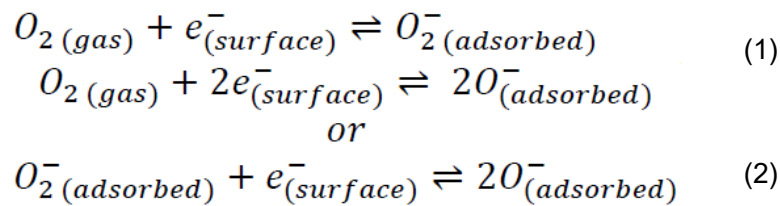
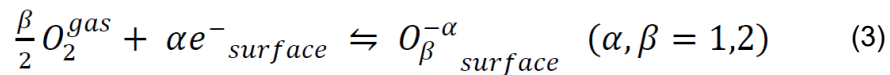


Figure 1.3 n-type metal oxide semiconductor with an electron depletion layer⁴¹

Therefore, the adsorption and desorption of oxygen molecules is transduced to corresponding changes in the measured electrical resistance on the surface of the metal oxide, and the chemisorption of oxygen on the metal oxide surface can be illustrated as given in Eq. 3, where O_2^{gas} is an oxygen molecule in the ambient atmosphere and e^- is an electron with enough energy to reach the metal oxide surface by crossing the potential barrier in the space charge region.



From an electrical point of view, the surface chemistry and the formation of space charge layers (receptor function) and the charge transportation in the sensing layer (transduction function) leads to a band bending at the surface of the grains, as shown in Figure 1.4 For electron-depletion layers, electrons need to overcome the energy barrier at the grain-grain contacts⁴².

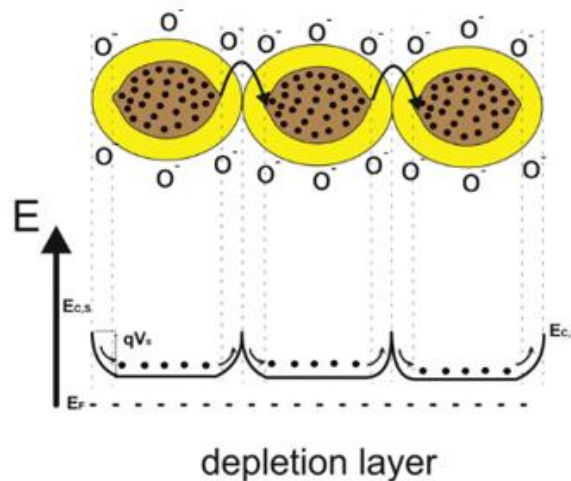


Figure 1.4 Illustration of conduction processes under depletion layer model⁴³

As shown in Figure 1.5, Wei et.al show how the depletion layer forms in (n-type) ZnO nanostructures and how the thickness of the depletion layer is changed when exposed to a reductive gas (H_2 , CO , CO_2 , NH_3 , H_2S and CH_4) or an oxidative gas (NO , NO_2 , O_3

and O_2). In both cases, initially, on exposure to ambient O_2 the resistance of the ZnO nanostructures increases as the electrons are extracted by the absorbed O_2^- , O^- or O^{2-} ions and the depletion layer is formed. For sensing a reductive gas, the gas reacts with the O^- ions and hence releases the electrons trapped on the surface and hence the depletion layer gets thinner and the resistance of the ZnO decreases. In contrast for an oxidative gas molecule, increased adsorption of species further extracts the electrons from the ZnO nanostructures instead of releasing them. Thus, the depletion layer gets thicker and the resistance of ZnO increases. The change of the resistance can be monitored to give a measure of the concentration of the analyte gas^{44,45}.

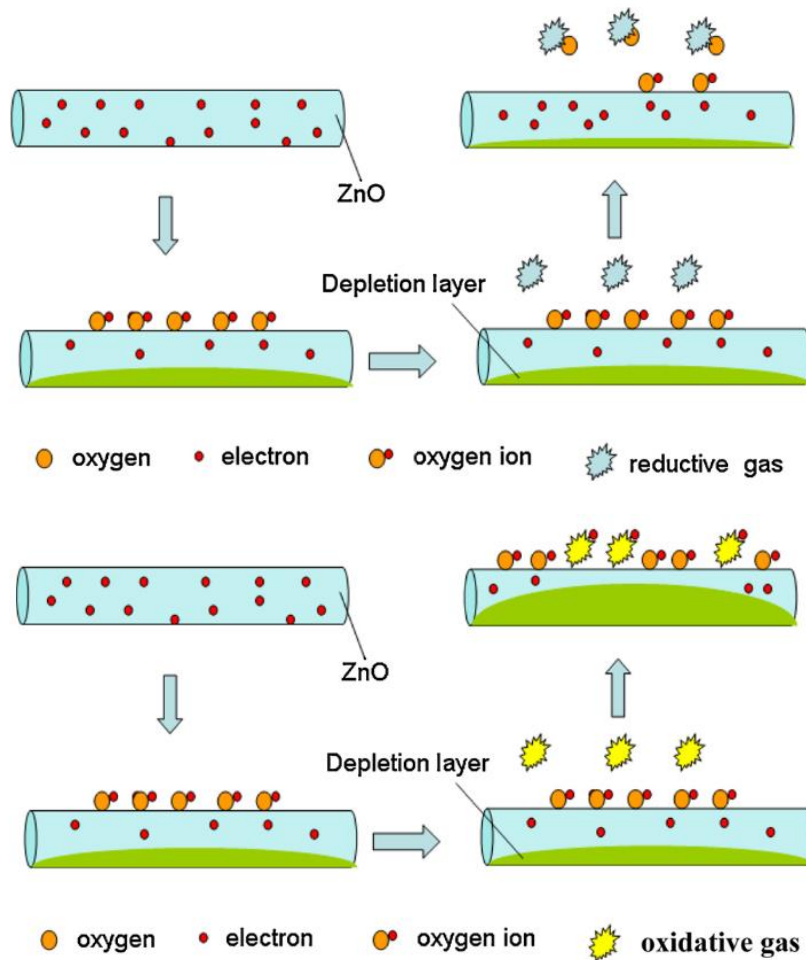


Figure 1.5 The illustration diagram of change of depletion layer of ZnO when exposure to (a) reductive and (b)oxidative gas⁴⁵

1.2.5 Limitations and improvements of semiconducting metal oxide gas sensors

Many papers and theoretical analyses conclude that the gas sensing performance of MOS gas sensors can be influenced by many factors, including intrinsic properties and external causes, such as base materials, noble metal additives, microstructure, surface area of the sensing thin film layer, and operating temperature and humidity⁴⁶.

1.2.5.1 Composite metal oxides

Over recent decades, the use of composite metal oxide have been extensively studied for the detection of simple gases as the selectivity and other important sensing parameters can be significantly enhanced^{47–50}. By incorporating two dissimilar metal oxides together, the Fermi levels across the physical interface can be equilibrated to the same energy, leading to a charge transfer and the formation of a charge depletion layer, as shown in Figure 1.6, Electrons have to overcome the potential energy barrier at the interface caused by different initial Fermi levels of the original materials, which is the basic principle for the enhancement of the sensing performance. These improvements can be attributed into two main categories, including electronic effects (band bending, charge carrier separation and depletion manipulation)^{51–53} and chemical effects (synergistic surface effect, catalytic activity and surface area enhancement)^{54–56}.

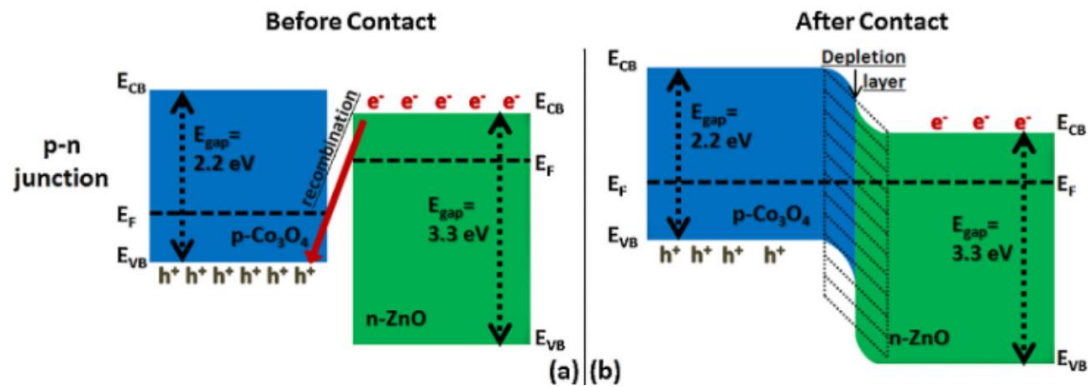


Figure 1.6 Explanation of Band bending at n-p heterojunction interface with no adsorbed species at the surface. (a) Tendency of forming a p-n junction between p-type Co_3O_4 and n-type ZnO. Holes at the lower-energy valence band stimulate electrons at the high-energy conduction band transfer across the interface to get an equilibrium in the Fermi energies (E_F) (b) The formation of depletion layers at the interface on both side of p-n junction due to recombination, generating a potential barrier for electron flow⁵⁷

Early in 1998, after a series of tests under identical sensing test conditions towards CO, Yu and Choi found that composite ZnO-SnO₂ sensors showed significantly enhanced sensitivity compared to pristine ZnO or SnO₂ sensors, which suggested that the sensors fabricated by mixed metal oxides were more sensitive than individual component alone, attributed to a synergistic effect between the two metal oxides components⁵⁸. However de Lacy Costello et al. concluded that the gas sensor performance will not always be enhanced for all composites as compared with those of the individual components and properties will only be enhanced when the components can complement each other⁵⁹. After a series of investigations, they showed that the sensitivity towards organic gases increased with an increasing addition of ZnO powder to SnO₂ powder only from 25 to 50 wt%^{56,59,60}. Therefore, in composite metal oxide materials, it is very important to understand clearly the actual dispersion state and composition of each components because it will greatly affect the behaviour of the material as a sensor⁶¹. For instance, Shaposhnik et al. found that for identical composition TiO₂-SnO₂ composite gas sensors, the optimum composition for H₂ sensing performance was different for different synthesis methods, with 10%TiO₂ the optimum addition for co-precipitation but 20% for mechanical mixing⁶².

Other than the synergistic effect, the heterojunction interface, a physical interface of two dissimilar materials, also contributes to the improvement of the composite metal oxide gas sensing performance^{63–65}. As one of the most common heterojunction interfaces, the p-n junction has been extensively studied in order to regulate gas sensing properties^{66–68}. Na et al. published that the gas sensitivity and selectivity towards NO₂ and C₂H₅OH of n-type ZnO nanowires were enhanced by the deposition of nano-scale p-type Co₃O₄ islands, ascribed to the catalytic effect of nanocrystalline Co₃O₄ and the effect of the p-n junction which caused an extension of the electron depletion layer⁶⁹. A similar study by Woo et al. showed that the gas response of n-type ZnO nanofibers towards the reducing gas tri-methylamine (TMA) can be significantly enhanced when decorated with nanoislands of p-type Cr₂O₃ decorated. In contrast a lower gas response was found when the ZnO nanofibers were completely coated by Cr₂O₃ indicating a synergistic effect between the two materials⁷⁰.

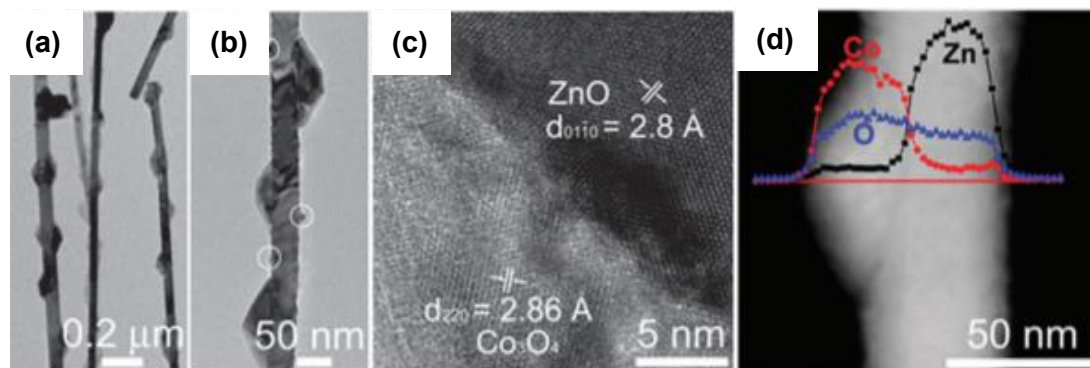


Figure 1.7 (a), (b) and (c) TEM images of Co₃O₄-ZnO composite metal oxide; (d) high-angle annular dark field (HAADF) scanning TEM (STEM) image⁷⁰

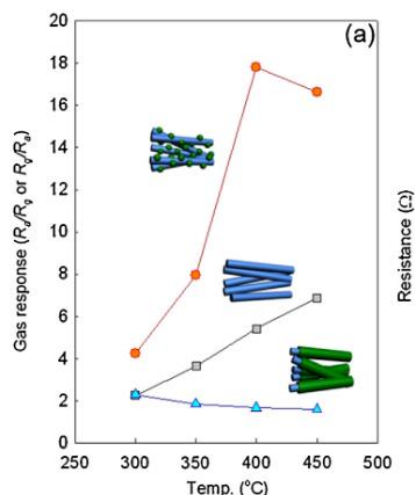


Figure 1.8 Gas response of pristine ZnO nanofibers (grey squares), Cr₂O₃ decorated ZnO nanofibers (red circles) and ZnO-Cr₂O₃ core-shell nanofibers (blue triangles) towards TMA⁷⁰

1.2.5.2 Doping and loading with an additional compound, typically noble metals

Gas sensing properties are strongly dependent on the structures of SMOX and the additional metal compound. As shown in Figure 1.9, the incorporation of noble metal additives can either on the surface of the metal oxide (loading, or decoration) or in the bulk lattice (doping)^{71,72}. Loading refers specifically to structures that are a separate additive phase, in which the dimensions are generally much smaller than SMOX^{73–76}.

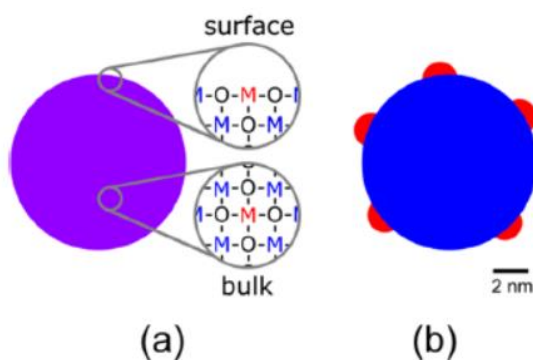


Figure 1.9 Structures of additional metal compounds (red) to SMOX (blue) (a) Doped SMOX and (b) loaded SMOX⁴²

Many studies have shown that addition of metal or metal oxide particles into a pristine material can greatly improve its gas sensing performance. In the gas-solid-phase reaction of the gas sensing tests, the number of surface-active sites is always a crucial

factor to determine the rate of the adsorption and desorption reactions. But in general, the surface-active sites of n-type SMOX, such as ZnO and SnO₂, etc. are very few. The addition of metal or metal oxide particles to the surface of the metal oxide layer provides more active sites for the reaction, which is conducive for gas-solid-phase and gas-gas-phase reactions on the surface of the SMOX gas sensors. Moreover, different types of active sites are beneficial to the adsorption of different gases, which greatly improves the selectivity of such metal or metal oxide particle modified gas sensors⁷⁷. In the 1980s, two fundamental mechanisms were put forward by Yamazoe et al.^{32,78} and Morrison³⁷ for understanding the role of noble metal additives in gas sensor research through chemical or electronic sensitization, viz the spill-over and Fermi-level control sensitization mechanisms respectively, shown in Figure 1.10. Many studies have shown the improvement of gas response after modification by noble metals, such as Au, Ag, Pt, Pd and etc⁷⁹⁻⁸³.

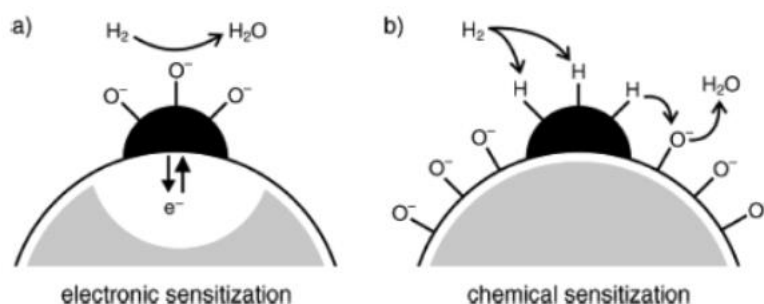


Figure 1.10 Sensitization mechanisms of additives loaded on SMOX gas sensors (a) electronic sensitization by Fermi-level control and (b) chemical sensitization by spill-over³³

The spill-over mechanism, as the most commonly recognized chemical sensitization of SMOX gas sensors, refers to a 'spill-over' of reactive species, viz the formation of reactive species on the metallic additive cluster phase and their subsequent transportation to another phase^{78,84}. Kolmakov et al. explored the mechanism in detail with the *in-situ* deposition of Pd nanoparticles on SnO₂ nanowires. The representative TEM images of Pd-loaded SnO₂ are shown in Figure 1.11. The sensitivity towards O₂ and H₂ exhibited a significant improvement, attributed to the catalytic dissociation of absorbed molecules on the Pd nanoparticle surfaces followed by the diffusion of

dissociated atomic species to the SnO_2 surface, which shown in Figure 1.12. Process 1 is the ionosorption of oxygen at the pristine surface of SnO_2 , whilst such ionosorption is greatly increased in process 2 as the Pd nanoparticles catalytically activate the dissociation of oxygen molecules, i.e., the “spill-over effect”, resulting in increasing of atomic oxygen ions located on the SnO_2 surface and a faster degree of electron withdrawal from the surface. The net result of these chemical effects is to significantly enhance the gas response toward oxygen, and consequently to changes in the surface oxygen concentration.

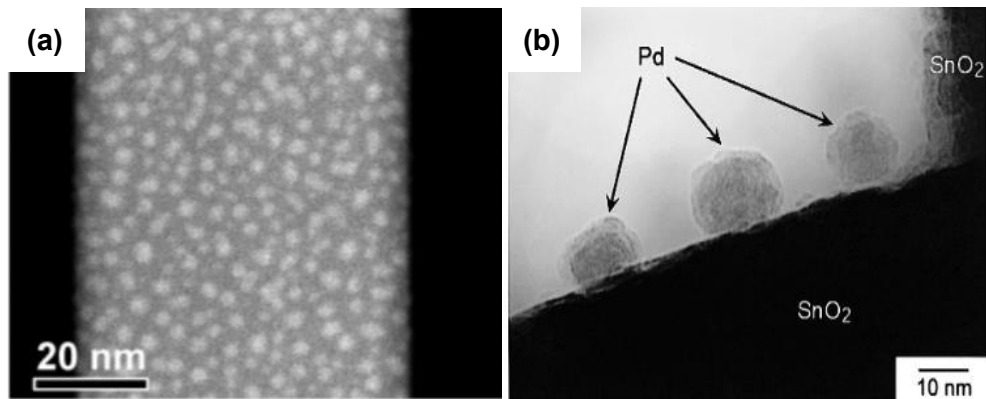


Figure 1.11 TEM images of Pd nanoparticles loaded on SnO_2 ^{77,85}

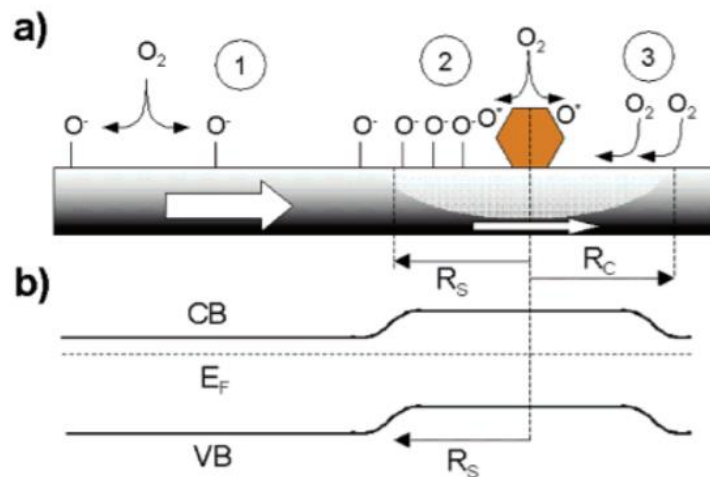


Figure 1.12 Schematic diagram of the processes taking place at a Pd nanoparticle loaded SnO_2 surface (R_s is the effective radius of the spill-over zone in process 2 and R_c is the effective capture radius of the collection zone in process 3)⁷⁷

Korotcenkov et al. presented a study on deposition of Au nanoparticles on the SnO₂ surface and proposed a mechanism of sensitization in these SnO₂: Au-based gas sensors. The results showed that the addition of Au nanoparticles was active to both reducing and oxidising gases. The optimal gas response was obtained with the smallest size of the gold nanoparticles. To interpret the results observed, three assumptions were made; (i) the chemical state of Au nanoparticles remains in a metallic state when interacting with reducing gases (ii) processes that occur around Au nanoparticles are responsible for improving the sensor's response and (iii) an inverse spill-over of oxygen (oxygen species are transferred from the surface of the metal oxide to the Au nanoparticles) is more likely to occur than forward spill-over⁸⁶.

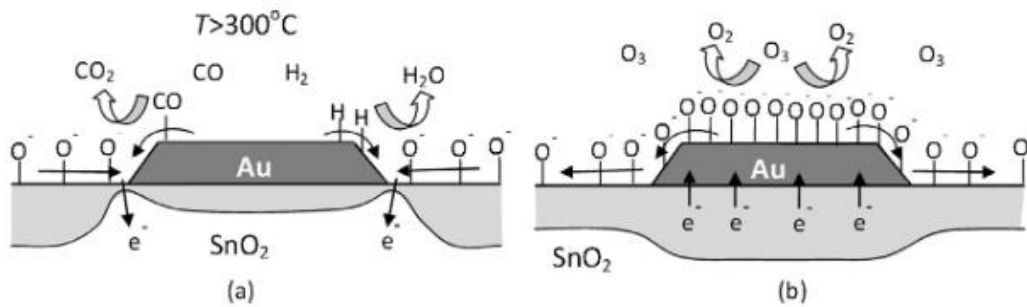


Figure 1.13 Schematic mechanisms of Au-loaded SnO₂ gas sensors in case of (a) reducing gases (CO and H₂) and (b) oxidising gases (O₃)⁸⁶

Electronic sensitization is related to the presence of dopants or loadings which have a significant electrical impact on the SMOX, thus affecting the conduction by shifting the bulk or surface Fermi level of the SMOX. Barsan et al.^{42,87} proposed two main electrical contributions to the sensing enhancement, including (i) for doped SMOX: the size of the initial band bending induced by the presence of charge located at the materials interface with the gas, which directly affects the transduction, and (ii) for loaded SMOX: the formation of a heterojunction space charge layer based on an electronic coupling of the additive and the SMOX, caused by the alignment of two Fermi levels and is shown in Figure 1.14.

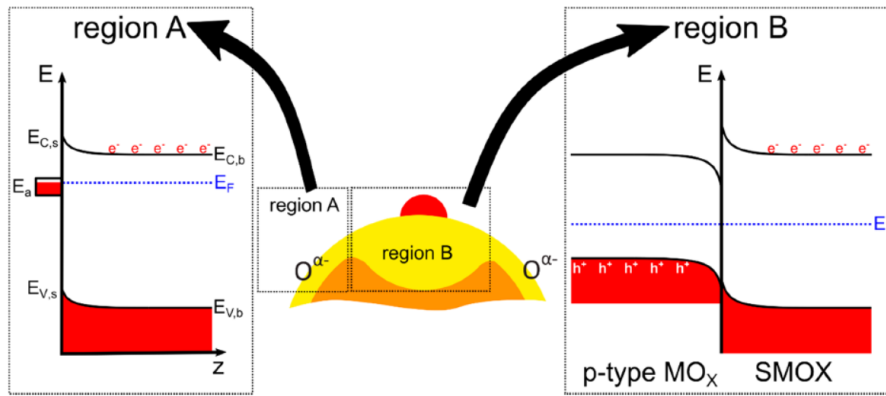


Figure 1.14 The illustration diagram of electronically coupled additive and SMOX interface for a loaded SMOX (A) unaffected surface and (B) heterojunction/space charge layer formed and controlled by the Fermi-level of the loading⁴²

1.2.5.3 Microstructure

Many studies have been proved that the sensor's sensitivity can be significantly improved by using materials with small grain size. Lu et al.⁸⁸ demonstrated that the sensitivity of SnO₂-based sensors toward 500 ppm CO increases with the reduction of the size of the SnO₂ particles. Particle size of 8-10 nm was optimal for fast response and recovery and was nearly 7 times more sensitive as compared to particle sizes larger than 20 nm, as shown in Figure 1.15. Similarly, Ansari et al.⁸⁹ studied the grain size effect of SnO₂ nanoparticles synthesized by sol-gel method on sensitivity toward H₂ gas. The results showed that the sensitivity for H₂ increased dramatically as the size of SnO₂ particles decreased.

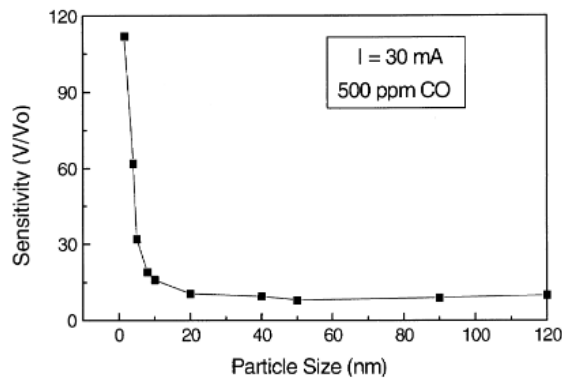


Figure 1.15 Effect of particle size of SnO₂ on gas sensitivity to 500 ppm CO⁸⁸

However, in some cases, the smaller grain size of nanostructures does not always correlate with an enhancement in gas response. Liu et al.⁹⁰ indicated that SnO₂ with more porous nanocrystalline microstructures (~50 nm) had a higher gas response and shorter response time towards H₂S than SnO₂ nanocrystals which were smaller in size (~12 nm) which was ascribed to their tendency to agglomerate into bulk particles. Korotcenkov et al.⁹¹ and Rao et al.⁹² suggested that finely dispersed small crystals limit the stability of the sensors as an excessive reduction in grain size will lead to a loss of its structural stability, and by that both surface and catalytic properties of the materials will be changed.

1.2.5.4 Humidity

In many cases, the gas response of sensors can be greatly impeded with an increase of humidity in the atmosphere^{32,93}. In wet atmosphere, water molecules are considered to undergo dissociative adsorption onto the SMOX surface as given in Eq. 4 and resultant ions adsorbed on the surface which significantly lower the sensitivity of SMOX gas sensors⁹⁴.



After a series of experiments using SnO₂ materials, Kohl and Heiland⁹⁵ have proposed two possible mechanisms for illustrating how humidity would affect a metal oxide surface, as shown in Figure 1.16. In mechanism (a), two free electrons are produced during the formation of Sn-OH bond in each oxygen vacancy. For both mechanisms, the hydroxyl group bonded to the metal oxide acts as a donor due to lower electron affinity than oxygen. Thus, the change in sensing properties resulting from changes in conductivity can be attributed to the production of free electrons on Sn-OH bond formation or simply the occupation of the active sites by the adsorbed water molecules^{96,97}.

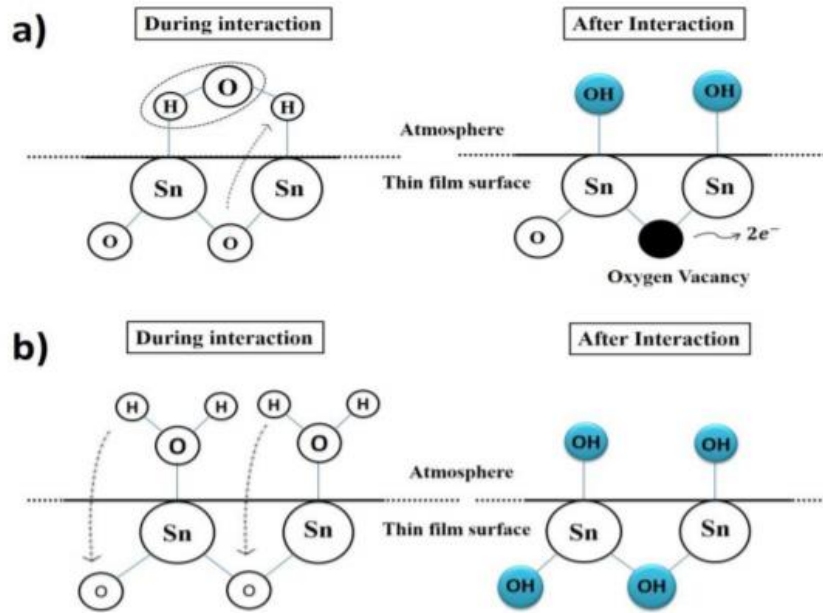


Figure 1.16 Schematic mechanisms of water molecules adsorbed on the surface of SnO₂ (a) one water molecule for two metal oxides and (b) one water molecule per metal oxide⁹⁵

Zai et al.⁹⁸ investigated the effect of humidity on the gas sensing property of a ZnO nanopowder sensor to 100 ppm ethanol. They observed an increase in the resistance when relative humidity (RH) levels range from 32 to 75% and a decrease in resistance at a higher RH level, range from 75 to 96%. An optimal sensitivity and stability of n-type ZnO gas sensor was obtained when RH levels were maintained at 50%. Hotovy et al.⁹⁹, who studied the sensing characteristics of p-type NiO gas sensor to NO₂ gas, also reported that RH levels around 50% is the optimal condition for sensing gases.

1.2.6 Background of oxygen gas sensors

Oxygen sensor is a common gas sensor in our daily lives. It is widely used in monitoring traffic, environment, medicine and other fields. Among them, oxygen sensors have been widely used to control the air/fuel ratio of automotive engines to improve combustion efficiency and reduce pollutant emissions²²¹. Another well-known application is to test the safety of human hypoxia. In a range from 0 to 30% vol measurement, if the human safety requirements of oxygen are less than 19.5% vol then it must be alarm, while for oxygen concentration over 23% vol it also need to be reminded, as oxygen enrichment can also cause human discomfort. The traditional

way to monitor oxygen is to use potential or amperometry sensors. In recent years, the resistance of metal oxide materials has been found strongly depended on the oxygen partial pressure, which makes it widely studied and promoted, such as SnO₂²²², CeO₂²²³ and Ga₂O₃²²⁴ thin film oxygen gas sensors. These resistive oxygen sensors are smaller, portable, and sensitive; however, they usually work at high operating temperatures.

Cukrov et al.²²² reported the successful production of separated nanosized SnO₂ particles via mechanochemical processing (24 nm) and spin coating (34 nm) other than conventional wet chemistry route or physical/ chemical vapour deposition methods. The result of oxygen sensing tests was concluded to be extremely stable and repeatable, with a response and decay time of about 2 min towards 1ppm to 10% Oxygen. It revealed that the optimal operating temperature is dependent on the O₂ concentration. A fast response and high sensitivity toward low ppm oxygen concentration was found when the operating temperature is at 400 °C. While for higher ppm oxygen concentration, optimal operating temperature is at about 300 °C to give the best performance.

1.3 Background of tungsten oxide and silver metal materials

1.3.1 Crystal Structure of tungsten oxide

Tungsten oxide(WO₃), as an excellent n-type semiconductor material with a wide band gap from 2.6 to 3.0 eV and sub-stoichiometric characteristics, has been widely explored in various fields and used in many applications, including photoelectric^{100,101}, photocatalytic^{102,103}, gas sensor^{18,104}, solar cells¹⁰⁵ and smart windows¹⁰⁶, etc. The interest in WO₃ began in the 17th century, when Wohler discovered a strong metallic sheen in LiWO₃ and coined the term “tungsten bronzes”. In 1950s and 1960s, Mott, Sienko et al. conducted a series of experimental and theoretical work on Na-tungsten bronzes for its unique physical properties such as superconductivity at very low

temperature and metal-insulator phase transitions¹⁰⁷. WO_3 with high melting point (1473 °C) and boiling point (1700 °C), is stable at high temperature and insoluble in water, slightly soluble in hydrofluoric acid and slowly soluble in ammonia water and hot sodium hydroxide solution. The ideal crystal structure of WO_3 , with tungsten atoms at the centre of the octahedron and oxygen atoms at the corners of the octahedron, is best described as a 3-D network of corner-sharing WO_6 octahedra, shown in Figure 1.17. The connectivity of this network can also be represented as a regular and cubic perovskite structure, such as ReO_3 . However, due to the tilting of WO_6 octahedra and displacement of tungsten from the centre of its octahedron, WO_3 usually cannot meet the ideal symmetry of the ReO_3 structure, leading to the formation of several distinct crystal phases, such as monoclinic II ($\epsilon\text{-WO}_3$), triclinic ($\delta\text{-WO}_3$), monoclinic I ($\gamma\text{-WO}_3$), orthorhombic ($\beta\text{-WO}_3$), tetragonal ($\alpha\text{-WO}_3$) and hexagonal (h-WO_3)^{5,108,109}.

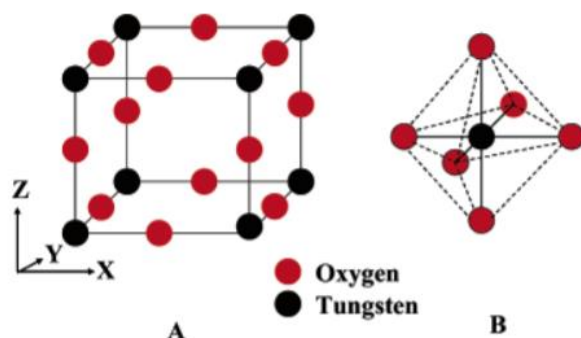


Figure 1.17 Crystal structure of WO_3 (A) ideal cubic structure of WO_3

Table 1.3 Lattice constant of different polymorphs of WO_3 ¹¹⁰

lattice constant (Å)	ϵ - WO_3 [11]	δ - WO_3 [11]	γ - WO_3 [11]	β - WO_3 [12]	α - WO_3 [12]	ideal cubic- WO_3 [13]
a	7.378	7.309	7.306	7.384	5.25	3.84
b	7.378	7.522	7.54	7.512	N/A	N/A
c	7.664	7.686	7.692	3.846	3.91	N/A

Similar to other metal oxides, the phase transition of WO_3 crystal can occur during

calcination and cooling process as: Monoclinic II (ϵ -WO₃, < -43 °C) → triclinic phase (δ -WO₃, -43 ~ 17 °C) → monoclinic phase (γ -WO₃, 17 ~ 330 °C) → orthorhombic (β -WO₃, 330 ~ 740 °C) → tetragonal (α -WO₃, > 740 °C). Monoclinic II (ϵ -WO) is only stable below 0 °C, therefore it is mainly prepared in laboratory^{111,112}. At room temperature, monoclinic I (γ -WO₃) is the most stable phase and the next stable phase is triclinic (δ -WO₃)⁵. Another stable crystal phase exists at room temperature is the hexagonal (h-WO₃)¹¹³.

Tungsten, as a transition metal element, has an outer atomic electron configuration of 5d⁴6s². The valence states of common compounds are +4, +5 and +6, and the corresponding oxides are WO₃ and WO₂. In general, owing to the unstable state of cubic structure of WO₃ and the presence of varying degrees of oxygen vacancies within the crystals, WO₃ does not meet the strict stoichiometric ratio and is usually expressed in the form of WO_{3-x}, in which 0 < x < 1, such as monoclinic W₁₇O₄₇ and W₂₅O₇₃, orthorhombic W₃₂O₈₄ and W₃O₈, tetragonal W₅O₁₄ and etc., named Magnéli phases. Migas al.¹¹⁴ found that the photoelectric properties of WO_{3-x} are influenced by oxygen deficiency, for instance the band gap is reduced to 2.4-2.8 eV and it can show strong light adsorption in both visible and near-infrared regions. In addition, the existence of oxygen deficiencies also makes WO_{3-x} more metallic, so it has been widely used in dye-sensitized solar cells¹¹⁵, photochemical^{116,117}, supercapacitor¹¹⁸, field emission^{119,120} and other aspects in recent years due to its good electrical conductivity and more active sites.

1.3.2 Different morphologies of WO₃ nanomaterials for gas sensing

Novel properties of nanostructured WO₃ as compared to the bulk material include (i) increased surface-to-volume ratio, which offers more opportunity for both chemical and physical interactions; (ii) altered surface energy, which can allow the properties of materials to be significantly adjusted and engineered because the bond structures of the atomic species near the surface will be different to those embedded in the bulk;

and (iii) quantum confinement effects, which influences optical properties, charge transport and electronic band structures caused by the inherently small size of nanostructured materials⁵.

In recent years, enormous efforts have been made in the synthesis of semiconducting WO₃-based materials with various morphologies in order to improve the gas-sensing performance. In general, the morphologies of SMOX can be classified by dimensionality^{121,122}. On the basis of this classification, WO₃ based materials have been extensively developed in zero-dimensional, one-dimensional, two-dimensional and three-dimensional nanostructures, which would be discussed comprehensively in the following paragraphs.

1.3.2.1 0-D WO₃ nanostructures

Structures that undergo isotropic growth and eventually form spherical or near-spherical structure are named 0-D structures¹⁸. The specific surface area of 0-D nanoparticles provides an opportunity for improving gas sensing performance¹²³. Meanwhile, sensing response can be improved by adjusting sensitive surface, agglomeration and nanoparticle size. Li et.al. synthesized WO₃ hollow spheres via a chemical deposition process, which showed great sensitivity to alcohol, acetone, CS₂ and many other organic gases¹²⁴. Zhang et al. described the successful synthesis of WO₃ microspheres with average diameter ~ 1 μm by a simple hydrothermal treatment¹²⁵. Shukla et al. reported fabrication and characterization of well-crystalline 0-D WO₃ nanoparticles via a facile solution process, as shown in Figure 1.18.

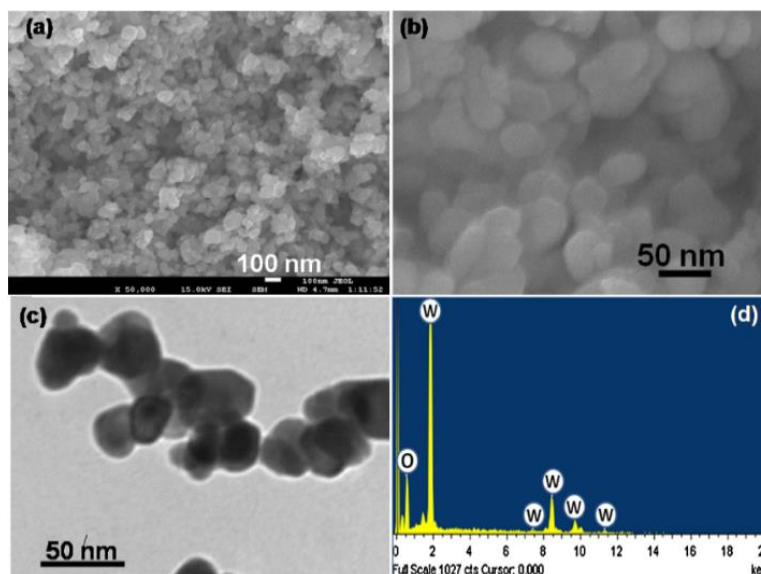


Figure 1.18 (a) low- and (b) high-magnification FESEM images, (c) TEM image and (d) EDS spectrum of prepared WO_3 nanoparticles¹²⁶

The sensitivity performance of 0-D WO_3 microspheres to various gases, such as acetone, NH_3 , ethanol, H_2S , NO_2 and H_2 is shown in Figure 1.19. The results showed highly sensitive and selectivity gas sensing as well as fast response behaviour of WO_3 microspheres to acetone vapour at 200 °C, indicating WO_3 -based sensor an excellent candidate for monitoring acetone at low temperature.

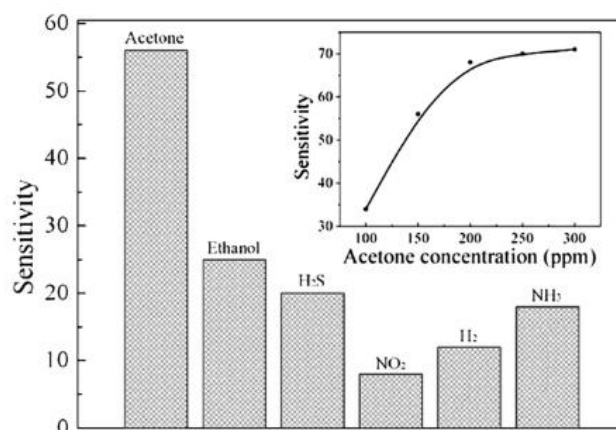
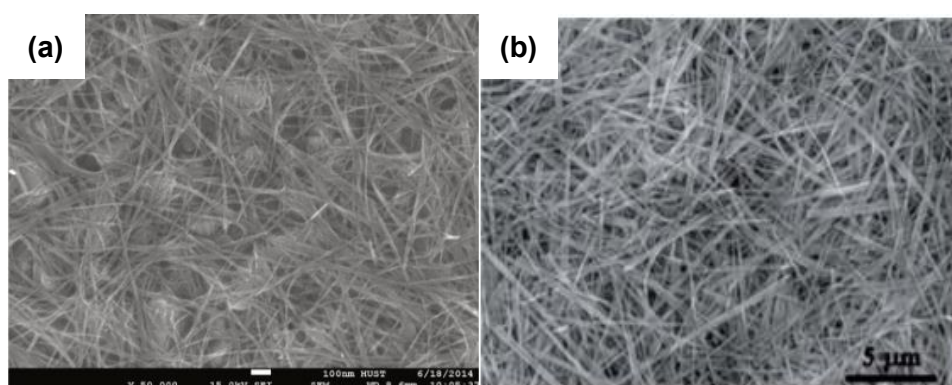


Figure 1.19 Sensitivity of WO_3 microspheres gas sensor to various 150 ppm gases at 200 °C; (insert) sensitivity of WO_3 microspheres gas sensor at 200 °C with an increase in concentration of acetone vapour¹²⁵

1.3.2.2 1-D WO₃ nanostructures

1-D WO₃ nanostructured materials, in the forms of nanorods¹²⁷, nanobelts⁶, needle-like¹²⁸, nanofibers¹²⁹ and nanowires¹³⁰ have been extensively developed in the gas sensing field mainly according to its high aspect ratio (length divided by width). In general, the length of 1-D SMOX nanomaterials can be a few millimetres long, but its thickness and widths are only limited in a nanometre scale (1 – 100 nm)¹³¹. Cai et al. described the formation of single crystalline WO₃ nanowires with diameters in the range of 15 – 20 nm on FTO substrate via a hydrothermal method, as shown in Figure 1.20a. The WO₃ nanowire-based sensor exhibited a remarkably high response ($S = 37$) to NO gas and a fast response and recovery speed (68 s/88 s) at 300 °C. The defects on the WO₃ nanowire surfaces as well as the reactions between the analyte gas NO and surface defects were considered to contribute to the enhancement in gas sensing¹³⁰. Bai et al.¹²⁷ studied and introduced a low-temperature (at 100°C) hydrothermal route for the fabrication of WO₃ nanorods with an diameter of ~200 nm an aspect ratio of ~ 50, shown in Figure 1.20b. A high gas sensing response of 209 was observed for WO₃ nanorod based sensors to 10 ppm NO₂ at an operating temperature of 200 °C. Selectivity towards NO₂ against CH₄ and CO were evaluated at a sensitivity ratio of 30 and 19, respectively.



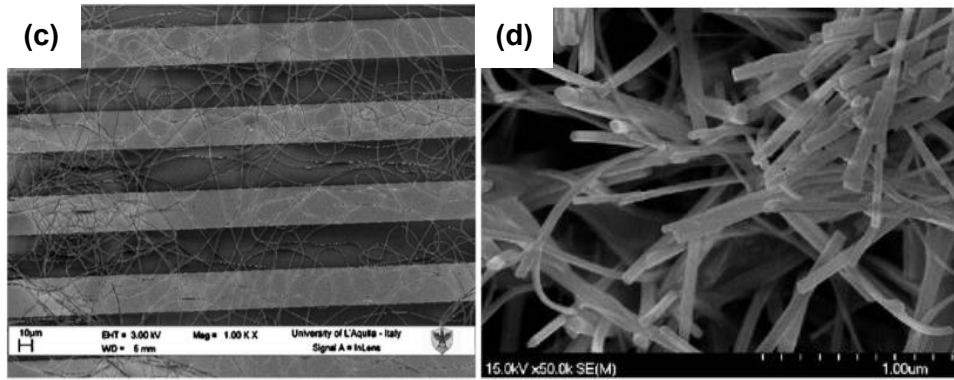


Figure 1.20 SEM images of 1-D WO_3 nanostructures (a) nanowires, (b) nanorods, (c) nanofibers and (d) nanobelts^{127,129,130,132}

1.3.2.3 2-D WO_3 nanostructures

Large surface-to-volume ratio related to thin nanosheet structure have shown ultra-sensitivity in gas sensing^{133–135}. For 2-D porous nanostructures, gas interaction can occur at both surface and internal structure, which enhances the gas sensing response. Rahmani et al.¹³⁶ described the fabrication of 2-D WO_3 nanosheets using high temperature anodization of W thin films, with the WO_3 nanosheet based sensors exhibiting excellent sensitivity and repeatability when exposed to H_2 , with an optimal gas response of 80% for 1% of H_2 at 250 °C, as shown in Figure 1.21 (right).

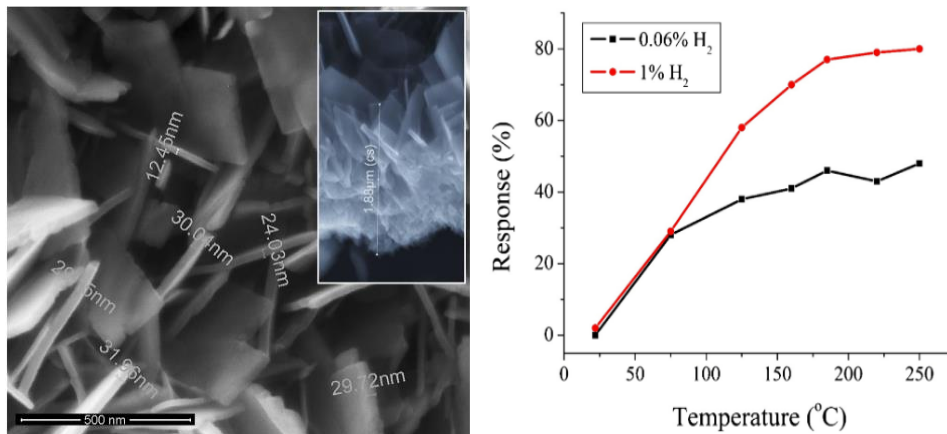


Figure 1.21 (left) FESEM images of WO_3 nanosheets (inset is the cross sectional FESEM of WO_3 nanosheets); (right) Response vs. temperature diagram for WO_3 nanosheet based sensor to 0.06 and 1% H_2 ¹³⁶

Wang et al.¹³⁷ conducted a series of experiments to control the synthesis of ultrathin 2-D WO₃ nanosheets. These 2-D WO₃ nanosheet based sensors exhibited both high sensitivity and selectivity toward NO₂ against other examined gases. The results revealed that the highest response was observed at 5.67 to 50 ppb NO₂ at 140 °C with response and recovery time of ~ 140 s and 75 s, respectively.

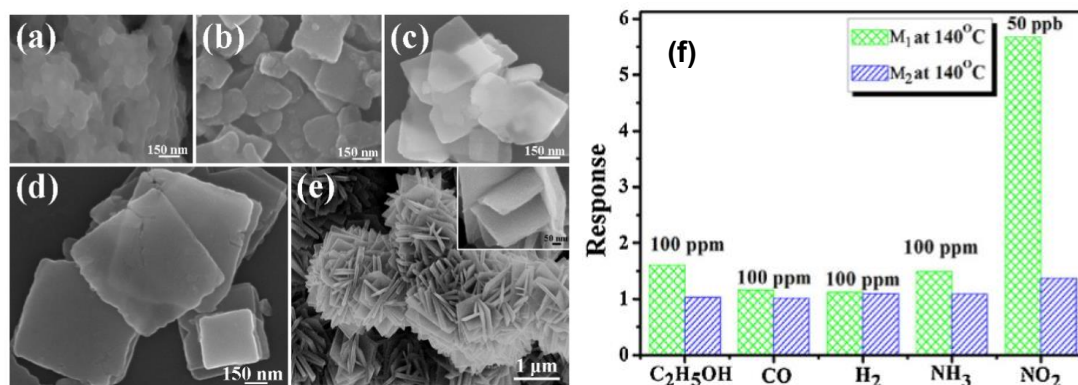


Figure 1.22 FESEM images of WO₃ nanosheets synthesized under different hydrothermal processing time (a) 5 min, (b) 1 h, (c) 2 h, (d) 4 h, (e) 8 h and (f) Response of M₁ (WO₃ nanosheets) and M₂ (WO₃ nanoparticles) to various gases (C₂H₅OH, CO, H₂ and NH₃ at 100ppm and NO₂ at 50 ppb) at 140 °C¹³⁷

1.3.2.4 3-D WO₃ nanostructures

3-D nanostructures (hierarchical) materials are generally assembled from low dimensional nanomaterials, including 0-D nanoparticles, 1-D nanorods and 2-D nanosheets. The advantages of 3-D nanostructures materials, include larger surface area, fast interfacial transport and abundant active sites^{138–140} Yan et al.¹³⁹ described the fabrication of 3-D WO₃ nanowall based sensors by a facile solvothermal approach, with the results showing that the sensitivity of WO₃ nanowall based sensor was higher than that of a commercial WO₃-based sensor, as shown in Figure 1.23.

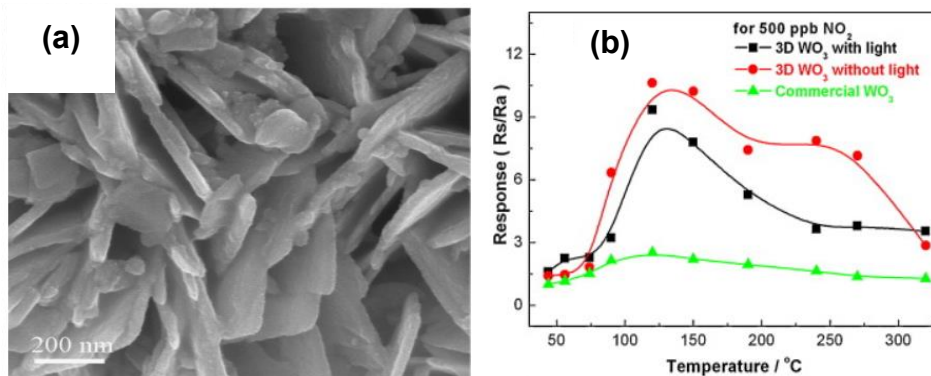
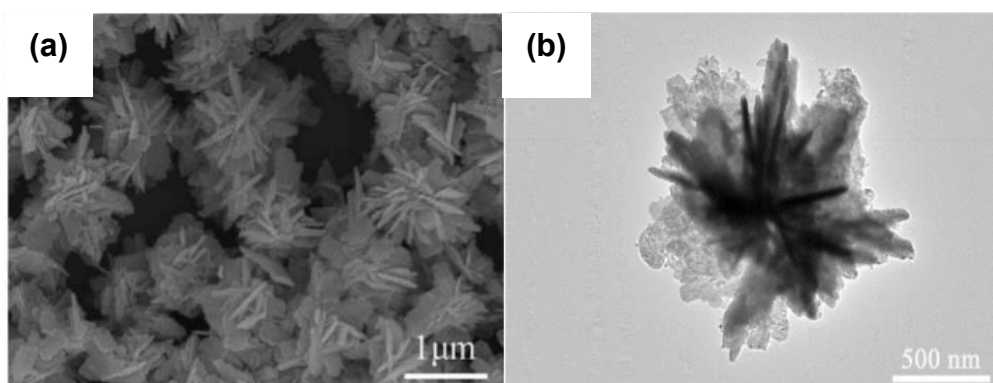


Figure 1.23 (a) SEM image of the 3-D WO₃ nanowall based nanostructures and (b) Response of 3-D WO₃ sensor as a function of operating temperature as compared to commercial WO₃ sensor¹³⁹

Wang et al.¹⁴¹ reported the successful synthesis of flower-like WO₃ nanostructures assembled from 2-D nanosheets *via* an acidification method combined with an annealing process, as shown in Figure 1.24. These hierarchical WO₃ based sensor exhibited excellent sensitivity and selectivity to NO₂ at a low operating temperature of 90 °C. The gas sensor response was about 13 to 2 ppb NO₂. The reasons for the high sensing performance were attributed to the unique hierarchical structures of WO₃ which provide more active sites on the surface. Meanwhile, the large amount of surface defects exhibited on single nanosheets make the adsorption and reaction of NO₂ much easier, as shown in Figure 1.24c.



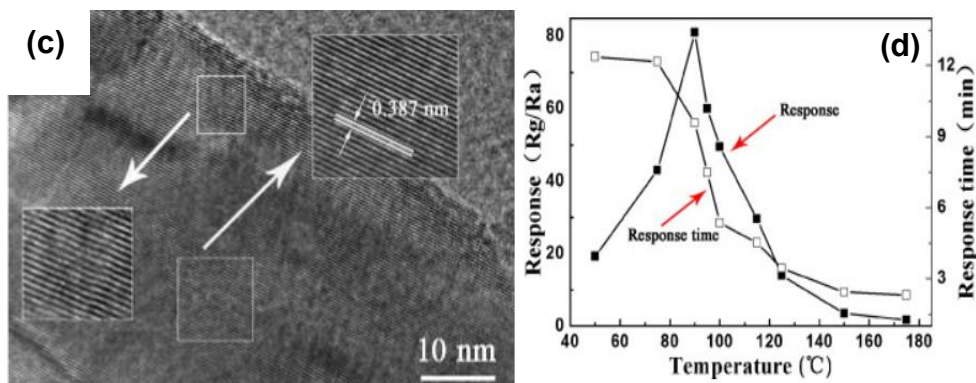


Figure 1.24 (a) SEM image as-synthesized hierarchical flower-like WO_3 nanostructures, (b) HRTEM image of an individual flower-like WO_3 structure, (c) HRTEM image of a nanosheet of the flower and (d) Response of WO_3 based sensor to 40 ppb NO_2 as a function of operating temperature¹⁴¹

1.3.3 Silver metal decorated metal oxide nanostructures

Metal nanoparticles have attracted increasing interest due to their use in a wide-ranging application areas, such as photoinduced optical effects¹⁴² and bio-sensing¹⁴³. Silver oxide (Ag_2O) nanoparticles have unique physical and chemical properties with many applications in the fields of fuel cells¹⁴⁴, sensors^{145,146}, photovoltaic cells¹⁴⁷ and oxidation catalysis¹⁴⁸.

A number of Ag-ZnO based nanostructures with outstanding performance have been reported^{149–151}. Uddin et al.¹⁴⁶ reported the fabrication of a Ag-loaded ZnO-graphene hybrid for the detection of C_2H_2 via a facile chemical route. A highest gas response value of 21.2 was observed for 3 wt% Ag-loaded ZnO-graphene hybrid at an optimum temperature of 150 $^\circ\text{C}$ for 100 ppm C_2H_2 . The enhancement in gas response was attributed to the additional active sites produced on the surface of the hybrid according to the spill-over effect, resulting in more C_2H_2 molecules be adsorbed on the surface.

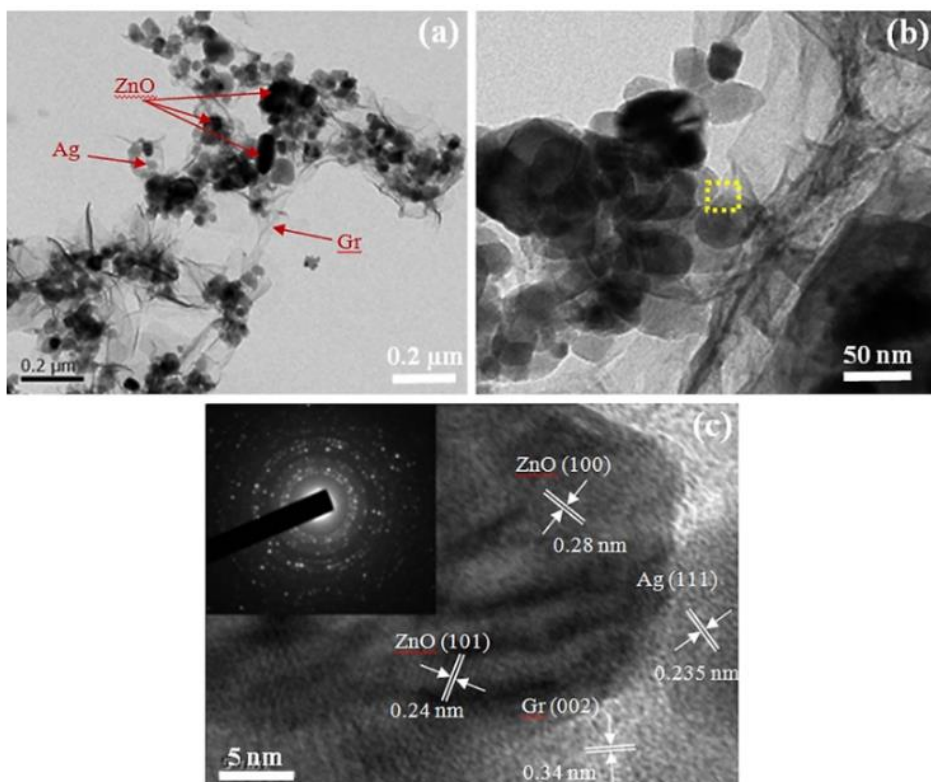


Figure 1.25 (a) TEM and (b-c) HRTEM images of the ZG-Ag 3 wt% hybrid sample. Inset: the corresponding SAED pattern of the ZG-Ag 3 wt% sample¹⁴⁶

Recently, Llobet et al.¹⁴⁵ reported a two-step synthesis of Ag-loaded WO_3 nanowires via AACVD by using an organometallic silver precursor $[\text{Ag}(\text{acac})_2]$. As shown in Figure 1.26, the EDX results revealed that instead of metallic Ag, clustered Ag_2O nanoparticles were non-homogenously dispersed on the WO_3 nanowires. The gas response showed silver oxide based WO_3 sensors are more sensitive to H_2 exposure.

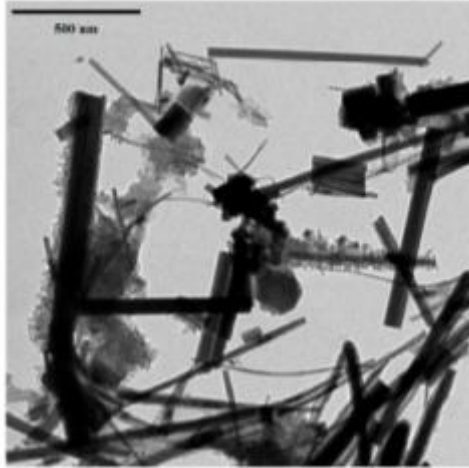


Figure 1.26 TEM image of WO_3 nanowires and Ag_2O nanoparticles¹⁴⁵.

1.4 Aerosol-assisted chemical vapour deposition

Over the last few decades, many fabrication methods have been developed and used to prepare WO_3 nanostructures, including hydrothermal method^{152,153}, thermal evaporation^{154,155}, chemical vapour deposition^{156,157} and template assisted growth¹⁵⁸ etc. But it is possible to divide them into two broad categories: “top-down” and “bottom up” approaches¹⁵⁹. The former approach of “top-down” refers to fabricating nanostructure materials by mechanically reducing the size of larger particles. The second approach “bottom up” can be represented as the assembly of molecular building blocks. Through these methods, it is possible to fabricate high purity nanocrystalline materials at low cost with controllable growth morphology. In the following paragraphs, it will focus on the vapour phase growth method used in our laboratory.

1.4.1 Process and principle of AACVD

CVD, as a conventional technique for the synthesis of solid-state thin films, has been developed over many years¹⁶⁰. Through this method, high purity materials with structural control at atomic or nanometre scales can be achieved. However, the problems of selection and delivery of the precursors still exist. The general lack of readily available volatile precursors and the difficulty in controlling the stoichiometry of

the deposits impedes the further development of CVD techniques¹⁶¹. As a branch of conventional CVD, aerosol-assisted chemical vapour deposition (AACVD) technique uses aerosol droplets to transport the chemical precursors¹⁶². Due to the process relying principally on the solubility of the chemical precursor instead of volatility, a wide range of low volatility or thermally unstable precursors can be used at ambient atmosphere or low temperature¹⁶³. In the AACVD process, the morphologies of the thin films can also be controlled by various reaction condition parameters such as deposition operating temperature, choice of solvent, gas flow rate, and reaction time¹⁶⁴. The schematic process of AACVD is shown in Figure 1.27. In AACVD the chemical precursor is dissolved in solvent and fine aerosol droplets are generated by an ultrasonic humidifier. With an aid of inert carrier gas, such as N₂, it can be further transported to a heated reaction chamber. The solvent then undergoes rapid decomposition or evaporation, leaving precursor vapour to further be synthesized into desired products via heterogeneous reaction¹⁶².

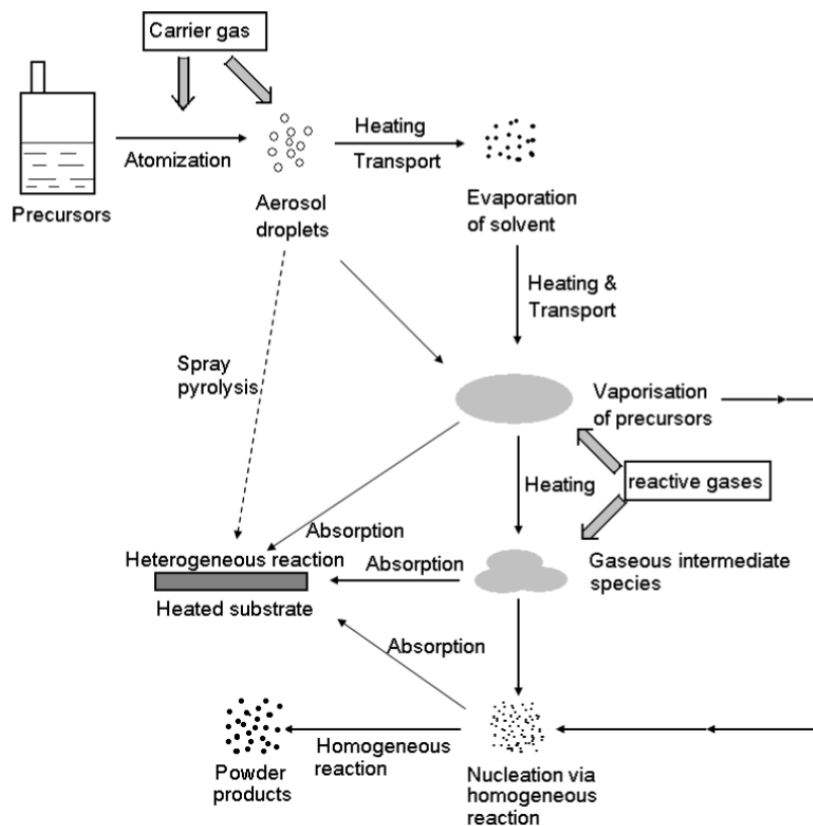


Figure 1.27 Schematic diagram of AACVD process for deposition of thin films¹⁶²

Metal oxide compounds are the most popular products fabricated by AACVD, as oxidation reactions can be simply carried out using water vapour or adventitious oxygen from the precursor, solvent or from the carrier gas.

1.4.2 AACVD fabricated tungsten oxide nanostructures

Many studies on the fabrication of nanostructured WO_3 via AACVD technique have been reported over the last few years. Ling and Blackman¹⁶⁴ reported the growth mechanism of planar or nanorod WO_x thin films via AACVD by using tungsten hexacarbonyl ($\text{W}(\text{CO})_6$) as precursor at 339 to 358 °C on quartz substrates. XRD analysis revealed that the crystal structures of as-deposited WO_x thin film were comprised of two phases, $\text{W}_{25}\text{O}_{73}$ and $\text{W}_{17}\text{O}_{47}$. SEM analysis showed that the morphology of the thin film surface varied from planar to nanorod structures as it deposited from the inlet towards outlet, as shown in Figure 1.28. They proposed that the variation of actual temperature on the substrate surface when placed in the heated reaction chamber with a difference of 19 °C, resulted in a change in growth mode.

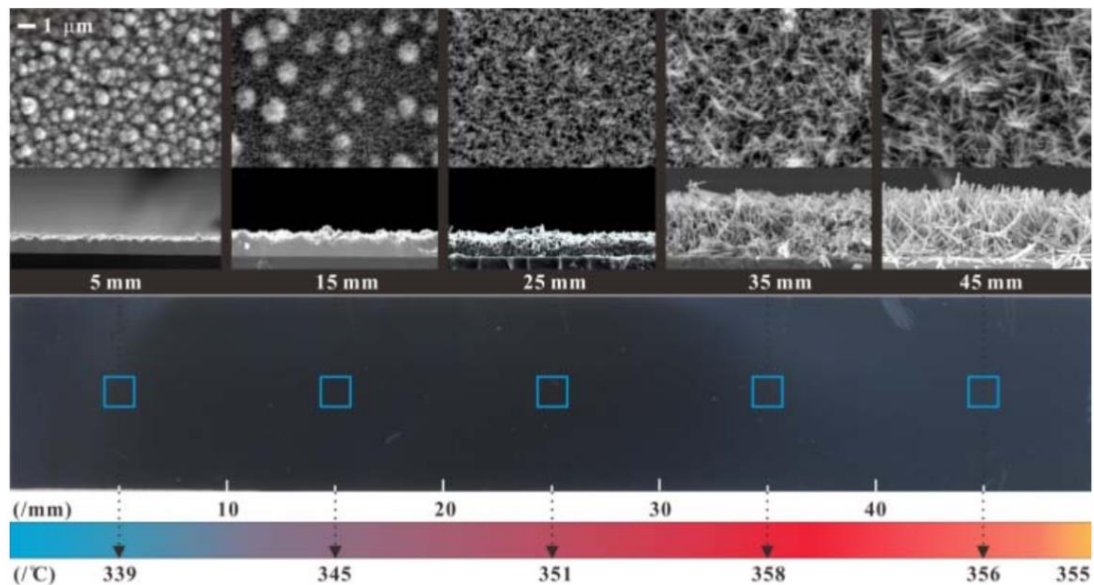


Figure 1.28 SEM images of as-deposited WO_x thin films on quartz substrate with a varying morphologies from planar to nanorods as function of distance from the reactor inlet (left) to outlet (right) and corresponding substrate surface temperature¹⁶⁴.

Recently, Shaukat et al.¹⁶⁵ reported the deposition of cauliflower like WO_x nanostructures by using $[W(CO)_6]$ and multiwalled carbon nanotubes (MTCNTs) in toluene on silica glass substrate at 400 °C via AACVD. By varying the concentration of MTCNTs reacting with WO_x thin films, SEM images, as shown in Figure 1.29 pointed that the growth of cauliflowers WO_x structures was due to the aggregation of spherical nanoparticles with high angle grain boundaries. The crystal phase of WO_x transformed from monoclinic to tetragonal with changing of preferred orientation from (020) to (001) with increase of doping of MTCNTs.

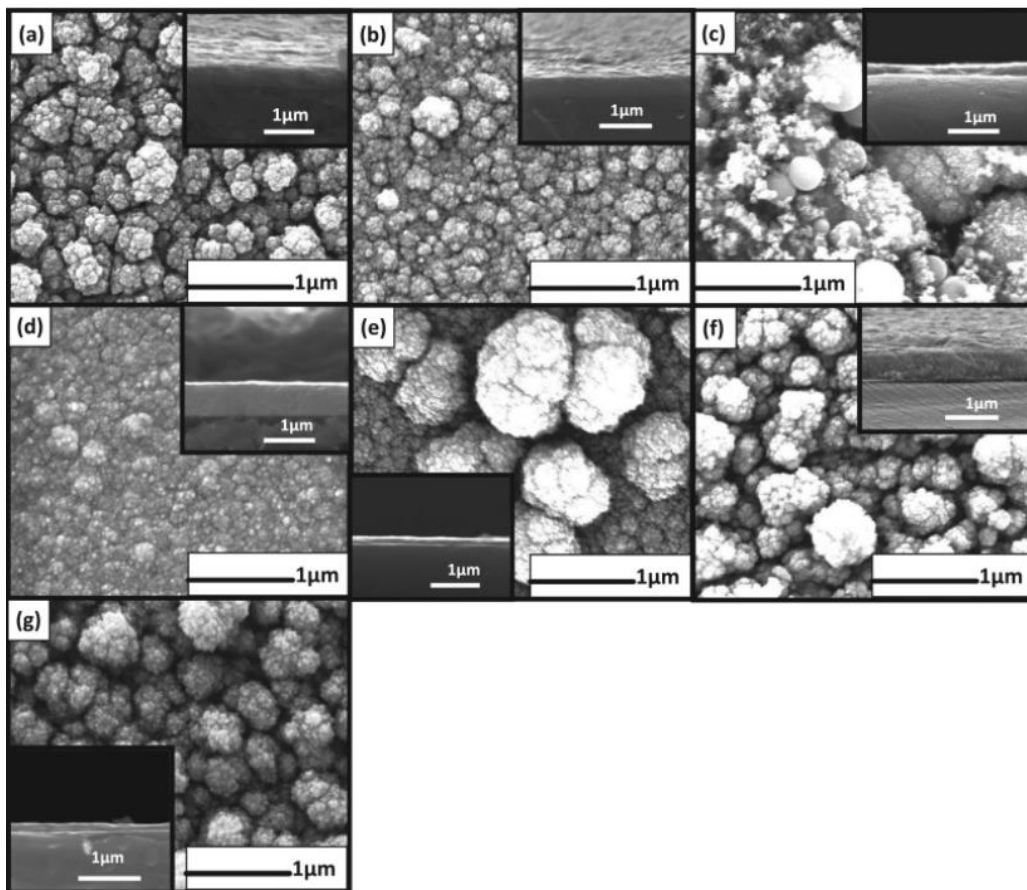


Figure 1.29 SEM image of plain and doped WO_x thin films produced via AACVD on silica glass substrate at 400 °C by varying the concentration of MTCNTs (a) 0% (b) 0.1% (c) 0.15% (d) 0.2% (e) 0.25% (f) 0.3% and (g) 0.35%-CNTWO¹⁶⁵

Instead of using $[W(CO)_6]$ as the primary precursor for the synthesis of WO_x nanostructures, Shujah et al.¹⁶⁶ introduced the synthesis of WO_3 based nanostructures on alumina substrate via AACVD by using tungsten hexaphenoxide $[W(OPh)_6]$. The

FESEM images as shown in Figure 1.30 illustrated the surface morphology of WO_3 thin film deposited at $425\text{ }^\circ\text{C}$ comprised of randomly oriented and overlapped nanorods and 2-D nanosheets. While the surface morphology of WO_3 thin film deposited at $450\text{ }^\circ\text{C}$ was comprised only homogeneously distributed nanorods.

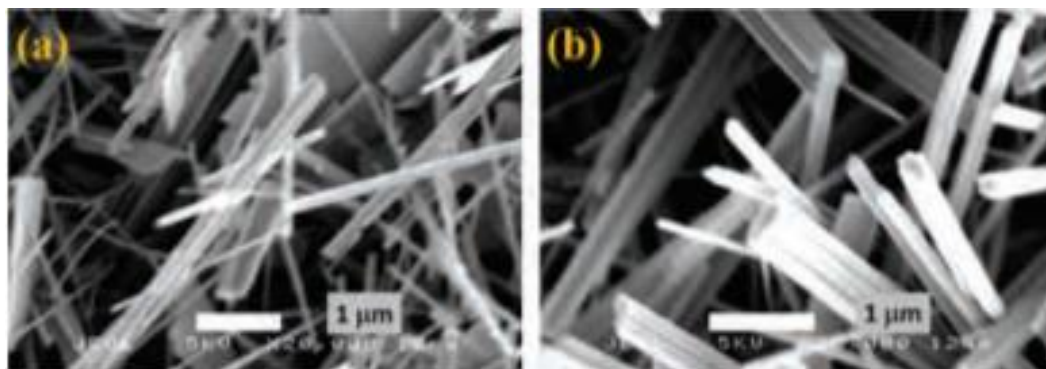


Figure 1.30 FESEM images of WO_3 thin films deposited on alumina substrate by AACVD at (a) $425\text{ }^\circ\text{C}$ and (b) $450\text{ }^\circ\text{C}$ ¹⁶⁶

1.4.3 AACVD fabricated noble metal decorated tungsten oxide

Many studies have demonstrated that both physical and chemical properties of tungsten oxide such as optical or electrical behaviour can be adjusted by the addition of external impurity dopants, either noble metal or metal oxide. In literature, it has been shown that the crystallographic texture and feature size of tungsten oxide can be altered by doping or loading noble metals, such as Au, Pt, Pd and etc^{167–169}. Functionalised noble metal nanoparticles can dramatically affect electronic, optical and magnetic properties of the material. Chemical methods have been recognised as excellent techniques for the synthesis of nanoparticles on MOX by forming a homogeneously distributed coverage as compared to physical methods of functionalising nanoparticles, such as sputtering^{170,171}. Synthesising nanoparticles in gas phase has greater advantages over liquid phase, including high purity product formed and continuous mode operation. Nanoparticles synthesized via AACVD shows excellent control in particle size, crystallinity, porosity and stoichiometry by simply adjusting the reaction parameters, such as operating temperature, solvent, reaction and etc¹⁷².

Vallejos et al.⁸¹ reported a single step synthesis of Au-functionalised WO₃ nanoneedles via AACVD for detecting ethanol at low concentration (1.5 ppm). TEM images showed the successful deposition of randomly distributed Au nanoparticles with diameter of 11.13±0.19 nm, along the WO₃ nanoneedles.

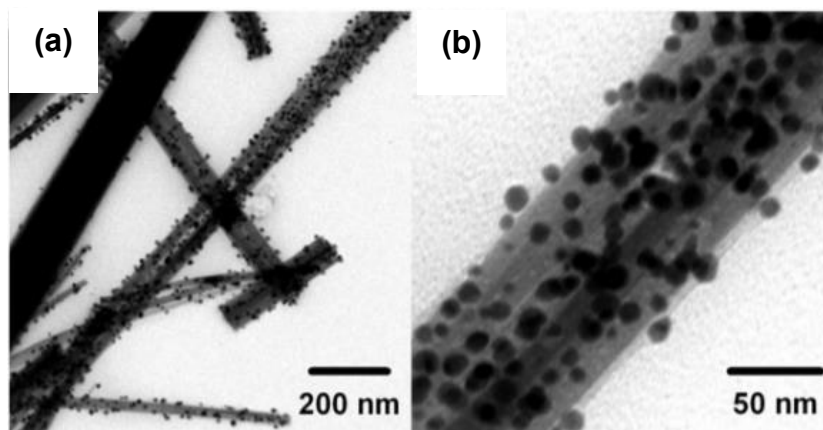


Figure 1.31 TEM images of WO₃ nanoneedles with dispersed Au nanoparticles on surface under (a) low magnification and (b) high magnification⁸¹

Annanouch et al.¹⁷³ reported the formation of a gas-sensitive hybrid material consisting of Cu₂O decorated on WO₃ via AACVD in a single step for the first time for the selective and humidity-resilient detection of H₂S. As shown in Figure 1.32, after analysing the fringe patterns within the HRTEM images, the results suggest the coexistence of Cu₂O and CuO adhered on the WO₃ surface.

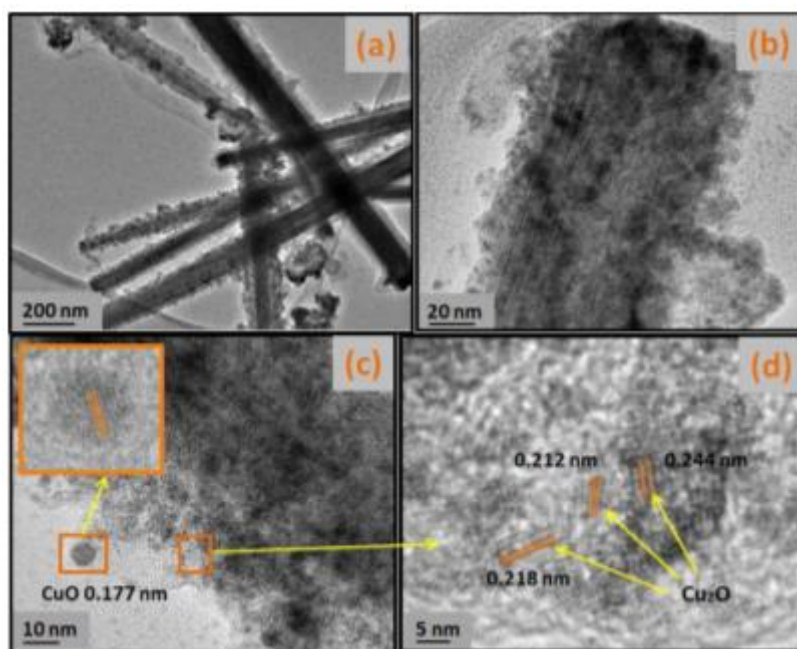


Figure 1.32 TEM and HRTEM images of the as-deposited Cu_2O functionalized WO_3 (a and b) low magnification; (c and d) high magnification¹⁷³

1.5 Motivation and aims

Oxygen gas sensors are widely used for various applications such as medical and pharmaceutical, environmental monitoring, food and beverages and waste management industries. In the era of innovation, the development of novel sensing materials and the advancement of processing technology in chemical sensors and biosensors have evolved quickly. However, the technology for oxygen sensors has remained in place for twenty years. Though Pb-free alternative electrochemical gas sensors to oxygen have been developed by introducing Zn, Fe or Al, but the defects such as short life-span and low sensitivity still remain. Other alternative oxygen gas sensors using optical methods have also been studied on the basis of light absorbance or photo-quenching, but still cannot meet the novel standard, such as cost-effective, compact and reliability even working at lower temperatures^{174–176}.

Semiconducting metal oxides (SMOX) based gas sensors have attracted an extensive attraction in sensing technologies. SMOX materials such as SnO_2 ¹⁷⁷, ZnO ¹⁷⁸, In_2O_3 ¹⁷⁹, and CeO_2 ¹⁸⁰ have already been explored as a potential oxygen gas sensor to replace

Pb. Meanwhile, many studies have reported that by adding noble metal nanoparticles onto the SMOX sensing material, the gas sensing properties, including both sensitivity and selectivity towards a target analyte gas can be greatly enhanced.

Therefore, the aims of this research project are to explore an alternative SMOX gas sensor, typically WO_3 based gas sensor, to see if it could be a potential oxygen gas sensor to replace Pb. Initially, undecorated WO_3 will be fabricated by using the home-built AACVD reactor in our laboratory and characterizations including XRD, XPS, SEM and TEM will be examined. Subsequently, noble metal additives, Ag, will be further deposited onto the WO_3 thin film followed by fully characterization of the $\text{Ag}@\text{WO}_3$ nanostructures. In the end, sensing performance towards oxygen will be tested and the gas sensing mechanism of Ag functionalized WO_3 towards will be discussed.

Chapter 2 Experimental

Aerosol-assisted chemical vapour deposition (AACVD) (a novel variant of chemical vapour deposition (CVD) based on transporting the precursor solution via aerosol droplets to the heated reaction chamber to form a layer of thin film) offers several noteworthy advantages as compared to the traditional CVD. For example, this method is normally undertaken at atmospheric pressure and relies on a solution-based transportation approach which allows a wider range of precursors to be utilized over traditional CVD^{162,181}. Meanwhile, the functionalization of semiconducting metal oxides (SMOX) nanostructures with the decoration of metal nanoparticles, in a single step via co-deposition, or via two processing steps, can be implemented, such as the incorporation of Pt¹⁸² and Au⁸¹ nanoparticles at the surface of tungsten oxide nanostructures. In this chapter, the technique to produce metal or metal oxide thin films via homebuilt AACVD reactors is introduced in detail.

The gas sensing tests were carried out using a specialized gas handling equipment previously installed at the School of Engineering, University of Warwick. The measurements of gas sensing performance were carried out by Ayyala, Sai Kiran and Sari, Wangi Pandan from University of Warwick. The fundamental principle and procedure of the test will be introduced below.

The physical characterizations, including XRD, XPS, SEM, EDX and TEM of the Silver nanoparticles (Ag), tungsten oxide (WO₃) and silver decorated tungsten oxide (Ag@WO₃) thin films on various substrates, including glass, quartz and alumina and the corresponding gas sensors were carried out within the department of chemistry at UCL.

2.1 Aerosol-assisted chemical vapour deposition

Two types of homebuilt AACVD reactors ('rectangular-based chamber' 3 cm x 6 cm x 2 mm and 'square-based chamber' 3 cm x 3 cm x 2 mm) were used for the preparation of Ag, WO₃ and Ag@WO₃ thin films on various substrates and their corresponding gas sensors. The integrated procedure mechanism and internal design of AACVD reactors were illustrated in Figure 2.1 and Figure 2.2, respectively. Height of reaction chamber can be adjusted by adding or removing the metal plate.

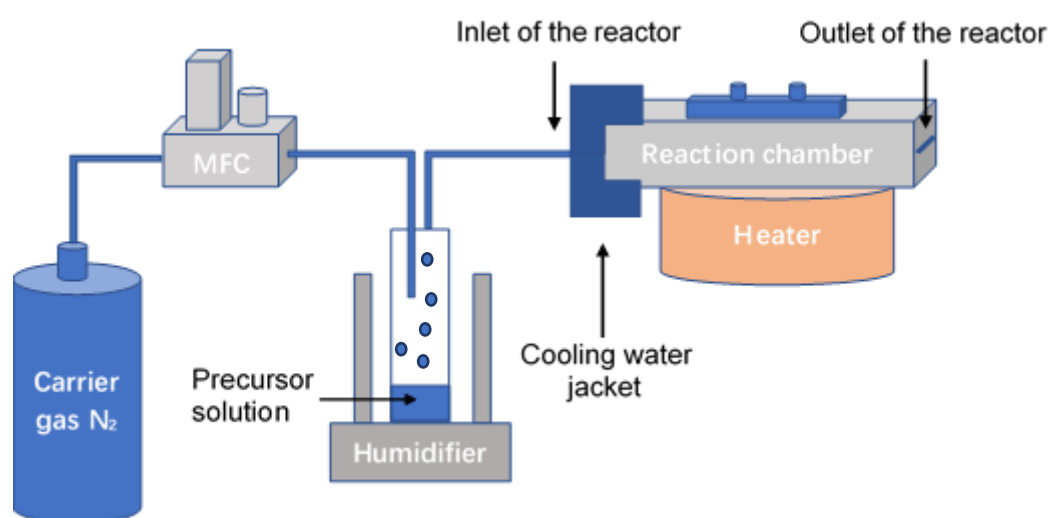


Figure 2.1 Schematic diagram of reaction process of AACVD technique

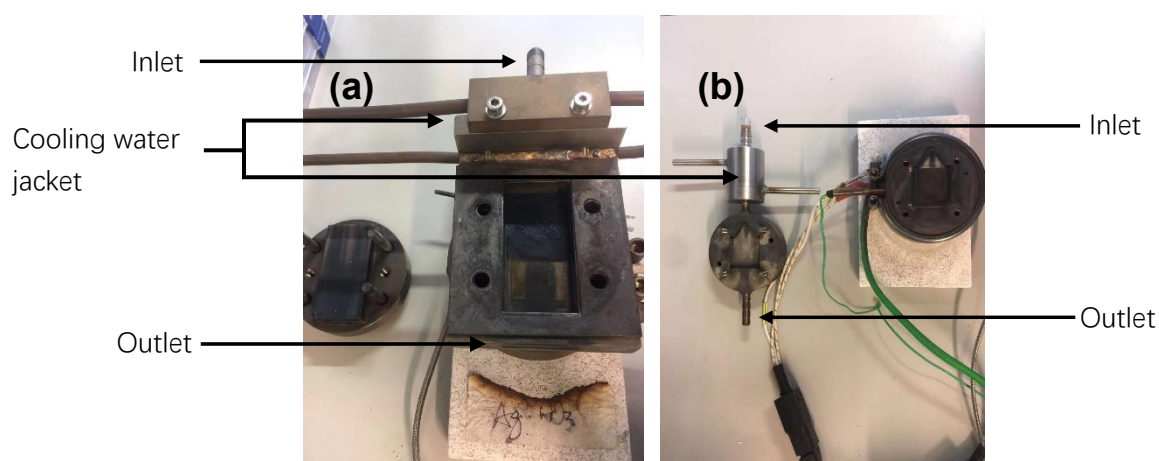


Figure 2.2 The internal design of homebuilt (a) rectangular-based and (b) square-based AACVD reactors

As demonstrated in the Figure 2.1 and 2.2 above, the cleaned substrate will be placed in the reaction chamber and preheated to a moderated temperature. The precursor solution is rested in the flask and aerosol droplets then generated by an ultrasonic humidifier, which can be further transported to the preheated reaction chamber by a flow of carrier gas controlled by a mass flow controller (MFC). The solvent and precursor droplets then rapidly evaporate and/or decompose within the reaction chamber and finally synthesized and deposited onto the substrate to form nano-scaled thin film via heterogeneous reaction (under moderated temperature) or powders via homogeneous reactions (usually under higher temperature). For both reactors, a cool water jacket is equipped and attached to the inlet of the reactor to prevent the early decomposition or consumption of the precursor before entering the reaction chamber. The exhaust gas is directly reeled out by the extraction system of the fume cupboard¹⁶⁴.

2.2 Measurement of gas sensing tests

The gas rig (Lehman Instrument, France) can supply a predefined concentration of oxygen by diluting with nitrogen (99.999%) with zero air (20% O₂). The variance in the concentration of oxygen is obtained by altering the flow rate of each gas using a mass flow controller (MFC, UFC 1100, Brooks) controlled by computer programme written in LabVIEW (National Instrument 2016). A water bubbler was added on the pathway of the tested gas mixture before entering the sensor chamber and used to simulate the humid environment. The measurement was monitored and recorded with a humidity data logger (Lascar Electronic).

The resistance changes during the tests regarding to different sensors while exposed to different concentration of oxygen gas were monitored and recorded by a sensor management system AS-330 (Atmospheric Sensor Ltd, UK). By using this device, the sensing performance under different ranges of operating temperatures, test period, and operating sequence can be carried out and analysed. The time interval for the

sensing test is 30 minutes with regarding to exposing to different test environment. The oxygen concentration is varied between 0% and 20%. The sensors were then purged with nitrogen for 30 minutes to ensure it recovery to the baseline value of the initial resistance and stabilise before a new measurement was taken. The sensor' response sensitivity was defined as being equivalent to R_g/R_a , where R_g is the sensor resistance in reference gas nitrogen when exposed to the target gas O_2 and R_a is the resistance of sensor baseline in the reference gas nitrogen. The response and recovery time of the sensors were defined as the corresponding time required to achieve a 90% change in the electrical resistance of the samples when exposed to the target gas O_2 and pure N_2 , with respectively.

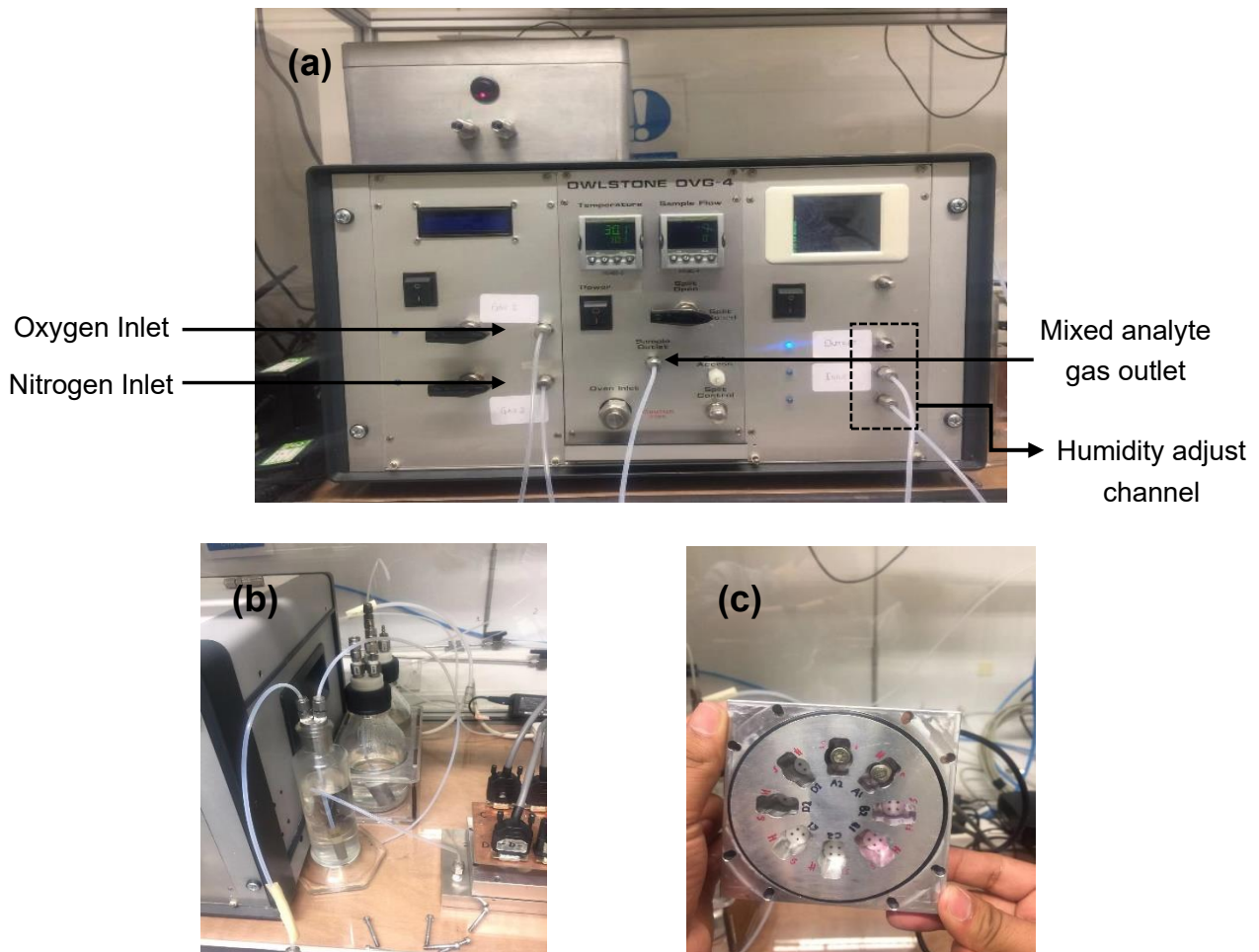


Figure 2.3 Equipment used in the oxygen gas sensing tests (a) OWLSTONE OVG-4 which controls the concentration of the oxygen, humidity environment and the operating temperature of the tested sensors (b) humidity adjust settings and (c) tested sensor chamber which allows eight sensors to be tested at a same time

2.3 Physical characterization

The crystalline structures of the synthesized thin film materials were obtained by X-Ray Diffraction (XRD) (Bruker D8-Discover LynxEye thin-film PXRD) equipped with a silicon strip detector using Cu K α radiation ($\lambda = 1.5418 \text{ \AA}$) and operated at a current of 40 mA and a voltage of 40 kV. The X-ray diffraction patterns were collected with a scanning rate of 0.05° step size over a 2 θ scan range from 10 to 66° counted at 1 s per step. Micro X-Ray Diffraction (μ XRD) was used to analyse the structure of crystalline materials on the sensor platforms for a very small area, relying on the dual wave/particle nature of X-rays. The patterns were obtained with a scanning rate 18° step size over a 2 θ scan range from 15 to 60° counted at 60 s per step for 3 steps. All XRD patterns were first analysed and further compared to literature standard data, PDFs stored in “Jade” software (Version 6.5, Materials Data, Inc.).

UV/vis spectra were obtained in a range from 200 nm to 800 nm by using PerkinElmer Lambda 950 UV-vis spectrometer. The transmittance (%T) spectra was carried out first and then the absorbance (A) spectra is based on the transmittance and simply estimated by using the formula shown in Eq. 5 below:

$$A = -\log (\%T / 100) \quad (5)$$

X-ray photoelectron spectroscopy (XPS) (Thermo Fisher Scientific) with a monochromatic Al K α X-Ray source (1846.6 eV) was used to measure the elemental composition and electronic states of the elements. C 1s (284.8 eV) peak calibration is conducted for the referencing of the other peaks' binding energy. The data were further analysed by software named “CasaXPS” (Version 2.3.16 RP 16, Casa Software Ltd.) and compared to literature standard data from the NIST XPS database.

Field Emission Scanning Electron Microscope (FESEM) (JEOL JSM-6301/ JSM-6300 with energy of 5/15 keV) was used to identify the morphology of the thin films from a

top-down configuration after Au-coating. High resolution transmission electron microscopy (HR-TEM) measurements were performed on a JEOL 2100 at a voltage of 200 kV. Features such as crystal structures, dislocations and grain boundaries can be analysed based on the interactions between the high energy electrons and the sample atoms through “Ganta microscopy suite” software (Version 3.22.1461.0, Gatan, Inc.).

Chapter 3 Nanostructured Tungsten Oxide Thin Film and Sensor: Synthesis and Characterization

3.1 Introduction

Tungsten oxide (WO_3) is a transition metal oxide which has attracted wide attention due to its unique physical and chemical properties, and has been used in electrochromic, photochromic, sensing and catalytic fields⁵. With the growing interest in nanotechnologies, nanostructured WO_3 exhibits unique and excellent properties and broadens its applications as compared to its bulk form by reducing grain size (involves increasing surface to volume ratio, altering surface energies and quantum confinement effects). A series of advances have been made in preparation of tungsten oxide powders and thin film nanostructures since the 1980s^{107,183}.

Up to now, tungsten oxide nanostructures with various morphologies and crystal structures have been investigated and developed, most of which are one-dimensional nanostructures, such as nanorods, nanowire, nanofibers and nanotubes. These properties including composition and performance are closely related to the synthesis method and experimental conditions^{132,184,185}. In addition to one-dimensional WO_3 nanostructures, the diversity of crystal structures determines that WO_3 grows in different crystal directions, so it is possible to form two-dimensional or three-dimensional nanostructures. Researchers have successfully synthesized nanosheets, nanoribbons and nanoplates with promising properties¹⁸⁶.

Activated Tungsten oxide (involves depositing a small amount of catalytic materials such as Pt on the surface of the WO_3 thin film) was firstly used for the detection of

airborne hydrogen for safety applications by P. J. Shaver. in 1967¹⁸⁷. WO₃ thick-film-based sensors have been developed and shown a highly sensitivity towards trace amount of VOC gases, especially aromatic hydrocarbon at ppb level in environmental measurement¹⁸⁸.

In this chapter, the as-deposited WO_{3-x} and WO₃ after annealing (AA) thin films via AACVD was initially conducted on various substrates, including glass, quartz and alumina with optimal reaction conditions from literature⁸² (reaction temperature 375°C and flow rate 300 sccm N₂) to investigate the influence of substrate on the formation of tungsten oxide thin film. Physical characterizations including XRD, XPS, SEM, TEM was carried out to clarify the phase of WO₃ presenting before and after the annealing process. Subsequently, the same deposition approach of WO_{3-x} and WO₃ AA thin films on alumina sensor platforms were carried out. A uniform WO₃ thin film with a monoclinic phase and nanoneedle-structure was obtained as demonstrated by combining with different analytical results.

3.2 Experimental

Tungsten hexacarbonyl [W(CO)₆] (≥97.0%) and reagents including acetone, methanol and isopropanol were purchased from Sigma-Aldrich Chemical corp. and used without any purification. All the substrates, including microscope slide (glass), quartz and alumina, were first cut into 2.5 cm × 2.5 cm pieces and cleaned in a sequence of acetone, methanol, isopropanol and distilled water, subsequently dried in stream of compressed air before use.

3.2.1 Preparation of WO₃ thin film

The WO₃ thin films were synthesized using AACVD on various substrates, including microscope slide (glass), quartz and alumina. The cleaned substrate was placed close

to the outlet of the rectangular AACVD reactor (3 cm × 6 cm × 2mm) shown in Figure 2.2 (a) and preheated to 375 °C. Tungsten hexacarbonyl [W(OC)₆] (0.06 g, 0.17 mmol) was dissolved in a mixed solution of 10 mL acetone and 5 mL methanol. After sonicating the mixture solution for 5 min, it was then transferred to a flask. An aerosol was generated by an ultrasonic humidifier (2 MHz, Johnson Matthey Liquifog) at room temperature. A gas flow of N₂ (99.99%, BOC) was passed through the aerosol mist at a flow rate of 300 standard cubic centimetre per minute (sccm), controlled by a mass flow controller (MFC, Brooks), to transport the aerosol droplets into the preheated reaction chamber. The deposition usually conducted for 30 min till all the precursor solution used up. The heater, humidifier and mass flow controller were then switched off and the film was allowed to cool down to room temperature under a flow of N₂. Finally, the as-deposited film was annealed in a muffle furnace at 500 °C for 2 h in air, heated up from room temperature to 500 °C at a rate of 10 °C/min. A series of repeat experiments with same reaction conditions, but on different substrates were carried out and listed in the table below, which A and M stand for acetone and methanol, respectively.

Table 3.1 Deposition conditions of as-deposited WO_{3-x} on different substrate, in which A and M stand for acetone and methanol

Exp. Name	W(CO) ₆ /g	Solvent /mL	Temperature/°C	Flow rate/ sccm	Substrate
WO _{3-x} (g)	0.06	10 A + 5 M	375	300	glass
WO _{3-x} (q)	0.06	10 A + 5 M	375	300	quartz
WO _{3-x} (a)	0.06	10 A + 5 M	375	300	alumina

3.2.2 Preparation of WO₃ sensor

An identical procedure to the synthesis of WO₃ films mentioned in Chapter 3.2.1 was used to make WO₃ sensors by AACVD. Instead of depositing on normal substrates, alumina sensor platforms (2 mm × 2 mm) and a shadow mask were used here. The sensor is consisting of gold electrodes along with a resistive platinum heater. A set of nine alumina-based gas sensors can be arranged in the mask at a time. Once the

deposition was finished, the sensors were allowed to cool down to room temperature naturally. The as-deposited sensors were then annealed in a muffle furnace at 500 °C for 2 h in air, heated up from room temperature to 500 °C at a rate of 10 °C/min. The reaction conditions for the fabrication of WO₃ thin film on alumina sensor was shown in the table below.

Table 3.2 Deposition conditions of as-deposited WO_{3-x} on alumina sensor

Exp. Name	W(CO) ₆ /g	Solvent /mL	Temperature/°C	Flow rate/ sccm	Substrate
WO _{3-x} (s)	0.06	10 A + 5 M	375	300	Alumina sensor

3.3 Results and discussion

3.3.1 Characterization of the WO₃ thin film

3.3.1.1 initial deposition

The various 2.5 cm x 2.5 cm substrates were placed close to the outlet of the reaction chamber during the deposition, rather than the inlet in order to get a more evenly distributed thin film. The as-deposited tungsten oxide thin films on various substrates were dark blue in colour, indicating the formation of sub-stoichiometric WO_{3-x}, which matched with the literature sub-stoichiometric tungsten oxide(PDF 36-0102, PDF 36-0103 and PDF 84-1516)¹⁸⁹. The blue colour of the deposited film indicated the loss of oxygen which then generates an additional valence state in the WO₃ structure. A set of annealing temperature tests were conducted (at 300, 400 and 500 °C) and a completely yellow-white thin film was obtained when annealed at 500 °C. Therefore, the optimal annealing temperatures was set to be 500 °C for 2 h in air as the standard for the rest annealing process. The yellow-white thin films were achieved, indicating the full transformation to oxidised stoichiometric WO₃¹⁹⁰. An example of as-deposited WO_{3-x} and WO₃ AA thin films on glass, quartz and alumina substrates as compared to its plain substrate was shown in Table 3.3 below.

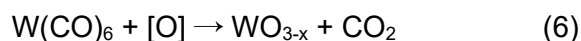
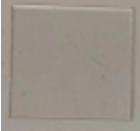


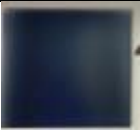
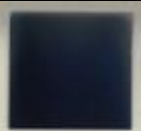
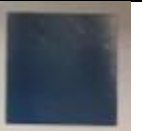


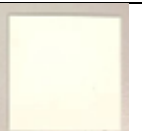


Table 3.3 As-deposited WO_{3-x} and annealed WO₃ thin film on glass, quartz and alumina substrate as compared to the plain substrates, respectively

	Glass	Quartz	Alumina
Plain substrate			
As-deposited WO _{3-x}			
WO ₃ After Annealing (AA)			

3.3.1.2 X-ray diffraction (XRD) analysis

The XRD patterns of as-deposited WO_{3-x} thin film on different substrates, including glass, quartz and alumina were put together in Figure 3.1 for comparison. Two highlighted peaks revealed on all three XRD patterns at 23.5 ° and 48.0 ° 2θ, corresponding to (010) and (020) reflections respectively, are in good agreement with the reference pattern of several sub-stoichiometric tungsten oxide WO_{3-x} (e.g. WO_{2.90} PDF 36-0102, a= 12.1 Å, b= 3.78 Å, c= 23.6 Å, α=90 °, β=94.6 °, γ=90 °; W₂₄O₆₈ PDF 36-0103, a= 18.3 Å, b= 3.78 Å, c= 17.1 Å, α=90 °, β=104.4 °, γ=90 °; W₁₈O₄₉ PDF 84-1516, a= 19.3 Å, b= 3.78 Å, c= 14.0 Å, α=90 °, β=115.2 °, γ=90 °), indicating the formation of monoclinic phase structure of sub-stoichiometric tungsten oxide before annealing. The additional weak peaks revealed in the WO_{3-x} on alumina XRD pattern were attributed to the presence of Al₂O₃ (PDF 82-1467). Therefore, there were no significant difference between XRD patterns of as-deposited WO_{3-x} thin films by

altering the substrates.

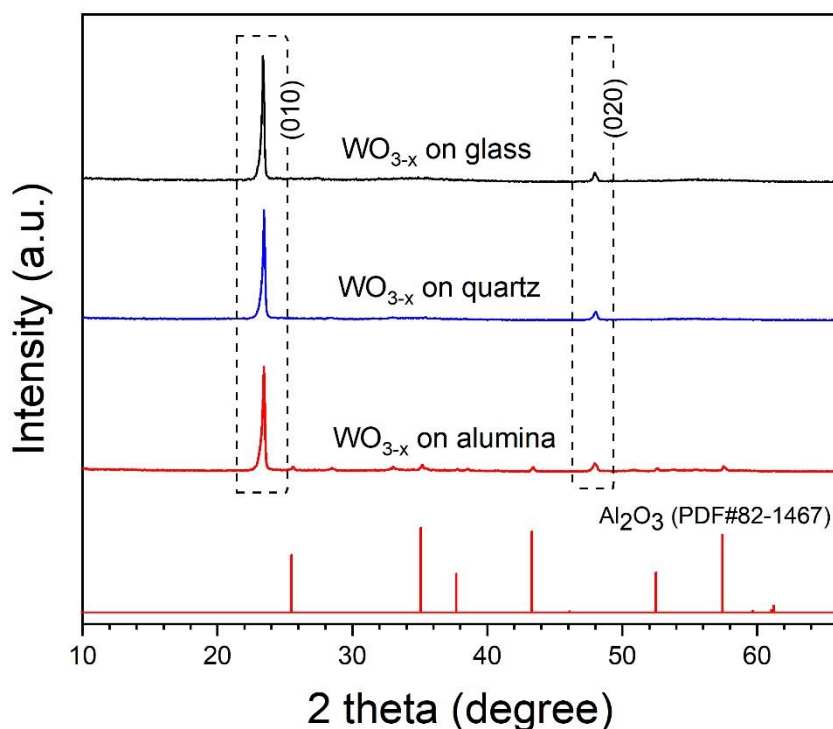


Figure 3.1 XRD patterns of as-deposited WO_{3-x} thin films on glass, quartz and alumina substrates before annealing with reference pattern of alumina Al₂O₃ (PDF 82-1467)

After annealing the WO_{3-x} thin films on different substrates at 500 °C in air for 2 h, the XRD patterns were collected and shown in figures below. Figure 3.2 illustrates the XRD pattern of WO₃ AA on glass, which was completely different from the other two patterns of WO₃ AA on quartz and alumina, which are shown in Figure 3.3. In Figure 3.2, the strong 2 theta peaks revealed at 10.84 °, 21.87 ° and 23.45 °, corresponding to (-101), (200) and (010) reflections respectively and showing the preferred orientation in the (010) direction, were in good agreement with the standard reference pattern of triclinic Na₂W₄O₁₃ (PDF#70-2022, a = 11.16 Å, b = 3.89 Å, c = 8.26 Å, α = 90.6 °, β = 131.36 ° and γ = 79.7 °). While the remaining strong 2theta peaks observed at 13.95 °, 23.20 °, 28.11 ° and 36.76 °, are attributed to (100), (002), (200) and (202) reflections respectively with preferred orientation in the (200) direction, were matched well with the standard reference pattern of hexagonal WO₃ (PDF#85-2459, a = 7.32 Å, b = 7.32

\AA , $c = 7.66 \text{ \AA}$, $\alpha = 90.0^\circ$, $\beta = 90.0^\circ$ and $\gamma = 120.0^\circ$). Therefore, the WO_3 thin film AA on glass probably consisted of the triclinic phase of $\text{Na}_2\text{W}_4\text{O}_{13}$ and the hexagonal phase of WO_3 . The reason to cause the formation of sodium tungsten oxide $\text{Na}_2\text{W}_4\text{O}_{13}$ is probably due to the migration of the sodium ion from the surface of the glass substrate entering into the unit cell of WO_3 at high temperature during the annealing process (e.g., 500°C), which can be further proved by analysis of the XRD patterns of WO_3 AA on quartz and alumina substrates.

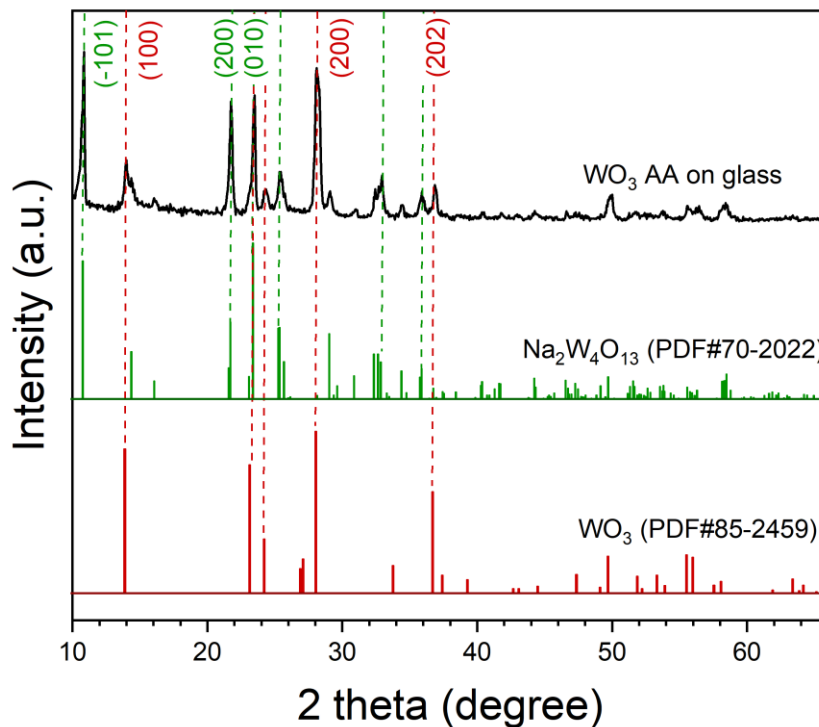


Figure 3.2 XRD patterns of WO_3 thin film on glass substrate after annealing at 500°C in air for 2 h with reference pattern of $\text{Na}_2\text{W}_4\text{O}_{13}$ (PDF#70-2022) and WO_3 (PDF#85-2459)

In Figure 3.3, the XRD patterns of WO_3 AA on quartz and alumina substrates show similar results (Ignoring the peaks attributed by Al_2O_3). The strong 2 theta peak highlighted at 23.1° and 47.4° , corresponding to the (002) and (004) reflections respectively with preferred orientation in (002) direction, were in good agreement with the standard reference pattern of monoclinic WO_3 (PDF#72-0677, $a = 7.31 \text{ \AA}$, $b = 7.54$

\AA , $c = 7.69 \text{ \AA}$, $\alpha = 90.0^\circ$, $\beta = 90.9^\circ$ and $\gamma = 90.0^\circ$). The pure monoclinic-phase WO_3 here further confirmed the formation of sodium tungsten oxide is due to existence of sodium ion within the glass substrate. The reference pattern of alumina Al_2O_3 (PDF#82-1467) shown in Figure 3.1 and 3.3 have been compared as a calibration and no shift was found, indicating that the two reflections of the WO_{3-x} (010) and (020) and WO_3 AA (002 and 004) is correct.

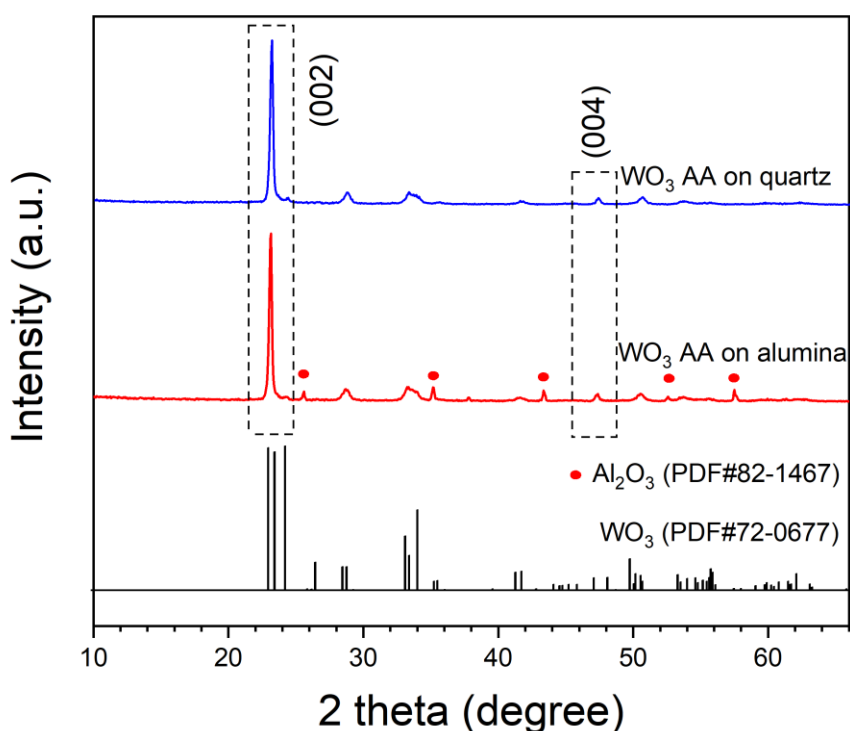


Figure 3.3 XRD patterns of tungsten oxide thin film on quartz and alumina substrates after annealing at 500 °C in air for 2 h with reference pattern of Al_2O_3 (PDF#82-1467) and WO_3 (PDF#72-0677)

3.3.1.3 Scanning electron microscope (SEM) analysis

The surface morphology of the synthesized tungsten oxide thin films was examined by SEM. All samples were gold-coated before analysing. As shown in Figure 3.7, SEM images of as-deposited WO_{3-x} and WO_3 AA on microscope slide (glass), quartz and alumina substrates were put together for a comparison. A high density of randomly oriented needle-like structures was observed.

The surface morphologies of the synthesized tungsten oxide thin films on various substrates were examined via SEM. All samples were gold-coated before any analysing. As shown in Figure 3.4 and 3.5 below, SEM images of cross section of as-deposited WO_{3-x} and SEM images of as-deposited WO_{3-x} and WO_3 AA thin films deposited on glass (a) and (b), alumina (c) and (d) and quartz (e) and (f) were put together for a comparison. The morphologies of as-deposited WO_{3-x} on various substrates were similar to each other, showing nano-needles (NNs) with sharp end structures with diameters ranging about 100 nm and length 1-2 μm , which in a good match with the formation of WO_3 NNs on Si substrate via AACVD at 500°C ¹⁹¹. After annealing these samples on various substrates at 500°C for 2 hours in air, no significant microstructure change was found for those deposited on alumina and quartz substrates; the NNs structures remains the same. However, the morphology of WO_3 AA thin film on glass was totally different to the as-deposited WO_{3-x} before annealing. Only trace amount of NNs can be found on the substrate. Most of the NNs coalesced into large sheets/plates and stacked together. This might proves the formation of triclinic phase of $Na_2W_4O_{13}$ and hexagonal phase of WO_3 from the analysis of XRD pattern of WO_3 AA on glass which mentioned before and matches well with plate-like crystal of $Na_2W_4O_{13}$ reported by SunHyung Lee¹⁹². The migration of the sodium ion from the surface of the glass substrate entered into the unit cell of WO_3 at high temperature during the annealing process (e.g., 500°C).

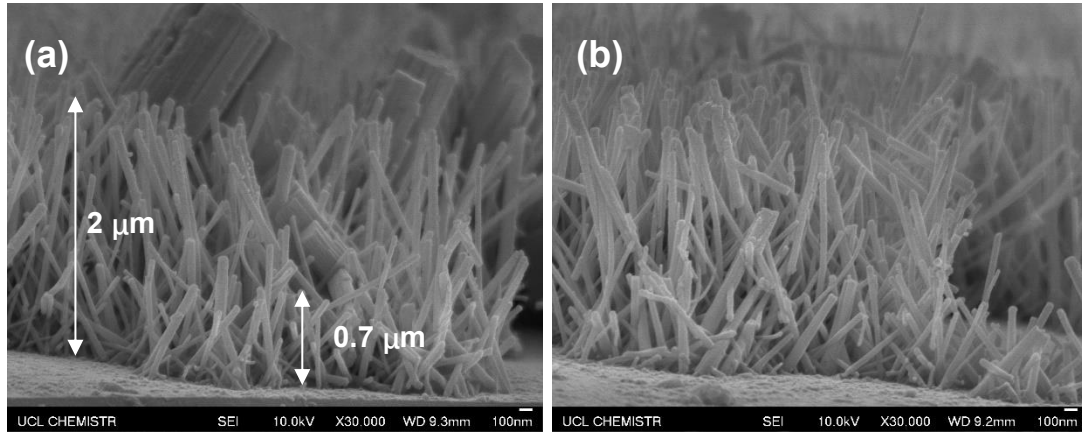
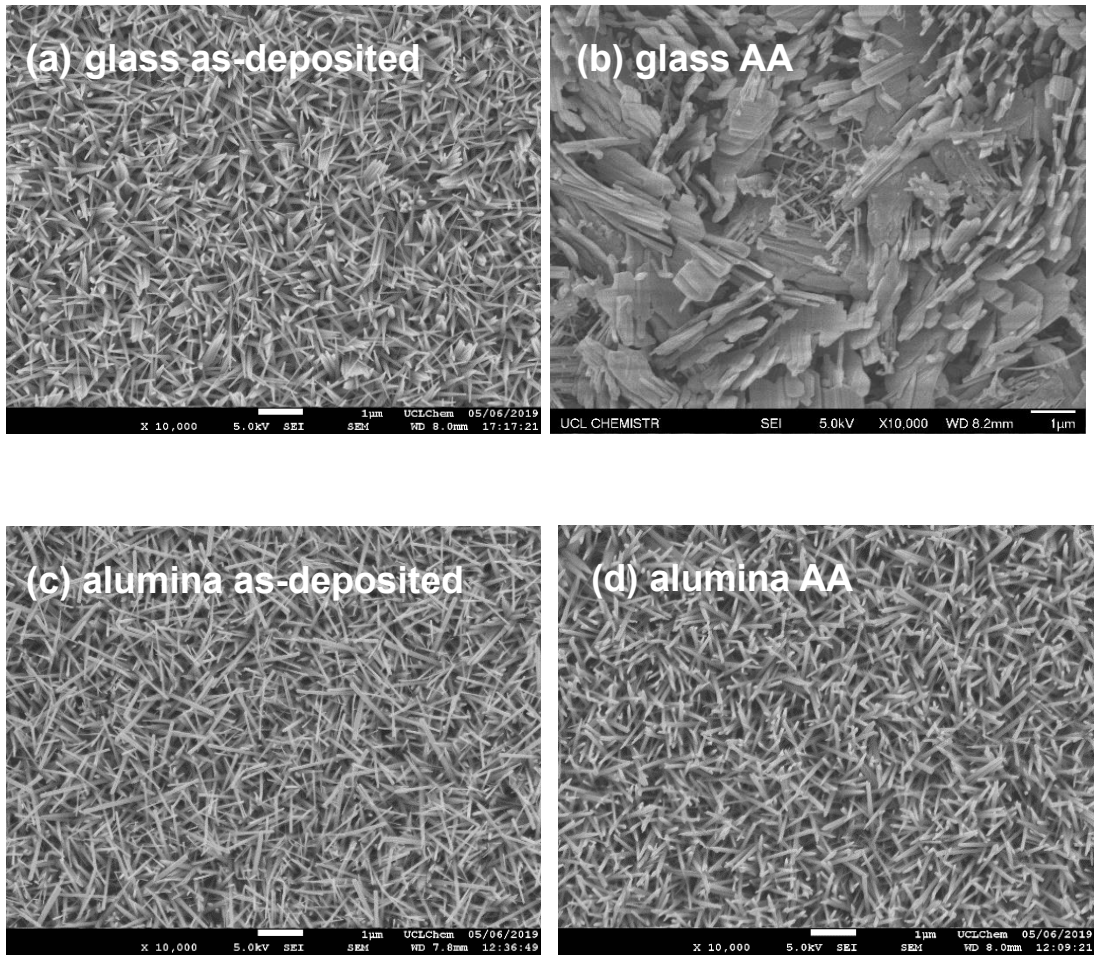


Figure 3.4 SEM images of cross section of as-deposited WO_{3-x} thin films



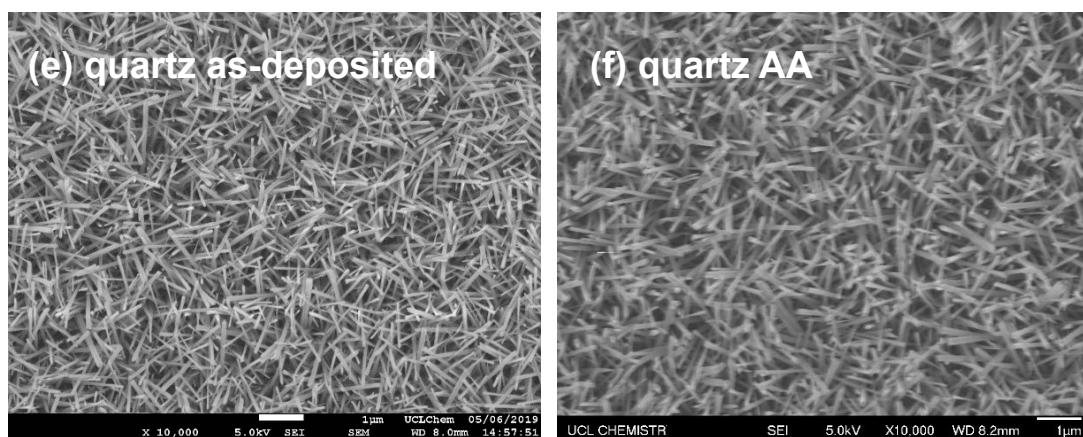


Figure 3.5 SEM images of as-deposited WO_{3-x} and WO_3 AA thin films on various substrates (a) WO_{3-x} on glass, (b) WO_3 AA on glass, (c) WO_{3-x} on alumina, (d) WO_3 AA on alumina, (e) WO_{3-x} on quartz and (f) WO_3 AA on quartz

3.3.1.4 X-ray photoelectron spectroscopy (XPS) analysis

The elemental electronic state and the elemental composition of as-deposited WO_{3-x} and annealed WO_3 thin films on glass, quartz and alumina substrates were conducted through XPS analysis. The examination of W 4f core-level spectra of all samples were shown below. The three spectra on the left are the as-deposited WO_{3-x} samples on glass (a), quartz (c) and alumina (e) and the corresponding WO_3 AA samples on the right. Analysis of W 4f core-level spectra of the as-deposited WO_{3-x} films revealed the presence of two 4f doublets of W, indicating of existence of two valence state. The main peaks (in red) located at 35.5 and 37.6 eV in Figure 3.6 (a) and the peaks (in red) located at 35.8 and 37.9 eV in Figure 3.8 (c) and (e) correspond to W 4f_{7/2} and W 4f_{5/2} peaks of stoichiometric WO_3 , respectively. The relatively lower binding energy peaks (in blue) observed at 33.9 and 36.4 eV in Figure 3.8 (a) and the peaks (in blue) 34.8 and 36.9 eV in Figure 3.6 (c) and (e) can be assigned to W 4f_{7/2} and W 4f_{5/2} peaks of sub-stoichiometric WO_{3-x} , respectively, and their values are in good agreement with those found in literature for stoichiometric WO_3 and sub-stoichiometric WO_{3-x} . After annealing at 500 °C in air for 2 hours, only one more pronounced and less overlapping 4f doublet of W was found for each W 4f core-level spectra on right and no shifts in the peak binding energies were observed. Two peaks (in red) at 35.3 and 37.5 eV in Figure

3.6 (b) and two peaks (in red) at 35.7 and 37.8 eV in Figure 3.6 (d) and (e) can be assigned to W $4f_{7/2}$ and W $4f_{5/2}$ peaks of W^{6+} , indicating the presence of stoichiometric WO_3 films on all substrates after the annealing process. While for glass substrate, as compared to the literature²²⁵, the binding energy of W $4f_{7/2}$ is approximately at 35.2 eV, which indicates the presence of WO_3 .

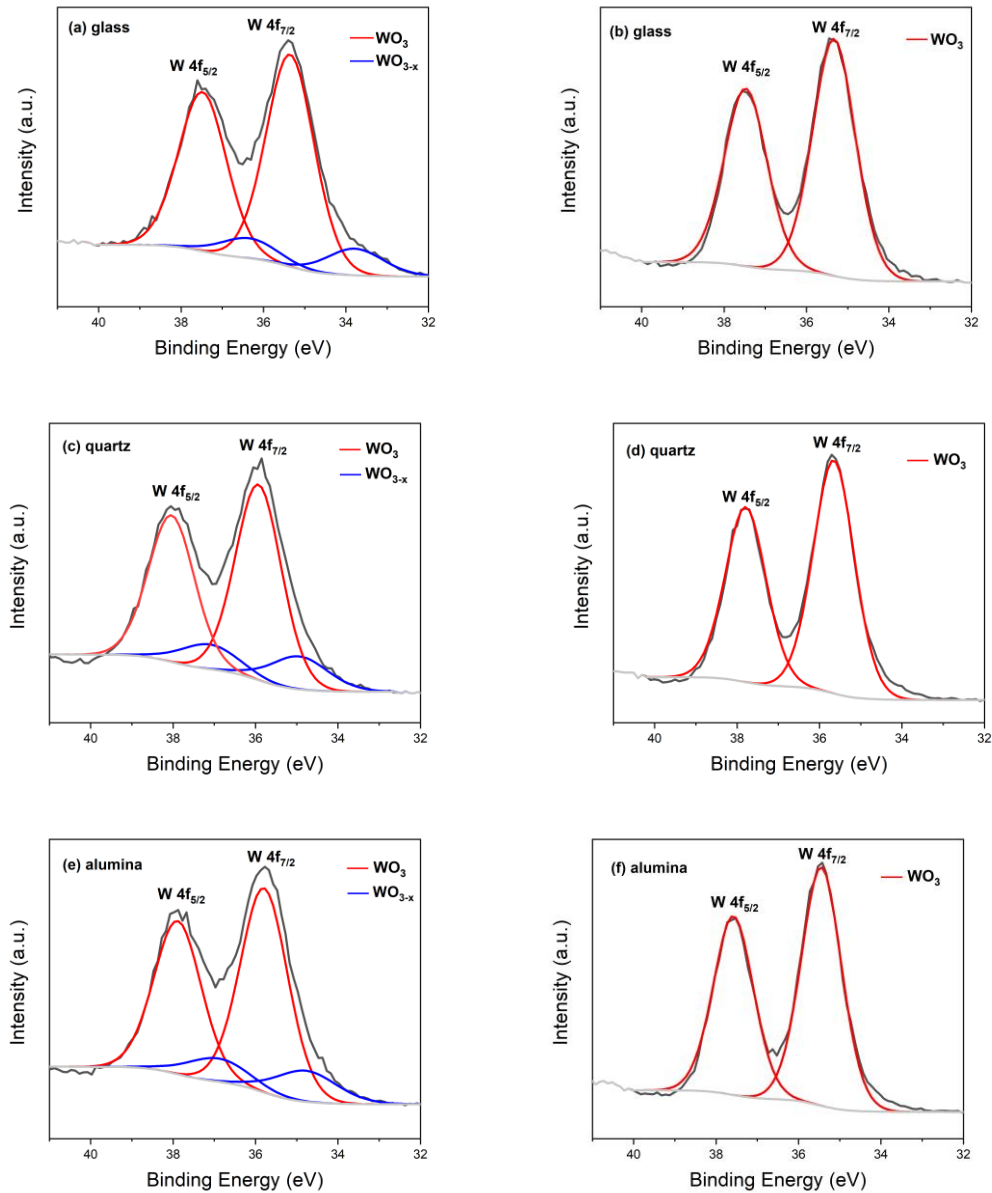


Figure 3.6 XPS W 4f core-level spectra (a) as-deposited WO_{3-x} on glass, (b) WO_3 AA on glass, (c) as-deposited WO_{3-x} on quartz, (d) WO_3 AA on quartz, (e) as-deposited WO_{3-x} on alumina and (f) WO_3 AA on alumina

As shown in Figure 3.7 below, XPS spectra of O1s for as-deposited WO_{3-x} on glass, quartz and alumina has been compared with the O 1s spectra for corresponding samples after annealing, no additional oxygen peaks were found for the as-deposited samples. For all samples, wider peaks have been seen for the as-deposited samples due to the shoulder on the high energy side by using a single Gaussian peak and peaks tend to move to lower binding energy after annealing.

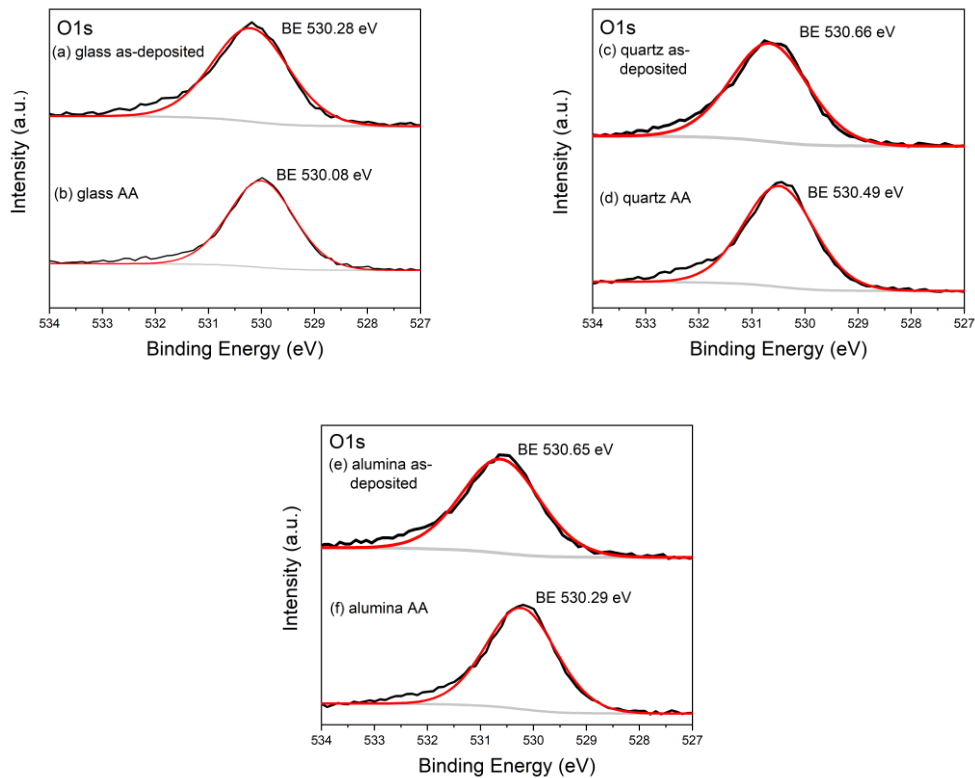


Figure 3.7 XPS O 1s core-level spectra (a) as-deposited WO_{3-x} on glass, (b) WO_3 AA on glass, (c) as-deposited WO_{3-x} on quartz, (d) WO_3 AA on quartz, (e) as-deposited WO_{3-x} on alumina and (f) WO_3 AA on alumina

3.3.2 Characterization of WO_3 sensor

3.3.2.1 Initial depositions analysis

Figure 3.8 shows an example of the blank alumina sensor, as-deposited WO_{3-x} and WO_3 after annealing on alumina sensor. As shown in the picture, the blank alumina sensor (left) is consisted of gold electrodes along with a resistive platinum heater on

the alumina substrate. The as-deposited WO_{3-x} sensor (mid) with an evenly coverage of dark blue thin film indicates the formation of sub-stoichiometric WO_{3-x} . After annealing at $500^{\circ}C$ for 2 hours in air, pale white-yellow thin film coated sensor(right) was obtained, revealing the fully oxidation occurred and formation of stoichiometric WO_3 . This colour transformation is in good agreement to the deposition of tungsten oxide on various substrates at the beginning.



Figure 3.8 Samples of 2 mm x 2mm blank alumina sensor (left), as-deposited WO_3 on alumina sensor(mid) and WO_3 AA on alumina sensor(right)

3.3.2.2 XRD of sensor before annealing and after annealing and blank sensor

The XRD pattern of a plain alumina sensor platform without any deposition was shown in Figure 3.9, which can be recognized as a combination of two materials obviously, corresponding to alumina and gold. Specifically, the diffraction peaks 25.6° , 35.2° , 37.8° , 43.4° , 52.6° , 57.5° , 66.5° and 68.2° are attributed to (012), (104), (110), (113), (024), (116), (214) and (300) reflections, which are in good agreement with the standard reference pattern of hexagonal alumina (PDF#82-1467, $a = 4.76 \text{ \AA}$, $b = 4.76 \text{ \AA}$, $c = 13.0 \text{ \AA}$, $\alpha = 90.0^{\circ}$, $\beta = 90.0^{\circ}$ and $\gamma = 120.0^{\circ}$). Rest of the peaks highlighted at 38.3° , 44.6° and 64.7° can be indexed to (111), (200) and (220) reflections and are in excellent match with the reference pattern of cubic gold (PDF#01-1174, $a = 4.06 \text{ \AA}$, $b = 4.06 \text{ \AA}$, $c = 4.06 \text{ \AA}$, $\alpha = 90.0^{\circ}$, $\beta = 90.0^{\circ}$ and $\gamma = 90.0^{\circ}$). Alumina is the base of the sensor platform and gold comes from the electrodes.

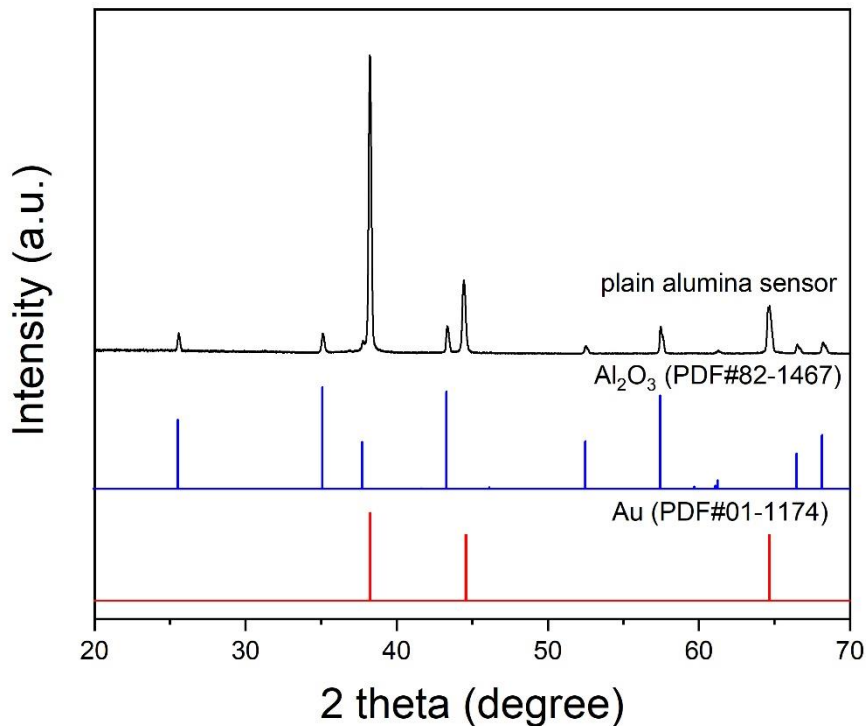


Figure 3.9 XRD patterns of plain alumina sensor with reference pattern of Al_2O_3 (PDF#82-1467) and Au (PDF#01-1174)

The XRD patterns of as-deposited WO_{3-x} and WO_3 AA on alumina sensor were put together in Figure 3.10 for a comparison. Ignoring the peaks attributed by Al_2O_3 and Au, the pattern of as-deposited WO_{3-x} exhibiting reflections in the (010) and (020) at 23.5° and 48.1° 2θ was identical to the XRD patterns of WO_{3-x} deposited on the glass/quartz and alumina substrates shown in Figure 3.1, indicating the formation of monoclinic phase structure of sub-stoichiometric WO_{3-x} before annealing. The diffraction peaks of WO_3 AA matched monoclinic WO_3 (PDF#72-0677, $a = 7.31 \text{ \AA}$, $b = 7.54 \text{ \AA}$, $c = 7.69 \text{ \AA}$, $\alpha = 90.0^\circ$, $\beta = 90.9^\circ$ and $\gamma = 90.0^\circ$). The strong peak at 23.1° and two relative weak peaks at 23.6° and 24.4° were attributed to (002), (020) and (200) reflections, showing the preferred orientation along the (002) direction. This is matched with the preferred orientation (002) when WO_3 deposited on the alumina substrate after annealing, shown in Figure 3.3.

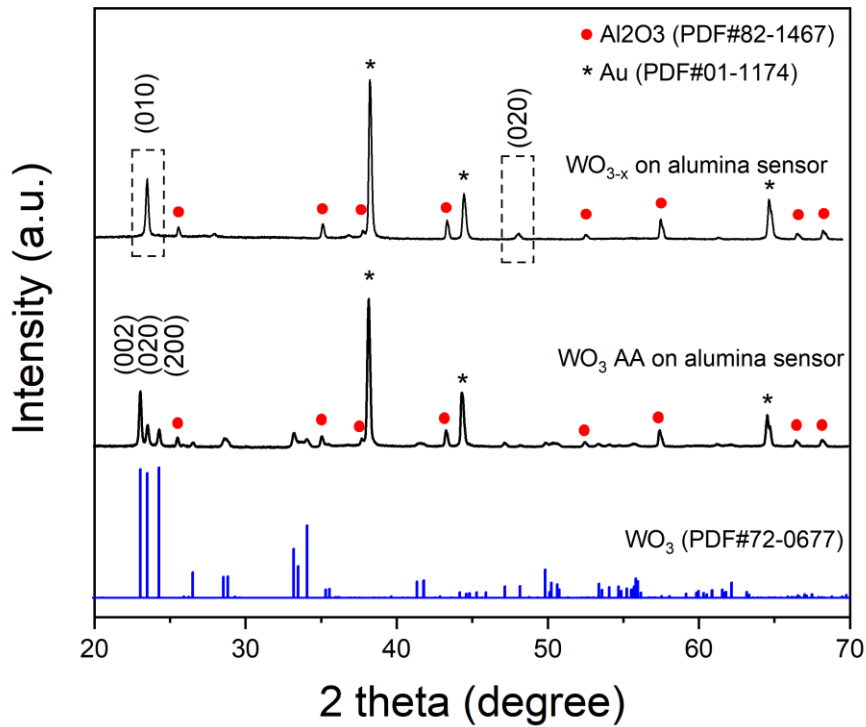


Figure 3.10 XRD patterns of as-deposited WO_3 before annealing and WO_3 after annealing at $500\text{ }^\circ\text{C}$ in air for 2 h on alumina sensor with reference pattern of WO_3 (PDF#72-0677)

3.3.2.3 SEM of bare sensor, as-deposited WO_{3-x} on sensor and WO_3 AA on sensor

The surface morphology of the bare sensor, as-deposited WO_{3-x} and WO_3 AA thin films on sensor were examined by SEM and shown in Figure 3.11. The SEM images shown in Figure 3.11 (a) low and (b) high magnification of bare sensor revealed that the sensor is consist of gold electrodes and alumina-based substrate. The surface morphology of as-deposited WO_{3-x} thin film on sensor were examined and shown in Figure 3.11 (c) and (d), indicating the formation of a thick layer of nonaligned NNs, which evenly distributed over the gold electrode area. Figure 3.11 (e) and (f) show the surface morphology of WO_3 thin film on sensor after annealing at $500\text{ }^\circ\text{C}$ in air for 2 h. From the SEM images, the sharp heads of the nanoneedle structures disappeared and long nanoneedles tend to break into short pieces. This transformation is identical to the WO_3 NNs formed on the alumina substrate shown in Figure 3.5 (c) and (d).

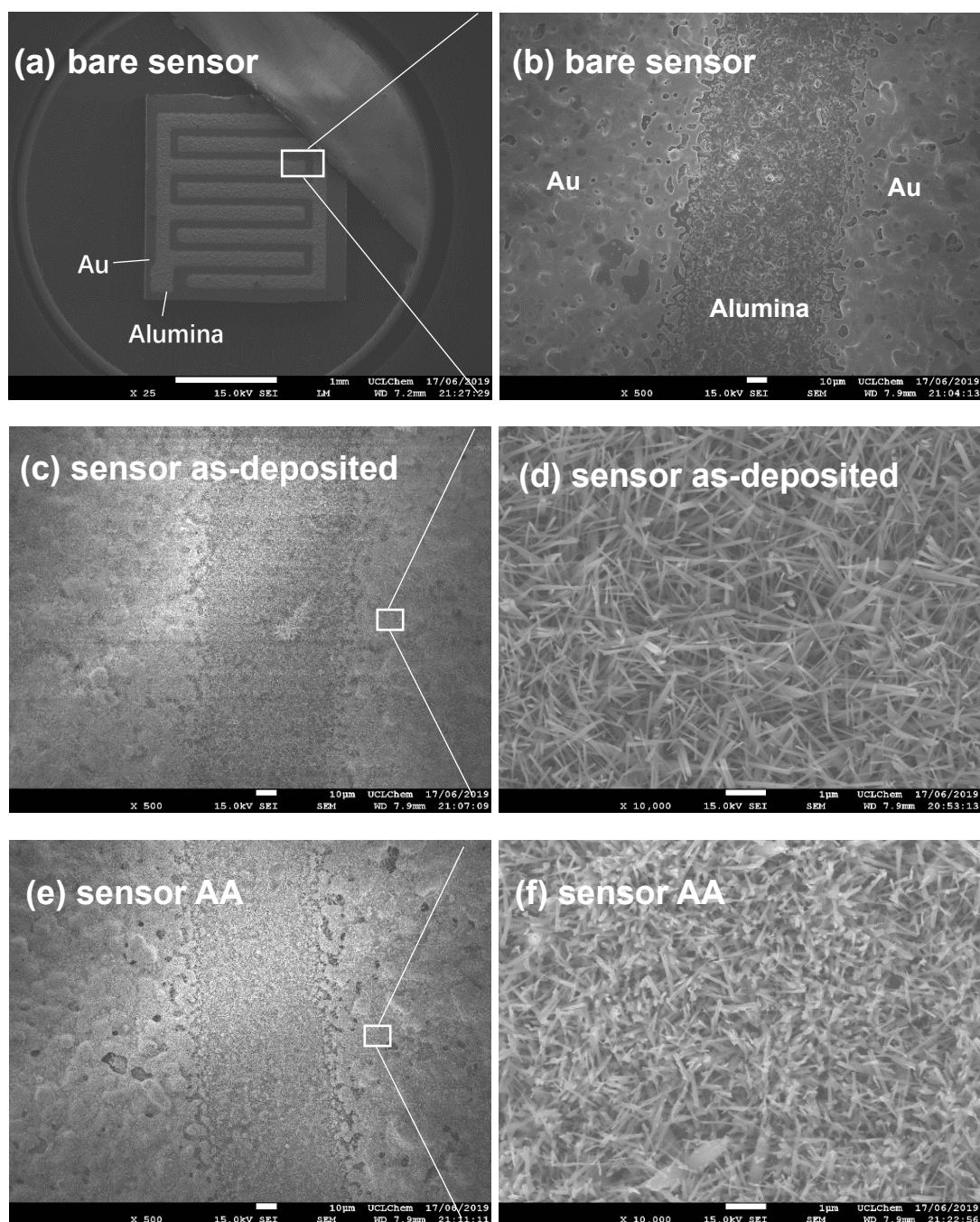


Figure 3.11 SEM images of (a) bare alumina sensor at low magnification, (b) at high magnification, (c) as-deposited WO_{3-x} on alumina sensor at low magnification, (d) at high magnification, (e) WO_3 AA on alumina sensor at low magnification and (f) at high magnification

3.3.2.4 XPS analysis of as-deposited WO_{3-x} and WO_3 AA on alumina sensor

Figure 3.12 displays the XPS W 4f core-level spectra recorded from the as-deposited

WO_{3-x} and WO₃ AA films on alumina sensor platform. After fitting the spectra for as-deposited WO_{3-x} shown in Figure 3.13 (a), two doublets of W 4f were obtained. The more intense one, with components centred at 35.7 and 37.8 eV, are associated with W 4f_{7/2} and W 4f_{5/2} for W⁶⁺ oxidation state, respectively, referring to the existence of stoichiometric WO₃. The low-intensity one at 34.7 and 36.9 eV can be assigned to W 4f_{7/2} and W 4f_{5/2}, indicating the presence of the sub-stoichiometric WO_{3-x}. The W 4f spectra of WO₃ AA film on sensor shown in Figure 3.12 (b) reveals only two intense peaks at 35.4 and 37.5 eV, is correspond to W 4f_{7/2} and W 4f_{5/2} for W⁶⁺ oxidation states, indicating the presence of only stoichiometric WO₃. By comparing the W 4f core spectra between WO₃ deposited on alumina and sensor substrate, no shift was found, indicating the consistency of formation of stoichiometric WO₃.

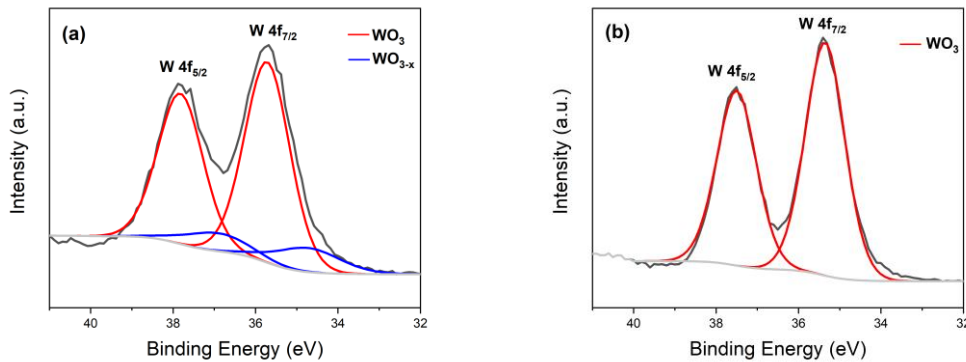


Figure 3.12 XPS W 4f core-level spectra of (a) as-deposited WO_{3-x} and (b) WO₃ AA on alumina sensor platform.

3.3.2.5 TEM of as-deposited WO₃ and WO₃ AA on sensor

Further characterization of the as-deposited WO_{3-x} and WO₃ AA thin films on sensors, such as the length and diameter of the WO_{3-x} / WO₃ NNs has been examined by HRTEM, as shown in Figure 3.13. Sensor samples were sonicated in methanol and the debris was collected on the copper grid for analysing. In Figure 3.13 (a), the WO_{3-x} NN shows an increasing of diameter from 20 to 110 nm and with a length of 2.14 μ m along the growth direction (bottom to top) which is perpendicular to the substrate. The square-enclosed area Figure 3.13 (b) revealed the d-spacing of 0.362 nm, which can be attributed to the (010) planes of monoclinic WO_{3-x}, indicating the growth direction of

WO_{3-x} NNs was along [010] direction. The NNs structure was almost maintained the same after annealing at 500 °C in air for 2 hours which shown in Figure 3.14 (d). The sharp head disappeared, and the surface became slightly coarser and rough. The square-enclosed area Figure 3.13 (e) revealed the d-spacing of 0.378 nm, which can be attributed to the (002) planes of monoclinic WO₃ (PDF#72-0677), indicating the growth direction of WO₃ NNs was along [002] direction. After comparing the two d-spacing values, it may suggest that lattice parameters influenced and increased due to the oxidization of WO_{3-x} to WO₃ during annealing process.

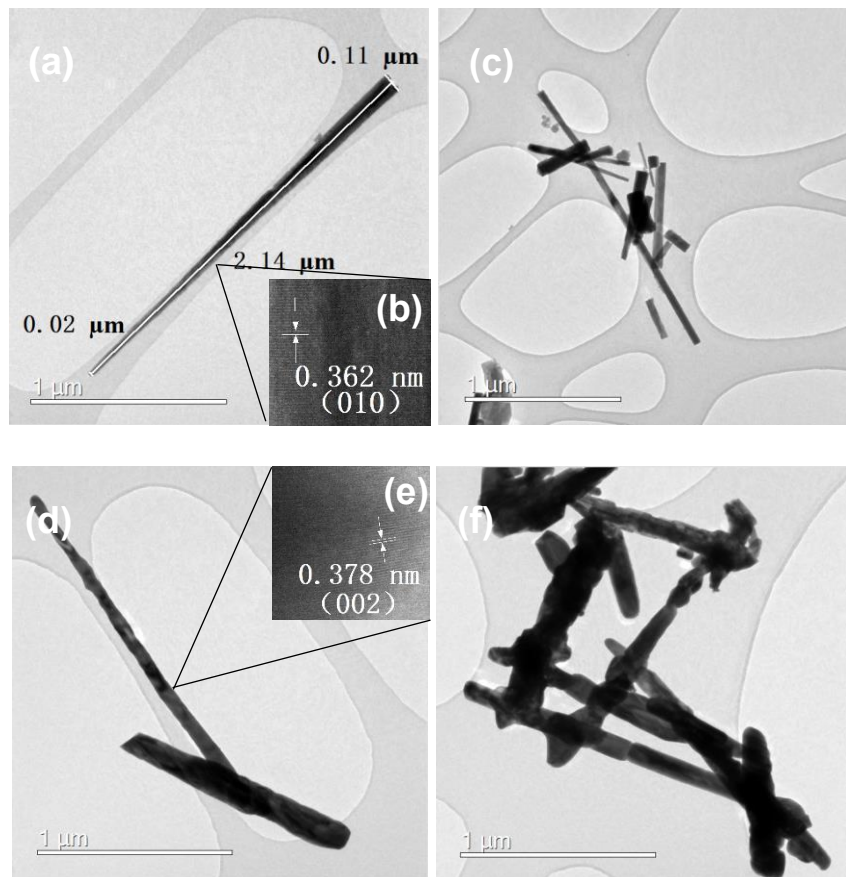


Figure 3.13 HRTEM images of (a) as-deposited WO_{3-x} with a length of 2.14 μm, (b) high magnification of selected section of as-deposited WO_{3-x}, (c) a cluster of as-deposited WO_{3-x} NNs, (d) annealed WO₃ NNs, (e) high magnification of selected section of annealed WO₃ NNs and (f) a cluster of annealed WO₃ NNs

3.4 Conclusion

Under the premise of optimized deposition temperature (375 °C), solvent ratio (2:1 acetone: methanol) and flow rate (300 sccm) conditions for the formation of WO₃ NNs thin films via AACVD explored by our research group previously, the influence of various substrates including glass, quartz and alumina on the morphology of WO₃ has been further studied. No obvious change was observed among the three as-deposited WO_{3-x} thin films on various substrates, which all show similar characterization results based on XRD and XPS. And SEM images show the successfully formation of sharp-end as-deposited WO_{3-x} NNs structures with diameters ranging about 100 nm and length ~ 1 to 2 μm before annealing process. After annealing at 500 °C for 2 hours in air, dark blue WO_{3-x} thin films on various substrates all turned into pale white-yellow in colour, combine with the analysis from XRD, XPS and TEM indicating the only presence of oxidised stoichiometric WO₃. The annealing temperature of 500 °C is much higher than the operating gas sensing temperature, which ensures the stability of the WO₃ sensors in the gas sensing test. No significant microstructure change was found for WO₃ deposited on alumina and quartz substrates before and after the annealing process. For tungsten oxide deposited on glass substrate, most of the NNs coalesced into large sheets/plates and stacked together, indicating the formation of triclinic phase of Na₂W₄O₁₃ and hexagonal phase of WO₃, based on the analysis of XRD, which can be attributed to the migration of the sodium ion from the surface of the glass substrate entered into the unit cell of WO₃ at high temperature (500 °C) during the annealing process.

WO₃ NNs thin film was also successfully grown onto sensor arrays printed on alumina substrate via AACVD at an optimal deposition temperature (375 °C). The XRD pattern indicates the formation of monoclinic phase of WO₃ after annealing, which matches well with the reference. XPS reveals the presence of fully oxidised stoichiometric WO₃ after annealing process as well. The microstructural transformation is identical to the nanostructure of the WO₃ NNs deposited on the substrates examined before (quartz

and alumina). Structural, composition and morphological analysis for both as-deposited and annealed WO_3 sensors were well examined and revealed that this method is effective for growing WO_3 NNs using a single-source precursor $\text{W}(\text{CO})_6$.

Chapter 4 Nanostructured Silver Decorated Tungsten Oxide Thin Films and Sensors Using Silver Nitrate Precursor: Synthesis and Characterization

4.1 Introduction

WO₃ nanoneedles (NNs) decorated with various noble metal nanoparticles (NPs) have been widely investigated and developed in many applications, especially the gas sensing area^{81,82,193–195}. Studies have shown that the addition of noble metal nanoparticles to the surface not only improves the sensitivity and stability of the sensor, but also improves the selectivity of the gas sensor¹⁹⁶. It has been demonstrated that AACVD is a flexible technique that facilitates the implementation and functionalization of WO₃ NNs with many different noble metal or metal oxide NPs (Au, Pt, Ni, PdO, Cu₂O and etc.)^{82,191,194,196}. But to our knowledge, very little research is devoted to the Ag NPs modified WO₃ in gas sensing application. Most recently, Navarrete et al. reported a two-step synthesis method for the fabrication of Ag₂O doped WO₃ via AACVD toward H₂S and H₂ gas sensing¹⁴⁵.

In this chapter, silver nitrate (AgNO₃) precursor is used as raw material to investigate the feasibility of modification of WO₃ NNs with Ag NPs via AACVD. After a series of optimization experiments by adjusting deposition temperature, flow rate of carrier gas N₂ and the precursor dosage, Ag@WO₃ thin films were obtained and their physical characterization examined through XRD, XPS, SEM and TEM.

4.2 Experimental

Silver nitrate (AgNO_3) ($\geq 99.0\%$) and tungsten hexacarbonyl [$\text{W}(\text{CO})_6$] ($\geq 97.0\%$) were purchased from Scientific Laboratory Supplies and Sigma-Aldrich Chemical corp., respectively and used without any purification. Reagents including acetone and methanol were purchased from Sigma-Aldrich Chemical corp. and used directly.

4.2.1 Preparation of Ag thin films

Ag thin films were deposited on glass substrates (2.5 cm x 5.5 cm) by AACVD. AgNO_3 (0.06 g, 0.35 mmol) was dissolved in a mixed solution of 10 mL acetone and 5 mL methanol. Aerosol was generated from the precursor solution and transported to the preheated reaction chamber at 350 °C with a flow of N_2 at 300 sccm initially. The film was cooled down to room temperature under a flow of N_2 once the reaction was finished (~30 mins). A series of experiments with various deposition temperatures were conducted on glass substrate to identify optimal temperature for the deposition of Ag thin films on glass substrate (Table 4.1).

Table 4.1 Reaction conditions of AgNO_3 deposited on glass substrate

Exp. No.	AgNO_3 / g	Temperature/ °C	Flow rate/ sccm	Substrate
1	0.06	150	300	glass
2	0.06	200	300	glass
3	0.06	250	300	glass
4	0.06	300	300	glass
5	0.06	350	300	glass

4.2.2 Preparation of Ag@WO₃ thin films on glass substrates

Ag@WO₃ thin film on glass substrate (2.5 cm x 2.5 cm) were fabricated via AACVD in two steps. The first step was the preparation of annealed WO₃ thin film on glass substrate, which is described in Chapter 3.2.1. The second step was the decoration of

Ag nanoparticles onto the annealed WO₃ thin films. Initially, AgNO₃ (0.06 g, 0.35 mmol) was dissolved in a mixed solution of 10 mL acetone and 5 mL methanol. The deposition was conducted at 200 °C with a flow of N₂ at 300 sccm. Once all the precursor solution was consumed, the film was allowed to cool down under N₂ atmosphere till it reached room temperature. After then, a series of experiments were carried out with various amount of the AgNO₃ precursor used, and varying deposition temperature and flow rate of carrier gas, to investigate how these parameters would affect the deposition of the Ag nanoparticles decorated on WO₃ AA on glass substrate. The details of the deposition conditions are shown in Table 4.2 below. Initially, experiments 7, 8 and 9 were conducted to figure out the optimal deposition temperature for the deposition of Ag on WO₃ AA. Experiments 9, 10 and 11 were carried out to study how various amounts of AgNO₃ precursor affected the Ag-loadings on WO₃ AA samples. Finally, experiments 9,12 and 13 were used to investigate how flow rate of carrier gas nitrogen would influence the deposition coverage of Ag NPs onto the WO₃ AA thin film substrate.

Table 4.2 Reaction conditions of Ag@WO₃ AA on glass substrate

Exp. No.	AgNO ₃ / g	Temperature/ °C	Flow rate/ sccm	Substrate
7	0.06	200	300	WO ₃ AA on glass
8	0.06	225	300	WO ₃ AA on glass
9	0.06	250	300	WO ₃ AA on glass
10	0.03	250	300	WO ₃ AA on glass
11	0.09	250	300	WO ₃ AA on glass
12	0.06	250	200	WO ₃ AA on glass
13	0.06	250	400	WO ₃ AA on glass

4.2.3 Preparation of Ag@WO₃ thin films on sensors

Ag@WO₃ sensors were fabricated by the same procedure mentioned in chapter 4.2.2 via a two-step AACVD technique, except that the glass substrate was substituted by an alumina-based gas sensor platform (2 mm x 2 mm). In the first stage, as-deposited

WO₃ thin films were deposited on sensors followed by annealing at 500 °C for 2 hr (described in Chapter 3.2.2). In the second step, silver nanoparticles were incorporated to the WO₃ thin films by dissolving 0.09 g of AgNO₃ in a mixed solution of 10 mL acetone and 5 mL methanol. The generated aerosol from the precursor solution was deposited at 250 °C and flow of N₂ at 300 sccm. The deposition conditions for the preparation of Ag@WO₃ sensor is detailed in the Table 4.3 below.

Table 4.3 Reaction conditions of formation of Ag@WO₃ on alumina sensor

Exp. No.	AgNO ₃ / g	Temperature/ °C	Flow rate/ sccm	Substrate
14	0.09	250	300	WO ₃ AA on alumina sensor

4.3 Results and discussions (AgNO₃)

4.3.1 Characterization of Ag thin films

4.3.1.1 Initial deposition

Attempts were made to synthesise Ag thin films on glass substrates (2.5 cm × 5.5 cm) with 0.06 g AgNO₃ via AACVD at different deposition temperatures, range from 150 to 350 °C, with an interval of 50 °C and a constant flow of N₂ at 300 sccm. The as-deposited thin films obtained appeared as a pale-white or almost transparent film deposited on the glass surface.

4.3.1.2 XRD analysis

The XRD pattern of the as-deposited Ag thin film on glass substrate at 150 °C, shown in Figure 4.1 is distinct to the XRD patterns of AgNO₃ deposited at other temperatures. It showed the presence peaks associated with hexagonal phase AgNO₃ (PDF#70-0198, R3c space group, a = 5.16 Å, b = 5.16 Å, c = 16.58 Å, and α = β = 90 °, γ = 120 °), which was in excellent agreement with those given in the standard data¹⁹⁷. This may

be due to that AgNO_3 aerosol droplets were directly transported through the reactor and deposited onto the glass substrate by evaporation without any decomposition at $150\text{ }^\circ\text{C}$.

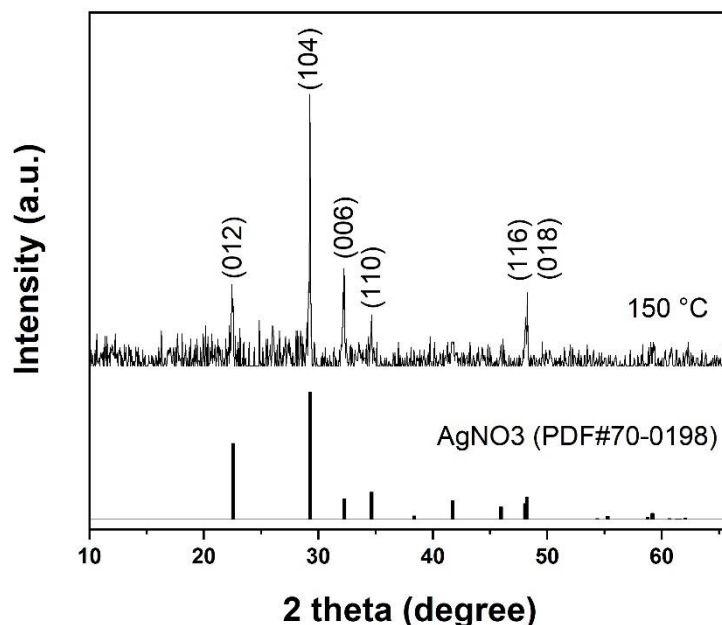


Figure 4.1 XRD patterns of as-deposited Ag thin film on glass substrate by using 0.06g AgNO_3 in a 2 :1 mixture of acetone and methanol, at $150\text{ }^\circ\text{C}$ and a constant flow of N_2 at 300 sccm, as compared to standard pattern of AgNO_3 (PDF#70-0198).
[corresponding to Exp. No. 1]

The XRD patterns of as-deposited Ag thin films on glass substrates at various deposition temperatures ranging from 200 to $350\text{ }^\circ\text{C}$ were recorded and are shown in Figure 4.2. For all XRD samples, the same position was chosen on various samples to be analysed. The patterns exhibit reflections in the (111), (200) and (220) planes at 38.12° , 44.30° and 64.45° 2θ respectively, indicating the presence of silver metal, which matched well with those given in the standard data (PDF#87-0718, Fm-3m (225) space group, $a = b = c = 4.0773\text{ \AA}$; $\alpha = \beta = \gamma = 90^\circ$). The most intense peak at 2θ 38.12° was recorded when the deposition temperature was set to $200\text{ }^\circ\text{C}$ and the intensity gradually decreased as the temperature increased up to $350\text{ }^\circ\text{C}$. Therefore, the optimal deposition temperature for deposition of Ag from the AgNO_3 precursor was inferred to be between 200 and $250\text{ }^\circ\text{C}$. At higher temperature such as 300 or $350\text{ }^\circ\text{C}$,

silver particles may form as powders with large particle size via homogeneous reactions. Therefore, some portion of the inlet precursor is consumed by these powder-forming reactions, and these preformed powders are exhausted from the reaction chamber with the nitrogen carrier gas, resulting in the decreasing intensity found in the XRD patterns (and UV-Vis spectra – see below).

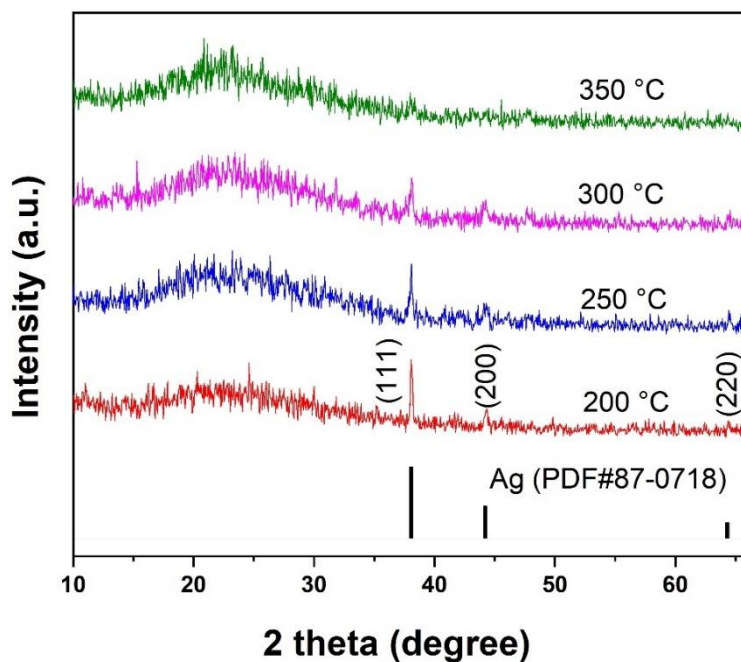


Figure 4.2 XRD patterns of as-deposited Ag thin film on glass substrate by using 0.06g AgNO₃ in a 2 :1 mixture of acetone and methanol, at 200, 250, 300 and 350 °C and a constant flow of N₂ at 300 sccm, as compared to standard pattern of metal Ag (PDF#87-0718).

[corresponding to Exp. No. 2,3,4 and 5]

4.3.1.3 UV-Vis analysis

The films on glass substrates deposited at various temperatures in the range from 200 to 300 °C were analysed by UV-Vis transmission spectrometry. Both the front part and back part of the Ag thin films (relative to the inlet and outlet of the reactor, respectively) were examined, and data is shown in Figure 4.3. The peaks highlighted at λ_{\max} ~560 nm were attributed to the presence Ag nanoparticles, which matched well with the value for the surface plasmon resonance (SPR) of Ag nanoparticles with size about 50

nm¹⁹⁸. The structure of the SPR peak is related to the size/shape of the Ag nanoparticles, therefore the broad peak observed in the UV-vis spectrum in the range from 400 to 600 nm might indicate a wide distribution of Ag nanoparticle sizes (i.e. 2 to 100 nm)¹⁹⁹. Meanwhile, the front part of thin films at both 200 and 250 °C gave the highest intensity peaks, indicating that more Ag particles were deposited close to the inlet of the reactor. The lack of a peak at 650 nm, which is the expected absorbance for Ag₂O, indicates that no significant Ag₂O was formed²⁰⁰. Therefore, the optimal deposition temperature for deposition of Ag from AgNO₃ as determined by UV-vis was inferred to be between 200 and 250 °C, which is identical to the result obtained from XRD.

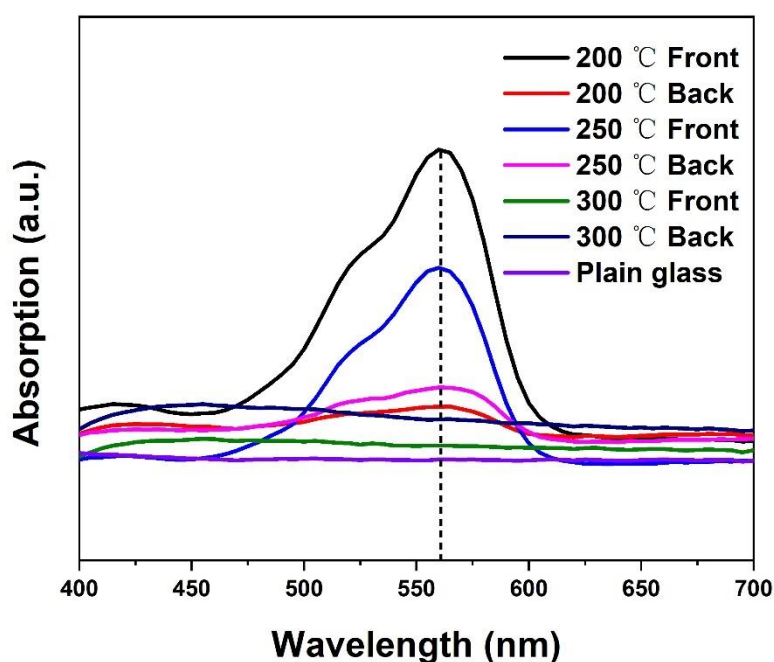


Figure 4.3 UV-Vis absorption spectra of as-deposited Ag thin film on glass substrate by using 0.06g AgNO₃ in a 2 :1 mixture of acetone and methanol, at 200, 250 and 300 °C and a constant flow of N₂ at 300 sccm

4.3.1.4 SEM analysis

Figure 4.4 is the SEM image of as-deposited Ag thin films on glass substrate using 0.06 g AgNO₃ at different magnifications. Two different structures were observed; at

low magnification shown in (a) and (b), a large number of small clusters were distributed on the surface, whilst at high magnifications (c), nanoparticles were found to be uniformly distributed around the large crystals, with the diameter of the nanoparticles decreasing with increasing distance from the central crystal. It was thought the large crystals might be attributed to the formation of NaNO_3 , consistent with the data from the XPS survey spectrum (Figure 4.6), and with similar structures observed on samples identified as NaNO_3 after treating glass substrates with $\text{Al}(\text{NO}_3)_3$ in a separate study, done by a MSc student, M. Prow. in our group. In Figure 4.4 (d), the diameters of the smaller, presumed Ag nanoparticles, range from 10 to 100 nm and were randomly deposited on the glass surface.

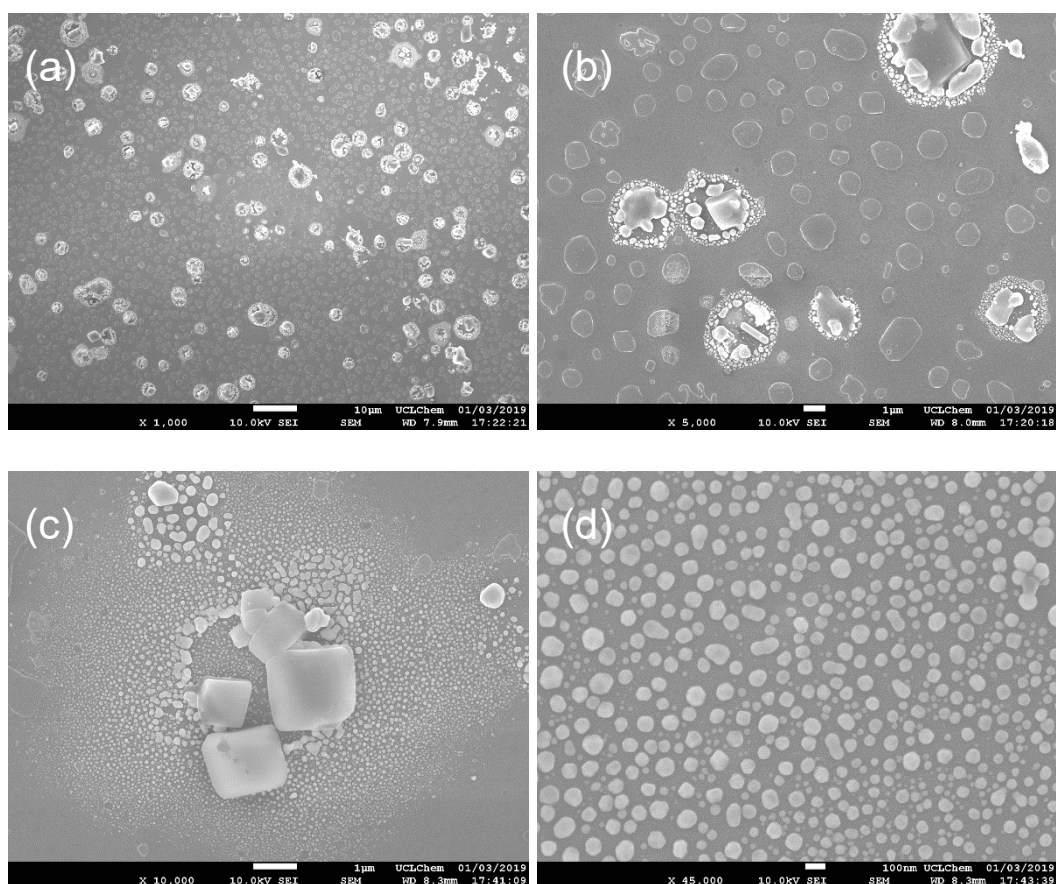


Figure 4.4 SEM images of as-deposited Ag thin film on glass substrate by using 0.06g AgNO_3 in a 2 :1 mixture of acetone and methanol, at 250 °C and a constant flow of N_2 at 300 sccm under different magnifications (a) 1000, (b) 5000, (c) 10000 and (d) 45000

4.3.1.5 XPS analysis

In the XPS Ag 3d core level spectra shown in Figure 4.5, two peaks were observed at 367.9 and 373.9 eV, corresponding to the binding energy of Ag 3d_{5/2} and Ag 3d_{3/2} with $\Delta E = 6$ eV, respectively, indicating the presence of Ag in +1 oxidation state²⁰¹. Meanwhile, the noisy background and low counts of Ag peaks indicated the relatively low amount of the Ag₂O NPs deposited on glass substrate. No obvious Ag peaks were found in XPS spectra for deposition temperatures above 250 °C despite weak peaks for Ag metal being observed in XRD at these temperatures.

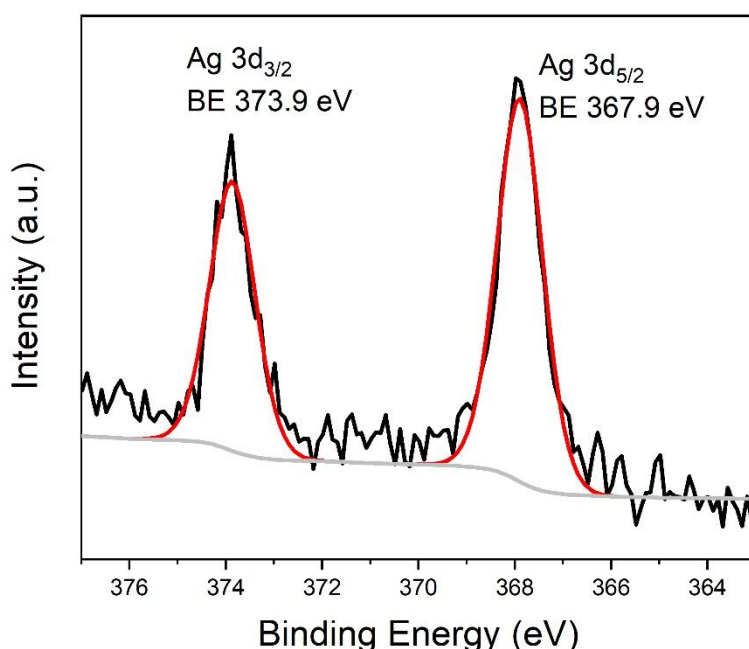


Figure 4.5 XPS Ag 3d core-level spectra of as-deposited Ag thin film on glass substrate by using 0.06g AgNO₃ in a 2 :1 mixture of acetone and methanol, at 250 °C and a constant flow of N₂ at 300 sccm

Figure 4.6 shows the XPS survey spectra of as-deposited Ag on glass and the plain glass. After comparison, there is an identifiable nitrogen peak at 408 .1 eV presented in the Ag loaded samples, whilst it is absent on plain glass. Since no evidence of AgNO₃ peaks is found at 250 °C in the XRD pattern shown in Figure 4.2, it may indicate the formation of NaNO₃, where Na is commonly seen in glass.

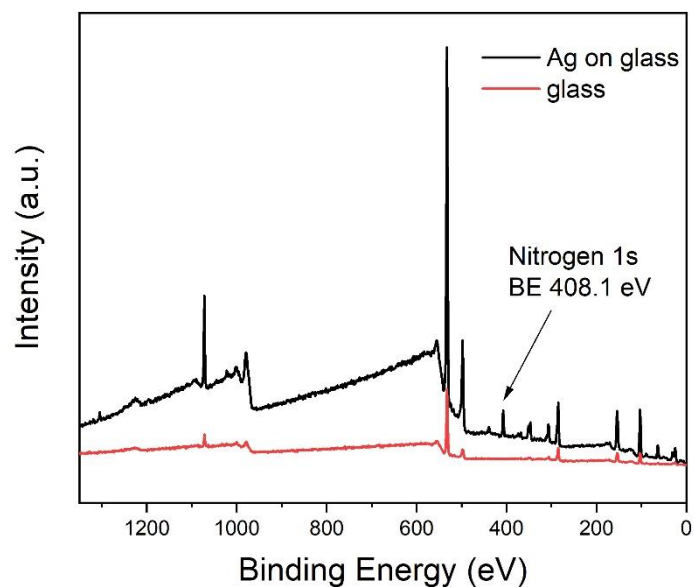


Figure 4.6 XPS survey spectra of as-deposited Ag thin film on glass by using AgNO_3 0.06g at 250 °C and a flow of N_2 at 300 sccm and plain glass.

The spherical structures shown in Figure 4.5d under high magnification were demonstrated as Ag nanoparticles, by the EDS spectra shown Figure 4.7 below. The presence of O, Na and Si peaks were attributed to the presence of SiO_2 and Na_2O in the glass substrate.

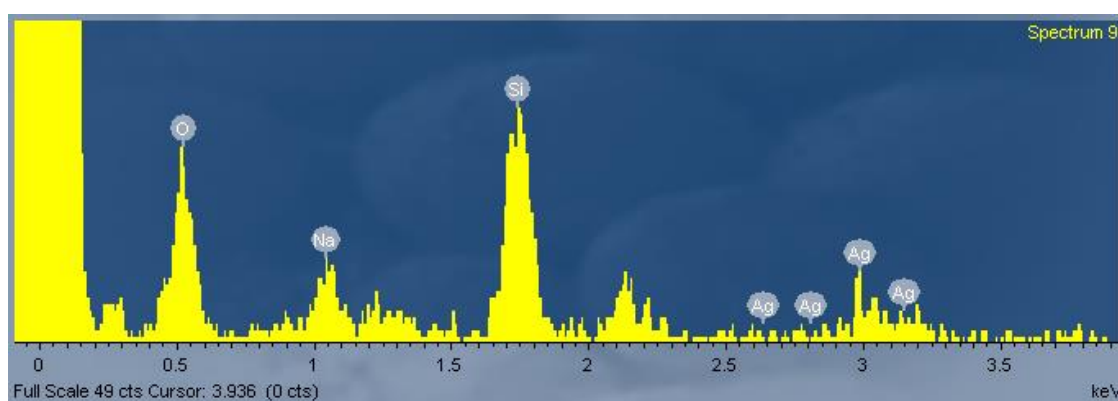


Figure 4.7 SEM-EDS spectrum of spherical structures of Ag nanoparticles deposited on glass substrate with 0.06g AgNO_3 at 250 °C and flow rate of N_2 at 300 sccm

4.3.2 Characterization of Ag@WO₃ thin films on glass substrates

4.3.1.1 Initial deposition

Ag@WO₃ thin films on glass substrates was successfully fabricated via AACVD in a two-step process. The first step was the preparation of the annealed WO₃ thin film on glass substrates (described in Chapter 3.2). Subsequently, silver was then deposited on the annealed WO₃ substrates by using AgNO₃ as precursor in a mixed solution of acetone and methanol. Pale purple colour was observed on the Ag@WO₃ substrates, which indicating the deposition of Ag metal with the colour arising from the metal surface plasmon resonance (SPR).

4.3.1.2 XRD analysis

The XRD patterns of as-deposited Ag@WO₃ thin film on glass substrate at 200, 225 and 250 °C were recorded and are displayed in Figure 4.8 for comparison. The peaks indicated that Na₂W₄O₁₃ was obtained after annealing, matching with the standard pattern of triclinic phase of sodium tungsten oxide (PDF#27-1425, P-1(2), a=8.255 Å, b= 8.425 Å, c= 3.894 Å, α = 103.10 °, β= 90.60 °, γ = 95.99 °). This is commonly observed when annealing WO₃ nanorod samples on glass substrates. However, no peaks were observed for Ag metal, as seen when depositing on glass substrates alone.

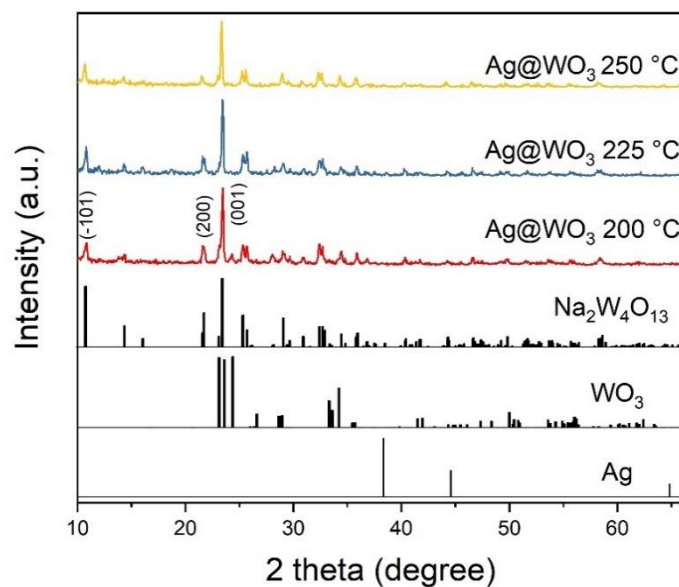


Figure 4.8 XRD patterns of Ag@WO₃ thin film on glass substrate by using 0.06g AgNO₃ in a 2 :1 mixture of acetone and methanol, at 200, 225 and 250 °C and a constant flow of N₂ at 300 sccm, as compared to standard pattern of Na₂W₄O₁₃ (PDF#70-2022) and metal Ag (PDF#87-0718)
[corresponding to Exp. No. 7, 8 and 9, respectively]

The amount of AgNO₃ precursor used and the flow rate of the carrier gas N₂ was altered being 0.03 and 0.09 g and 200 and 400 sccm respectively, whilst keeping the other parameters the same. Similar XRD patterns were obtained with no obvious presence of silver peaks (Figure 4.9). This could be due to the relatively low amount of Ag present or the small size of the Ag nanoparticles, particularly given the background from the crystalline Na₂W₄O₁₃ in the diffraction pattern.

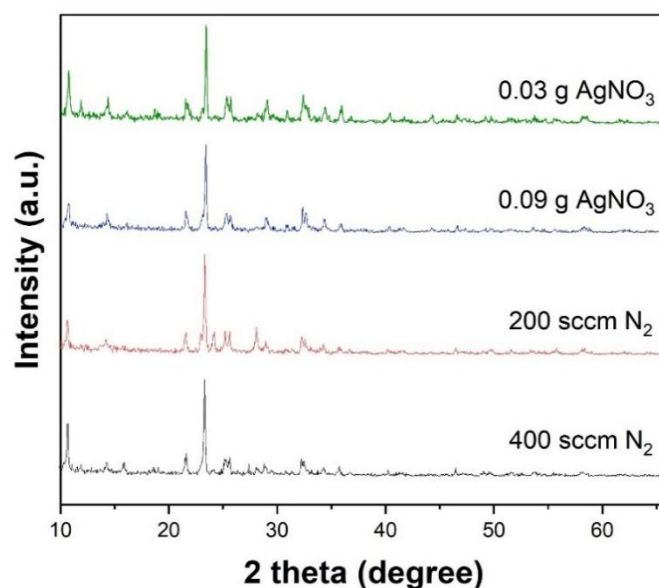


Figure 4.9 XRD patterns of as-deposited Ag@WO₃ thin film on glass substrate with various initial amount of AgNO₃ (0.03 and 0.09 g with 300 sccm of N₂) and different flow rate of N₂ (200 and 400 sccm with 0.06 g of AgNO₃) at 250 °C² [corresponding to Exp. No. 10,11,12 and 13, respectively]

4.3.1.3 XPS analysis

Figure 4.10 displays the XPS 3d Ag core level spectra recorded from as-deposited Ag thin film on plain glass substrate and Ag@WO₃ thin films on glass substrate. In Figure 4.10a, when deposited on the plain glass substrate, the two intense peaks centred at binding energy of 373.9 and 367.9 eV were previously assigned as the Ag 3d_{3/2} and Ag 3d_{5/2} peaks respectively, indicating the presence of silver metals (Ag⁰) in agreement with values given in literature²⁰². In Figure 4.10b, when deposited on the annealed WO₃ substrate, the two intense peaks were slightly shifted by ~ 0.3 eV to 373.6 and 367.6 eV for the Ag 3d_{3/2} and the Ag 3d_{5/2} respectively. Such a shift to lower binding energy may indicate the formation of some silver oxide (Ag₂O) species^{203, 227}, or could be due to the electronic interaction (Schottky Junction) formed between Ag and WO₃, indicating electron transfer is from Ag to WO₃. What's more, the lack of loss feature/any satellite peak in Ag 3d spectra also indicate the presence of Ag in ionic form. The wt.% ratio of Ag:W is 3.6%:96.4%, calculated from at% ratio of Ag:W(6.07%:93.93%). In the

XPS spectrum of the O 1s region, Figure 4.10 (c), the dominant peak is at a binding energy of 530.0 eV, indicating that most O²⁻ existed in the form of WO₃ NNs rather than the in Ag₂O, in which the binding energy is expected to be located around 528.8-529.2 eV²⁰³. However, this might be expected for a relatively low amount of Ag compared to a larger amount of W. By comparing Figure 4.10 (d) and (e), it was found that with the addition of Ag NPs, sub-stoichiometric WO_{3-x} was generated and this could happen due to the formation of Ag₂O via Ag NPs extracting the oxygen species from the WO₃.

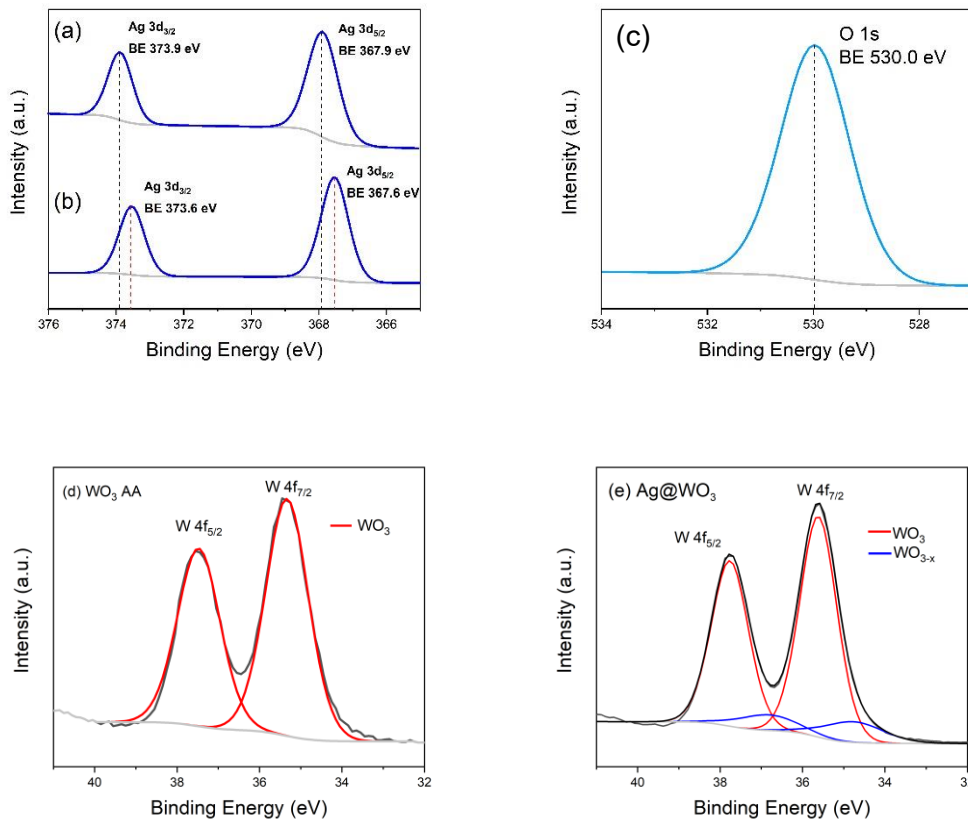


Figure 4.10 XPS Ag 3d core level spectra of as-deposited (a) Ag thin film on glass substrate, (b) Ag@WO₃ on glass substrate by using 0.06 g AgNO₃ in a 2 :1 mixture of acetone and methanol, at 250 °C and a constant flow of N₂ at 300 sccm, (c) O 1s core level spectra of as-deposited Ag@WO₃ on glass substrate, (d) W 4f spectra of WO₃ AA on glass substrate and (e) W 4f spectra of as-deposited Ag@WO₃ AA on glass substrate

4.3.1.4 SEM analysis

SEM image of as-deposited Ag@WO₃ on glass substrate, shown in Figure 4.11 shows evenly distributed nanoparticles on a thick film of WO₃ nanorods, with a large number of nanoparticles found when the deposition temperature was set at 250 °C. As compared to SEM image of as-deposited Ag thin film on a plain glass substrate shown in Figure 4.5, large cubic crystals appearing on the glass substrate were not found. The transformation of microstructure of the Ag@WO₃ AA on glass substrate is identical to plain WO₃ AA on glass substrate. The formation of nanoplate/ nanorod structures might be attributed to the formation of sodium tungsten oxide and hexagonal phase.

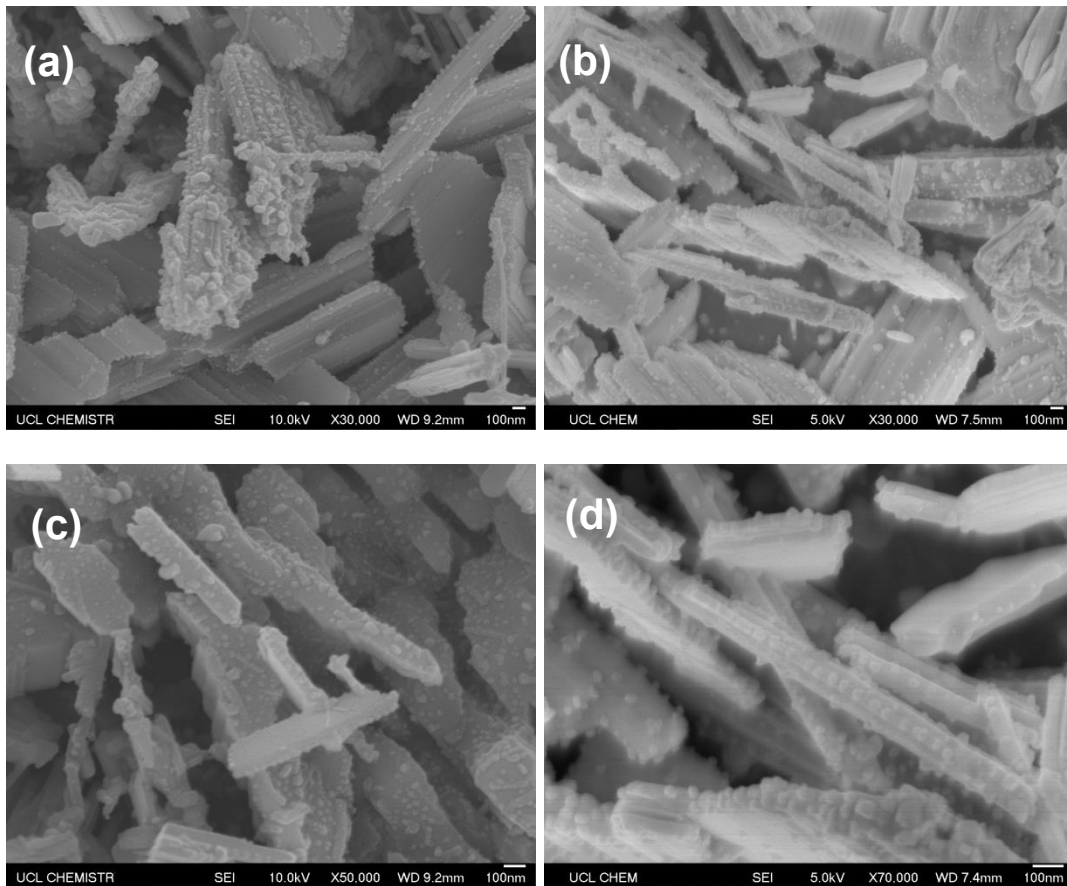


Figure 4.11 SEM images of as-deposited Ag@WO₃ thin film on glass substrate by using 0.06g AgNO₃ in a 2 :1 mixture of acetone and methanol, at 250 °C and a constant flow of N₂ at 300 sccm under different magnifications (a and b) 30000, (c) 50000 and (d) 70000.

The EDS mapping (Figure 4.12) shown below illustrated the distribution of the O, Ag and W elements in the chosen SEM graph. A large number of silver nanoparticles were found evenly distributed on the WO₃ nanorods, matching with the SEM images.

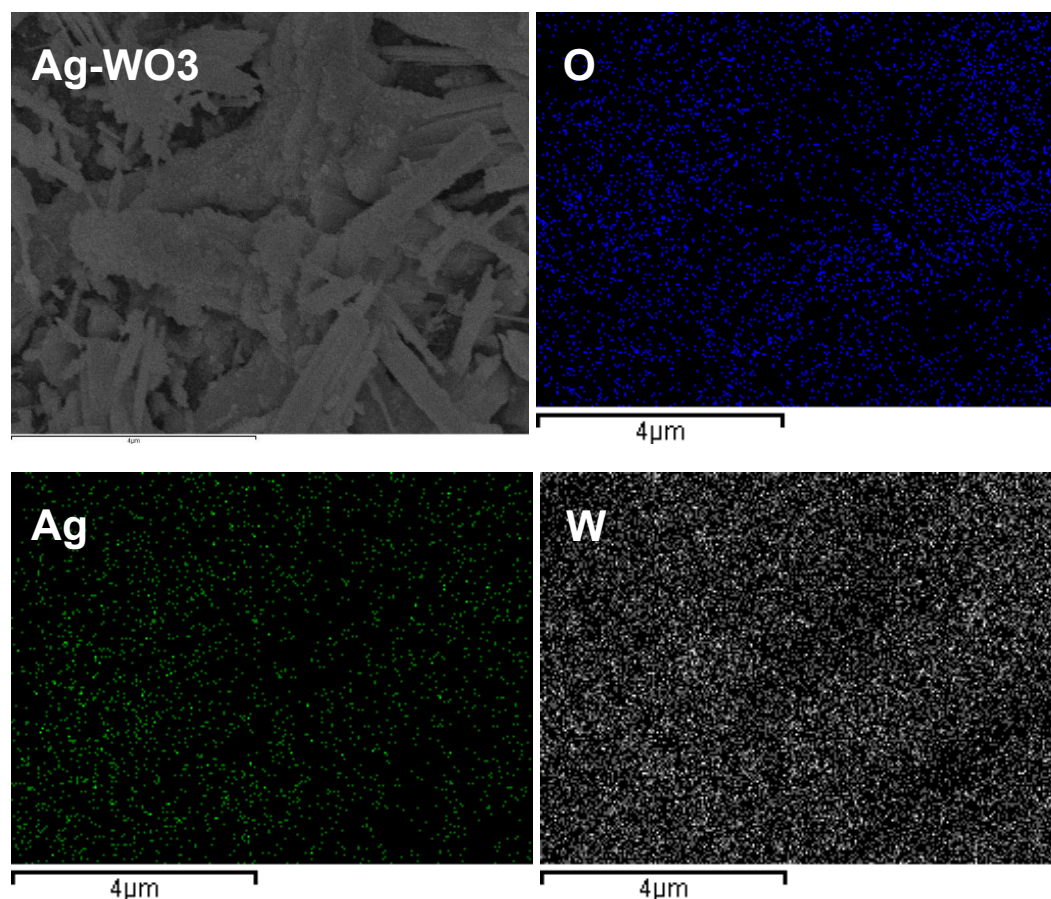


Figure 4.12 SEM-EDS mapping of as-deposited Ag@WO₃ on glass substrate by using 0.03g AgNO₃ at 250 °C and a flow of N₂ at 300 sccm

The Na peak shown in the EDS spectra (Figure 4.13) was attributed to the presence of Na ions in the glass substrate and the Au peak is due to the Au-coating process. The final elemental analysis report of this spectrum is shown in Table 4.4 below. The wt% of Ag/W is 14%: 86%, in which the Ag wt% is higher than that calculated by XPS.

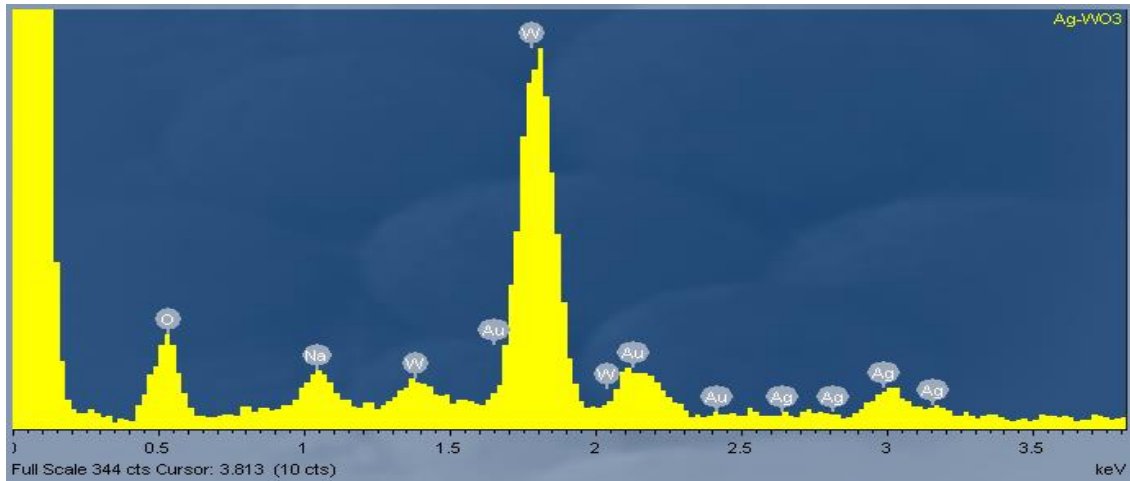


Figure 4.13 EDS spectra of as-deposited Ag@WO₃ on glass substrate by using 0.03g AgNO₃ at 250 °C and a flow of N₂ at 300 sccm

Table 4.4 Elemental analysis of SEM-EDS spectrum of Ag decorated WO₃ substrate

Element	O	Na	Ag	W	Au	Total
wt%	15.14	2.11	9.68	58.85	14.22	100

4.3.3 Characterization of Ag@WO₃ thin films on sensors

4.3.1.1 Initial deposition

An Ag@WO₃ alumina-based gas sensor was attempted to be fabricated *via* AACVD in a two-step process using optimal conditions determined by deposition of WO₃ and Ag thin films on glass substrates. The first step was the preparation of the WO₃ thin film alumina-based sensor platform, in which a pale-yellow thin film was observed on the sensor platform after annealing at 500 °C for 2 hr. In the subsequent step, after depositing AgNO₃ (0.09 g) at 250 °C and a flow of N₂ at 300 sccm, the as-deposited Ag@WO₃ was obtained which had no significant difference in appearance compared to the undecorated WO₃ sensor.

4.3.1.2 XRD analysis

The XRD patterns of as-deposited undecorated-WO₃ and Ag@WO₃ on alumina sensors were recorded and shown in Figure 4.14. The presence of peaks associated with monoclinic phase of WO₃ with strong orientation in the (002) directions, matched well with the standard pattern (PDF#72-0677, $a = 7.31 \text{ \AA}$, $b = 7.54 \text{ \AA}$, $c = 7.69 \text{ \AA}$, $\alpha = 90.0^\circ$, $\beta = 90.9^\circ$ and $\gamma = 90.0^\circ$). No peaks for Na₂W₄O₁₃ were observed after annealing on alumina due to the lack of sodium ions in the substrate. No peaks for silver were observed for the decorated Ag@WO₃ samples, possibly due to the relatively low amount Ag present small size of the Ag particles. No shift in WO₃ peak position were observed as compared between the undecorated- and decorated-WO₃ sensors, which revealed that there was no change of the monoclinic crystal structure of WO₃ during the addition of Ag metal.

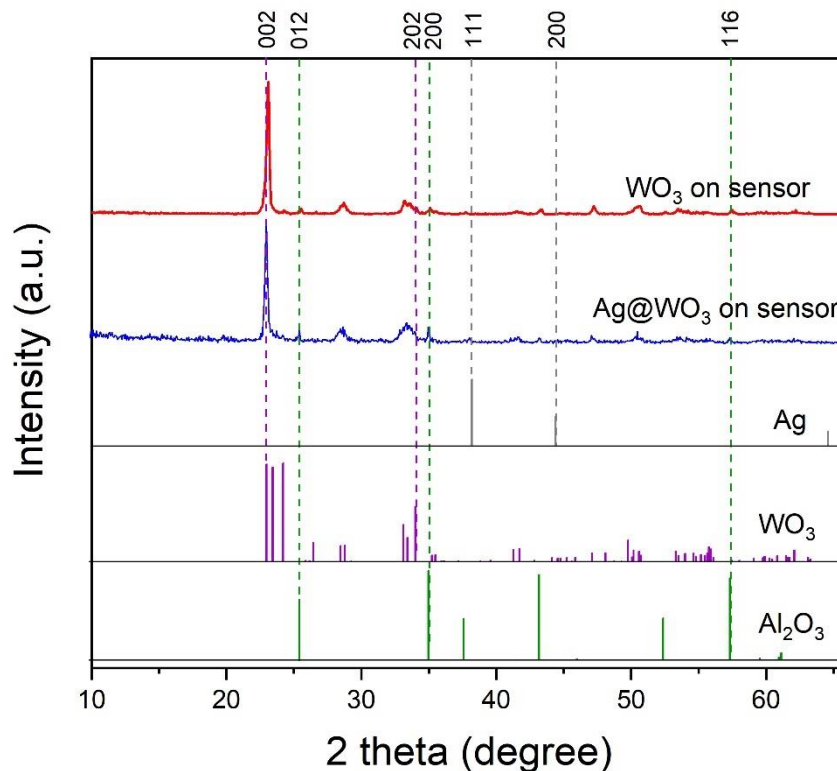


Figure 4.14 XRD patterns of as-deposited WO₃ and Ag@WO₃ deposited on alumina gas sensor with 0.09g AgNO₃ at 250 °C and a flow of N₂ at 300 sccm

4.3.1.3 XPS analysis

Detailed information on the elemental composition of the as-deposited Ag@WO₃ sensor was obtained by XPS. Analysis of W4f core level spectra of decorated-WO₃ sample appeared identical to the undecorated-WO₃ sample. As shown in Figure 4.15a, the core level spectra of W 4f showed the presence of two intense peaks at 37.6 and 35.5 eV associated with the W4f_{5/2} and W4f_{7/2} doublets respectively, which are similar with the reference binding energies for stoichiometric WO₃ with the oxidation state of W⁶⁺²⁰⁴. The XPS of Ag 3d core level spectra (Figure 4.15b) showed the presence of two peaks centred at 373.5 and 367.5 eV associated with the Ag 3d_{3/2} and Ag 3d_{5/2} respectively. The peak of Ag 3d_{5/2} shifts to lower binding energy, corresponding to the presence of metallic Ag⁰ metal.

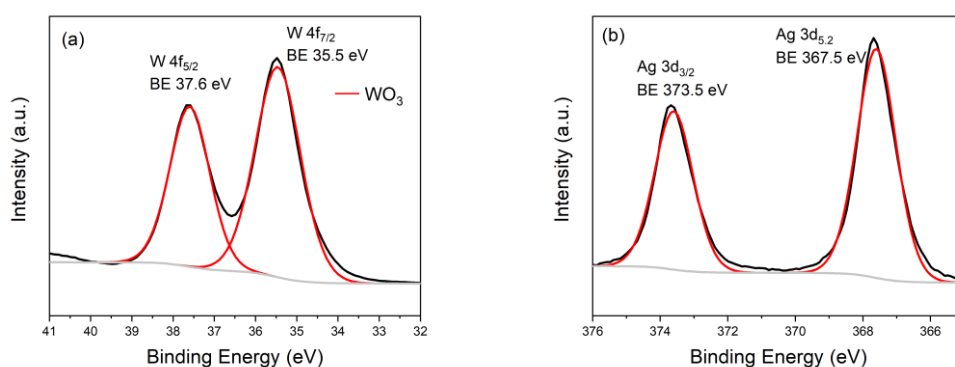


Figure 4.15 XPS core level spectra of as-deposited Ag@WO₃ on alumina sensor (a) W 4f and (b) Ag 3d

4.3.1.4 SEM analysis

An SEM image of an as-deposited Ag@WO₃ on alumina sensor sample is shown in Figure 4.16. Similar to the SEM image of Ag@WO₃ on glass substrates shown in Figure 4.11, a large amount of Ag nanoparticles was found evenly distributed over the surface of WO₃ nanorods. The diameter of WO₃ nanorods is in range of 300 to 700 nm (Figure 4.16a) and the diameter of Ag nanoparticles is in range of 17 to 33 nm (in Figure 4.16d). However, this morphology of Ag decorated WO₃ sensor is completely different to the undecorated WO₃ sensor, which shown in Figure 3.11f. A small amount

of relatively thick rod-shaped WO_3 was formed after AgNO_3 deposition instead of the large amount of the nanoneedle-structured WO_3 present prior to Ag decoration. Such morphology change to WO_3 nanoneedle structures was also observed in Figure 4.11, attributing to the addition of AgNO_3 .

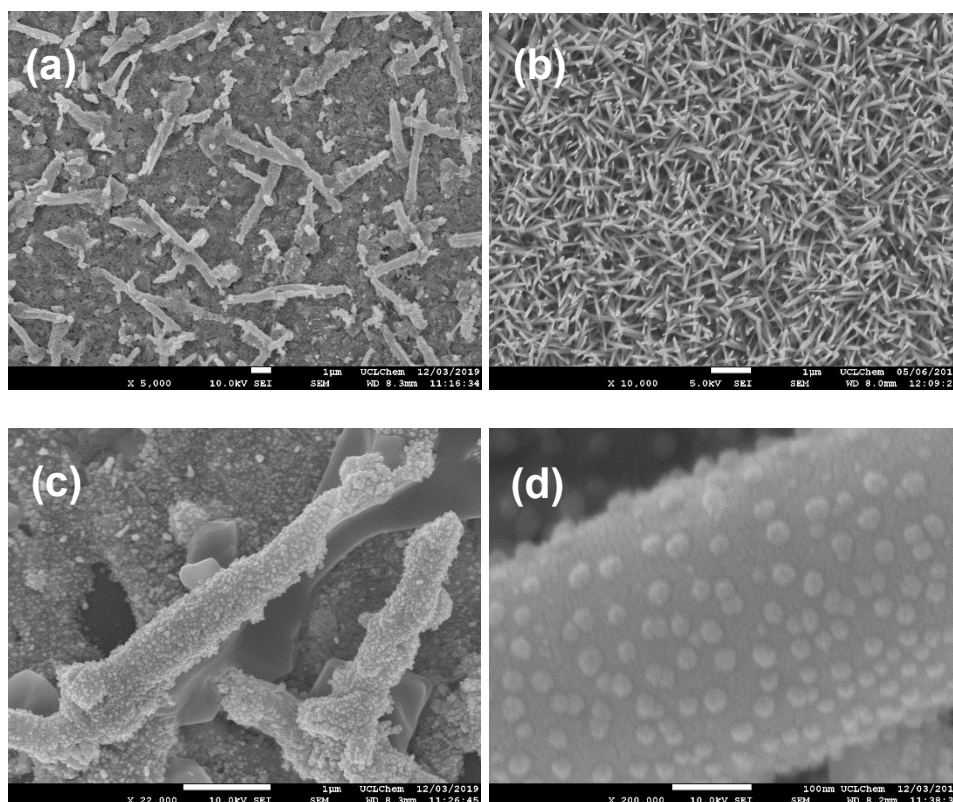


Figure 4.16 SEM images of (a) as-deposited WO_3 thin film on alumina sensor substrate, as-deposited Ag@WO_3 thin film on glass substrate by using 0.06g AgNO_3 in a 2 : 1 mixture of acetone and methanol, at 250 °C and a constant flow of N_2 at 300 sccm under different magnifications (b) 5000, (c)20000 and (d) 200000

4.3.1.5 TEM analysis

Further information about of structure of as-deposited Ag@WO_3 on alumina sensor was obtained by TEM, which is shown in Figure 4.17. The WO_3 NNs surface is homogeneously covered with well-dispersed Ag NPs, similar with the ones seen for Au and Pd functionalized WO_3 NNs^{81,82}. The diameter of Ag NPs is between 8 and 20 nm. The diameter of WO_3 nanoneedles is in range of 20 to 50 nm. Cubic Ag with (111) crystal planes ($d=0.238$ nm) can be observed from the fringe image shown in Figure 4.17b. Here, Ag_2O ($d=0.274$ nm) was also observed alongside Ag metal. The combined

XPS and TEM suggest that the particles observed are an Ag/Ag₂O clusters (e.g., an Ag core where air-exposed faces are oxidised to Ag₂O) on the Ag@WO₃ on sensor.

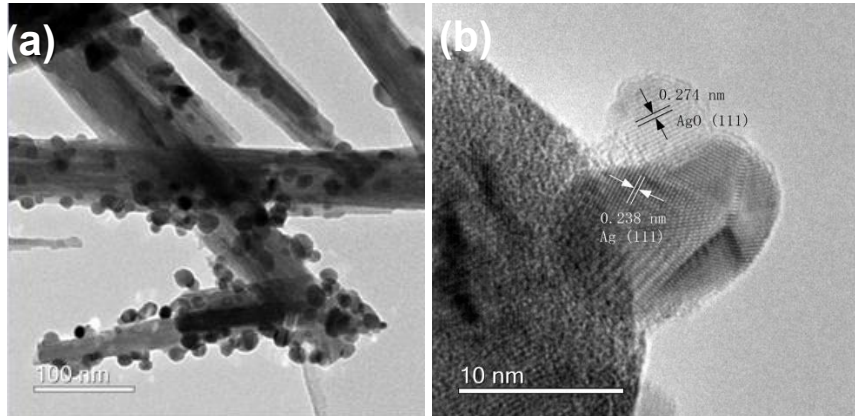


Figure 4.17 TEM image of (a) as-deposited Ag@WO₃ thin film on sensor by using 0.09 g AgNO₃ in a 2 : 1 mixture of acetone and methanol, at 250 °C and a constant flow of N₂ at 300 sccm and (b) HR-TEM of Ag@WO₃ sample

The identification of the components of nanoparticles was further proved by Energy-dispersive X-ray spectroscopy (EDS), which is shown in Figure 4.18. The Ag peak demonstrated the observed NPs were composed of Ag (the presence of copper peak is due to the copper TEM grid used).

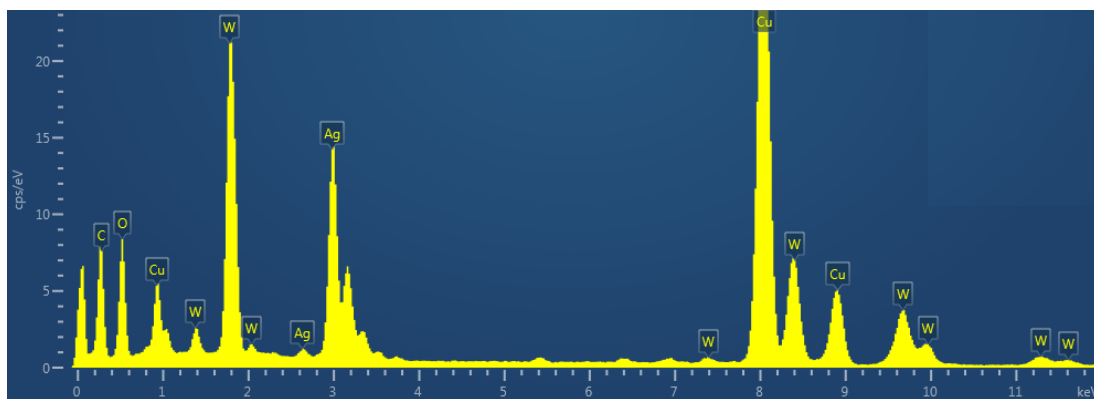


Figure 4.18 HR-TEM EDS spectrum of Ag@WO₃ on sensor regarding to Figure 4.17a

4.4 Conclusion

In this chapter the synthesis of Ag NPs decorated WO_3 NNs has been reported via AACVD using AgNO_3 as the silver precursor. The effect of various deposition temperatures, in the range of 150 to 350 °C, was first investigated on glass substrate. The influences of flow rate of carrier gas N_2 and amount of the AgNO_3 precursor used were further studied on WO_3 AA thin films which pre-deposited on glass substrate. Finally, Ag@WO_3 alumina-based sensor was synthesized using the optimal deposition condition with 0.09 g AgNO_3 precursor used at 250 °C and a flow of N_2 at 300 sccm.

Several material characterization techniques have been carried out to reveal the success of depositing Ag NPs onto the glass substrate by using AgNO_3 as a precursor. XRD results shows no decomposition happened for AgNO_3 under 150 °C. Both XRD and UV-Vis revealed that optimal deposition temperature for Ag deposition is in a range of 200 to 250 °C and more Ag NPs were found to be deposited close to the inlet of the reaction chamber. XPS confirmed the presence of metallic Ag^0 only, without any presence of silver oxides. SEM image shows the presence of large NaNO_3 crystals surrounded by evenly distributed Ag nanoparticles with diameter less than 100 nm.

Subsequently, Ag@WO_3 thin film on glass substrate were successfully fabricated using different amounts of AgNO_3 precursor and different flow rate of carrier gas N_2 . XRD patterns show no significant difference among all samples, which are all visually identical to the undecorated WO_3 thin film. This might due to the small size and the relatively low amount of Ag deposited on WO_3 thin films. Also, this could be attribute to the formation of amorphous Ag_2O . XPS shows a shift for Ag peaks to lower binding energy, when Ag nanoparticle deposited on WO_3 thin films on sensor platforms, indicating Ag^0 is oxidised to Ag^{1+} with the formation of Ag_2O or possibly due to the electron exchange between Ag and WO_3 .

Finally, Ag NPs decorated WO_3 NNs were successfully grown on an alumina sensor

via a two-step synthesis by AACVD method. Similarly, no silver peaks were observed in XRD pattern for the Ag@WO₃ thin film on sensors, which is the same result as the Ag@WO₃ thin film on glass substrate due to the relatively low amount or small size of Ag. XPS result demonstrates the presence of Ag metal, indicating the formation of Ag NPs. SEM and TEM images show that Ag NPs were evenly distributed on the WO₃ NNs.

Chapter 5 Silver Decorated Tungsten Oxide Thin Films and Sensors Using Organometallic Silver Metal Precursors: Synthesis and Characterization

5.1 Introduction

In this chapter, instead of using AgNO_3 as the silver precursor, three organometallic Ag metal precursors, 'Ag-EP', 'Ag-AP' and 'Ag-AMP' were introduced and used for the synthesis of Ag@WO_3 thin films via AACVD. After optimizing the reaction conditions, Ag NPs were successfully decorated and adhered on the WO_3 NNs. Physical characterizations, including XRD, UV-VIS, XPS, SEM and TEM were carried out further to investigate the composition and morphology of the thin films and the diameter/size of the Ag NPs was measured and counted.

Organometallic chemistry is the study of organometallic compounds, chemical compounds containing at least one chemical bond between a carbon atom of an organic molecule and a metal, including alkaline, alkaline earth, and transition metals. Many organometallic compounds are air sensitive (reactive towards oxygen and moisture), and thus they must be handled under an inert atmosphere. An advantage of organometallic compounds, as compared with inorganic or organic compounds, is that they are often more reactive, for instance in this study the organometallic Ag precursors are easily decomposed at a relatively low temperature as compared with inorganic AgNO_3 .

Organometallic silver metal precursor complexes, including silver 2-aminoethanol (Ag-EA), silver 1-aminopropan-2-ol (Ag-AP) and silver 2-methyl-2-aminopropan-1-ol (Ag-AMP) were synthesized and supplied by Miss Bhide, Malavika and Mr. Ye Zhou from Dr. Caroline E. Knapp's research group (UCL), shown in the Figure 5.1 below.

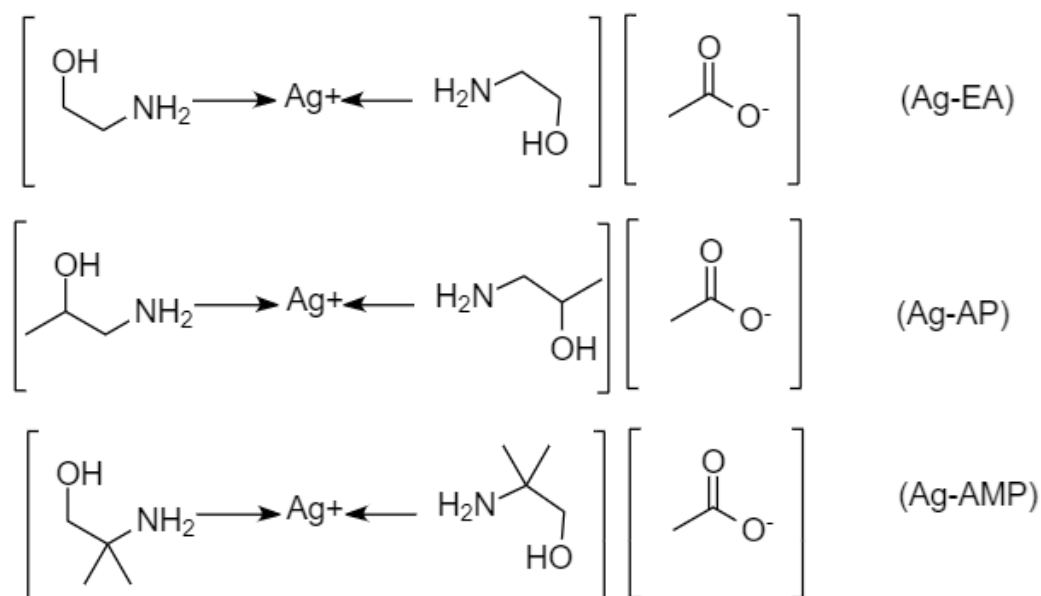


Figure 5.1 Chemical formula of three organometallic Ag precursors: Ag-EA, Ag-AP and Ag-AMP

Structurally, all three silver precursors Ag-EA, Ag-AP and Ag-AMP are composed of two alkanolamine groups which coordinate to a Ag^+ cation in the centre in the same way as the formation of reactive silver inks with central Ag^+ coordinated with two NH_3 groups, $[\text{Ag}(\text{NH}_3)_2]^+[\text{C}_2\text{H}_3\text{O}_2]^-$, according to the work of Walker et al.²⁰⁶ The decomposition temperature for Ag-EA and Ag-AMP are similar at about 180 °C and Ag-AP has the lowest decomposition temperature at around 160 °C. All the TGA and DSC curves for three organometallic Ag precursors have been put in the appendix chapter. The stabilities of these precursors are expected to be increased over the previous amine complex due to the longer carbon backbone and additional functionalities, which may facilitate the transportation of aerosol mist through the reaction chamber via AACVD and prevent the early decomposition and pre-reaction of the highly thermally sensitive amine precursor within the reaction flask or at the inlet of the reactor.

5.2 Experimental

At the beginning of this series of experiments, the rectangular-based AACVD reactor (W: 3 cm × L: 6 cm × H: 2 mm), shown in Figure 2.2 (a) was used for the attempted deposition of Ag thin films from these new precursors. However, there were no macroscopic films formed after a series of experiments despite altering the deposition temperature (range between 150 to 350 °C, with interval 50 °C), flow rate of the carrier gas nitrogen (200, 300, 400, 500 and 1000 sccm) and the amount of the precursor solution (10, 20, 50 and 100 µL). After constant trial and analysis, it was concluded that the inlet part of the reactor was still too hot, leading to the early decomposition and pre-reaction of these highly temperature sensitive precursors, even though it was connected to a water jacket cooler. To test this conjecture, another square-based AACVD reactor, shown in Figure 2.2 (b) was used here, with a size of W: 3 cm × L: 3 cm × H: 2 mm. It is obvious from the figure that the water jacket cooler is separated from the reaction chamber in the square-based reactor and the inlet part shrinks in size compared to the rectangular AACVD reactor reducing the residence time of the aerosol before entering the reactor proper. Thus, the aerosol would directly enter the reaction chamber for decomposition and deposition, avoiding any early consumption.

5.2.1 Preparation of Ag thin films

The Ag thin films were fabricated using a home-built squared-based AACVD reactor. Initially, each Ag metal precursor solution was diluted and dissolved in 10 mL methanol. After sonicating the mixture solution for 5 min, it was transferred into an ice-cold reaction flask. A cleaned 2.5 cm × 2.5 cm microscope slide was placed in the centre of the reaction chamber, which was preheated to the depositing temperature. Flow rate of the carrier gas N₂ was controlled by a mass flow controller (MFC, Brooks) with a max flow rate of 0.5 L/min. Once all the precursor solution was used up, the film was allowed to cool down to ambient temperature naturally under a flow of N₂. The deposition conditions for the Ag thin films are listed in the table below. Flow rate was

considered as the first variable parameter to be altered in the reaction conditions in order to get a uniformly distributed Ag thin film. After then, a series of experiments were carried out to investigate the influence of temperature on the silver thin film deposition at a constant flow rate.

Table 5.1 Reaction conditions of organometallic Ag metal precursor on glass

Exp. No.	Type of Ag ink	Volume/ μL	Temperature/ $^{\circ}\text{C}$	Flow rate/ sccm	Substrate
1	AMP	10	275	400	glass
2	AMP	10	275	200	glass
3	AMP	10	275	190	glass
4	AMP	10	275	170	glass
5	AMP	10	275	160	glass
6	AMP	10	275	150	glass
7	AMP	10	200	170	glass
8	AMP	10	225	170	glass
9	AMP	10	250	170	glass
10	AMP	10	300	170	glass
11	AMP	10	350	170	glass
12	AP	10	225	170	glass
13	AP	10	250	170	glass
14	AP	10	275	170	glass
15	AP	10	300	170	glass
16	AP	10	350	170	glass
17	EA	10	225	170	glass
18	EA	10	250	170	glass
19	EA	10	275	170	glass
20	EA	10	300	170	glass
21	EA	10	350	170	glass

5.2.3 Preparation of organometallic Ag@WO₃ thin films on sensors

The process of fabricating Ag-decorated WO₃ gas sensors is identical to the

preparation of Ag-decorated WO₃ thin films on glass substrates, consisting of two parts. The first step was the preparation of an annealed WO₃ gas sensor as described in Chapter 3.2.2. Subsequently, organometallic silver metal precursors were deposited via AACVD on the annealed WO₃ gas sensors using the optimal conditions determined during Ag deposition on glass substrates. Depositions with various volumes of the Ag-precursor solutions were carried out to explore the effect of different Ag-loading on WO₃ gas sensors for gas sensing performance towards oxygen. The experiment conditions are listed in the table below.

Table 5.2 Reaction conditions of organometallic Ag metal precursors on WO₃ sensors

Exp. No.	Type of Ag ink	Volume / μ L	Temperature/ $^{\circ}$ C	Flow rate/ sccm	Substrate
1	AMP	1	275	170	WO ₃ AA sensor
2	AMP	3	275	170	WO ₃ AA sensor
3	AMP	5	275	170	WO ₃ AA sensor
4	AMP	10	275	170	WO ₃ AA sensor
5	AP	1	275	170	WO ₃ AA sensor
6	AP	3	275	170	WO ₃ AA sensor
7	AP	5	275	170	WO ₃ AA sensor
8	AP	10	275	170	WO ₃ AA sensor
9	EA	1	275	170	WO ₃ AA sensor
10	EA	3	275	170	WO ₃ AA sensor
11	EA	5	275	170	WO ₃ AA sensor
12	EA	10	275	170	WO ₃ AA sensor

5.3 Results and discussion

5.3.1 Characterization of Ag thin films

5.3.1.1 Flow rate variance (Ag-AMP)

Ag-AMP initial depositions

After switching from the rectangular-based AACVD reactor to the square-based

AACVD reactor, a visible film was observed under reaction conditions of deposition temperature at 275 °C and flow rate of 400 sccm, as shown in Figure 5.1(left). Two parallel yellowish straight lines were observed indicating the successful formation of a thin film. The formation of the thin film in this shape can be attributed to the internal structure of the square-based reactor, which is shown in Figure 2.2 (b). The triangular shape of the inlet causes the flow rate on both sides to be greater than in the middle. Therefore, in order to achieve a more evenly distributed thin film, a set of optimization experiments was conducted by altering the flow rate, ranging from 400 to 150 sccm. As shown in the Figure 5.2 below, when the flow rate halves to 200 sccm, an arch-shaped brown thin film was observed (again because of the internal structure of the squared-based reactor and resultant flow conditions). This was followed by a gradual lowering of the flow rate from 190 to 150 sccm in 10 sccm intervals. The result was that the middle part of the arch-shaped thin film was filled up gradually, but the coverage of the thin film decreased a lot. Considering factors including uniformity and coverage area, the flow rate of 170 was defined as the optimal experimental conditions.

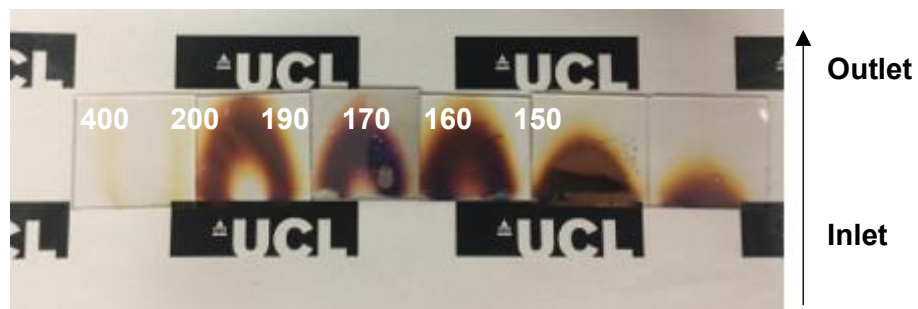


Figure 5.2 Ag-AMP deposited on glass with constant deposition temperature at 275°C and flow rate adjustment 400, 200, 190, 170, 160 and 150 sccm

5.3.1.2 Temperature variance (Ag-AMP, Ag-AP and Ag-EA)

Ag-AMP initial depositions

Temperature, as the most important parameter in AACVD, was optimized for the deposition of Ag thin films on glass substrates by using Ag-AMP as the precursor through a series of experiments, ranging from 200 to 400 °C with a constant optimized flow rate at 170 sccm. As shown in the Figure 5.3, the as-deposited Ag thin films were

obtained under various deposition temperatures. When the deposition temperature is at 200 °C or below, no visible thin film is formed. A yellowish thin film was formed when the temperature was increased to 225 °C and became darker in colour as the temperature went higher. Again, arch-shaped films were obtained between 225 to 275 °C, which was attributed to the reactor design described earlier. As temperature increases, the as-deposited Ag thin film's coverage on glass decreases likely due to the early decomposition of the Ag-AMP precursor at higher temperatures, i.e. most of the precursor droplets decomposed and reacted immediately leading to the formation of thin films only close to the inlet part of the glass substrate.

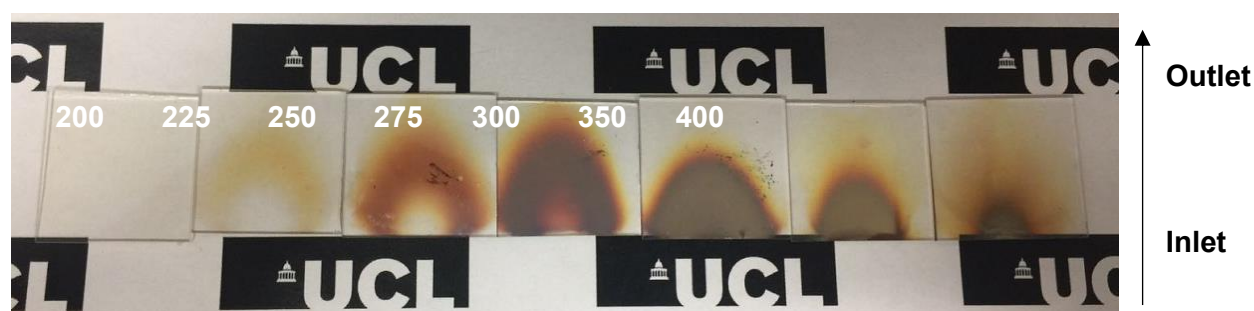


Figure 5.3 Ag-AMP deposited on glass with constant flow rate of N₂ at 170 sccm and different deposition temperature 200, 225, 250, 275, 300, 350 and 400 °C

Ag-AMP XRD analysis

The XRD patterns of as-deposited Ag-AMP thin film on glass is shown in Figure 5.4. The major diffraction peaks of Ag are observed when the deposition temperature reaches 300 and 350 °C. The peaks at 38.1°, 44.3° and 64.5° can be assigned to (110), (200) and (220) reflection of Ag metal, which matched well with the standard pattern (Fm-3m (225) space group, $a = b = c = 4.0773 \text{ \AA}$; $\alpha = \beta = \gamma = 90^\circ$, PDF#87-0718). No obvious peaks are found in XRD patterns at temperature below 275 °C. The result is opposite to the XRD patterns when AgNO₃ deposited on glass substrates, in which Ag peaks appeared at 200 and 250 °C and gradually disappear when temperature goes higher. Similarly, in Llobet's work¹⁴⁵, no obvious peak for silver nanoparticle was observed due to its small size and relatively low concentration and is below the instrument limit detection.

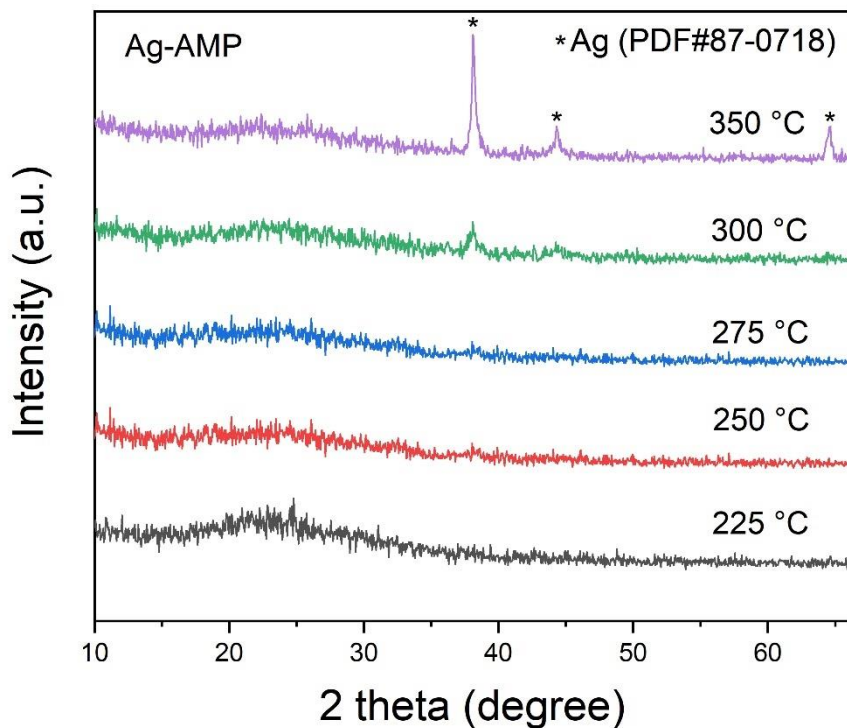


Figure 5.4 XRD patterns of as-deposited Ag-AMP thin film on glass with different temperatures, ranging from 225 to 350 °C and a constant flow rate of N₂ at 170 sccm

Ag-AMP UV-Vis analysis

UV-Vis adsorption of as-deposited Ag-AMP thin films on glass synthesized at different temperatures are investigated and shown in Figure 5.5. The peak in range of 240-250 nm can be attributed to the adsorption in glass substrate. With increasing deposition temperature, the surface plasmon resonance (SPR) band of silver particles ($\lambda_{\max} \sim 453$ nm, deposition temperature at 225 °C) is shifted to the red ($\lambda_{\max} \sim 496$ nm, deposition temperature at 350 °C), except for deposition temperature at 300 °C. As compared to the UV/Vis spectra of AgNO₃ deposited on glass substrate shown in Figure 4.3, the additional peak at around 530 nm has been found shift to lower frequency of 360 nm. This could be attributed to the change the shape of Ag NPs or this could because of the increase the size. In addition, an extra band at ~ 370 nm is observed for deposition temperatures over 300 °C, matched with literature, indicating the formation of Ag nanoparticles with size greater than 80 nm²²⁶. This is a result of quadrupole resonance,

in addition to the primary dipole resonance. Figure 5.4 also shows that the intensity of SPR band and its full width at half maxima (FWHM) increases with increasing deposition temperature. These characterization results of the adsorption spectrum suggest increasing size of the Ag nanoparticles with increasing deposition temperature. As shown in Figure 5.3, it is obvious that with the increasing of deposition temperature, the thicker the silver layer formed and the closer to the inlet of the reaction chamber. The appearance of peak around 700 nm indicated the formation of $\text{Ag}_2\text{O}^{200}$. This may result in the increase size of silver particles through rapid decomposition and heterogeneous reaction under high deposition temperature. With the increase of the size of Ag nanoparticles, the multipole transition of surface plasma becomes more obvious, which is reflected in the increase of the intensity at 370 nm as well²⁰⁷.

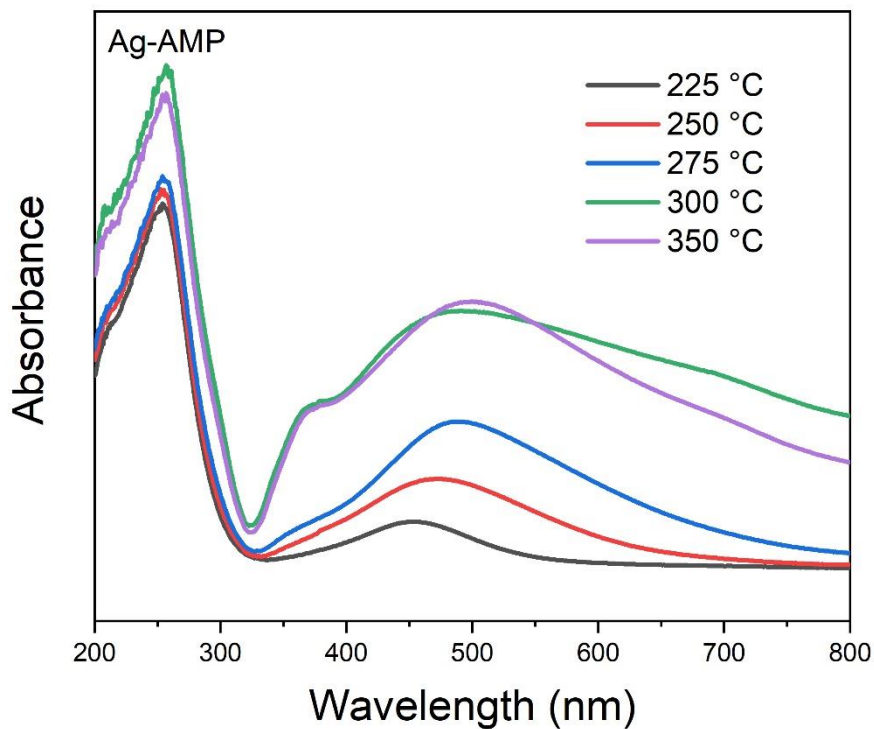


Figure 5.5 UV-VIS adsorption spectra of as-deposited Ag-AMP thin film on glass with increase in temperature from 225 to 350 °C

Ag-AP initial depositions

Figure 5.6 shows the as-deposited Ag-AP thin film on glass substrate with various deposition temperatures. Similar to the previous set of depositions of Ag-AMP on glass, as the deposition temperature increases, the colour gradually darkens and turns from bright yellow to brownish. Arch-shaped films were obtained between 225 to 300 °C, which was attributed to the triangular-shaped inlet as mentioned early. Under a constant flow rate at 170 sccm, the coverage of the Ag thin film shrinks as deposition temperature increases. This is due to the rapid decomposition and heterogeneous reaction when aerosol droplets entering into the hot reaction chamber under a higher deposition temperature, which caused the early consumption of all the precursor.

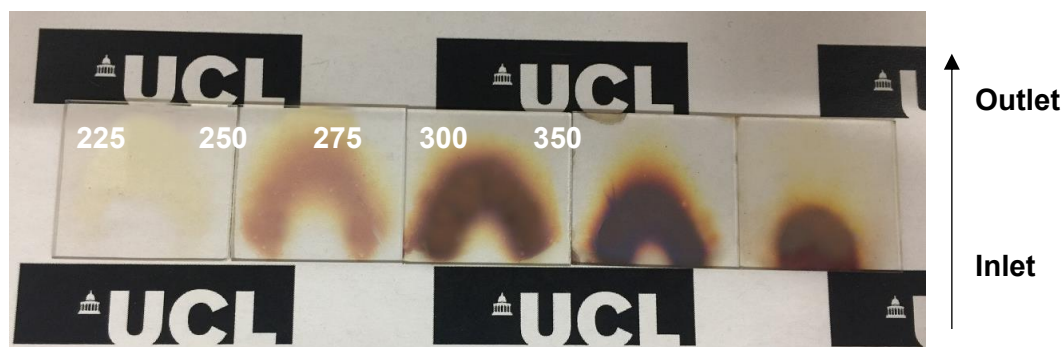


Figure 5.6 Ag-AP deposited on glass with constant flow rate of N₂ at 170 sccm and different deposition temperature at 225, 250, 275, 300 and 350 °C

Ag-AP XRD analysis

The XRD patterns of as-deposited Ag-AP thin film on glass is shown in Figure 5.7. Similar to the previous XRD patterns of Ag-AMP, the major diffraction peaks of Ag are observed when deposition temperature reaches 300 and 350 °C, while the weak peaks at 44.3 ° and 64.5 ° indicated that the (200) and (220) reflections are missing. The peak at 38.2° can be assigned to (110) reflection of Ag metal, which are matched well with the standard pattern (Fm-3m (225) space group, $a = b = c = 4.0773 \text{ \AA}$; $\alpha = \beta = \gamma = 90^\circ$, PDF#87-0718). No obvious peaks are found in XRD patterns at temperatures below 275 °C, indicating the small size of the nanoparticle or relative low amount presented.

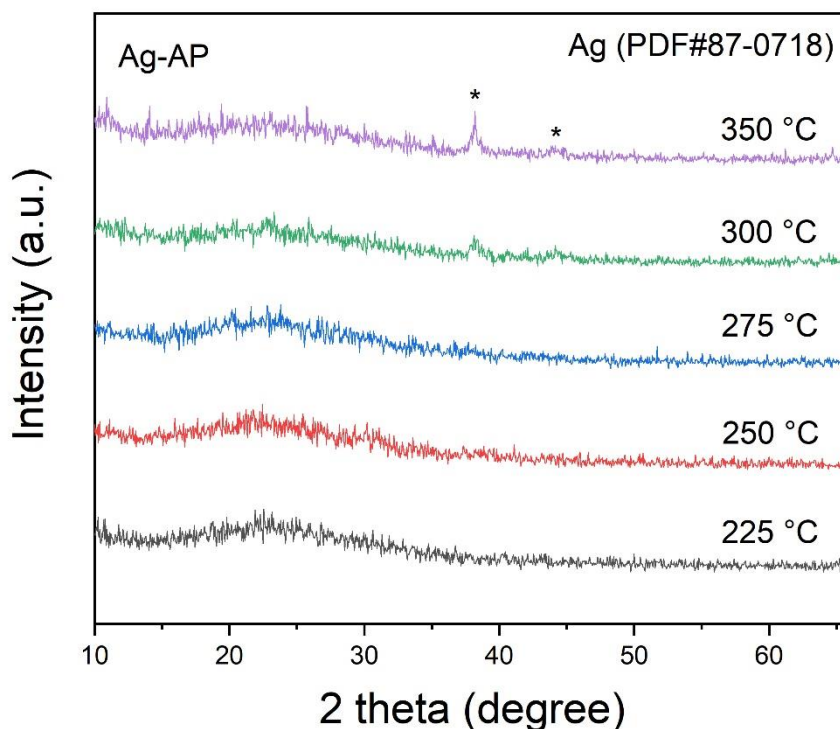


Figure 5.7 XRD patterns of as-deposited Ag-AP thin film on glass with different temperatures, ranging from 225 to 350 °C and a constant flow rate of N₂ at 170 sccm

Ag-AP UV-Vis analysis

UV-Vis adsorption of as-deposited Ag-AP thin films on glass synthesized at different temperatures were investigated and shown in Figure 5.8. With the increasing of deposition temperature, the surface plasmon resonance (SPR) band of silver particles ($\lambda_{\max} \sim 439$ nm, deposition temperature at 225 °C) is shifted to the red ($\lambda_{\max} \sim 535$ nm, deposition temperature at 300 °C). No obvious additional band at ~ 370 nm is appeared as compared to the previous spectra of Ag-AMP at 300 and 350 °C, but the band at 700 nm became more apparent. Figure 5.8 also shows that the intensity of the SPR band and its full width at half maxima (FWHM) increases with the increasing of the deposition temperature. These characterization results of the adsorption spectrum suggest increasing size of the Ag nanoparticles with increasing deposition temperature, which also matches with the results from the UV/Vis spectra of Ag-AMP.

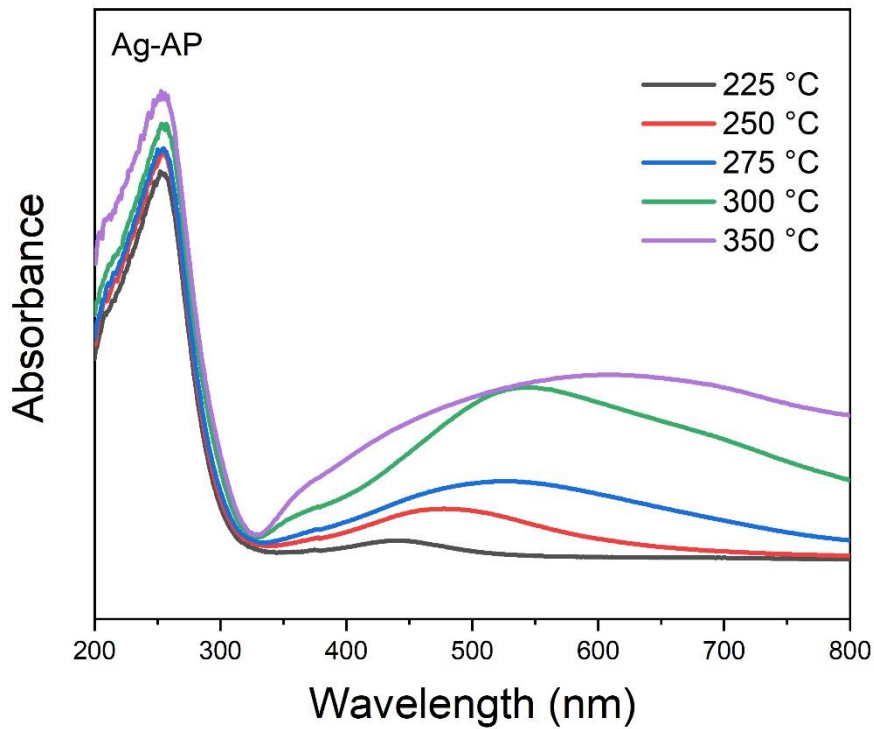


Figure 5.8 UV-Vis adsorption spectra of as-deposited Ag-AP thin film on glass with increase temperature from 225 to 350 °C

Ag-EA initial depositions

Figure 5.9 shows the as-deposited Ag-EA thin film on glass substrate. Similar to the previous set of depositions of Ag-AMP and Ag-AP on glass, as the deposition temperature increases, the colour gradually darkens and turns from bright yellow to brownish. Arch-shaped films were obtained between 225 to 275 °C, which was attributed to the triangular-shaped inlet as mentioned early. Under a constant flow rate at 170 sccm, the coverage of the thin film shrinks as the deposition temperature increases, which was consistent with previous results.

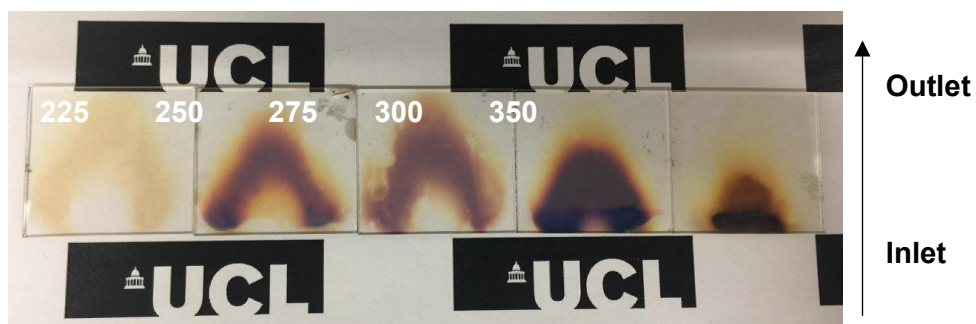


Figure 5.9 Ag-EA deposited on glass with constant flow rate of N₂ at 170 sccm and different deposition temperature at 225, 250, 275, 300 and 350 °C

Ag-EA XRD analysis

The XRD patterns of as-deposited Ag-EA thin film on glass is shown in Figure 5.10. Similar to the previous XRD patterns of Ag-AMP and Ag-AP, the major diffraction peaks of Ag are observed when deposition temperature reaches at 350 °C. The peaks at 38.1° can be assigned to (110) reflection of Ag metal, which are matched well with the standard pattern (Fm-3m (225) space group, $a = b = c = 4.0773 \text{ \AA}$; $\alpha = \beta = \gamma = 90^\circ$, PDF#87-0718). Different from the previous XRD results, a peak at 38.1° was shown when deposition temperature was set at 250 °C, relatively a lower temperature. This might due to the formation of the relatively thicker and darker Ag film as shown in Figure 5.9. No obvious peaks are found in XRD patterns at other deposition temperatures, indicating the small size of the nanoparticle or relative low amount presented.

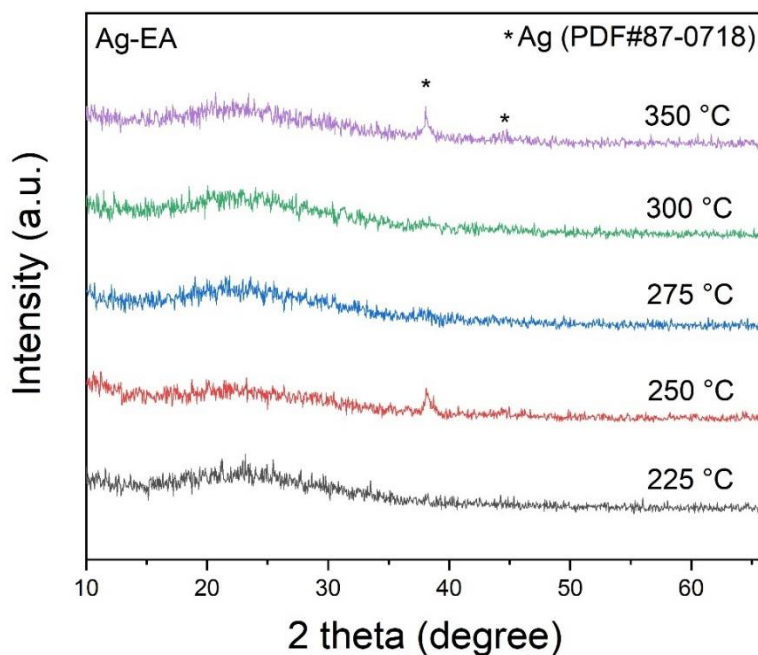


Figure 5.10 XRD patterns of as-deposited Ag-EA thin film on glass with different temperatures, ranging from 225 to 350 °C and a constant flow rate of N₂ at 170 sccm

Ag-EA UV-Vis analysis

UV-Vis adsorption of as-deposited Ag-EA thin films on glass, synthesized at different temperatures are shown in Figure 5.11. With increasing deposition temperature, the surface plasmon resonance (SPR) band of silver particles ($\lambda_{\max} \sim 443$ nm, deposition temperature at 225 °C) is shifted to the red ($\lambda_{\max} \sim 574$ nm, deposition temperature at 300 °C). Different from the previous UV-Vis spectra of Ag-AMP and Ag-AP, when deposition temperature reaches 350 °C, SPR band of silver particles is shifted back to blue ($\lambda_{\max} \sim 463$ nm) and an additional band at ~ 370 nm is appeared. It is worth noting that peak at 700 nm is also visible in high temperature spectra. In generally, when deposition temperatures were set between 225 and 300 °C, the intensity of SPR band and its full width at half maxima (FWHM) increases with the increasing of the temperature. These characterization results suggest increasing size of the Ag nanoparticles with increasing deposition temperature, which matched well with the previous result. However, the blue shift of the SPR band when deposition temperature

at 350 °C suggests the formation of relatively smaller size Ag NPs than seen for the Ag-AMP and Ag-AP precursors at this temperature.

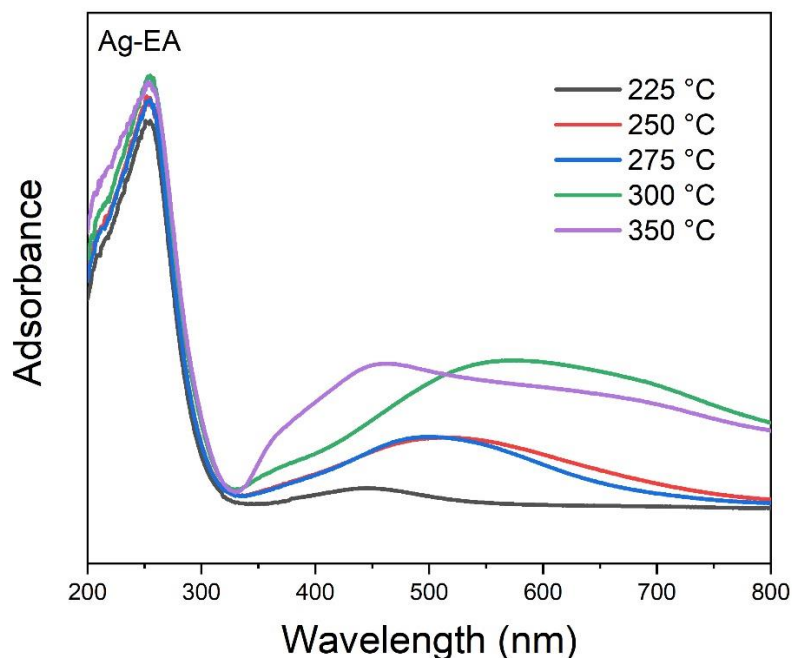


Figure 5.11 UV-Vis adsorption spectra of as-deposited Ag-EA thin film on glass with increase temperature from 225 to 350 °C

Organometallic Ag precursor SEM analysis

The surface morphology and distribution of as-deposited Ag thin film on glass was examined by SEM. An example of Ag-AMP thin film on glass is shown in Figure 5.12 (a). Other precursors show identical morphologies as the spherical particles evenly distribute over the surface shown in Figure 5.12 (a). The uniform film was composed of spherical particles agglomerated together with diameters ~10 nm, which has a high consistency with the morphology of silver nanoparticles studied by Lee et al., shown in Figure 5.12 (b). Other AACVD studies, which have deposited silver films using different precursors and deposition conditions, have also observed spherical particles^{208–210}.

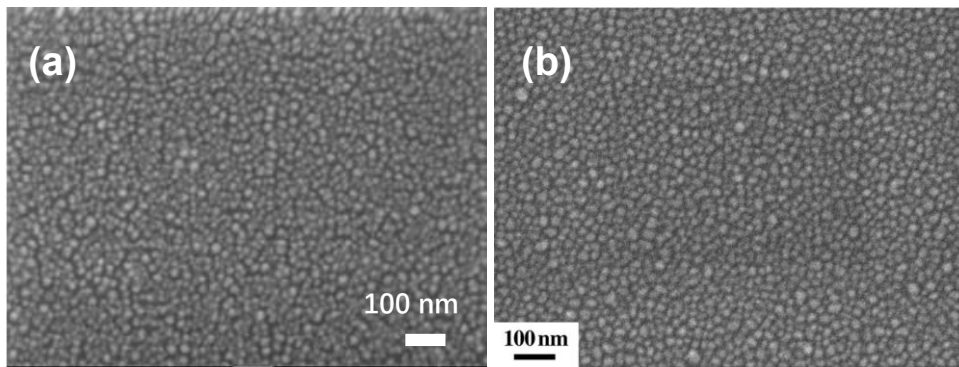


Figure 5.12 SEM image of (a) as-deposited Ag-AMP thin film on glass with 10 μ L Ag-AMP silver precursor, deposition temperature at 275 $^{\circ}$ C and flow rate of N₂ at 170 sccm and (b) literature SEM image of silver film²¹¹

TEM analysis Ag-AMP on glass

Details of the morphological features of the Ag NPs from Ag-AMP deposited thin films on glass were further examined by HR-TEM. Images shown in Figure 5.13(a) displays a cluster of small Ag NPs with diameter \sim 6 to 8 nm. Largest size Ag NPs are formed with diameters \sim 14 nm might due to the aggregation of the small Ag NPs. Instead of spherical shape of the NPs, some rod shape of the Ag NPs is also observed.

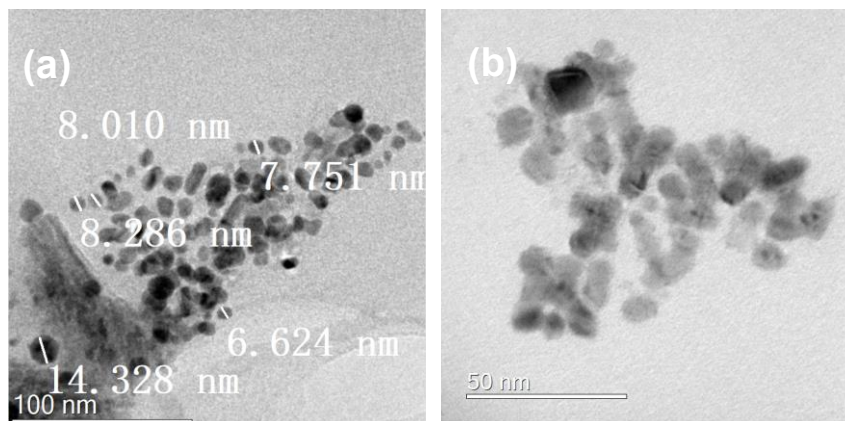


Figure 5.13 HR-TEM image of Ag nanoparticles on as-deposited Ag-AMP thin film on glass with 10 μ L silver Ag-AMP precursor, deposition temperature at 275 $^{\circ}$ C and flow rate of N₂ at 170 sccm under (a) high magnification and (b) low magnification

5.3.2 Characterization of Ag@WO₃ gas sensor

5.3.2.1 initial deposition

After a series of optimization experiments of organometallic Ag metal precursors on glass, the optimized reaction conditions were as follows: deposition temperature at 275 °C and flow rate of N₂ at 170 sccm. Subsequently, these Ag precursor solutions were deposited on pre-prepared annealed WO₃ gas sensors (described in Chapter 3.2.2) with various amounts of precursor solution (1, 3, 5 or 10 μL). As shown in the Figure 5.14 below, with increasing amount of Ag-precursor, the colour of the obtained Ag@WO₃ sensors turns darker, indicating the loading of silver particles increases.

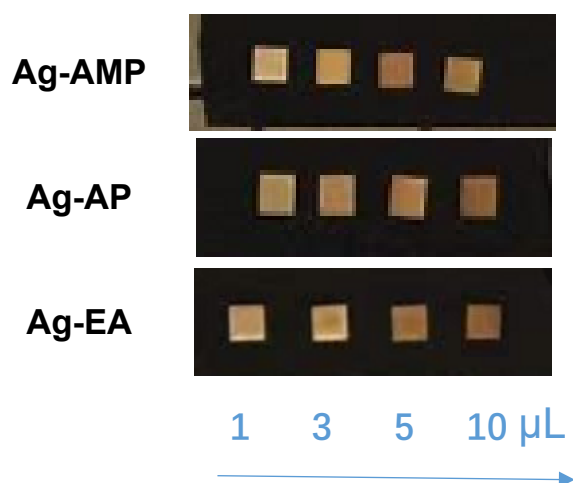


Figure 5.14 Pictures of the as-deposited Ag thin film on WO₃ on alumina sensors with an increasing volume of initial Ag precursor (1, 3, 5 and 10 μL, left to right)

5.3.2.2 XRD analysis

The XRD patterns of as-deposited Ag-decorated WO₃ gas sensors and the XRD pattern of an annealed WO₃ gas sensor are shown in Figure 5.15 for comparison. No significant difference was found after the deposition of Ag-precursors on WO₃ gas sensors because the peaks of silver (38.2°, 44.3° and 64.5°, PDF#87-0718, $a = b = c = 4.0773 \text{ \AA}$; $\alpha = \beta = \gamma = 90^\circ$) overlap with the peaks of gold (38.3°, 44.6° and 64.5°; PDF#01-1174, $a = 4.06 \text{ \AA}$, $b = 4.06 \text{ \AA}$, $c = 4.06 \text{ \AA}$, $\alpha = 90.0^\circ$, $\beta = 90.0^\circ$ and $\gamma = 90.0^\circ$) from the electrodes contained on the surface of the gas sensor.

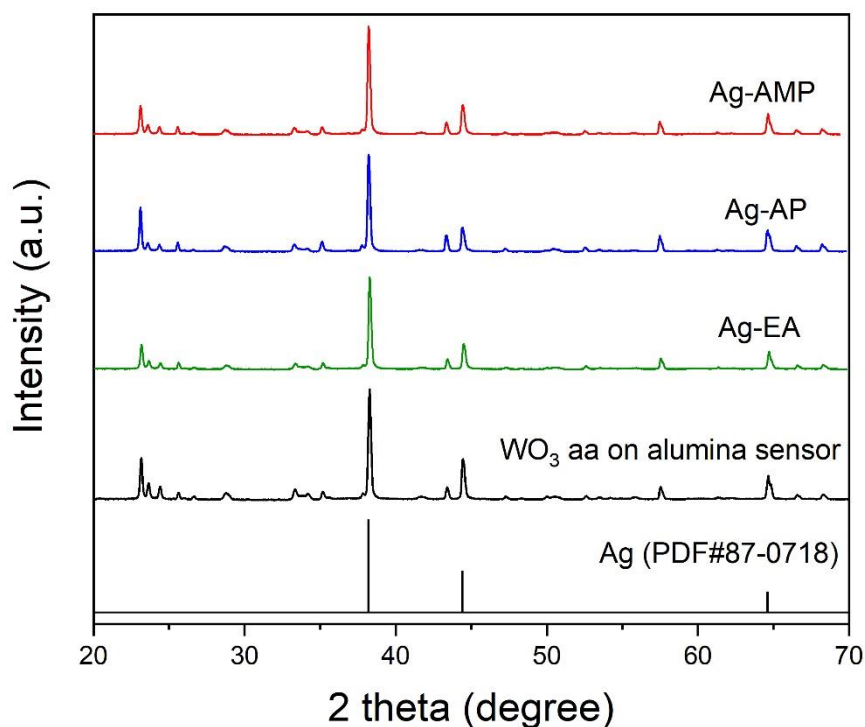


Figure 5.15 XRD patterns of as-deposited Ag decorated WO_3 sensors by using three organometallic Ag metal precursors with 10 μL of the initial precursor solution deposited at 275 $^\circ\text{C}$ with a flow rate of N_2 at 170 sccm and the XRD pattern of annealed WO_3 sensor, along with reference pattern of Ag (PDF#87-0718)

5.3.2.3 XPS analysis

XPS measurements were further examined on the prepared $\text{Ag}@\text{WO}_3$ via using various volumes of initial precursor solution (1,3,5 and 10 μL). Figure 5.16 displays the XPS spectra of the Ag3d regions for all three organometallic Ag metal precursors with various volumes of initial precursor solution used, and their corresponding area ratio of Ag3d to W4f regions. Two clear peaks at ~ 374.2 and 368.1 eV were identified clearly and can be assigned to Ag $3d_{3/2}$ and Ag $3d_{5/2}$, respectively, indicating the successful deposition of Ag NPs on WO_3 sensors. The differences between the $3d_{5/2}$ and $3d_{3/2}$ peaks for all Ag samples (~ 6.0 eV), listed in Table 5.1 were the same as literature values of zero valent silver, indicating the formation of metallic Ag particles²¹². No peak shift to higher binding energies was observed. indicating there is no oxidation from Ag^0 to Ag^{1+} during and after the deposition²¹³. Some small chemical shift for Ag core level

has been observed with different amount of loadings, which can be attributed to the initial state effect caused by the size of the particles²¹⁴. For Ag nanoparticles, a 0.5-2 eV chemical shift have been observed for small particles as compared to the core levels of respective bulk Ag crystals²¹⁵. The figure also illustrates that the intensity of the Ag peaks for all three organometallic Ag metal precursors increases as the amount of precursor increased. Figure 5.16(d), (e) and (f) further demonstrated an increase in silver deposition on WO₃ as amount of Ag precursor solution increases. However, it is worth noting that as the amount increases, the increase becomes smaller.

Table 5.3 XPS peaks for Ag nanoparticles

		Ag-AMP (eV)	Difference	Ag-AP (eV)	Difference	Ag-EA (eV)	Difference
1uL	Ag 3d _{5/2}	368.11		367.34		368.10	
	Ag 3d _{3/2}	374.14	6.03	373.36	6.02	374.07	5.97
3uL	Ag 3d _{5/2}	368.15		367.55		368.22	
	Ag 3d _{3/2}	374.17	6.02	373.55	6.00	374.22	6.00
5uL	Ag 3d _{5/2}	368.26		367.43		368.20	
	Ag 3d _{3/2}	374.27	6.01	373.43	6.00	374.21	6.01
10uL	Ag 3d _{5/2}	367.99		367.27		368.32	
	Ag 3d _{3/2}	373.99	6.00	373.27	6.00	374.33	6.00

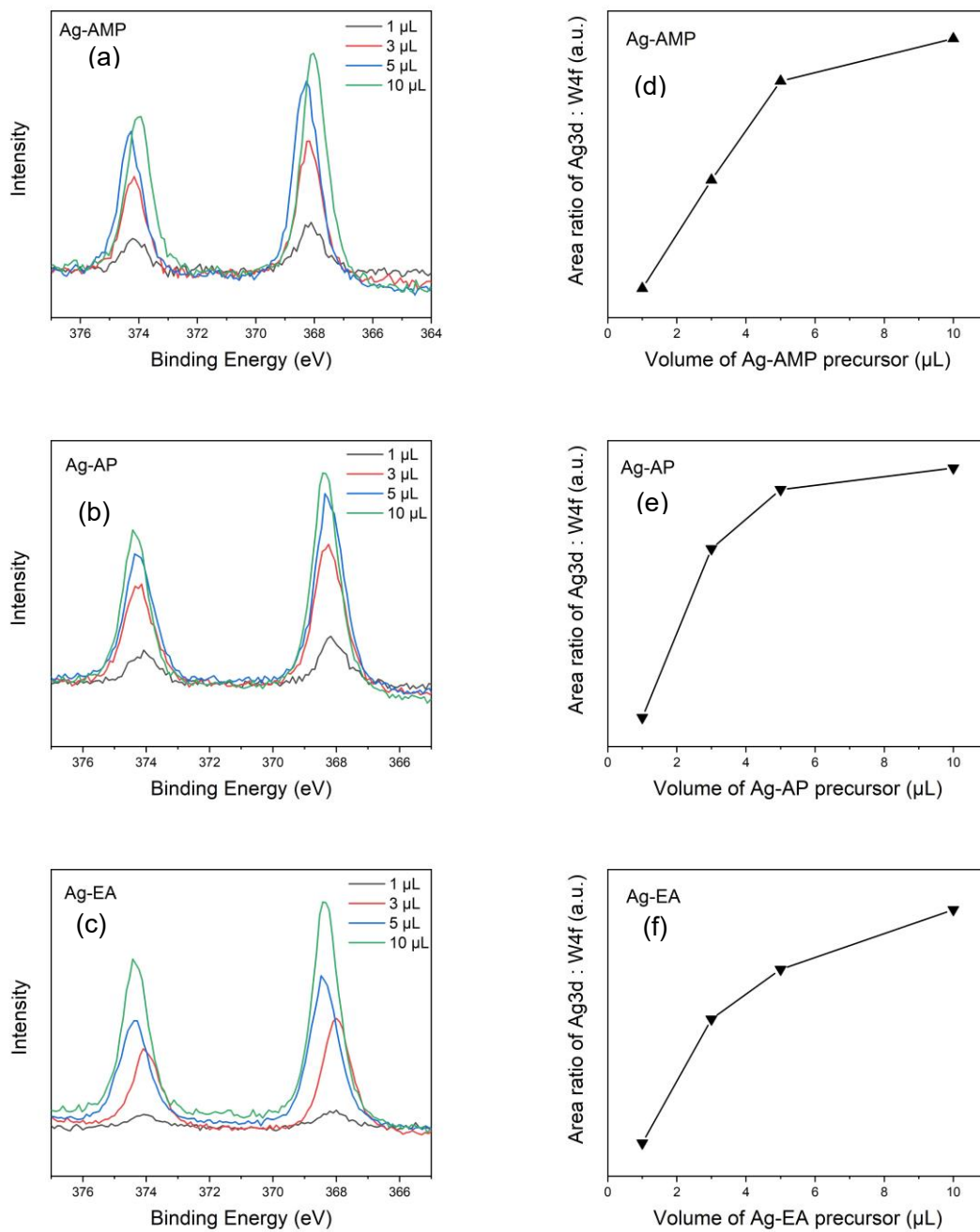
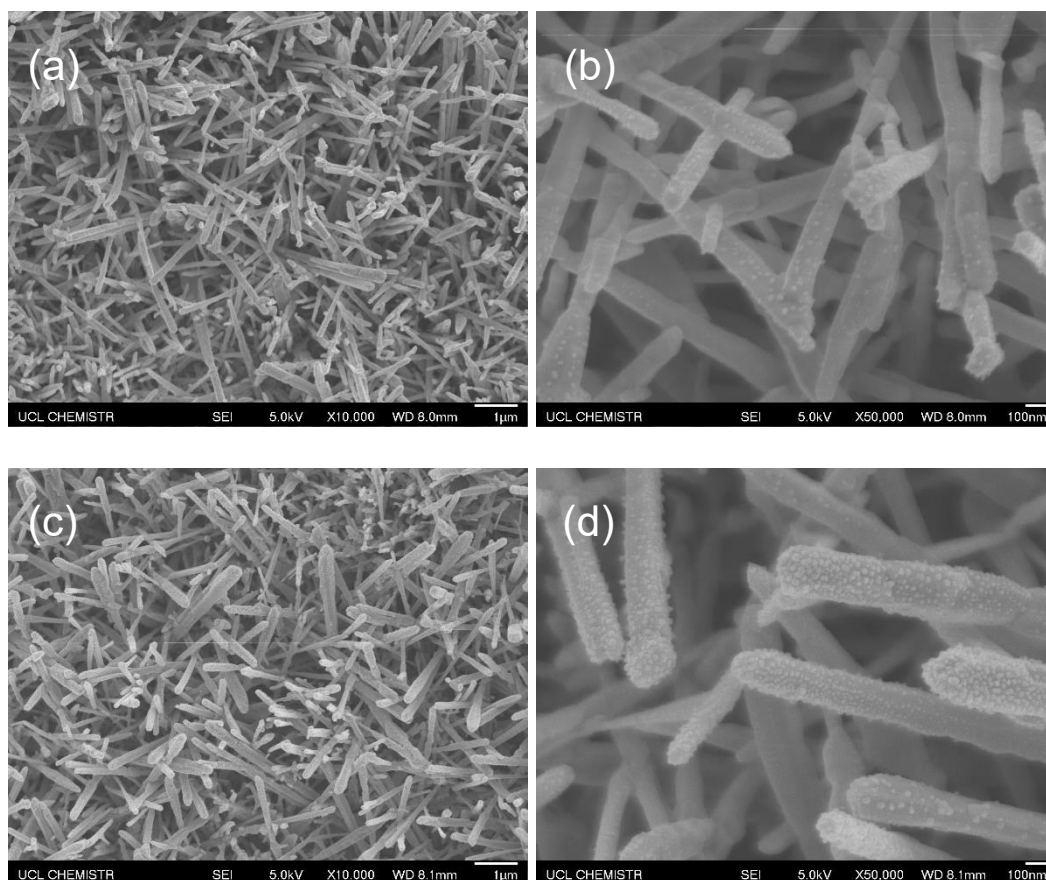


Figure 5.16 XPS Ag3d core-level spectra of (a)Ag-AMP, (b) Ag-AP and (c) Ag-EA with various volume of initial precursor solution used and their corresponding area ratio Ag 3d: W 4f (d) Ag-AMP, (e)Ag-AP and (f)Ag-EA

5.3.2.4 SEM analysis

SEM characterizations of as-deposited Ag-decorated WO_3 gas sensors via organometallic Ag metal precursors, including Ag-AMP, Ag-AP and Ag-EA with different amounts of precursor solution used for deposition are shown in Figures 5.17, 5.18 and 5.19, respectively. It shows relatively spherical-shaped Ag nanoparticles with diameters that range from 10 to 20 nm on the needle-shaped WO_3 nanostructures (diameters 100 to 200 nm). As can be seen from the all three figures, the coverage of the Ag NPs on the surface of WO_3 NNs increases gradually as the amount of the initial precursor increases and becomes almost saturated when it increases to 10 μL . This could explain why the growth slopes in Figure 5.16 (d), (e) and (f), tending to reduce as the initial amount of precursor solution increases. No morphology changes for both nanoparticles and the nanoneedles was found as the amount of Ag loading increases.



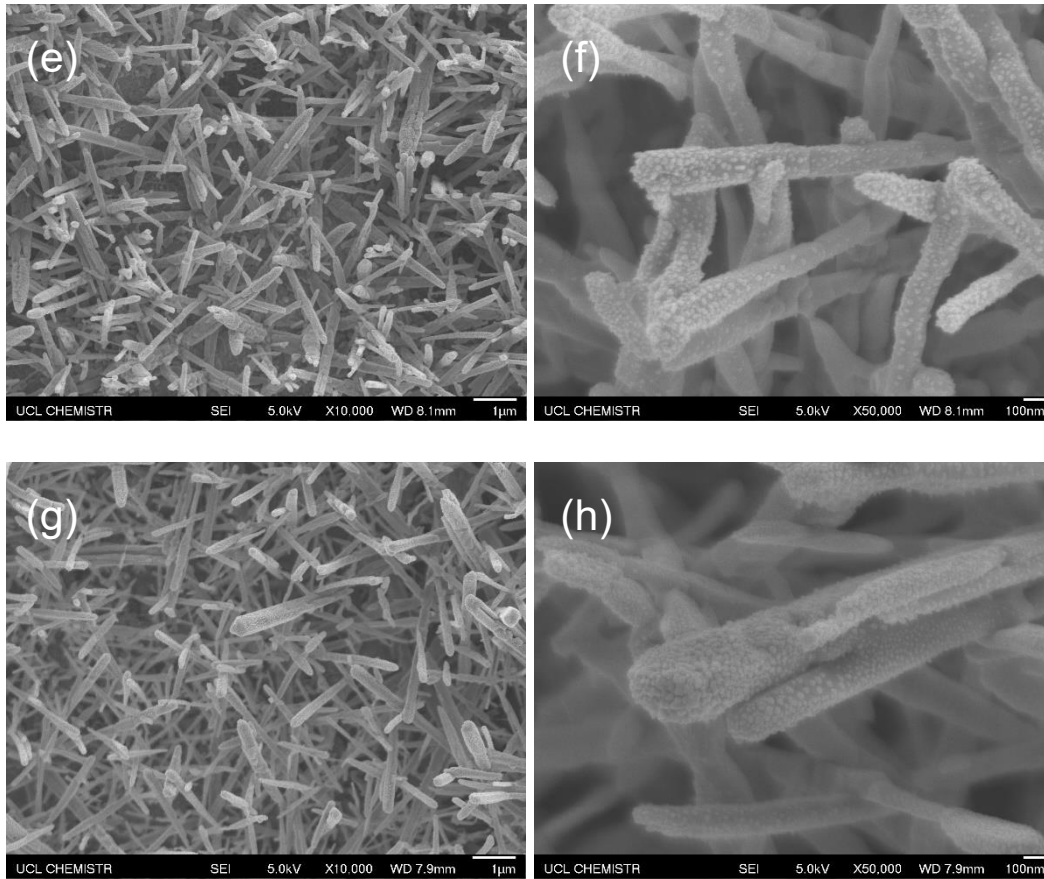
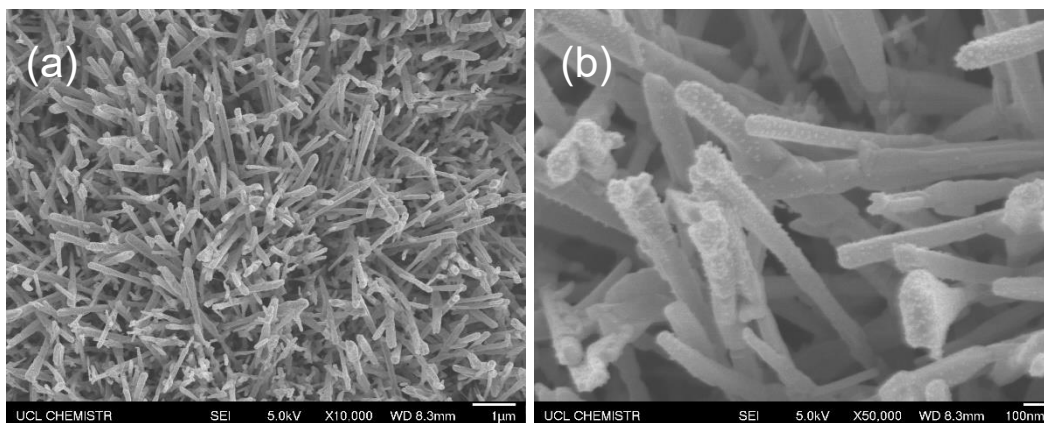


Figure 5.17 SEM images of as-deposited Ag@WO₃ sensors by using Ag-AMP as precursor with various amount of initial precursor solution (a) and (b) 1 μL, (c) and (d) 3 μL, (e) and (f) 5 μL and (g) and (h) 10 μL, taken under low and high magnification, respectively



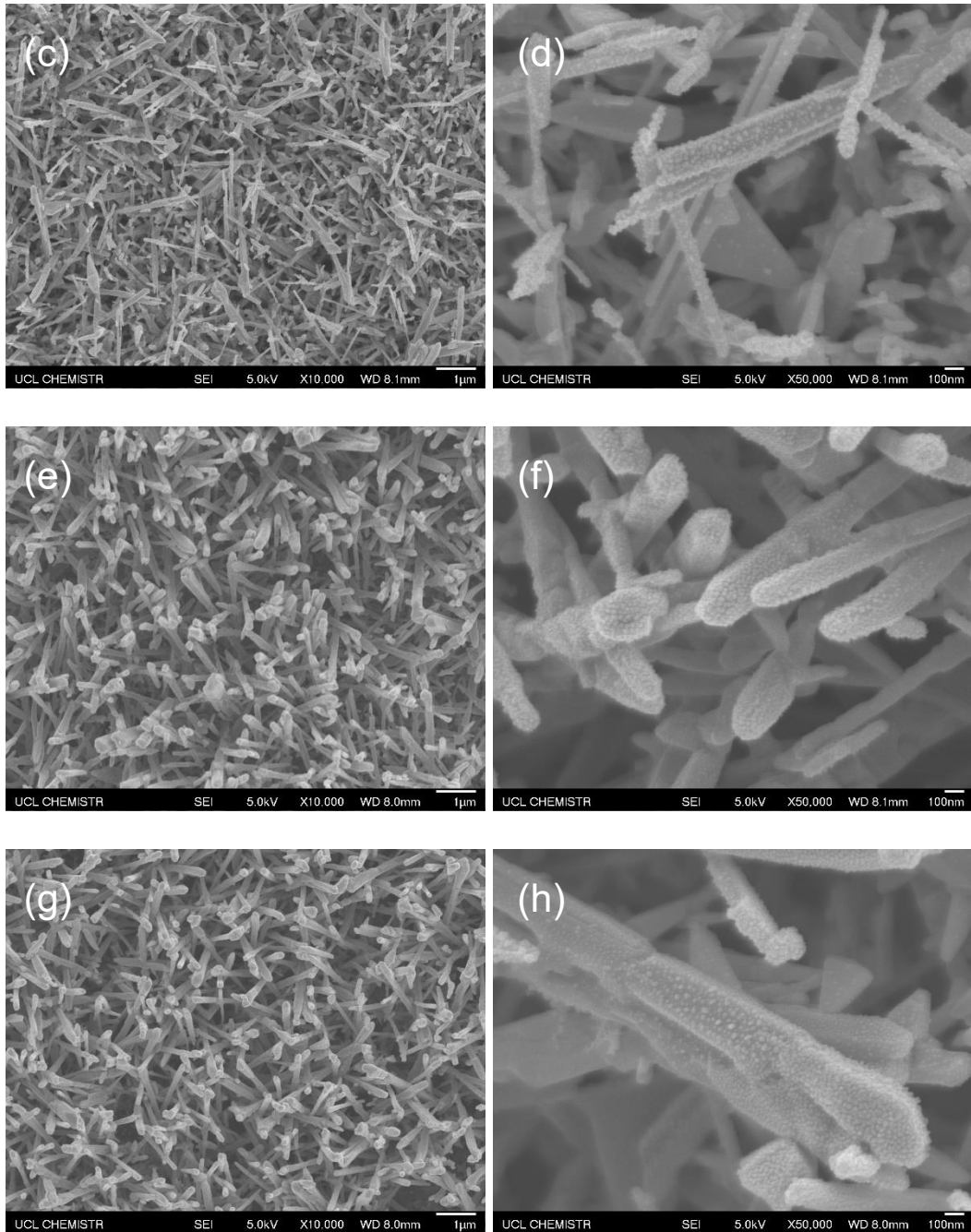
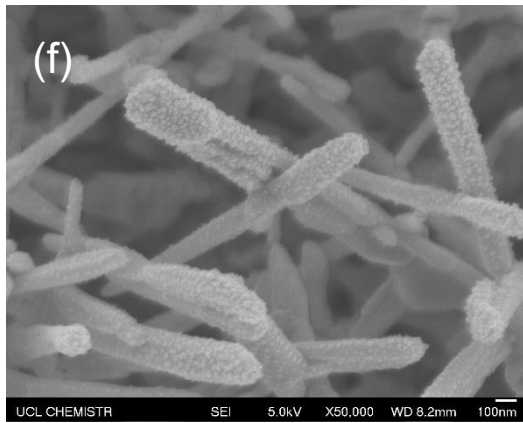
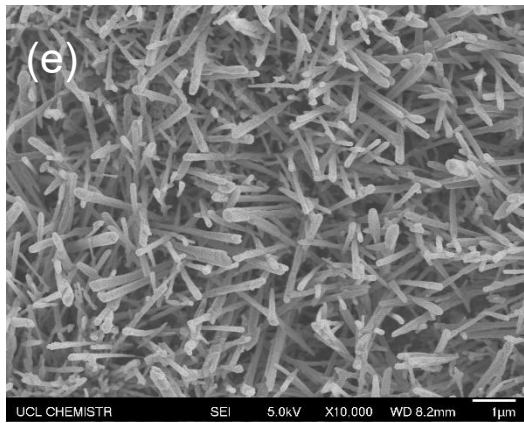
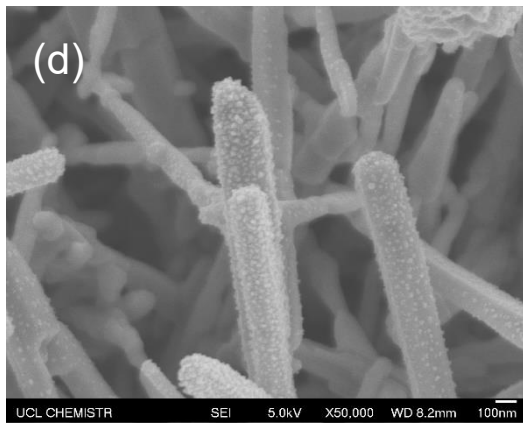
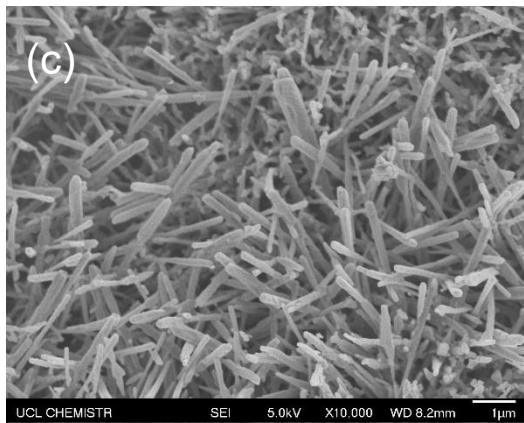
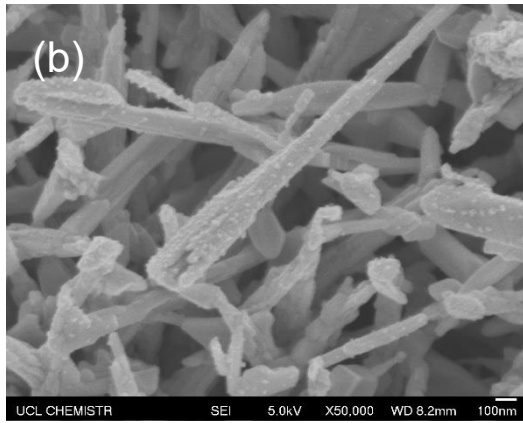
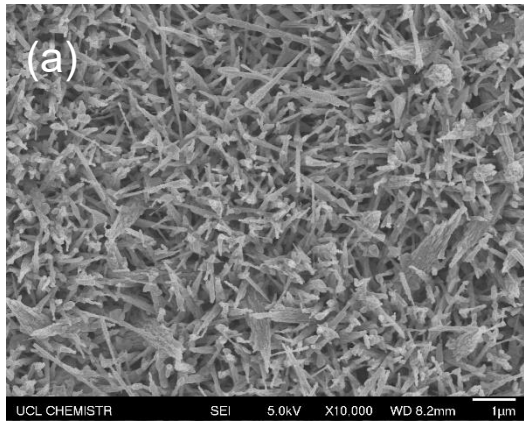


Figure 5.18 SEM images of as-deposited Ag@WO₃ sensors by using Ag-AP as precursor with various amount of initial precursor solution (a) and (b) 1 μL, (c) and (d) 3 μL, (e) and (f) 5 μL and (g) and (h) 10 μL, taken under low and high magnification, respectively



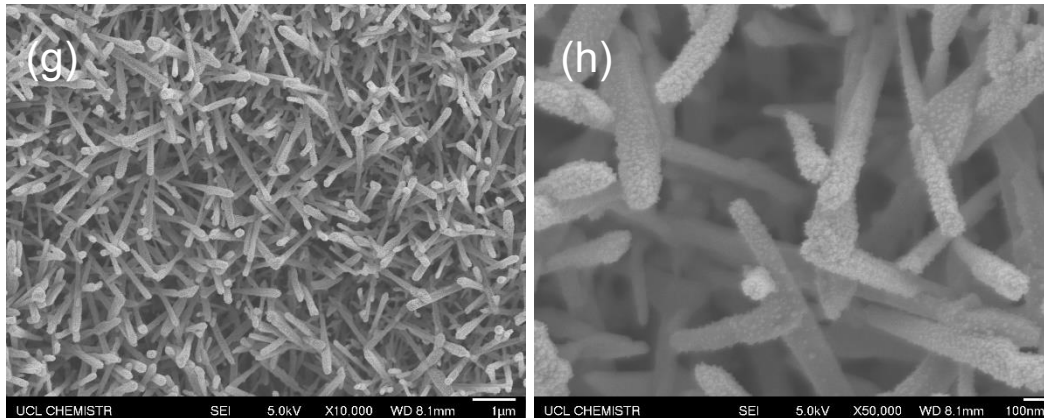
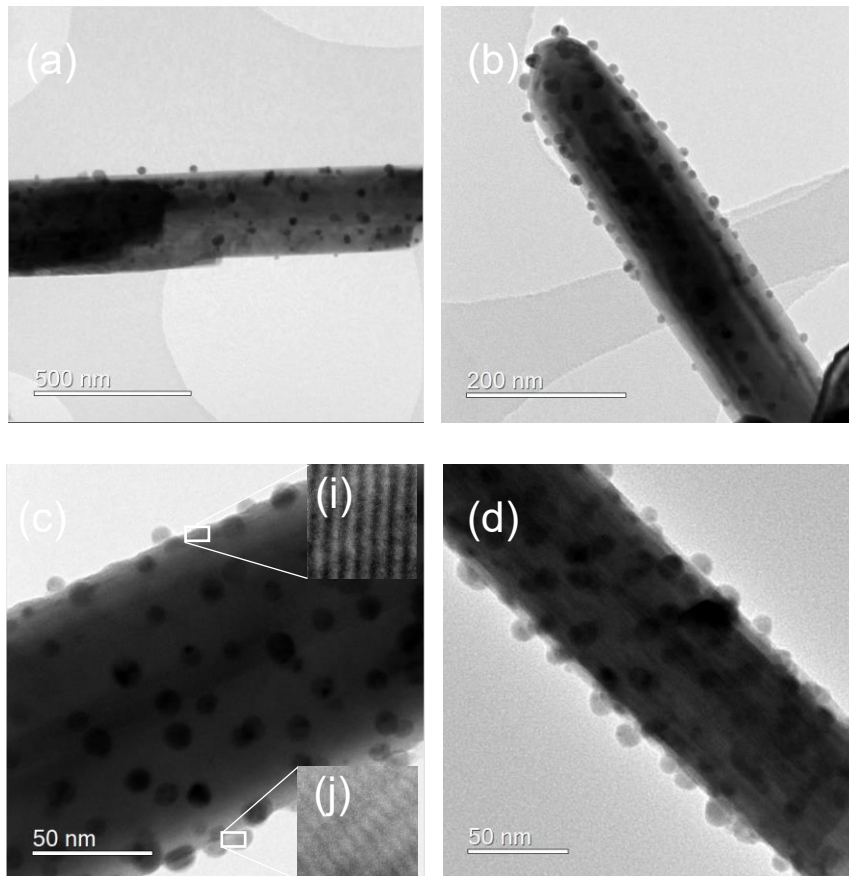


Figure 5.19 SEM images of as-deposited Ag@WO₃ sensors by using Ag-EA as precursor with various amount of initial precursor solution (a) and (b) 1 µL, (c) and (d) 3 µL, (e) and (f) 5 µL and (g) and (h) 10 µL, with low and high magnification, respectively

5.3.2.6 TEM analysis

Further information about the structures of the nanoparticles and the nanoneedles were obtained by TEM. TEM images of Ag@WO₃ sensors with various Ag-loading produced using the Ag-AMP precursor were examined (Figure 5.20). The diameter of WO₃ nanoneedles was in the range of 100-300 nm. The WO₃ NNs are monophasic and Ag NPs are multiphasic. The clear lattice fringes can be observed in two insets in Figure 5.20 (i) and (j) with interplanar spacing of 0.378 nm and 0.235 nm, respectively, consistent with an internal order of WO₃ in the (020) direction and with the (111) planes of Ag. The WO₃ nanoneedle surface is homogeneously covered with well-dispersed spherical Ag NPs. The particle size distribution of the Ag NPs with different loadings were counted and shown in Figure 5.21. The diameter of Ag NPs is mostly distributed between 9 and 13 nm. Large size particles were also formed with diameters ~ 20 nm. The atomic planes of WO₃ under the Ag nanoparticles are not affected by the presence of the particle suggesting a weak physical interaction between the WO₃ surface and Ag nanoparticles. [9] Except for UV-vis, which demonstrated that an increase in the deposition would increase the silver nanoparticle size, there is no significant evidence that the particle size is related to the amount of the initial precursor solution used, rather the amount of the particles increases as the amount of the initial precursor

solution increases, similar to observation by SEM. EDS element mapping was carried out to study element composition of the as-deposited Ag@WO₃ on gas sensor platforms. From the EDS spectrum of the sample shown in Figure 5.22 (e), four main elements, including Au, W, O and Ag were detected. The presence of a large amount of Au elements is due to the use of a gold TEM grid. Also, it could be because the gold electrode from the sensor substrate. Corresponding EDS elemental mapping is shown in Figure 5.22(a)-(d), respectively, revealing that W, O and Ag were all well distributed along the nanoneedle.



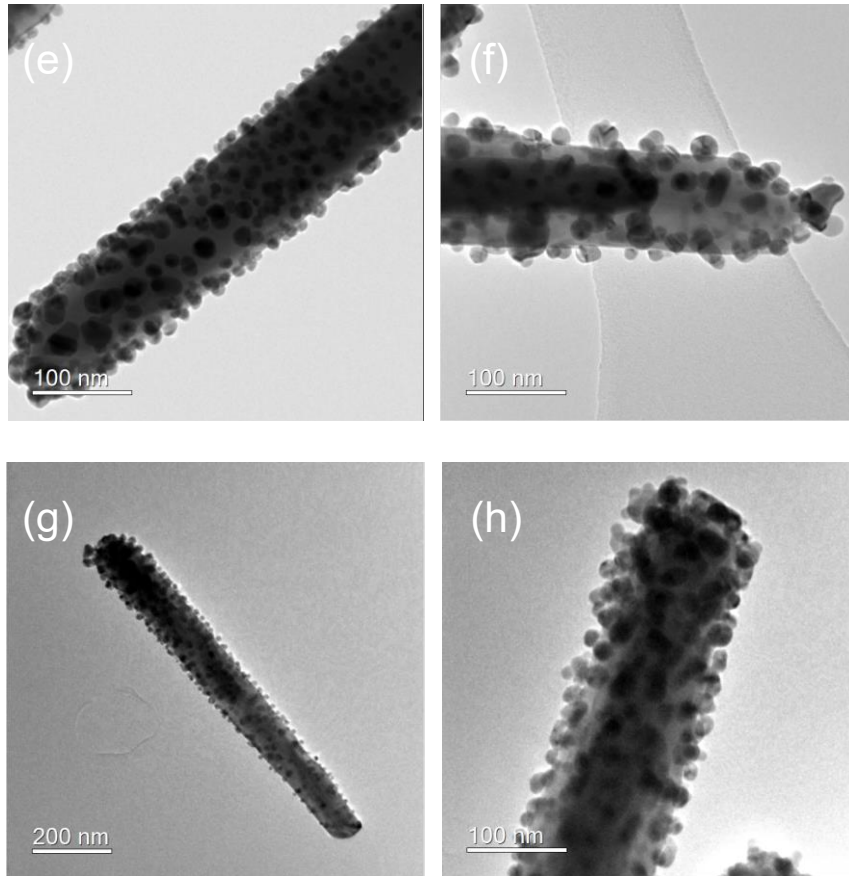


Figure 5.20 TEM images of as-deposited Ag@WO₃ sensor by using Ag-AMP as precursor with various amount of initial precursor solution (a) and (b) 1 μ L, (c) and (d) 3 μ L, (e) and (f) 5 μ L and (g) and (h) 10 μ L; (i) and (j) the inset shows the crystalline structure of WO₃ NNs and Ag NPs, respectively

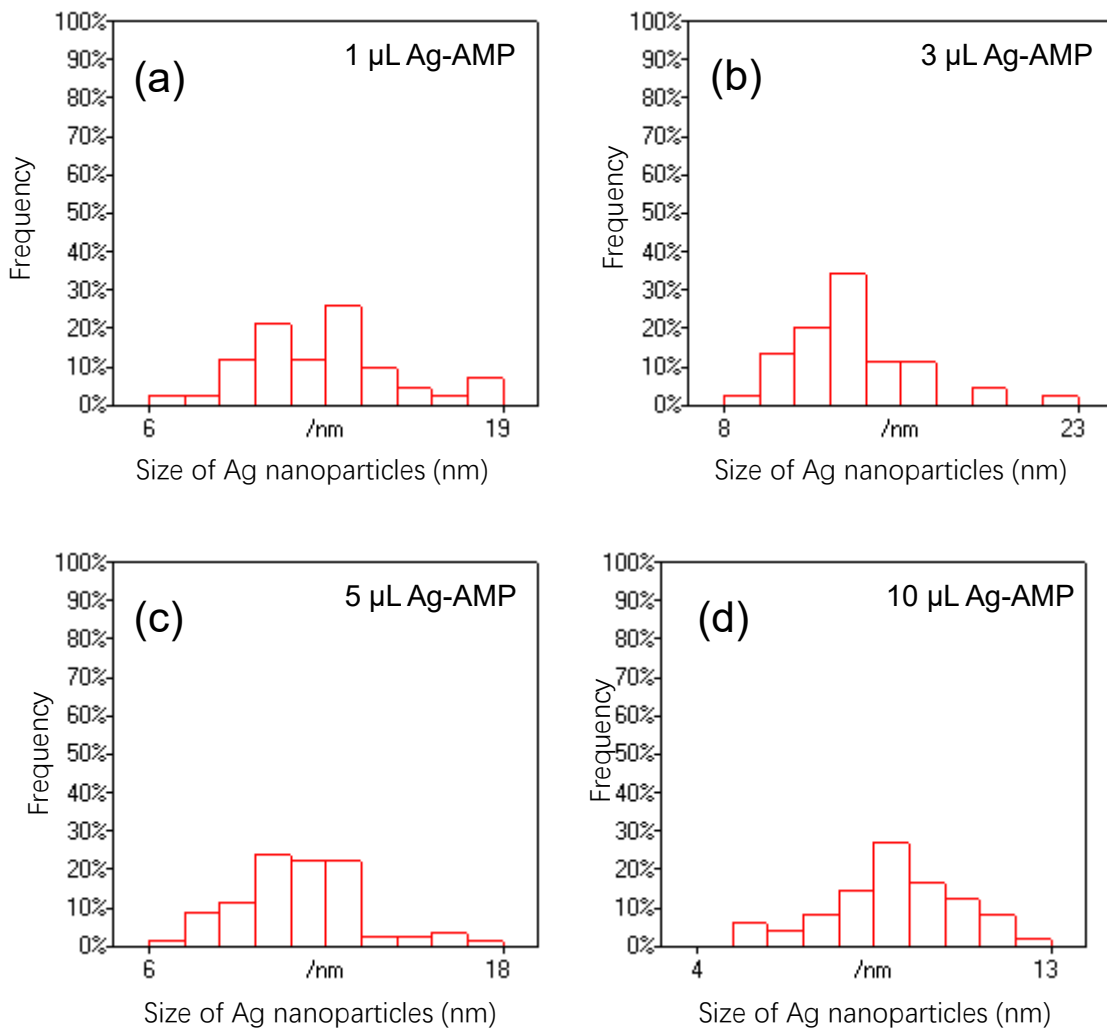


Figure 5.21 Size distribution of Ag nanoparticles on WO_3 sensors via Ag-AMP precursor (a) 1 μ L (b) 3 μ L (c) 5 μ L and (d) μ L 10 corresponding to Figure 5.18 (b), (c), (e) and (g), respectively

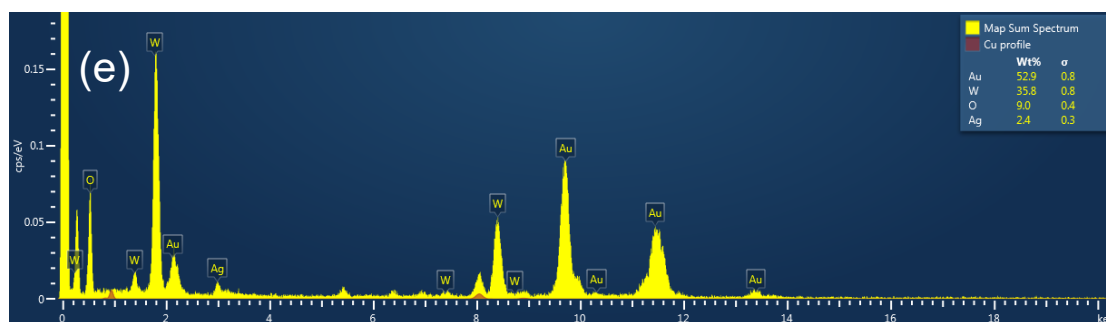
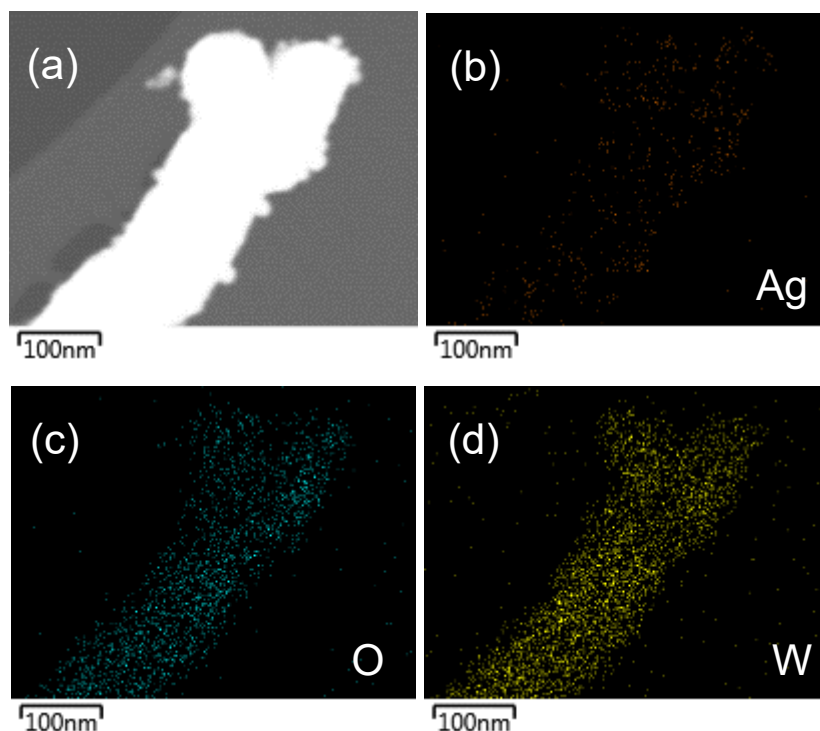


Figure 5.22 EDS mapping images of Ag@WO₃ on sensor platform (a) electronic image of Ag@WO₃ sample, (b) Ag distribution, (c) O distribution, (d) W distribution and (e) EDS spectrum of the Ag@WO₃ sensor sample

5.4 Conclusion

In this chapter, three organometallic silver metal precursors (Ag-AMP, Ag-AP and Ag-EA) with different chemical structures of the carbon backbones have been introduced and successfully deposited onto glass substrates via AACVD. After switching the rectangular-based reactor to the square-based reactor, which prevents the early decomposition and reaction of the aerosol precursor droplets before entering into the reaction chamber, an obvious yellowish Ag thin film was achieved via AACVD. XRD

analysis reveals the presence of Ag peaks under higher deposition temperature (350 °C) for all three organometallic Ag metal precursors, while no obvious peaks were found for the thin films deposited under lower temperatures, indicating the small size of the nanoparticles and the relatively low amount existed. UV-Vis spectra further demonstrated that deposition temperature had an influence on the as-deposited Ag thin films. As the temperature increases, the plasmon peak shifts to longer wavelengths and broadens, indicating the size of the Ag particles gets larger. After a series of experiments altering the deposition parameters, an optimal reaction condition was concluded with a flow rate of N₂ at 170 sccm and deposition temperature at 275 °C, which gave an evenly distributed brownish Ag thin film. SEM and TEM images confirm the formation of a uniform Ag film composed with spherical particles agglomerated together with average diameters ~8 nm.

Subsequently, three organometallic Ag metal precursors were successfully deposited onto pre-prepared annealed WO₃ gas sensors with various amounts of initial precursor solution (1,3,5 and 10 μL) under the optimized deposition conditions. No significant change between the XRD patterns of a plain WO₃ gas sensor and Ag@WO₃ gas sensor were observed due to the overlap of the Ag peaks and the Au peaks, which originated from the gold electrodes on the sensor surface. XPS demonstrated increasing the amount of precursor used increased the Ag loadings on the WO₃ gas sensor. The formation of metallic Ag⁰ particles was also confirmed by the XPS analysis, indicating no oxidation from Ag⁰ to Ag¹⁺ during and after the deposition, which is different to the XPS results when AgNO₃ was used as the Ag precursor. SEM images for all three precursors shows that the coverage of spherical Ag NPs adhered on the surface of WO₃ NNs increases with increasing precursor amount and tends to saturation at 10 μL. The size of Ag NPs was further investigated by TEM which showed that the diameters of the Ag NPs mainly ranged from 9 to 13 nm, regardless of the amount of initial precursor used.

Chapter 6 Gas sensing response

In this chapter, gas sensors described and fabricated in chapter 3.2.2 (WO_3), chapter 4.2.3 (Ag@WO_3) and in chapter 5.2.3 ($\text{Ag-EA/Ag-AMP/Ag-AP@WO}_3$) were tested for gas response to oxygen at University of Warwick. The gas responses were analysed, and a gas sensing 'mechanism' inferred by reference to experimental data and literature precedent.

6.1 Gas sensing response of Ag@WO_3 prepared using AgNO_3 as precursor

The Ag@WO_3 sensor was made in a two-step synthesis by using a plain WO_3 sensor made in a one-step synthesis (using 0.06 g $\text{W}(\text{CO})_6$ at 375 °C under a flow of nitrogen of 300 sccm followed by annealing in air at 500 °C for 2 h as described in Chapter 3.2.2) *via* AACVD and decorating with Ag NPs (using 0.09 g AgNO_3 at 250 °C under a flow of nitrogen of 300 sccm as described in Chapter 4.2.3) again *via* AACVD.

Gas sensing tests were carried out towards different oxygen concentration ranging between 0% to 20% (200,000 ppm) in a humid environment (relative humidity (RH) level \sim 85%) for both undecorated and Ag@WO_3 sensors at sensor operating temperatures ranging between 150 and 400 °C with an interval of 50 °C to examine the influence of temperature on sensor response, as shown in Figure 6.1. No significant change in resistance was observed when operating temperature was lower than 200 °C. When operating temperature was increased, a maximum gas response for undecorated WO_3 sensor was observed at 400 °C with a response value of 6, whilst for Ag@WO_3 sensor, a maximum gas response was observed at 350 °C with a response value of 23. Therefore, 400 and 350 °C are assigned as the optimal operating temperature for these sensors, respectively. It is worth noting that the optimal gas response for Ag@WO_3 sensor is 400% more sensitive than the undecorated WO_3

sensor with the operating temperature also being lowered by 50 °C. A small peak (lower response) shown at 250 °C could be attributed to the phase change of Ag NPs in bulk with larger particles, and more intense peak found at 350 °C refers to the sensing response for Ag NPs with smaller size. Also, the reason for the presence of two response peaks may be that carbon reacts with oxygen at the lower peak, while silver reacts with oxygen at the higher peak., since 2nd annealing process haven't been done after depositing of Ag NPs on WO₃ sensor, so that the possibility of carbon contamination has not been ruled out. A relative humidity level of 85% is used to simulate sensor stability in extreme conditions.

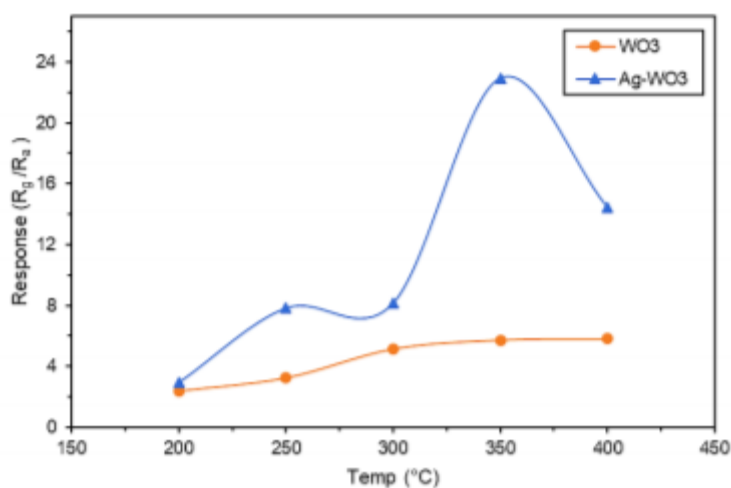


Figure 6.1 Response of undecorated and Ag@WO₃ sensor to 20% O₂ as a function of operating temperature

The change in resistance of both WO₃ and Ag@WO₃ sensors toward O₂ concentration ranging from 0 to 20 % at 85 % RH is shown in Figure 6.2. Both sensors resistance increased upon exposure to O₂ and decreased again in the presence of pure N₂. Ag@WO₃ sensor showed a lower baseline resistance, in the range of 10³ to 10⁴ Ω, in comparison to an undecorated WO₃ sensor at 10⁵ to 10⁶ Ω.

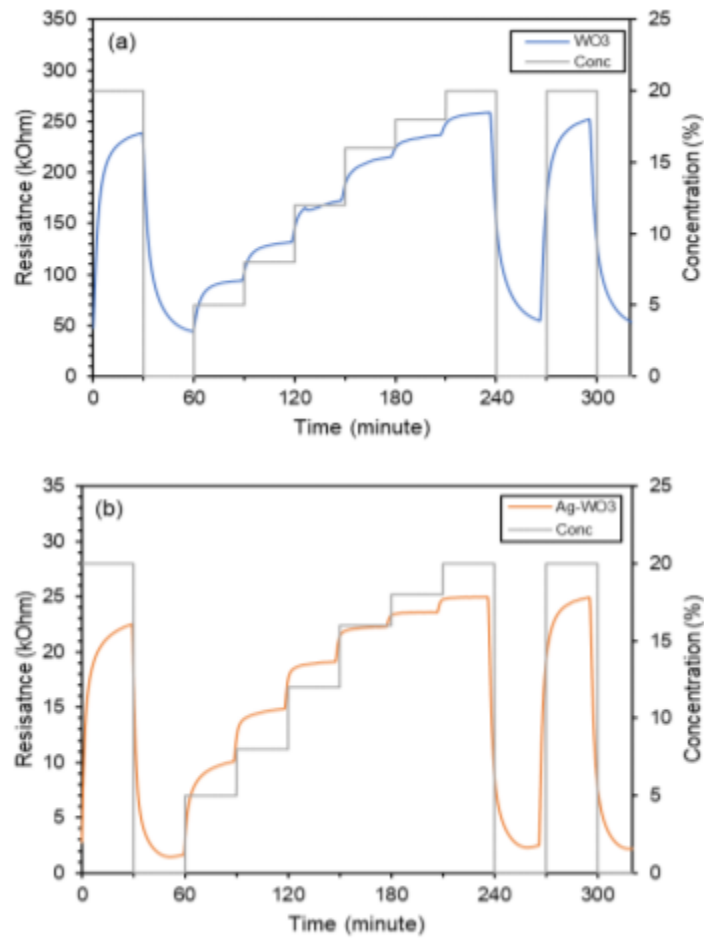


Figure 6.2 Sensor resistance changes of (a) WO_3 sensor and (b) $\text{Ag}/\text{Ag}_2\text{O}@/\text{WO}_3$ sensor to various O_2 concentration at 85% RH.

The response and recovery times were examined at 20% O_2 for WO_3 and $\text{Ag}/\text{Ag}_2\text{O}@/\text{WO}_3$ sensors, as shown in Figure 6.3. The results reveal that increasing the operating temperature gradually reduced the response and recovery time. A complete recovery of the baseline was observed at 9 and at 13.7 minutes for $\text{Ag}/\text{Ag}_2\text{O}@/\text{WO}_3$ and WO_3 sensors, respectively. In all, $\text{Ag}/\text{Ag}_2\text{O}@/\text{WO}_3$ sensor showed a faster response and recovery time in all temperature ranges.

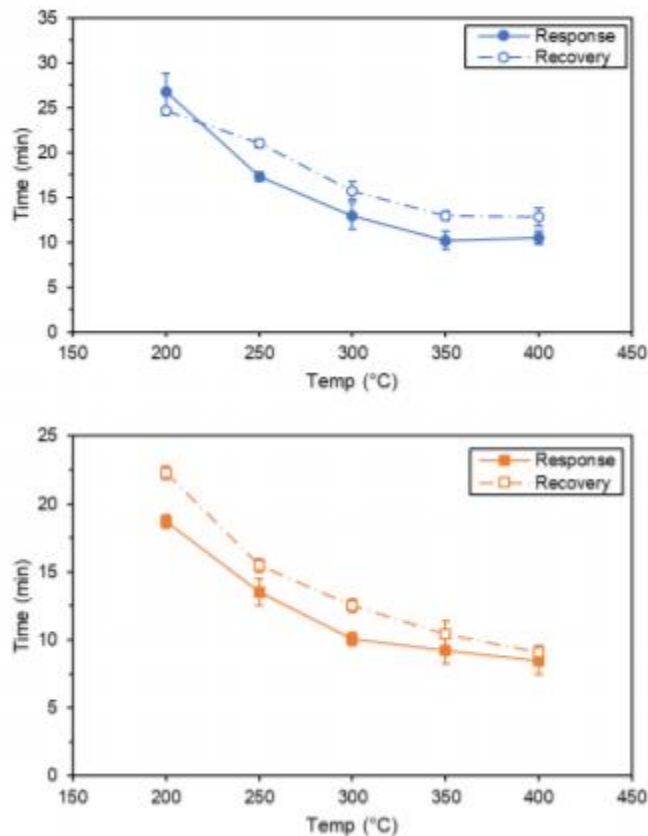


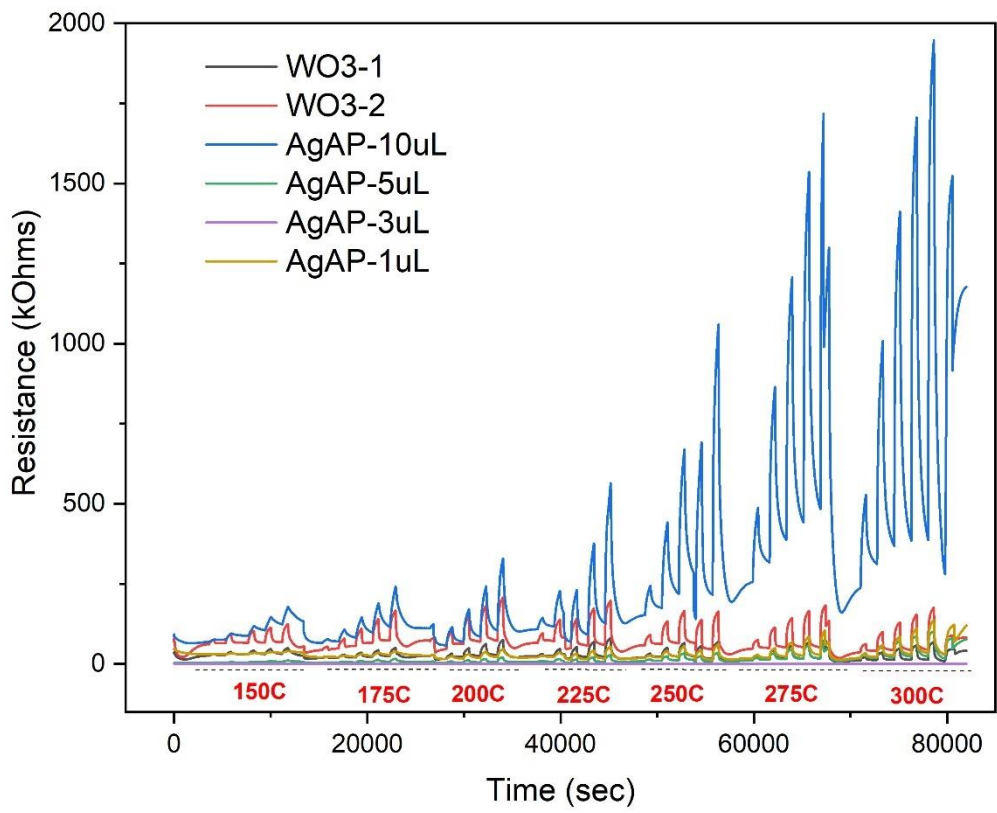
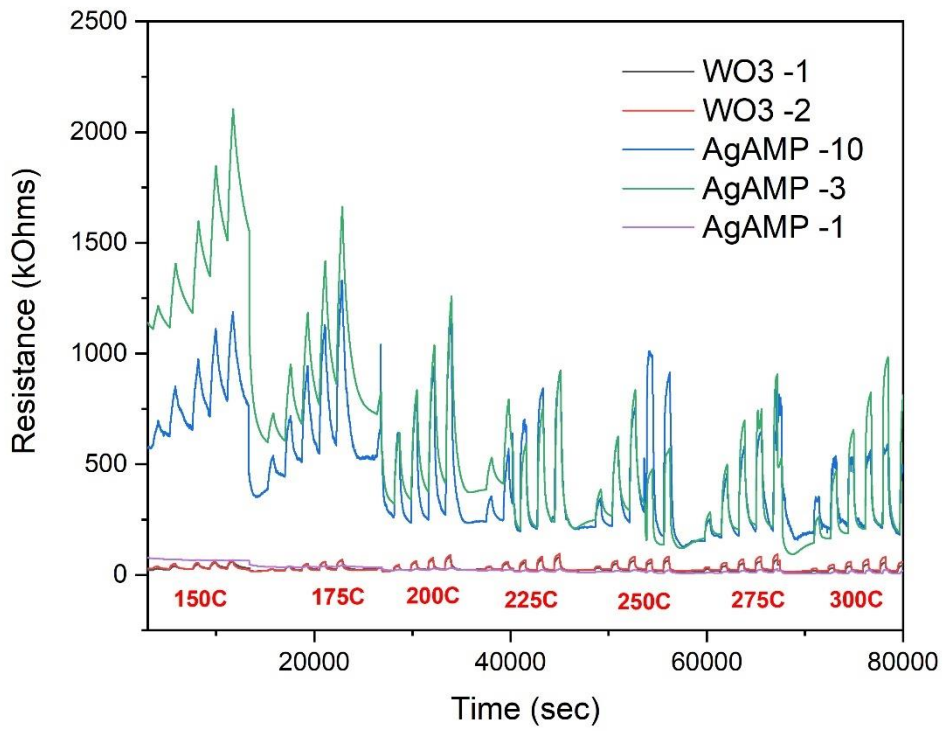
Figure 6.3 Response and recovery time of (a) WO₃ and (b) Ag@WO₃ sensors at various operating temperature.

6.2 Gas sensing response of Ag@WO₃ by using organometallic Ag precursors

The Ag@WO₃ sensors were made in a two-step synthesis by using a plain WO₃ sensor made in a one-step synthesis (using 0.06 g W(CO)₆ at 375 °C under a flow of nitrogen of 300 sccm followed by annealing in air at 500 °C for 2 h as described in Chapter 3.2.2) *via* AACVD and decorating with Ag NPs by using different amounts of three organometallic silver precursors (Ag-AP, Ag-EA and Ag-AMP deposited at 275 °C under a flow of 170 sccm nitrogen as described in Chapter 5.2.3.) also, *via* AACVD. Unfortunately, some sensors did not successfully pass the sensing tests due to suffering from some terminal problems (not possible to measure a resistance through sensor, heater or both), which were Ag-AMP 5μL, Ag-AP 3μL and Ag-EA 1 and 10 μL

sensors.

Gas sensing tests were carried out to different oxygen concentrations ranging between 0% to 20% (200,00 ppm) in ambient environment (~ 50% RH) for all undecorated and silver-decorated WO_3 sensors at operating temperatures ranging between 150 and 300 °C with an interval of 25 °C to examine their sensing properties. The change in resistance of all Ag-AMP@ WO_3 , Ag-EA@ WO_3 , Ag-Ap@ WO_3 and undecorated WO_3 sensors toward various O_2 concentration (1-5-10-15-20%) is shown in Figure 6.4. Similar to the results shown in Figure 6.2, all sensors resistance increased upon exposure to O_2 (an oxidising gas) while reduced when subsequently exposed to N_2 , indicating an n-type semiconductor behaviour. In contrast to the result observed for the Ag@ WO_3 sensors decorated using $\text{Ag}(\text{NO}_3)$, where a lower resistance was observed in the decorated sensor as compared to an undecorated WO_3 sensor, the resistance of the sensors decorated using organometallic silver precursors increased dramatically as the amount of silver precursor used increased. For the smallest amount of Ag precursor solution used (1 μL) an identical change in resistance was observed compared to an undecorated WO_3 sensor when exposed to various O_2 concentrations at different operating temperatures. Resistance values significantly increased for precursor loading greater than 3 μL . The largest resistance change was observed for 10 μL Ag-AP@ WO_3 to 20% O_2 at an operating temperature of 300 °C. As shown in Figure 6.4 below, it is obvious to see that the gas sensitivity of Ag metal decorated WO_3 sensor is much higher than the gas sensitivity obtained the plain WO_3 sensor. From the Figure 6.4 (c), it is clear that the 3 ul loading of AgEA gives the highest gas sensing response and 1 ul sample did not show any resistance change which might be because of a short circuit.



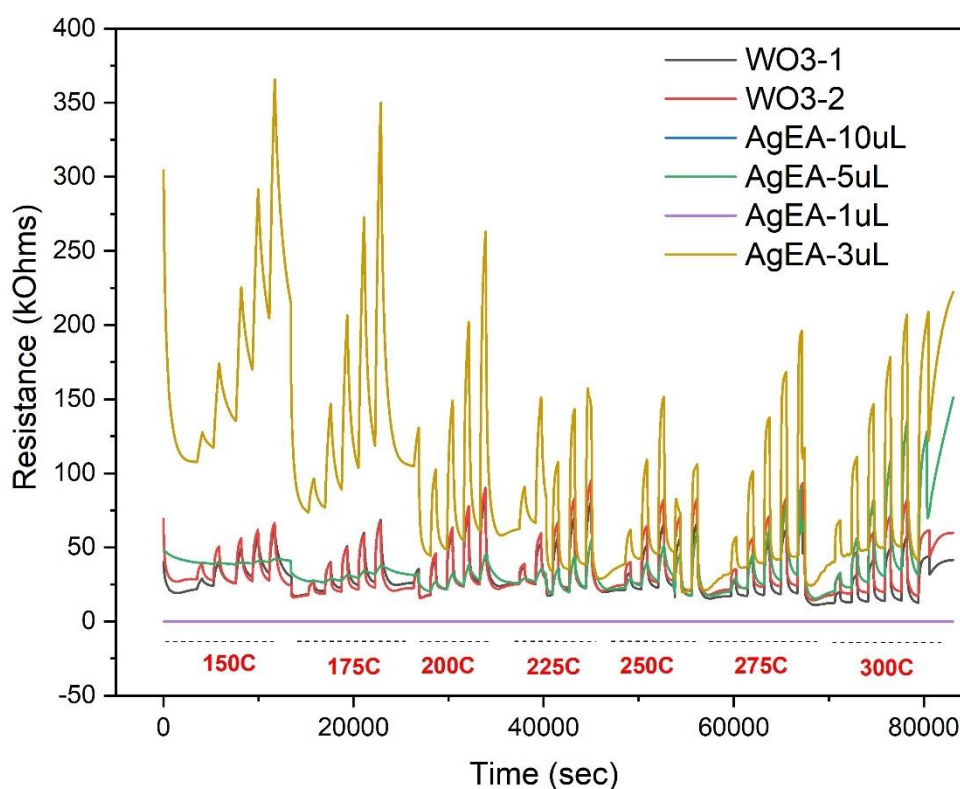


Figure 6.4 Sensor resistance changes of (a) Ag-AMP@WO₃ sensors, (b) Ag-AP@WO₃ sensors and (c) Ag-EA@WO₃ sensors to various O₂ concentration (1-5-10-15-20 %) at different operating temperatures ranging from 150 to 300 °C with an undecorated WO₃ for comparison

The resistance of Ag-AMP 3 μ L@WO₃ to various temperature (150-175-200-225-250-275-300 °C) and O₂ concentration (1-5-10-15-20 %) is shown in Figure 6.5. A big shift in the baseline resistance was found at temperature 150 and 175 °C with increasing of the O₂ concentration, while it tended to get stable after 200 °C. This phenomenon might happen because of the carbon contamination of the sample due to the un-annealing of the 2nd deposition. Once the carbon was all reacted, the baseline resistance tends to get stable. Or it could be attributed due to the insufficient initial setting time for letting the sensor to reach its' baseline resistance. The baseline resistance for Ag-AMP@WO₃ sensors is much higher than the undecorated one's might due to that Ag acts as an electron reservoir which attracts the electrons in hetero-structure Ag@WO₃ from WO₃²²⁸, therefore changing its' conductance.

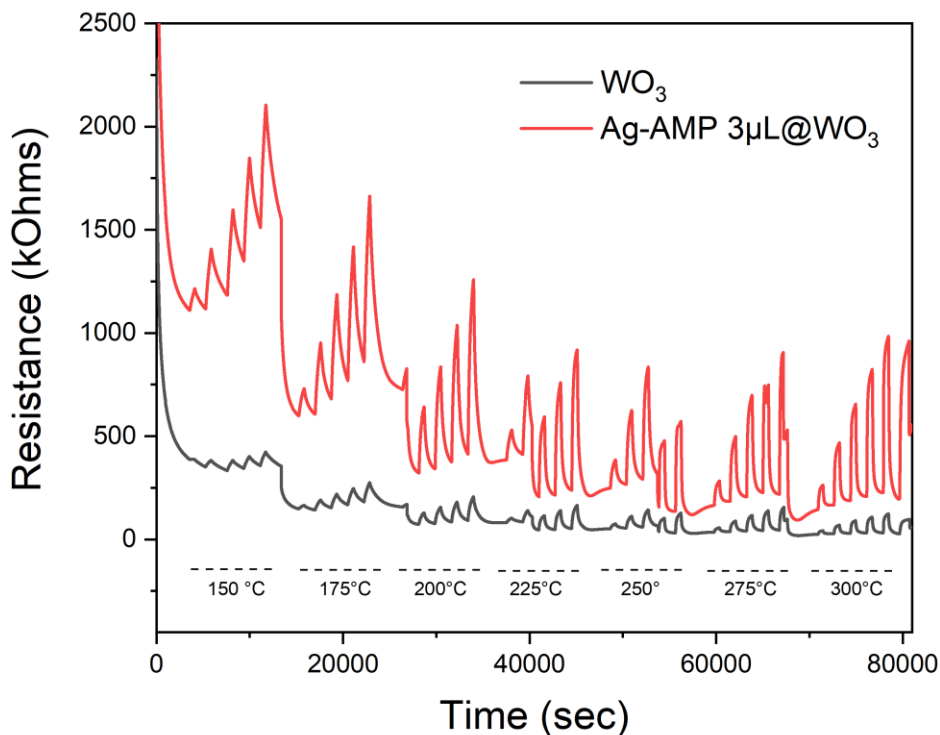


Figure 6.5 Sensor resistance changes of WO_3 sensor and $Ag-AMP\ 3\mu L@WO_3$ sensor to various O_2 concentration (1-5-10-15-20 %) and temperature (150-175-200-225-250-275-300 °C) in ambient environment (~50 % RH)

As shown in Figure 6.6, the response of $Ag-AMP\ 3\mu L@WO_3$ and WO_3 to different operating temperature under max O_2 concentration (20 %) were put together for comparison. From 150 to 250 °C, both sensor shown an increasing in the sensing response with the increase of the setting temperature. While for WO_3 sensor, the highest sensing response was found at 250 °C with a response of 4, which is similar to the result given by $Ag-AMP\ 3\mu L@WO_3$. After 250°C, Ag decorated sensor still shown a growth trend of response and with a highest response of 4.4. However, for the response decreased afterwards, it is different as compared to the WO_3 response in Figure 6.1.

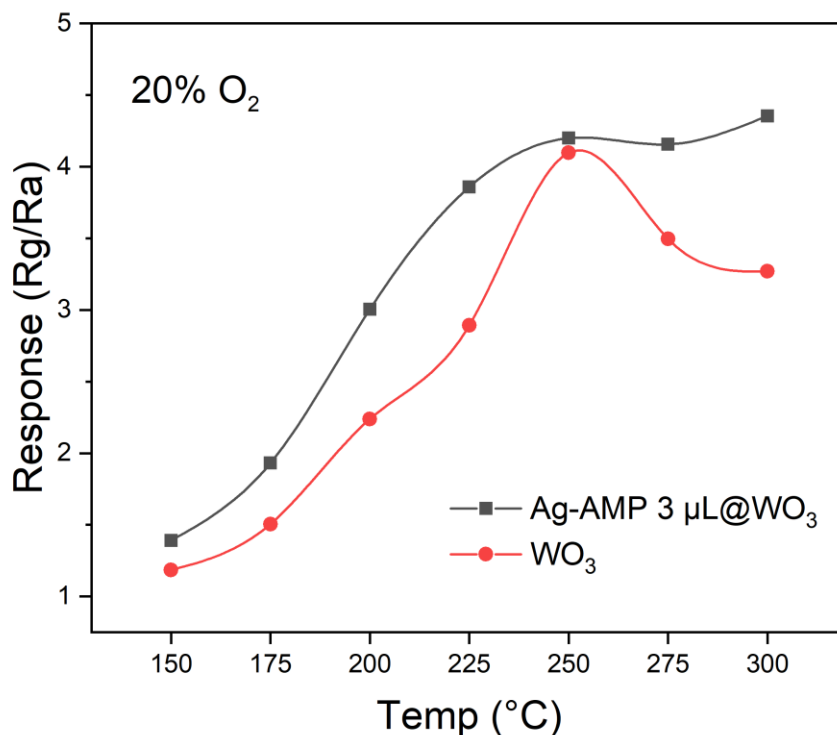


Figure 6.6 Response of WO₃ and Ag-AMP 3μL@WO₃ sensor to 20% O₂ as a function of operating temperature

The resistance of Ag-AP 10μL@WO₃ to various temperature (150-175-200-225-250-275-300 °C) and O₂ concentration (1-5-10-15-20 %) was shown in Figure 6.7. The starting baseline resistance were found to similar for both sensors. While for the Ag decorated sensor, resistance change significantly after 225 °C within the increase of the O₂ concentration and also the baseline resistance was found not to be stable throughout the whole process.

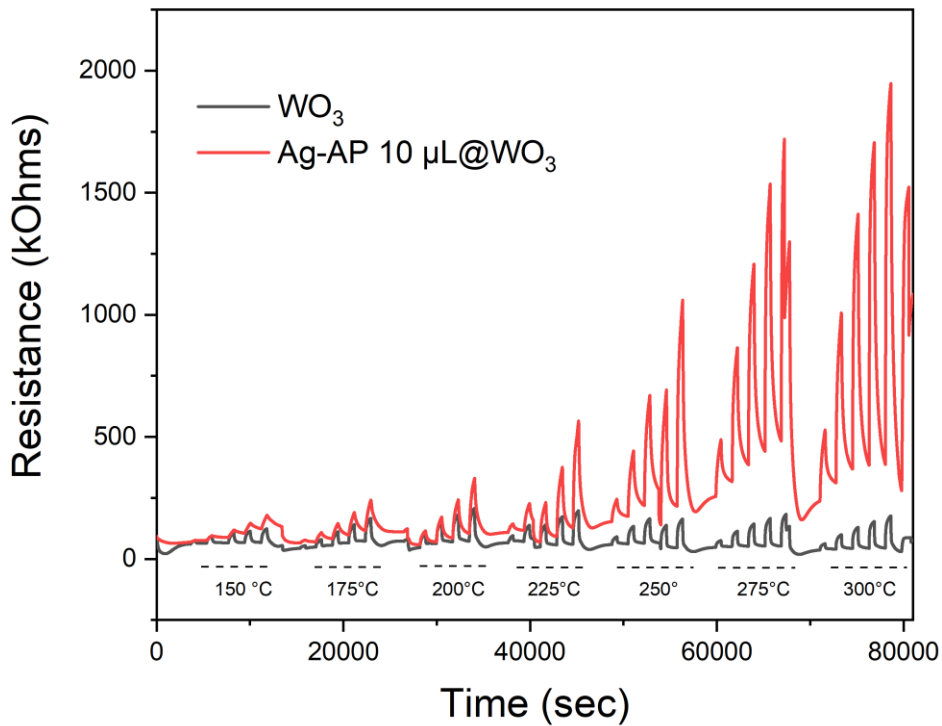


Figure 6.7 Sensor resistance changes of WO_3 sensor and $Ag-AP\ 10\ \mu L@WO_3$ sensor to various O_2 concentration (1-5-10-15-20 %) and temperature (150-175-200-225-250-275-300 °C) in ambient environment (~50 % RH)

The gas response curve of WO_3 in shown in Figure 6.8 was found to be similar to the one in Figure 6.1, with a maximum response value of 4 at 300 °C. While the maximum response value of 5 was found at 240 °C for the $Ag-AP$ decorated sensor. It is worth noting that curve increased dramatically between 275 and 300 °C for Ag loaded sensor, which may indicate a higher sensor response value may get for higher operating temperature, which was matched with the trend shown in Figure 6.1 of $Ag@WO_3$ sensor, with a 2nd maximum response value at 350 °C.

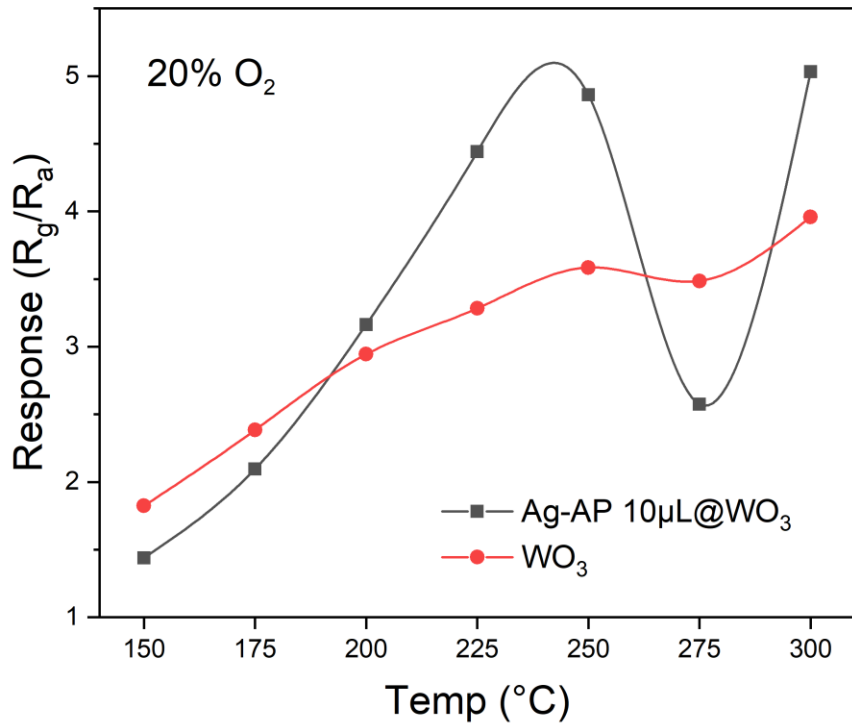


Figure 6.8 Response of WO₃ and Ag-AP 10µL@WO₃ sensor to 20% O₂ as a function of operating temperature

The resistance of Ag-EA 3µL@WO₃ to various temperature (150-175-200-225-250-275-300 °C) and O₂ concentration (1-5-10-15-20 %) was shown in Figure 6.9. The same as Figure 6.5, baseline resistance shifted a lot for Ag decorated sensor at temperature 150 and 175 °C and it tended to get stable afterwards. The maximum resistance is much lower than the other two Ag-AMP and Ag-AP decorated sensor.

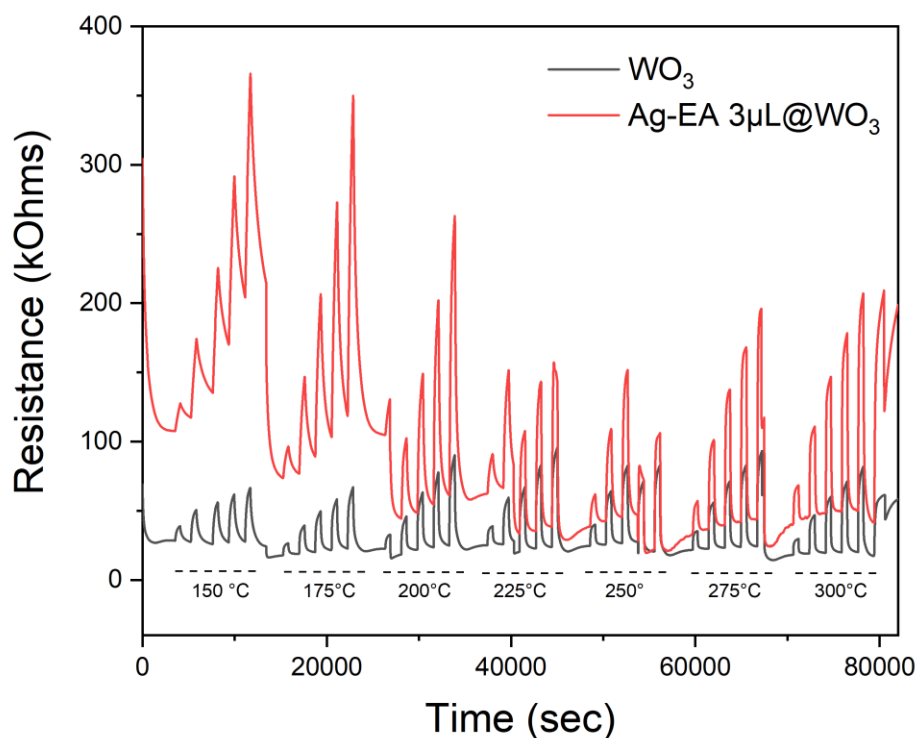


Figure 6.9 Sensor resistance changes of WO_3 sensor and $Ag-EA\ 3\mu L@WO_3$ sensor to various O_2 concentration (1-5-10-15-20 %) and temperature (150-175-200-225-250-275-300 °C) in ambient environment (~50 % RH)

As shown in Figure 6.10, two max response peaks were found with response value of 4.4 and 4.7 at 200 and 250 °C, respectively, which is identical to the result shown in Figure 6.1. But both peaks shift to lower operating temperature, which may indicate that the size of Ag NPs for $Ag-EA@WO_3$ is larger than the Ag NPs size when used $AgNO_3$ as the precursor. For all organometallic $Ag@WO_3$ sensors, the response is not that noticeable as compared to the $Ag@WO_3$ when using $AgNO_3$ as the precursor.

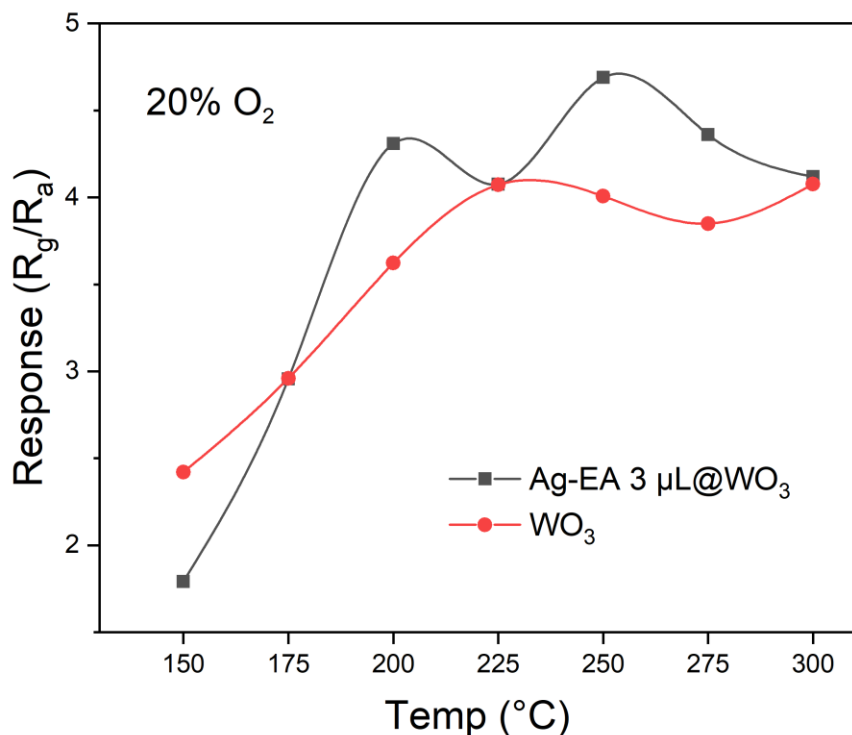


Figure 6.10 Response of WO₃ and Ag-EA 3 μL@WO₃ sensor to 20% O₂ as a function of operating temperature

6.4 Inferred sensing ‘mechanism’

6.4.1 AgNO₃ (Ag@WO₃ sensor)

The addition of Ag NPs on WO₃ improved sensor performance as well as lower the optimum operating temperature. The role of catalyst particles in sensitising semiconducting metal oxides has been discussed in the context of two mechanisms, i.e. chemical and electronic sensitisation³². In chemical sensitization, Ag₂O nanoparticles could facilitate the chemical reactions and hence increase the rate of reaction between the tungsten oxide surface and oxygen molecules *via* a spill-over-type mechanism^{32,46}.

Electronic sensitisation occurs through direct electronic interaction between the silver oxide and the tungsten oxide surface. It is proposed that upon contact, the Ag₂O nanoparticles will exchange electrons with WO₃. The data found in literature showed

6.4.2 Organometallic Ag precursors (Ag@WO₃ sensor)

Similar to the sensitization mentioned above, by adding Ag nanoparticles (NPs) on the tungsten oxide surface, the possible contribution in sensitivity to oxygen can be ascribed to the function of electronic sensitization derived from the interface between Ag NPs and WO₃ surface and the effect of chemical sensitization of Ag NPs (spill-over effect). The data found in literature showed a relative low work function of Ag (4.26 eV) and a high work function of WO₃ (5.1 eV)²¹⁹, resulting in electrons transferring from Ag NPs to n-type semiconductor WO₃ (electronic sensitisation) in order to equalize the Fermi levels, as shown in Figure 6.11, which would lead to a decrease in baseline resistance. Conversely, under chemical sensitisation more oxygen molecules can be adsorbed on the Ag-WO₃ surface through a spillover-type mechanism, leading to a large change in the thickness of the electron depletion layer, which will increase the baseline resistance. The net dramatic increase in the baseline resistance indicated that the spill-over effect is more dominant (increases baseline resistance) here than electronic sensitization (decreases baseline resistance). What's more, Ag NPs might tend to form Ag₂O on exposure to O₂ over the surface. Under higher temperature above the decomposition temperature, which around 180 °C Ag₂O tends to decompose and forms Ag and O₂. After gas sensing tests, the XPS shows the metallic form of Ag spectra which means that the reaction is reversible. At lower temperature, it should be Ag₂O and at high temperature it should be Ag. The measurement is done at low T. However, the form of the silver is function of both temperature and pO₂. A strong electron depletion layer will be produced as electrons will be captured from the WO₃ surface, contributing to a resistance change²¹⁹, as shown in Figure 6.12, which were observed experimentally as well.

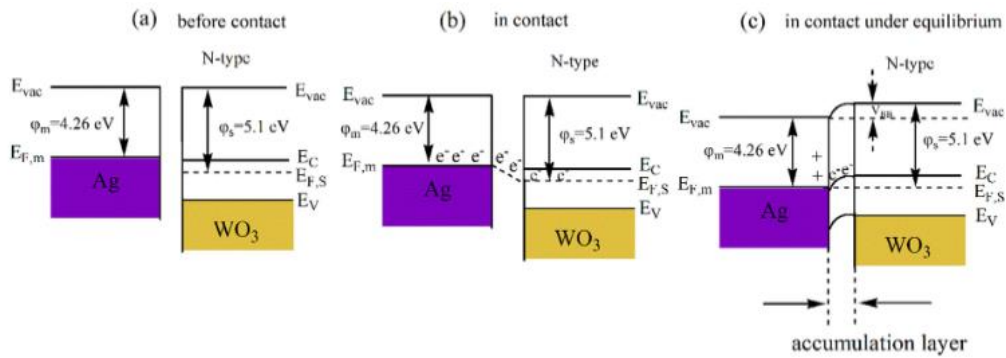


Figure 6.11 Energy band structure schematic diagrams of Ag and n-type WO₃ semiconductors (a) before contact (b) in contact and (c) Ag-WO₃ M-S junction²²⁰

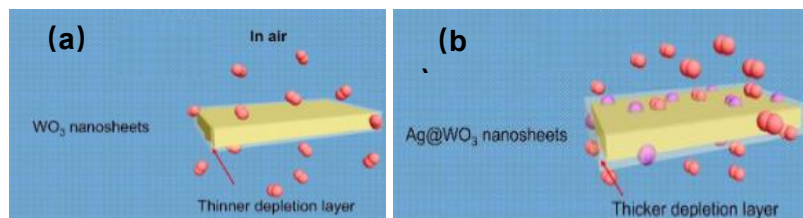


Figure 6.12 Schematic model of depletion layer for (a) undecorated WO₃ nanosheets and (b) Ag decorated WO₃ nanosheets when exposure in air(O₂)²²⁰

6.5 Conclusion

The gas sensing results revealed that the decoration of Ag NPs on WO₃ sensor substrate, which significantly enhanced the sensor sensitivity by 400% and lower the optimum operating temperature from 400 to 350 °C. Ag@WO₃ sensor showed a faster response and recovery time in all temperature ranges as compared to undecorated WO₃ sensor. In both cases, the decoration of Ag NPs is proposed to lower the baseline resistance with the transferring of electrons from Ag to WO₃. However, a dramatically increasing in baseline resistance on adding Ag nanoparticles to WO₃, which might be ascribed as Ag enrich WO₃ with more oxygen species that overcomes the resistance reduced by the electronic exchange between Ag and WO₃. The reasons for the observed enhancement in the sensing response towards oxygen are not possible to extract from the data although possible gas sensing ‘mechanisms’ for both sets of

sensors have been inferred in the context of chemical and electronic sensitizations. Further development and investigation on sensor selectivity, stability and cross-sensitivity to other gases still need to be studied in the future to make Ag@WO₃ based materials a potential oxygen gas sensor. Under higher temperature above the decomposition temperature, which around 180 °C Ag₂O starts to decompose and forms Ag and O₂. After gas sensing tests, the XPS shows the metallic form of Ag spectra which means that the reaction is reversible. The 10 ul loading of Ag-AP gives the highest gas sensing response.

Chapter 7 Conclusion and future work

7.1 Conclusions

In summary, Ag nanoparticles (NPs) decorated WO₃ nanoneedles (NNs) thin film were successfully synthesized on glass, quartz and alumina substrates via Aerosol-assisted chemical vapour deposition (AACVD) technique. The optimal conditions were applied to the alumina sensor platform. Optimal reaction conditions were obtained after a series experiment by adjusting the deposition parameters, and finally its' gas sensing sensitivity tests towards oxygen gas have been examined.

WO_{3-x} and WO₃ AA NNs thin film has been conducted in a single-step synthesis *via* AACVD. After carrying out a series of deposition experiments on various substrates, including glass, quartz and alumina, SEM images revealed that the surface morphology of as-deposited WO₃ NNs wasn't affected by the substrates. XRD analysis showed a combination of triclinic phase Na₂W₄O₁₃ and hexagonal phase WO₃ when using glass as the substrate, which can be ascribed as the migration of sodium ions from surface of the glass substrate into the unit cell of WO₃ at high temperature during annealing process. Subsequently, WO₃ NNs thin film was finally deposited onto an alumina sensor platform under the optimal deposition condition.

The fabrication of Ag NPs decorated WO₃ NNs was successfully achieved on an alumina sensor platform in a two-step synthesis method *via* AACVD by using AgNO₃ as the precursor at the beginning. Due to the relatively low amount and small size of the silver particles, XRD showed no Ag peaks. The SEM images and XPS analysis indicated the formation of NaNO₃ during the deposition process. TEM images revealed the formation of a oxidised silver NPs on WO₃ NNs. Since nitrate group might affect the surface morphologies of WO₃ NNs structures, three organometallic silver metal precursor solutions were subsequently used, including silver 2-aminoethanol (Ag-EA), silver 1-aminopropan-2-ol (Ag-AP) and silver 2-methyl-2-aminopropan-1-ol (Ag-AMP).

Characterizations demonstrated the formation of only metallic Ag NPs on WO₃ NNs, with diameter in a range of 9 to 13 nm.

Gas sensing sensitivity results toward oxygen gas revealed that the decoration of both Ag NPs on WO₃ AA would significantly improve the sensors performance by 400% and lower the optimum operating temperature when using AgNO₃ as the Ag precursor. While for organometallic Ag precursors decorated WO₃ sensor, no significant enhancement was found in the sensing response as compared to the bare WO₃. Gas sensing mechanisms for both sensors have been explored, on the basis of chemical and electronic sensitizations.

7.2 Future work

1. Further development and investigation on sensor selectivity, stability and cross-sensitivity to other gases still need to be studied in the future to make Ag@WO₃ based materials a potential oxygen gas sensor.
2. Figure out the reason to cause to the formation of NaNO₃ by using AgNO₃ as precursor
3. Using AgNO₃ to make a bare Ag deposited sensor to compare with other sensors
4. Investigate if the deposition time would control the size of the Ag NPs formation and further improve sensing response towards oxygen gas
5. Investigate the sensing properties of Ag NPs decorated on 2-D, 3-D WO₃ microstructures and other noble such as Gold, aluminum metal decorated 1-D, 2-D, 3-D WO₃ for oxygen gas response
6. Further analysis and collected gas sensors after testing need to be further studied and re-analysed in order to figure out either metallic Ag NPs or Ag₂O metal oxide that deposited on the sensor, which including XPS and HR-TEM
7. Measure the particle size of the silver nanoparticles and control it more precisely in order to minimise the possibility of two peaks observed in the sensing graph
8. Control the amount of Ag loading on WO₃ sensors by altering the reaction

conditions such as initially amount of precursor used to achieve a similar loading of 0.5, 1 and 2 wt% loading of Ag/W and compare with the literature for gas sensing performance

9. XRD mapping for all samples need to be carried out in the future to clearly check whether the deposition gives a uniform coverage on the substrate
10. A second annealing process need to be conducted after depositing Ag NPs on WO_3 thin films, due to the presence of contaminants carbon residue left in the sample might react with the oxygen gas to generate a peak as a sensing response.
11. Higher sensing operation temperature ($>300\text{ }^\circ\text{C}$) is required for the organometallic Ag decorated WO_3 gas sensors. As for AP and EA, the sensing response still shown an enhancement trend with the increasing of temperature.

REFERENCE

- 1 S. Zampolli, I. Elmi, F. Ahmed, M. Passini, G. C. Cardinali, S. Nicoletti and L. Dori, An electronic nose based on solid state sensor arrays for low-cost indoor air quality monitoring applications, *Sensors Actuators B Chem.*, 2004, **101**, 39–46.
- 2 C.-P. Xie, Y. Li and M.-J. Lan, Thermal desorption-gas chromatography/mass spectrometric analysis of volatile organic compounds emitted from automobile chair in thermal condition, *Chin. J. Anal. Chem.*, 2011, **39**, 265–268.
- 3 A. A. Tomchenko, G. P. Harmer, B. T. Marquis and J. W. Allen, Semiconducting metal oxide sensor array for the selective detection of combustion gases, *Sensors Actuators B Chem.*, 2003, **93**, 126–134.
- 4 S. M. Kanan, O. M. El-Kadri, I. A. Abu-Yousef and M. C. Kanan, Semiconducting metal oxide based sensors for selective gas pollutant detection, *Sensors*, 2009, **9**, 8158–8196.
- 5 H. Zheng, J. Z. Ou, M. S. Strano, R. B. Kaner, A. Mitchell and K. Kalantar-zadeh, Nanostructured tungsten oxide—properties, synthesis, and applications, *Adv. Funct. Mater.*, 2011, **21**, 2175–2196.
- 6 Y. B. Li, Y. Bando, D. Golberg and K. Kurashima, WO₃ nanorods/nanobelts synthesized via physical vapour deposition process, *Chem. Phys. Lett.*, 2003, **367**, 214–218.
- 7 B. Li and Y. Wang, Facile synthesis and enhanced photocatalytic performance of flower-like ZnO hierarchical microstructures, *J. Phys. Chem. C*, 2009, **114**, 890–896.
- 8 J.-H. Lee, Gas sensors using hierarchical and hollow oxide nanostructures: overview, *Sensors Actuators B Chem.*, 2009, **140**, 319–336.
- 9 A.-M. Gurban, D. Burtan, L. Rotariu and C. Bala, Manganese oxide based screen-printed sensor for xenoestrogens detection, *Sensors Actuators B Chem.*, 2015, **210**, 273–280.

- 10 Ü. Özgür, Y. I. Alivov, C. Liu, A. Teke, Ma. Reshchikov, S. Doğan, V. Avrutin, S.-J. Cho and H. Morkoç, A comprehensive review of ZnO materials and devices, *J. Appl. Phys.*, 2005, **98**, 11.
- 11 S. Dutta and B. N. Ganguly, Characterization of ZnO nanoparticles grown in presence of Folic acid template, *J. Nanobiotechnology*, 2012, **10**, 29.
- 12 A. S. Arico, P. Bruce, B. Scrosati, J.-M. Tarascon and W. Van Schalkwijk, in *Materials for sustainable energy: a collection of peer-reviewed research and review articles from Nature Publishing Group*, World Scientific, 2011, pp. 148–159.
- 13 W. Ouyang, F. Teng, J. He and X. Fang, Enhancing the Photoelectric Performance of Photodetectors Based on Metal Oxide Semiconductors by Charge-Carrier Engineering, *Adv. Funct. Mater.*, 2019, **29**, 1807672.
- 14 S.-Y. Lee, X. Gao and H. Matsui, Biomimetic and aggregation-driven crystallization route for room-temperature material synthesis: growth of β -Ga₂O₃ nanoparticles on peptide assemblies as nanoreactors, *J. Am. Chem. Soc.*, 2007, **129**, 2954–2958.
- 15 A. Margaryan, Prospects of using germanium-dioxide-based glasses for optics.
- 16 Y. Wang, T. Wu, Y. Zhou, C. Meng, W. Zhu and L. Liu, TiO₂-based nanoheterostructures for promoting gas sensitivity performance: designs, developments, and prospects, *Sensors*, 2017, **17**, 1971.
- 17 L. Zhu and W. Zeng, Room-temperature gas sensing of ZnO-based gas sensor: A review, *Sensors Actuators A Phys.*, 2017, **267**, 242–261.
- 18 H. Long, W. Zeng and H. Zhang, Synthesis of WO₃ and its gas sensing: a review, *J. Mater. Sci. Mater. Electron.*, 2015, **26**, 4698–4707.
- 19 H. Yun, B. Park, Y. C. Choi, J. Im, T. J. Shin and S. Il Seok, Efficient Nanostructured TiO₂/SnS Heterojunction Solar Cells, *Adv. Energy Mater.*, 2019, **9**, 1901343.
- 20 L. Petitjean, R. Gagne, E. S. Beach, D. Xiao and P. T. Anastas, Highly selective hydrogenation and hydrogenolysis using a copper-doped porous metal oxide

- catalyst, *Green Chem.*, 2016, **18**, 150–156.
- 21 A. Lueking and R. T. Yang, Hydrogen spillover from a metal oxide catalyst onto carbon nanotubes—implications for hydrogen storage, *J. Catal.*, 2002, **206**, 165–168.
- 22 U. Nerle and M. K. Rabinal, Thermal oxidation of copper for favorable formation of cupric oxide (CuO) semiconductor, *IOSR J. Appl. Phys.*, 2013, **5**, 1–7.
- 23 W. H. Brattain and J. Bardeen, Surface properties of germanium, *Bell Syst. Tech. J.*, 1953, **32**, 1–41.
- 24 W. H. Brattain and C. G. B. Garrett, Surface properties of semiconductors, *Physica*, 1954, **20**, 885–892.
- 25 Cgb. Garrett and W. H. Brattain, Physical theory of semiconductor surfaces, *Phys. Rev.*, 1955, **99**, 376.
- 26 N. Taguchi, 1971.
- 27 T. Seiyama and S. Kagawa, Study on a Detector for Gaseous Components Using Semiconductive Thin Films., *Anal. Chem.*, 1966, **38**, 1069–1073.
- 28 T. Seiyama, A. Kato, K. Fujiishi and M. Nagatani, A new detector for gaseous components using semiconductive thin films., *Anal. Chem.*, 1962, **34**, 1502–1503.
- 29 R. Kumar, S. A. Imam and M. R. Khan, A critical review of Taguchi gas sensor for the detection of voc's, *MASAUM J. Rev. Surv.*, 2009, **1**, 177–183.
- 30 A. M. Azad, S. A. Akbar, S. G. Mhaisalkar, L. D. Birkefeld and K. S. Goto, Solid-state gas sensors: A review, *J. Electrochem. Soc.*, 1992, **139**, 3690–3704.
- 31 A. Dey, Semiconductor metal oxide gas sensors: A review, *Mater. Sci. Eng. B*, 2018, **229**, 206–217.
- 32 N. Yamazoe, New approaches for improving semiconductor gas sensors, *Sensors Actuators B Chem.*, 1991, **5**, 7–19.
- 33 M. E. Franke, T. J. Koplín and U. Simon, Metal and metal oxide nanoparticles in chemiresistors: does the nanoscale matter?, *small*, 2006, **2**, 36–50.
- 34 Y. Zhang, L. Guo, L. Tao, Y. Lu and S. Wang, Defect-Based Single-Atom

- Electrocatalysts, *Small Methods*, 2019, **3**, 1800406.
- 35 L. Zhang, Q. Fang, Y. Huang, K. Xu, P. K. Chu and F. Ma, Oxygen vacancy enhanced gas-sensing performance of CeO₂/graphene heterostructure at room temperature, *Anal. Chem.*, 2018, **90**, 9821–9829.
- 36 N. Zhang, C. Gao and Y. Xiong, Defect engineering: A versatile tool for tuning the activation of key molecules in photocatalytic reactions, *J. Energy Chem.*, 2019, **37**, 43–57.
- 37 S. R. Morrison, Selectivity in semiconductor gas sensors, *Sensors and actuators*, 1987, **12**, 425–440.
- 38 M. Paulose, O. K. Varghese, G. K. Mor, C. A. Grimes and K. G. Ong, Unprecedented ultra-high hydrogen gas sensitivity in undoped titania nanotubes, *Nanotechnology*, 2005, **17**, 398.
- 39 N. Barsan and U. Weimar, Conduction model of metal oxide gas sensors, *J. electroceramics*, 2001, **7**, 143–167.
- 40 N. Yamazoe, G. Sakai and K. Shimano, Oxide semiconductor gas sensors, *Catal. Surv. from Asia*, 2003, **7**, 63–75.
- 41 H.-J. Kim and J.-H. Lee, Highly sensitive and selective gas sensors using p-type oxide semiconductors: Overview, *Sensors Actuators B Chem.*, 2014, **192**, 607–627.
- 42 D. Degler, U. Weimar and N. Barsan, Current Understanding of the Fundamental Mechanisms of Doped and Loaded Semiconducting Metal-Oxide-Based Gas Sensing Materials, *ACS sensors*, 2019, **4**, 2228–2249.
- 43 N. Bârsan, M. Hübner and U. Weimar, Conduction mechanisms in SnO₂ based polycrystalline thick film gas sensors exposed to CO and H₂ in different oxygen backgrounds, *Sensors Actuators B Chem.*, 2011, **157**, 510–517.
- 44 K. Wetchakun, T. Samerjai, N. Tamaekong, C. Liewhiran, C. Siriwong, V. Kruefu, A. Wisitsoraat, A. Tuantranont and S. Phanichphant, Semiconducting metal oxides as sensors for environmentally hazardous gases, *Sensors Actuators B Chem.*, 2011, **160**, 580–591.

- 45 A. Wei, L. Pan and W. Huang, Recent progress in the ZnO nanostructure-based sensors, *Mater. Sci. Eng. B*, 2011, **176**, 1409–1421.
- 46 C. Wang, L. Yin, L. Zhang, D. Xiang and R. Gao, Metal oxide gas sensors: sensitivity and influencing factors, *Sensors*, 2010, **10**, 2088–2106.
- 47 C. L. Zhu, Y. J. Chen, R. X. Wang, L. J. Wang, M. S. Cao and X. L. Shi, Synthesis and enhanced ethanol sensing properties of α -Fe₂O₃/ZnO heteronanostructures, *Sensors Actuators B Chem.*, 2009, **140**, 185–189.
- 48 J. Zhang, X. Liu, L. Wang, T. Yang, X. Guo, S. Wu, S. Wang and S. Zhang, Synthesis and gas sensing properties of α -Fe₂O₃@ ZnO core–shell nanospindles, *Nanotechnology*, 2011, **22**, 185501.
- 49 W. J. Moon, J. H. Yu and G. M. Choi, The CO and H₂ gas selectivity of CuO-doped SnO₂–ZnO composite gas sensor, *Sensors Actuators B Chem.*, 2002, **87**, 464–470.
- 50 D. Barreca, E. Comini, A. P. Ferrucci, A. Gasparotto, C. Maccato, C. Maragno, G. Sberveglieri and E. Tondello, First example of ZnO– TiO₂ nanocomposites by chemical vapour deposition: structure, morphology, composition, and gas sensing performances, *Chem. Mater.*, 2007, **19**, 5642–5649.
- 51 L. Wang, Y. Kang, Y. Wang, B. Zhu, S. Zhang, W. Huang and S. Wang, CuO nanoparticle decorated ZnO nanorod sensor for low-temperature H₂S detection, *Mater. Sci. Eng. C*, 2012, **32**, 2079–2085.
- 52 X. Yu, G. Zhang, H. Cao, X. An, Y. Wang, Z. Shu, X. An and F. Hua, ZnO@ ZnS hollow dumbbells–graphene composites as high-performance photocatalysts and alcohol sensors, *New J. Chem.*, 2012, **36**, 2593–2598.
- 53 A. Kusior, M. Radecka, M. Rekas, M. Lubecka, K. Zakrzewska, A. Reszka and B. J. Kowalski, Sensitization of gas sensing properties in TiO₂/SnO₂ nanocomposites, *Procedia Eng.*, 2012, **47**, 1073–1076.
- 54 C. Liangyuan, B. Shouli, Z. Guojun, L. Dianqing, C. Aifan and C. C. Liu, Synthesis of ZnO–SnO₂ nanocomposites by microemulsion and sensing properties for NO₂, *Sensors Actuators B Chem.*, 2008, **134**, 360–366.

- 55 M. Rumyantseva, V. Kovalenko, A. Gaskov, E. Makshina, V. Yuschenko, I. Ivanova, A. Ponzoni, G. Faglia and E. Comini, Nanocomposites SnO₂/Fe₂O₃: sensor and catalytic properties, *Sensors Actuators B Chem.*, 2006, **118**, 208–214.
- 56 B. P. J. de Lacy Costello, R. J. Ewen, N. M. Ratcliffe and P. S. Sivanand, Thick film organic vapour sensors based on binary mixtures of metal oxides, *Sensors Actuators B Chem.*, 2003, **92**, 159–166.
- 57 W. Zeng, T. Liu and Z. Wang, Sensitivity improvement of TiO₂-doped SnO₂ to volatile organic compounds, *Phys. E Low-dimensional Syst. Nanostructures*, 2010, **43**, 633–638.
- 58 J. H. Yu and G. M. Choi, Electrical and CO gas sensing properties of ZnO–SnO₂ composites, *Sensors Actuators B Chem.*, 1998, **52**, 251–256.
- 59 B. P. J. de Lacy Costello, R. J. Ewen, P. R. H. Jones, N. M. Ratcliffe and R. K. M. Wat, A study of the catalytic and vapour-sensing properties of zinc oxide and tin dioxide in relation to 1-butanol and dimethyldisulphide, *Sensors Actuators B Chem.*, 1999, **61**, 199–207.
- 60 B. P. J. de Lacy Costello, R. J. Ewen, N. Guernion and N. M. Ratcliffe, Highly sensitive mixed oxide sensors for the detection of ethanol, *Sensors Actuators B Chem.*, 2002, **87**, 207–210.
- 61 D. R. Miller, S. A. Akbar and P. A. Morris, Nanoscale metal oxide-based heterojunctions for gas sensing: a review, *Sensors Actuators B Chem.*, 2014, **204**, 250–272.
- 62 D. Shaposhnik, R. Pavelko, E. Llobet, F. Gispert-Guirado and X. Vilanova, Hydrogen sensors on the basis of SnO₂-TiO₂ systems, *Procedia Eng.*, 2011, **25**, 1133–1136.
- 63 Y. Hu, X. Zhou, Q. Han, Q. Cao and Y. Huang, Sensing properties of CuO–ZnO heterojunction gas sensors, *Mater. Sci. Eng. B*, 2003, **99**, 41–43.
- 64 S. Aygün and D. Cann, Hydrogen sensitivity of doped CuO/ZnO heterocontact sensors, *Sensors Actuators B Chem.*, 2005, **106**, 837–842.

- 65 Z. Ling and C. Leach, The effect of relative humidity on the NO₂ sensitivity of a SnO₂/WO₃ heterojunction gas sensor, *Sensors Actuators B Chem.*, 2004, **102**, 102–106.
- 66 Q.-H. Xu, D.-M. Xu, M.-Y. Guan, Y. Guo, Q. Qi and G.-D. Li, ZnO/Al₂O₃/CeO₂ composite with enhanced gas sensing performance, *Sensors Actuators B Chem.*, 2013, **177**, 1134–1141.
- 67 Y. Liu, G. Zhu, J. Chen, H. Xu, X. Shen and A. Yuan, Co₃O₄/ZnO nanocomposites for gas-sensing applications, *Appl. Surf. Sci.*, 2013, **265**, 379–384.
- 68 G. Korotcenkov, Metal oxides for solid-state gas sensors: What determines our choice?, *Mater. Sci. Eng. B*, 2007, **139**, 1–23.
- 69 C. W. Na, H.-S. Woo, I.-D. Kim and J.-H. Lee, Selective detection of NO₂ and C₂H₅OH using a Co₃O₄-decorated ZnO nanowire network sensor, *Chem. Commun.*, 2011, **47**, 5148–5150.
- 70 H.-S. Woo, C. W. Na, I.-D. Kim and J.-H. Lee, Highly sensitive and selective trimethylamine sensor using one-dimensional ZnO–Cr₂O₃ hetero-nanostructures, *Nanotechnology*, 2012, **23**, 245501.
- 71 D. Koziej, M. Hübner, N. Barsan, U. Weimar, M. Sikora and J.-D. Grunwaldt, Operando X-ray absorption spectroscopy studies on Pd-SnO₂ based sensors, *Phys. Chem. Chem. Phys.*, 2009, **11**, 8620–8625.
- 72 M. Hübner, D. Koziej, M. Bauer, N. Barsan, K. Kvashnina, M. D. Rossell, U. Weimar and J. Grunwaldt, The Structure and Behavior of Platinum in SnO₂-Based Sensors under Working Conditions, *Angew. Chemie Int. Ed.*, 2011, **50**, 2841–2844.
- 73 M. Labeau, B. Gautheron, F. Cellier, M. Vallet-Regi, E. Garcia and J. M. G. Carbet, Pt nanoparticles dispersed on SnO₂ thin films: a microstructural study, *J. Solid State Chem.*, 1993, **102**, 434–439.
- 74 D. Degler, S. Rank, S. Müller, H. W. Pereira de Carvalho, J.-D. Grunwaldt, U. Weimar and N. Barsan, Gold-loaded tin dioxide gas sensing materials:

- mechanistic insights and the role of gold dispersion, *Acs Sensors*, 2016, **1**, 1322–1329.
- 75 A. Staerz, T.-H. Kim, J.-H. Lee, U. Weimar and N. Barsan, Nanolevel control of gas sensing characteristics via p–n heterojunction between Rh₂O₃ clusters and WO₃ crystallites, *J. Phys. Chem. C*, 2017, **121**, 24701–24706.
- 76 D. Degler, H. W. P. de Carvalho, U. Weimar, N. Barsan, D. Pham, L. Mädler and J.-D. Grunwaldt, Structure–function relationships of conventionally and flame made Pd-doped sensors studied by X-ray absorption spectroscopy and DC-resistance, *Sensors Actuators B Chem.*, 2015, **219**, 315–323.
- 77 A. Kolmakov, D. O. Klenov, Y. Lilach, S. Stemmer and M. Moskovits, Enhanced Gas Sensing by Individual SnO₂ Nanowires and Nanobelts Functionalized with Pd Catalyst Particles, *Nano Lett.*, 2005, **5**, 667–673.
- 78 S. Matsushima, Y. Teraoka, N. Miura and N. Yamazoe, Electronic interaction between metal additives and tin dioxide in tin dioxide-based gas sensors, *Jpn. J. Appl. Phys.*, 1988, **27**, 1798.
- 79 D. Haridas, K. Sreenivas and V. Gupta, Improved response characteristics of SnO₂ thin film loaded with nanoscale catalysts for LPG detection, *Sensors Actuators B Chem.*, 2008, **133**, 270–275.
- 80 A. M. Ruiz, A. Cornet, K. Shimanoe, J. R. Morante and N. Yamazoe, Effects of various metal additives on the gas sensing performances of TiO₂ nanocrystals obtained from hydrothermal treatments, *Sensors Actuators B Chem.*, 2005, **108**, 34–40.
- 81 S. Vallejos, T. Stoycheva, P. Umek, C. Navio, R. Snyders, C. Bittencourt, E. Llobet, C. Blackman, S. Moniz and X. Correig, Au nanoparticle-functionalised WO₃ nanoneedles and their application in high sensitivity gas sensor devices, *Chem. Commun.*, 2011, **47**, 565–567.
- 82 F. E. Annanouch, Z. Haddi, M. Ling, F. Di Maggio, S. Vallejos, T. Vilic, Y. Zhu, T. Shujah, P. Umek and C. Bittencourt, Aerosol-assisted CVD-grown PdO nanoparticle-decorated tungsten oxide nanoneedles extremely sensitive and

- selective to hydrogen, *ACS Appl. Mater. Interfaces*, 2016, **8**, 10413–10421.
- 83 W. P. Sari, C. Blackman, Y. Zhu and J. A. Covington, AACVD Grown WO₃ Nanoneedles Decorated With Ag/Ag₂O Nanoparticles for Oxygen Measurement in a Humid Environment, *IEEE Sens. J.*, 2018, **19**, 826–832.
- 84 K. Fujimoto, in *Studies in Surface Science and Catalysis*, Elsevier, 1993, vol. 77, pp. 9–16.
- 85 T. Hyodo, Y. Baba, K. Wada, Y. Shimizu and M. Egashira, Hydrogen sensing properties of SnO₂ varistors loaded with SiO₂ by surface chemical modification with diethoxydimethylsilane, *Sensors Actuators B Chem.*, 2000, **64**, 175–181.
- 86 G. Korotcenkov, V. Brinzari, L. B. Gulina and B. K. Cho, The influence of gold nanoparticles on the conductivity response of SnO₂-based thin film gas sensors, *Appl. Surf. Sci.*, 2015, **353**, 793–803.
- 87 N. Yamazoe, Y. Kurokawa and T. Seiyama, Effects of additives on semiconductor gas sensors, *Sensors and Actuators*, 1983, **4**, 283–289.
- 88 F. Lu, Y. Liu, M. Dong and X. Wang, Nanosized tin oxide as the novel material with simultaneous detection towards CO, H₂ and CH₄, *Sensors Actuators B Chem.*, 2000, **66**, 225–227.
- 89 S. G. Ansari, P. Boroojerdian, S. R. Sainkar, R. N. Karekar, R. C. Aiyer and S. K. Kulkarni, Grain size effects on H₂ gas sensitivity of thick film resistor using SnO₂ nanoparticles, *Thin Solid Films*, 1997, **295**, 271–276.
- 90 H. Liu, S. P. Gong, Y. X. Hu, J. Q. Liu and D. X. Zhou, Properties and mechanism study of SnO₂ nanocrystals for H₂S thick-film sensors, *Sensors Actuators B Chem.*, 2009, **140**, 190–195.
- 91 G. Korotcenkov, V. Brinzari, M. Ivanov, A. Cerneavschi, J. Rodriguez, A. Cirera, A. Cornet and J. Morante, Structural stability of indium oxide films deposited by spray pyrolysis during thermal annealing, *Thin Solid Films*, 2005, **479**, 38–51.
- 92 C. N. R. Rao, G. U. Kulkarni, P. J. Thomas and P. P. Edwards, Size-dependent chemistry: properties of nanocrystals, *Chem. Eur. J.*, 2002, **8**, 28–35.
- 93 D. H. Kim, J. Y. Yoon, H. C. Park and K. H. Kim, CO₂-sensing characteristics of

- SnO₂ thick film by coating lanthanum oxide, *Sensors Actuators B Chem.*, 2000, **62**, 61–66.
- 94 O. Wurzinger and G. Reinhardt, CO-sensing properties of doped SnO₂ sensors in H₂-rich gases, *Sensors Actuators B Chem.*, 2004, **103**, 104–110.
- 95 D. Kohl, Surface processes in the detection of reducing gases with SnO₂-based devices, *Sensors and actuators*, 1989, **18**, 71–113.
- 96 N. Barsan, M. Schweizer-Berberich and W. Göpel, Fundamental and practical aspects in the design of nanoscaled SnO₂ gas sensors: a status report, *Fresenius. J. Anal. Chem.*, 1999, **365**, 287–304.
- 97 P. K. Kannan, R. Saraswathi and J. B. B. Rayappan, A highly sensitive humidity sensor based on DC reactive magnetron sputtered zinc oxide thin film, *Sensors Actuators A Phys.*, 2010, **164**, 8–14.
- 98 Z. Bai, C. Xie, M. Hu, S. Zhang and D. Zeng, Effect of humidity on the gas sensing property of the tetrapod-shaped ZnO nanopowder sensor, *Mater. Sci. Eng. B*, 2008, **149**, 12–17.
- 99 I. Hotovy, V. Rehacek, P. Siciliano, S. Capone and L. Spiess, Sensing characteristics of NiO thin films as NO₂ gas sensor, *Thin Solid Films*, 2002, **418**, 9–15.
- 100 P. Dias, T. Lopes, L. Meda, L. Andrade and A. Mendes, Photoelectrochemical water splitting using WO₃ photoanodes: the substrate and temperature roles, *Phys. Chem. Chem. Phys.*, 2016, **18**, 5232–5243.
- 101 B. Cole, B. Marsen, E. Miller, Y. Yan, B. To, K. Jones and M. Al-Jassim, Evaluation of nitrogen doping of tungsten oxide for photoelectrochemical water splitting, *J. Phys. Chem. C*, 2008, **112**, 5213–5220.
- 102 I. M. Szilágyi, B. Fórizs, O. Rosseler, Á. Szegedi, P. Németh, P. Király, G. Tárkányi, B. Vajna, K. Varga-Josepovits and K. László, WO₃ photocatalysts: Influence of structure and composition, *J. Catal.*, 2012, **294**, 119–127.
- 103 Y. Wicaksana, S. Liu, J. Scott and R. Amal, Tungsten trioxide as a visible light photocatalyst for volatile organic carbon removal, *Molecules*, 2014, **19**, 17747–

- 17762.
- 104 S. Ashraf, C. S. Blackman, R. G. Palgrave, S. C. Naisbitt and I. P. Parkin, Aerosol assisted chemical vapour deposition of WO₃ thin films from tungsten hexacarbonyl and their gas sensing properties, *J. Mater. Chem.*, 2007, **17**, 3708–3713.
- 105 H. Simchi, B. E. McCandless, T. Meng and W. N. Shafarman, Structural, optical, and surface properties of WO₃ thin films for solar cells, *J. Alloys Compd.*, 2014, **617**, 609–615.
- 106 V. R. Buch, A. K. Chawla and S. K. Rawal, Review on electrochromic property for WO₃ thin films using different deposition techniques, *Mater. Today Proc.*, 2016, **3**, 1429–1437.
- 107 S. K. Deb, Opportunities and challenges in science and technology of WO₃ for electrochromic and related applications, *Sol. Energy Mater. Sol. Cells*, 2008, **92**, 245–258.
- 108 S. Balaji, Y. Djaoued, A.-S. Albert, R. Z. Ferguson and R. Brüning, Hexagonal tungsten oxide based electrochromic devices: spectroscopic evidence for the Li ion occupancy of four-coordinated square windows, *Chem. Mater.*, 2009, **21**, 1381–1389.
- 109 P. M. Woodward, A. W. Sleight and T. Vogt, Ferroelectric tungsten trioxide, *J. Solid State Chem.*, 1997, **131**, 9–17.
- 110 C. V Ramana, S. Utsunomiya, R. C. Ewing, C. M. Julien and U. Becker, Structural stability and phase transitions in WO₃ thin films, *J. Phys. Chem. B*, 2006, **110**, 10430–10435.
- 111 E. K. H. Salje, S. Rehmman, F. Pobell, D. Morris, K. S. Knight, T. Herrmannsdörfer and M. T. Dove, Crystal structure and paramagnetic behaviour of, *J. Phys. Condens. Matter*, 1997, **9**, 6563.
- 112 T. Vogt, P. M. Woodward and B. A. Hunter, The high-temperature phases of WO₃, *J. Solid State Chem.*, 1999, **144**, 209–215.
- 113 B. Gerand, G. Nowogrocki, J. Guenot and M. Figlarz, Structural study of a new

- hexagonal form of tungsten trioxide, *J. Solid State Chem.*, 1979, **29**, 429–434.
- 114 D. B. Migas, V. L. Shaposhnikov and V. E. Borisenko, Tungsten oxides. II. The metallic nature of Magnéli phases, *J. Appl. Phys.*, 2010, **108**, 93714.
- 115 H. Zhou, Y. Shi, L. Wang, H. Zhang, C. Zhao, A. Hagfeldt and T. Ma, Notable catalytic activity of oxygen-vacancy-rich WO_{2.72} nanorod bundles as counter electrodes for dye-sensitized solar cells, *Chem. Commun.*, 2013, **49**, 7626–7628.
- 116 M. Seifollahi Bazarjani, M. Hojamberdiev, K. Morita, G. Zhu, G. Cherkashinin, C. Fasel, T. Herrmann, H. Breitzke, A. Gurlo and R. Riedel, Visible light photocatalysis with c-WO_{3-x}/WO₃·H₂O nanoheterostructures in situ formed in mesoporous polycarbosilane-siloxane polymer, *J. Am. Chem. Soc.*, 2013, **135**, 4467–4475.
- 117 G. Xi, J. Ye, Q. Ma, N. Su, H. Bai and C. Wang, In situ growth of metal particles on 3D urchin-like WO₃ nanostructures, *J. Am. Chem. Soc.*, 2012, **134**, 6508–6511.
- 118 X. Lu, T. Zhai, X. Zhang, Y. Shen, L. Yuan, B. Hu, L. Gong, J. Chen, Y. Gao and J. Zhou, WO_{3-x}@Au@MnO₂ core-shell nanowires on carbon fabric for high-performance flexible supercapacitors, *Adv. Mater.*, 2012, **24**, 938–944.
- 119 X. Liu, M. Song, S. Wang and Y. He, Structure and field-emission properties of W/WO_{2.72} heterostructures fabricated by vapour deposition, *Phys. E Low-dimensional Syst. Nanostructures*, 2013, **53**, 260–265.
- 120 D. R. Shinde, P. G. Chavan, S. Sen, D. S. Joag, M. A. More, S. C. Gadkari and S. K. Gupta, Enhanced field-emission from SnO₂:WO_{2.72} nanowire heterostructures, *ACS Appl. Mater. Interfaces*, 2011, **3**, 4730–4735.
- 121 V. V. Pokropivny and V. V. Skorokhod, Classification of nanostructures by dimensionality and concept of surface forms engineering in nanomaterial science, *Mater. Sci. Eng. C*, 2007, **27**, 990–993.
- 122 H. Gleiter, Nanostructured materials: basic concepts and microstructure, *Acta Mater.*, 2000, **48**, 1–29.

- 123 H. Gao, H. Jia, B. Bierer, J. Wöllenstein, Y. Lu and S. Palzer, Scalable gas sensors fabrication to integrate metal oxide nanoparticles with well-defined shape and size, *Sensors Actuators B Chem.*, 2017, **249**, 639–646.
- 124 X.-L. Li, T.-J. Lou, X.-M. Sun and Y.-D. Li, Highly sensitive WO₃ hollow-sphere gas sensors, *Inorg. Chem.*, 2004, **43**, 5442–5449.
- 125 Y. Zhang, W. He, H. Zhao and P. Li, Template-free to fabricate highly sensitive and selective acetone gas sensor based on WO₃ microspheres, *Vacuum*, 2013, **95**, 30–34.
- 126 S. Shukla, S. Chaudhary, A. Umar, G. R. Chaudhary and S. K. Mehta, Tungsten oxide (WO₃) nanoparticles as scaffold for the fabrication of hydrazine chemical sensor, *Sensors Actuators B Chem.*, 2014, **196**, 231–237.
- 127 S. Bai, K. Zhang, R. Luo, D. Li, A. Chen and C. C. Liu, Low-temperature hydrothermal synthesis of WO₃ nanorods and their sensing properties for NO₂, *J. Mater. Chem.*, 2012, **22**, 12643–12650.
- 128 S. Ashraf, C. S. Blackman, R. G. Palgrave and I. P. Parkin, Aerosol-assisted chemical vapour deposition of WO₃ thin films using polyoxometallate precursors and their gas sensing properties, *J. Mater. Chem.*, 2007, **17**, 1063–1070.
- 129 S. Piperno, M. Passacantando, S. Santucci, L. Lozzi and S. La Rosa, WO₃ nanofibers for gas sensing applications, *J. Appl. Phys.*, 2007, **101**, 124504.
- 130 Z.-X. Cai, H.-Y. Li, X.-N. Yang and X. Guo, NO sensing by single crystalline WO₃ nanowires, *Sensors Actuators B Chem.*, 2015, **219**, 346–353.
- 131 R. S. Devan, R. A. Patil, J. Lin and Y. Ma, One-dimensional metal-oxide nanostructures: recent developments in synthesis, characterization, and applications, *Adv. Funct. Mater.*, 2012, **22**, 3326–3370.
- 132 X. Song, Y. Zhao and Y. Zheng, Hydrothermal synthesis of tungsten oxide nanobelts, *Mater. Lett.*, 2006, **60**, 3405–3408.
- 133 F. Ji, X. Ren, X. Zheng, Y. Liu, L. Pang, J. Jiang and S. F. Liu, 2D-MoO₃ nanosheets for superior gas sensors, *Nanoscale*, 2016, **8**, 8696–8703.
- 134 J. Xu, Z. Xue, N. Qin, Z. Cheng and Q. Xiang, The crystal facet-dependent gas

- sensing properties of ZnO nanosheets: Experimental and computational study, *Sensors Actuators B Chem.*, 2017, **242**, 148–157.
- 135 R. Godbole, V. P. Godbole and S. Bhagwat, Surface morphology dependent tungsten oxide thin films as toxic gas sensor, *Mater. Sci. Semicond. Process.*, 2017, **63**, 212–219.
- 136 M. B. Rahmani, M. H. Yaacob and Y. M. Sabri, Hydrogen sensors based on 2D WO₃ nanosheets prepared by anodization, *Sensors Actuators B Chem.*, 2017, **251**, 57–64.
- 137 Z. Wang, D. Wang and J. Sun, Controlled synthesis of defect-rich ultrathin two-dimensional WO₃ nanosheets for NO₂ gas detection, *Sensors Actuators B Chem.*, 2017, **245**, 828–834.
- 138 T. Lin, X. Lv, S. Li and Q. Wang, The morphologies of the semiconductor oxides and their gas-sensing properties, *Sensors*, 2017, **17**, 2779.
- 139 A. Yan, C. Xie, D. Zeng, S. Cai and H. Li, Synthesis, formation mechanism and illuminated sensing properties of 3D WO₃ nanowall, *J. Alloys Compd.*, 2010, **495**, 88–92.
- 140 Y. Qin, F. Wang, W. Shen and M. Hu, Mesoporous three-dimensional network of crystalline WO₃ nanowires for gas sensing application, *J. Alloys Compd.*, 2012, **540**, 21–26.
- 141 C. Wang, R. Sun, X. Li, Y. Sun, P. Sun, F. Liu and G. Lu, Hierarchical flower-like WO₃ nanostructures and their gas sensing properties, *Sensors Actuators B Chem.*, 2014, **204**, 224–230.
- 142 K. Ozga, M. Oyama, M. Szota, M. Napiórek, I. V. Kityk, A. Ślęzak, A. A. Umar and K. Nouneh, Photoinduced absorption of Ag nanoparticles deposited on ITO substrate, *J. Alloys Compd.*, 2011, **509**, S424–S426.
- 143 A. N. Shipway, E. Katz and I. Willner, Nanoparticle arrays on surfaces for electronic, optical, and sensor applications, *ChemPhysChem*, 2000, **1**, 18–52.
- 144 E. Sanli, B. Z. Uysal and M. L. Aksu, The oxidation of NaBH₄ on electrochemically treated silver electrodes, *Int. J. Hydrogen Energy*, 2008, **33**,

- 2097–2104.
- 145 E. Navarrete, E. González, T. Vilic and E. Llobet, in *Multidisciplinary Digital Publishing Institute Proceedings*, 2017, vol. 1, p. 438.
- 146 A. S. M. I. Uddin, D.-T. Phan and G.-S. Chung, Low temperature acetylene gas sensor based on Ag nanoparticles-loaded ZnO-reduced graphene oxide hybrid, *Sensors Actuators B Chem.*, 2015, **207**, 362–369.
- 147 Y. Ida, S. Watase, T. Shinagawa, M. Watanabe, M. Chigane, M. Inaba, A. Tasaka and M. Izaki, Direct electrodeposition of 1.46 eV bandgap silver (I) oxide semiconductor films by electrogenerated acid, *Chem. Mater.*, 2008, **20**, 1254–1256.
- 148 W. Wang, Q. Zhao, J. Dong and J. Li, A novel silver oxides oxygen evolving catalyst for water splitting, *Int. J. Hydrogen Energy*, 2011, **36**, 7374–7380.
- 149 Q. Simon, D. Barreca, D. Bekermann, A. Gasparotto, C. Maccato, E. Comini, V. Gombac, P. Fornasiero, O. I. Lebedev and S. Turner, Plasma-assisted synthesis of Ag/ZnO nanocomposites: First example of photo-induced H₂ production and sensing, *Int. J. Hydrogen Energy*, 2011, **36**, 15527–15537.
- 150 Q. Xiang, G. Meng, Y. Zhang, J. Xu, P. Xu, Q. Pan and W. Yu, Ag nanoparticle embedded-ZnO nanorods synthesized via a photochemical method and its gas-sensing properties, *Sensors Actuators B Chem.*, 2010, **143**, 635–640.
- 151 M. E. Aguirre, H. B. Rodríguez, E. San Román, A. Feldhoff and M. A. Grela, Ag@ ZnO core–shell nanoparticles formed by the timely reduction of Ag⁺ ions and zinc acetate hydrolysis in N, N-dimethylformamide: mechanism of growth and photocatalytic properties, *J. Phys. Chem. C*, 2011, **115**, 24967–24974.
- 152 V. V Kondalkar, S. S. Mali, R. R. Kharade, K. V Khot, P. B. Patil, R. M. Mane, S. Choudhury, P. S. Patil, C. K. Hong and J. H. Kim, High performing smart electrochromic device based on honeycomb nanostructured h-WO₃ thin films: hydrothermal assisted synthesis, *Dalt. Trans.*, 2015, **44**, 2788–2800.
- 153 F. Zheng, M. Zhang and M. Guo, Controllable preparation of WO₃ nanorod arrays by hydrothermal method, *Thin Solid Films*, 2013, **534**, 45–53.

- 154 C. Cantalini, H. T. Sun, M. Faccio, M. Pelino, S. Santucci, L. Lozzi and M. Passacantando, NO₂ sensitivity of WO₃ thin film obtained by high vacuum thermal evaporation, *Sensors Actuators B Chem.*, 1996, **31**, 81–87.
- 155 A. Ponzoni, E. Comini, M. Ferroni and G. Sberveglieri, Nanostructured WO₃ deposited by modified thermal evaporation for gas-sensing applications, *Thin Solid Films*, 2005, **490**, 81–85.
- 156 A. Kafizas, L. Francàs, C. Sotelo-Vazquez, M. Ling, Y. Li, E. Glover, L. McCafferty, C. Blackman, J. Darr and I. Parkin, Optimizing the activity of nanoneedle structured WO₃ photoanodes for solar water splitting: direct synthesis via chemical vapour deposition, *J. Phys. Chem. C*, 2017, **121**, 5983–5993.
- 157 R. U. Kirss and L. Meda, Chemical vapour deposition of tungsten oxide, *Appl. Organomet. Chem.*, 1998, **12**, 155–160.
- 158 C. C. Chen, C.-H. Cheng and C.-K. Lin, Template assisted fabrication of TiO₂ and WO₃ nanotubes, *Ceram. Int.*, 2013, **39**, 6631–6636.
- 159 E. Comini, C. Baratto, I. Concina, G. Faglia, M. Falasconi, M. Ferroni, V. Galstyan, E. Gobbi, A. Ponzoni and A. Vomiero, Metal oxide nanoscience and nanotechnology for chemical sensors, *Sensors Actuators B Chem.*, 2013, **179**, 3–20.
- 160 K. L. Choy, Chemical vapour deposition of coatings, *Prog. Mater. Sci.*, 2003, **48**, 57–170.
- 161 H. O. Pierson, *Handbook of chemical vapour deposition: principles, technology and applications*, William Andrew, 1999.
- 162 X. Hou and K. Choy, Processing and Applications of Aerosol-Assisted Chemical Vapour Deposition, *Chem. Vap. Depos.*, 2006, **12**, 583–596.
- 163 C. E. Knapp and C. J. Carmalt, Solution based CVD of main group materials, *Chem. Soc. Rev.*, 2016, **45**, 1036–1064.
- 164 M. Ling and C. Blackman, Growth mechanism of planar or nanorod structured tungsten oxide thin films deposited via aerosol assisted chemical vapour

- deposition (AACVD), *Phys. status solidi*, 2015, **12**, 869–877.
- 165 S. Shaukat, M. Khaleeq-ur-Rahman, I. M. Dildar and R. Binions, Aerosol assisted chemical vapour deposition (AACVD) synthesis of nanostructured cauliflower patterning in MWCNT doped tungsten oxide, *Ceram. Int.*, 2019, **45**, 1918–1927.
- 166 T. Shujah, D. M. Ikram, A. Butt, M. Shahzad, K. Rashid and Q. Zafar, H₂S Gas Sensor Based on WO₃ Nanostructures Synthesized via Aerosol Assisted Chemical Vapour Deposition Technique, *Nanosci. Nanotechnol. Lett.*, 2019, **Vol. 11**, 1–10.
- 167 D. P. DePuccio and C. C. Landry, Photocatalytic oxidation of methanol using porous Au/WO₃ and visible light, *Catal. Sci. Technol.*, 2016, **6**, 7512–7520.
- 168 S. Jayaraman, T. F. Jaramillo, S.-H. Baeck and E. W. McFarland, Synthesis and characterization of Pt–WO₃ as methanol oxidation catalysts for fuel cells, *J. Phys. Chem. B*, 2005, **109**, 22958–22966.
- 169 A. Boudiba, C. Zhang, P. Umek, C. Bittencourt, R. Snyders, M.-G. Olivier and M. Debliqy, Sensitive and rapid hydrogen sensors based on Pd–WO₃ thick films with different morphologies, *Int. J. Hydrogen Energy*, 2013, **38**, 2565–2577.
- 170 X. Fang, L. Hu, C. Ye and L. Zhang, One-dimensional inorganic semiconductor nanostructures: a new carrier for nanosensors, *Pure Appl. Chem.*, 2010, **82**, 2185–2198.
- 171 A. Kolmakov, X. Chen and M. Moskovits, Functionalizing nanowires with catalytic nanoparticles for gas sensing application, *J. Nanosci. Nanotechnol.*, 2008, **8**, 111–121.
- 172 M. T. Swihart, Vapour-phase synthesis of nanoparticles, *Curr. Opin. Colloid Interface Sci.*, 2003, **8**, 127–133.
- 173 F. E. Annanouch, Z. Haddi, S. Vallejos, P. Umek, P. Guttman, C. Bittencourt and E. Llobet, Aerosol-assisted CVD-grown WO₃ nanoneedles decorated with copper oxide nanoparticles for the selective and humidity-resilient detection of H₂S, *ACS Appl. Mater. Interfaces*, 2015, **7**, 6842–6851.

- 174 R. C. Evans, P. Douglas, J. A. G. Williams and D. L. Rochester, A novel luminescence-based colorimetric oxygen sensor with a “traffic light” response, *J. Fluoresc.*, 2006, **16**, 201–206.
- 175 H. Aizawa, T. Katsumata and S. Komuro, in *SICE Annual Conference 2007*, IEEE, 2007, pp. 1762–1765.
- 176 N. Shehata, K. Meehan, I. Ashry, I. Kandas and Y. Xu, Lanthanide-doped ceria nanoparticles as fluorescence-quenching probes for dissolved oxygen, *Sensors Actuators B Chem.*, 2013, **183**, 179–186.
- 177 A. Tiburcio-Silver and A. Sanchez-Juarez, SnO₂: Ga thin films as oxygen gas sensor, *Mater. Sci. Eng. B*, 2004, **110**, 268–271.
- 178 C.-Y. Lu, S.-P. Chang, S.-J. Chang, T.-J. Hsueh, C.-L. Hsu, Y.-Z. Chiou and I.-C. Chen, ZnO nanowire-based oxygen gas sensor, *IEEE Sens. J.*, 2009, **9**, 485–489.
- 179 G. Neri, A. Bonavita, G. Micali, G. Rizzo, N. Pinna and M. Niederberger, In₂O₃ and Pt-In₂O₃ nanopowders for low temperature oxygen sensors, *Sensors Actuators B Chem.*, 2007, **127**, 455–462.
- 180 N. Izu, W. Shin, N. Murayama and S. Kanzaki, Resistive oxygen gas sensors based on CeO₂ fine powder prepared using mist pyrolysis, *Sensors Actuators B Chem.*, 2002, **87**, 95–98.
- 181 S. Vallejos, S. Selina, F. E. Annanouch, I. Gràcia, E. Llobet and C. Blackman, Aerosol assisted chemical vapour deposition of gas sensitive SnO₂ and Au-functionalised SnO₂ nanorods via a non-catalysed vapour solid (VS) mechanism, *Sci. Rep.*, 2016, **6**, 28464.
- 182 S. Vallejos, P. Umek, T. Stoycheva, F. Annanouch, E. Llobet, X. Correig, P. De Marco, C. Bittencourt and C. Blackman, Single-Step Deposition of Au- and Pt-Nanoparticle-Functionalized Tungsten Oxide Nanoneedles Synthesized Via Aerosol-Assisted CVD, and Used for Fabrication of Selective Gas Microsensor Arrays, *Adv. Funct. Mater.*, 2013, **23**, 1313–1322.
- 183 Y. Baek and K. Yong, Controlled growth and characterization of tungsten oxide

- nanowires using thermal evaporation of WO₃ powder, *J. Phys. Chem. C*, 2007, **111**, 1213–1218.
- 184 Z. Gu, Y. Ma, W. Yang, G. Zhang and J. Yao, Self-assembly of highly oriented one-dimensional h-WO₃ nanostructures, *Chem. Commun.*, 2005, 3597–3599.
- 185 M. J. Hudson, J. W. Peckett and P. J. F. Harris, A new and effective synthesis of non-stoichiometric metal oxides such as oxygen-deficient WO_{2.72}, *J. Mater. Chem.*, 2003, **13**, 445–446.
- 186 M. Righettoni, A. Amann and S. E. Pratsinis, Breath analysis by nanostructured metal oxides as chemo-resistive gas sensors, *Mater. Today*, 2015, **18**, 163–171.
- 187 P. J. Shaver, Activated tungsten oxide gas detectors, *Appl. Phys. Lett.*, 1967, **11**, 255–257.
- 188 K. Kanda and T. Maekawa, Development of a WO₃ thick-film-based sensor for the detection of VOC, *Sensors Actuators B Chem.*, 2005, **108**, 97–101.
- 189 D. Gogova, K. Gesheva, A. Kakanakova-Georgieva and M. Surtchev, Investigation of the structure of tungsten oxide films obtained by chemical vapour deposition, *Eur. Phys. Journal-Applied Phys.*, 2000, **11**, 167–174.
- 190 W. B. Cross, I. P. Parkin, S. A. O'Neill, P. A. Williams, M. F. Mahon and K. C. Molloy, Tungsten oxide coatings from the aerosol-assisted chemical vapour deposition of W (OAr)₆ (Ar= C₆H₅, C₆H₄F-4, C₆H₃F₂-3, 4); photocatalytically active γ -WO₃ films, *Chem. Mater.*, 2003, **15**, 2786–2796.
- 191 C. Navío, S. Vallejos, T. Stoycheva, E. Llobet, X. Correig, R. Snyders, C. Blackman, P. Umek, X. Ke and G. Van Tendeloo, Gold clusters on WO₃ nanoneedles grown via AACVD: XPS and TEM studies, *Mater. Chem. Phys.*, 2012, **134**, 809–813.
- 192 S. Lee, K. Teshima, M. Fujisawa, S. Fujii, M. Endo and S. Oishi, Fabrication of highly ordered, macroporous Na₂W₄O₁₃ arrays by spray pyrolysis using polystyrene colloidal crystals as templates, *Phys. Chem. Chem. Phys.*, 2009, **11**, 3628–3633.
- 193 F. E. Annanouch, S. Roso, Z. Haddi, S. Vallejos, P. Umek, C. Bittencourt, C.

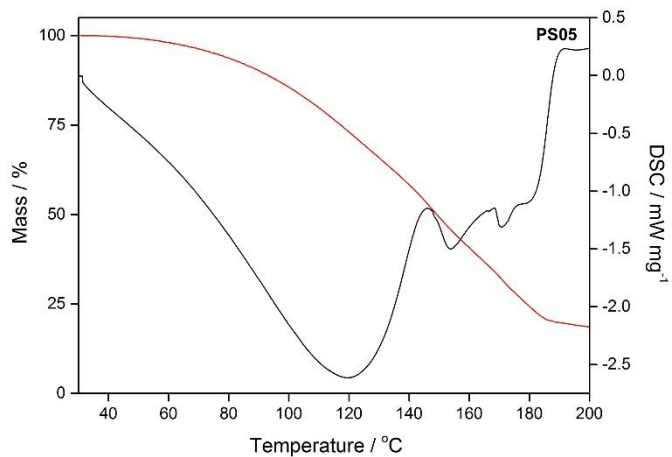
- Blackman, T. Vilic and E. Llobet, p-Type PdO nanoparticles supported on n-type WO₃ nanoneedles for hydrogen sensing, *Thin Solid Films*, 2016, **618**, 238–245.
- 194 T. Vilic and E. Llobet, Nickel doped WO₃ nanoneedles deposited by a single step AACVD for gas sensing applications, *Procedia Eng.*, 2016, **168**, 206–210.
- 195 F. Di Maggio, M. Ling, A. Tsang, J. Covington, J. Saffell and C. Blackman, Aerosol-assisted CVD synthesis, characterisation and gas-sensing application of gold-functionalised tungsten oxide, *J. Sensors Sens. Syst.*, 2014, **3**, 325–330.
- 196 S. Vallejos, I. Gràcia, J. Bravo, E. Figueras, J. Hubálek and C. Cané, Detection of volatile organic compounds using flexible gas sensing devices based on tungsten oxide nanostructures functionalized with Au and Pt nanoparticles, *Talanta*, 2015, **139**, 27–34.
- 197 S. Aziz, R. Abdulwahid, M. Rasheed, O. Abdullah and H. Ahmed, Polymer blending as a novel approach for tuning the SPR peaks of silver nanoparticles, *Polymers (Basel)*, 2017, **9**, 486.
- 198 A. J. Haes and R. P. Van Duyne, A nanoscale optical biosensor: sensitivity and selectivity of an approach based on the localized surface plasmon resonance spectroscopy of triangular silver nanoparticles, *J. Am. Chem. Soc.*, 2002, **124**, 10596–10604.
- 199 E. Albitar, M. A. Valenzuela, S. Alfaro, G. Valverde-Aguilar and F. M. Martínez-Pallares, Photocatalytic deposition of Ag nanoparticles on TiO₂: Metal precursor effect on the structural and photoactivity properties, *J. Saudi Chem. Soc.*, 2015, **19**, 563–573.
- 200 O. A. D. Gallardo, R. Moiraghi, M. A. Macchione, J. A. Godoy, M. A. Pérez, E. A. Coronado and V. A. Macagno, Silver oxide particles/silver nanoparticles interconversion: susceptibility of forward/backward reactions to the chemical environment at room temperature, *RSC Adv.*, 2012, **2**, 2923–2929.
- 201 B. Boruah, R. Gupta, J. M. Modak and G. Madras, Novel insights into the properties of AgBiO₃ photocatalyst and its application in immobilized state for 4-nitrophenol degradation and bacteria inactivation, *J. Photochem. Photobiol. A*

- Chem.*, 2019, **373**, 105–115.
- 202 J. Xu, X. Han, H. Liu and Y. Hu, Synthesis and optical properties of silver nanoparticles stabilized by gemini surfactant, *Colloids Surfaces A Physicochem. Eng. Asp.*, 2006, **273**, 179–183.
- 203 M. F. Al-Kuhaili, Characterization of thin films produced by the thermal evaporation of silver oxide, *J. Phys. D. Appl. Phys.*, 2007, **40**, 2847.
- 204 F. Y. Xie, L. Gong, X. Liu, Y. T. Tao, W. H. Zhang, S. H. Chen, H. Meng and J. Chen, XPS studies on surface reduction of tungsten oxide nanowire film by Ar⁺ bombardment, *J. Electron Spectros. Relat. Phenomena*, 2012, **185**, 112–118.
- 205 J.-B. Lee, S.-Y. Jeong, W.-J. Moon, T.-Y. Seong and H.-J. Ahn, Preparation and characterization of electro-spun RuO₂–Ag₂O composite nanowires for electrochemical capacitors, *J. Alloys Compd.*, 2011, **509**, 4336–4340.
- 206 S. B. Walker and J. A. Lewis, Reactive silver inks for patterning high-conductivity features at mild temperatures, *J. Am. Chem. Soc.*, 2012, **134**, 1419–1421.
- 207 D. K. Bhui, H. Bar, P. Sarkar, G. P. Sahoo, S. P. De and A. Misra, Synthesis and UV–vis spectroscopic study of silver nanoparticles in aqueous SDS solution, *J. Mol. Liq.*, 2009, **145**, 33–37.
- 208 A. Panneerselvam, M. A. Malik, P. O'Brien and J. Raftery, The CVD of silver sulfide and silver thin films from a homoleptic crystalline single-source precursor, *J. Mater. Chem.*, 2008, **18**, 3264–3269.
- 209 A. Panneerselvam, M. A. Malik, P. O'Brien and M. Helliwell, The Aerosol-Assisted CVD of Silver Films from Single-Source Precursors, *Chem. Vap. Depos.*, 2009, **15**, 57–63.
- 210 S. D. Ponja, S. K. Sehmi, E. Allan, A. J. MacRobert, I. P. Parkin and C. J. Carmalt, Enhanced Bactericidal Activity of Silver Thin Films Deposited via Aerosol-Assisted Chemical Vapour Deposition, *ACS Appl. Mater. Interfaces*, 2015, **7**, 28616–28623.
- 211 K.-C. Lee, S.-J. Lin, C.-H. Lin, C.-S. Tsai and Y.-J. Lu, Size effect of Ag nanoparticles on surface plasmon resonance, *Surf. Coatings Technol.*, 2008,

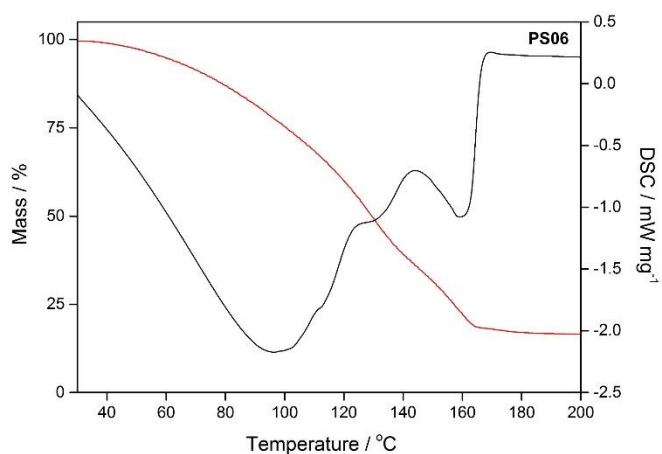
- 202**, 5339–5342.
- 212 D. Briggs, Handbook of X-ray Photoelectron Spectroscopy CD Wanger, WM Riggs, LE Davis, JF Moulder and GE Muilenberg Perkin-Elmer Corp., Physical Electronics Division, Eden Prairie, Minnesota, USA, 1979. 190 pp. \$195, *Surf. Interface Anal.*, 1981, **3**, v–v.
- 213 S. W. Han, Y. Kim and K. Kim, Dodecanethiol-derivatized Au/Ag bimetallic nanoparticles: TEM, UV/VIS, XPS, and FTIR analysis, *J. Colloid Interface Sci.*, 1998, **208**, 272–278.
- 214 B. Richter, H. Kuhlbeck, H.-J. Freund and P. S. Bagus, Cluster core-level binding-energy shifts: the role of lattice strain, *Phys. Rev. Lett.*, 2004, **93**, 26805.
- 215 I. Lopez-Salido, D. C. Lim and Y. D. Kim, Ag nanoparticles on highly ordered pyrolytic graphite (HOPG) surfaces studied using STM and XPS, *Surf. Sci.*, 2005, **588**, 6–18.
- 216 D. P. Kumar, N. L. Reddy, M. Karthik, B. Neppolian, J. Madhavan and M. V Shankar, Solar light sensitized p-Ag₂O/n-TiO₂ nanotubes heterojunction photocatalysts for enhanced hydrogen production in aqueous-glycerol solution, *Sol. Energy Mater. Sol. Cells*, 2016, **154**, 78–87.
- 217 S. Rtimi, R. Sanjines, C. Pulgarin, A. Houas, J.-C. Lavanchy and J. Kiwi, Coupling of narrow and wide band-gap semiconductors on uniform films active in bacterial disinfection under low intensity visible light: Implications of the interfacial charge transfer (IFCT), *J. Hazard. Mater.*, 2013, **260**, 860–868.
- 218 G. R. Bamwenda, K. Sayama and H. Arakawa, The effect of selected reaction parameters on the photoproduction of oxygen and hydrogen from a WO₃–Fe²⁺–Fe³⁺ aqueous suspension, *J. Photochem. Photobiol. A Chem.*, 1999, **122**, 175–183.
- 219 C. Dong, X. Liu, B. Han, S. Deng, X. Xiao and Y. Wang, Nonaqueous synthesis of Ag-functionalized In₂O₃/ZnO nanocomposites for highly sensitive formaldehyde sensor, *Sensors Actuators B Chem.*, 2016, **224**, 193–200.
- 220 X. Yang, H. Fu, L. Zhang, X. An, S. Xiong, X. Jiang and A. Yu, Enhanced gas

- sensing performance based on the fabrication of polycrystalline Ag@ TiO₂ core-shell nanowires, *Sensors Actuators B Chem.*, 2019, **286**, 483–492.
- 221 C. Lu, Chang. S Chang. S, Hsueh. T, Hsu. C, Chiou. Y, and Chen. I, ZnO Nanowire-Based Oxygen Gas Sensor, *IEEE Sensors Journal*, 2009, **9**, no. 4, 485-489.
- 222 L. M. Cukrov, P. G. McCormick, K. Galatsis and W. Wlodarski, Gas sensing properties of nanosized tin oxide synthesized by mechanochemical processing, *Sens. Actuators B*, 2001, **77**, pp. 491-495.
- 223 N. Izu, W. Shin, N. Murayama and S. Kanzaki, Resistive oxygen gas sensors based on CeO₂ fine powder prepared using mist pyrolysis, *Sens. Actuators B*, 2002, **87**, 95-98.
- 224 T. Schwebel, M. Fleischer and H. Meixner, A selective temperature compensated O₂ sensor based on Ga₂O₃ thin films, *Sens. Actuators B*, 2000, **65**, 176-180.
- 225 Z. Jiang, C. Yu, X. Fan, et al. Oxide/support interaction and surface reconstruction in the sodium tungstate (Na₂WO₄)/silica system. *The Journal of Physical Chemistry*, 1993, **97**(49): 12870-12875.
- 226 Rogers, J.V., Parkinson, C.V., Choi, Y.W. et al. A Preliminary Assessment of Silver Nanoparticle Inhibition of Monkeypox Virus Plaque Formation. *Nanoscale Res Lett*, 2008, **3**, 129.
- 227 P. Prieto, V. Nistor, K. Nouneh, M. Oyama, M. Lefdil, R. Díaz, XPS study of silver, nickel and bimetallic silver–nickel nanoparticles prepared by seed-mediated growth, *Applied Surface Science*, 2012, **258**, Issue 22, 8807-8813.
- 228 V. Tran, T. Nguyen, V. Le, I. Kim, S. Lee, C. Nguyen, Excellent photocatalytic activity of ternary Ag@WO₃@rGO nanocomposites under solar simulation irradiation, *Journal of Science: Advanced Materials and Devices*, 2021, **6**, Issue 1, 108-117.

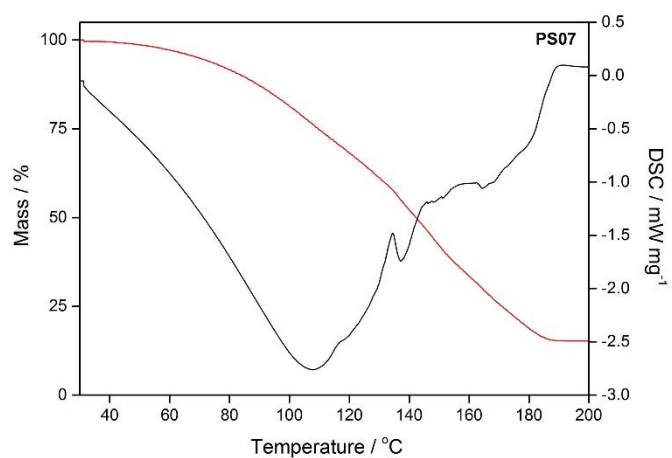
APPENDIX



(Ag-AP)



(Ag-AMP)



(Ag-EA)

Apx 1 TGA (red) and DSC (black) curves of three organometallic Ag precursors